N71-20403

NASA CR-72712

PWA FR-3704

VOLUME I

CASE FILE COPY

FINAL REPORT

STUDY OF INDUCER LOAD AND STRESS

PRATT & WHITNEY AIRCRAFT
FLORIDA RESEARCH AND DEVELOPMENT CENTER

Prepared for

NATIONAL AERONAUTICS AND SPACE ADMINISTRATION

NASA Lewis Research Center
Contract NAS3-11216
D. D. Scheer, Project Manager

NASA CR-72712
PWA FR-3704
VOLUME I

FINAL REPORT

STUDY OF INDUCER LOAD AND STRESS

PRATT & WHITNEY AIRCRAFT
FLORIDA RESEARCH AND DEVELOPMENT CENTER
BOX 2691, WEST PALM BEACH, FLORIDA 33402

Prepared for

NATIONAL AERONAUTICS AND SPACE ADMINISTRATION

31 DECEMBER 1970

Contract NAS3-11216

NASA Lewis Research Center
Cleveland, Ohio
D. D. Scheer, Project Manager
Chemical Rocket Division

FOREWORD

This report presents a summary of the work conducted under Contract NAS3-11216, "Study of Inducer Load and Stress," by the Florida Research and Development Center of Pratt & Whitney Aircraft, Mr. W. E. Young, Program Manager. The Contract was sponsored by the Lewis Research Center of the National Aeronautics and Space Administration, Cleveland, Ohio, and was administered under the technical direction of the Chemical Rocket Division with Mr. D. D. Scheer, Project Manager. This report, which covers the period 15 February 1968 to 28 February 1970, is divided into two volumes: Volume I summarizes the analytical and experimental effort devoted to developing computer programs for predicting inducer loads and stresses; Volume II presents the listings of the programs and instructions for their use.

Special recognition is hereby extended to the following Pratt & Whitney personnel who contributed in a large measure to the successful completion of the contract effort:

Mr. R. E. Davis, who supervised and directed the entire analytical effort.

Mr. L. L. Coons and Mr. C. G. Roberts, who were responsible for the formulation and development of the hydrodynamic program.

Mr. H. J. Barten, who formulated and developed the stress and vibration computer programs.

Mr. J. A. Scheurenbrand, who was responsible for programing the vibration and stress equations for computer solution.

Mr. J. M. Reddecliff, who was responsible for the conduct of the test program and the successful application of the pressure scanning valve.

ABSTRACT

A program of analysis, design, fabrication and testing has been conducted to develop computer programs for predicting rocket engine turbopump inducer hydrodynamic loading, stress magnitude and distribution, and vibration characteristics. Methods of predicting blade loading, stress, and vibration characteristics were selected from a literature search and used as a basis for the computer programs. An inducer, representative of typical rocket engine inducers, was designed fabricated, and tested with special instrumentation selected to provide measurements of blade surface pressures and stresses. Data from the tests were compared with predicted values and the computer programs were revised as required to improve correlation.

CONTENTS

SECTION		PAGE
	ILLUSTRATIONS	ix
	TABLES	xvi
	SUMMARY	1
I	INTRODUCTION	3
II	TECHNICAL PROGRAM	5
	A. Task I - Literature Survey	5
	1. General	5
	2. Hydrodynamic Loading of Inducer Blades	6
	3. Stresses and Vibrations in Inducer Blades	7
	B. Task II - Formulation of Computer Programs	8
	1. Hydrodynamic Computer Program	8
	2. Stress and Vibration Computer Programs	40
	C. Task III - Design of Test Inducer	74
	1. Inducer Design and Analysis	74
	2. Instrumentation Design	78
	3. Test Rig Design	84
	D. Task IV - Detail Design	86
	E. Task V - Fabrication	86
	F. Task VI - Experimental Testing and Computer Program Development	86
	1. Static Load Testing	88
	2. Vibration Testing	91
	3. Operational Testing	110
	G. References	203
III	CONCLUDING REMARKS	205
	APPENDIX A - Literature Survey	207
	APPENDIX B - Resumes of Source Material	217
	APPENDIX C - Formulation of Hydrodynamic Computer Program	223

CONTENTS (Continued)

SECTION		Page
	APPENDIX D - Derivation of Basic Relations for Stress and Vibration Computer Programs	243
	APPENDIX E - Nomenclature	267

ILLUSTRATIONS

FIGURE		PAGE
1	Distinct Vapor Cavity Forms During Cavitation	10
2	Thickness Distribution of Typical Blade	11
3	Typical Velocity Diagram	13
4	Schematic of Flow Passage	13
5	Inducer Velocity Diagram	15
6	Effect of Inertial Lag on Deviation Due to Incidence .	16
7	Schematic Cascade Section for Normal Loading Analysis	21
8	Conversion of Blade Normal Loading to Blade Circumferential Loading	24
9	Fluid Element with Vapor Cavity	28
10	Surfaces of Fluid Element	29
11	Pressure Force Due to Streamtube Convergence	31
12	Pressure Force Due to Cavity Growth and Passage Convergence	31
13	Centrifugal Force on Liquid Element	32
14	Typical Cavity Collapse	34
15	Paddle Wheel Geometry and Operating Conditions	35
16	Paddle Wheel Test Case - Radial Equilibrium	36
17	Comparison of Predicted and Actual Head-Flow Coefficient for NASA 12-deg Inducer	37
18	Comparison of Predicted and Actual Ideal Head Coefficient for NASA 12-deg Inducer	38
19	Comparison of Predicted and Actual Head Loss Coefficient for NASA 12-deg Inducer	38
20	Comparison of Predicted and Actual Efficiency for NASA 12-deg Inducer	39

ILLUSTRATIONS (Continued)

FIGURE		PAGE
21	Comparison of Cavity Height Prediction	41
22	Comparison of Credited and Actual Suction Performance for NASA 12-deg Inducer	42
23	Turbopump Inducer	44
24	Geometric Parameters of Middle Surface of Inducer Blade	45
25	Local [$\bar{x}$, $\bar{y}$, $\bar{z}$] and Common [x, y, z] Rectangular Coordinate System for Triangular Element	45
26	Triangulation of Inducer Blade	46
27	Generalized Nodal Local Membrane Displacements and Forces on Flat Triangular Element	50
28	Generalized Nodal Bending Displacements and Forces on Flat Triangular Element	50
29	Common Node of 6 Neighboring Triangles	54
30	Division of System Into Subsystems	55
31	Definition of Quasi-Normal Coordinate System	58
32	Breakup of 45-Degree Sector	62
33	Radial Displacements in Rotating 45-Degree Sector . . .	63
34	Radial Membrane Stresses in Rotating 45-Degree Sector with 30 Free Nodes	63
35	Radial Membrane Stresses in Rotating 45-Degree Sector at Midchord	64
36	Transverse Midchord Displacement of Uniformly Loaded 45-Degree Cantilevered Sector	64
37	Radial Bending Stresses in Uniformly Loaded 45-Degree Cantilever Sector with 30 Free Nodes	65
38	Radial Bending Stresses in Uniformly Loaded 45-Degree Cantilevered Sector [Midchord]	65
39	Breakup of 2-inch by 3-inch Rectangle into 48 Triangular Elements and 30 Free Nodes	66

ILLUSTRATIONS (Continued)

FIGURE		PAGE
40	Radial Displacements in Rotating Rectangle with 30 Free Nodes	66
41	Radial Stresses in Rotating Rectangle with 30 Free Nodes	67
42	Transverse Midchord Displacement of Uniformly Loaded Cantilever with 30 Free Nodes	67
43	Radial Bending Stress in Uniformly Loaded Cantilever with 30 Free Nodes	68
44	Breakup of Circular Disk into 96 Triangular Elements and 48 Free Nodes	69
45	Radial Displacements in 48 Node Spinning Disk	69
46	Radial and Tangential Membrane Stresses in 48 Node Spinning Disk	70
47	Breakup of 1-inch by 2-inch Rectangular Plate into 64 Triangular Elements and 40 Free Nodes	72
48	Comparison of Mode Shapes of Cantilever Plate	72
49	Relative Vibratory Bending Stresses in a Cantilever Beam (2 x 1)	73
50	Inducer Flow Path and Blade Angle Distribution	77
51	Inducer Mean Passage Velocity Profile	78
52	Pressure Scanning Valve - Transducer Assembly	79
53	Schematic of Pressure Scanning Valve	79
54	Pressure Scanning Valve in Inducer Hub	80
55	Blade Surface Pressure Tap Locations - Blades	82
56	Miniature Transducer	83
57	Miniature Transducer Locations - Blade No. 3	84
58	Inducer Test Rig Design	85
59	Test Rig Modifications	87

ILLUSTRATIONS (Continued)

FIGURE		PAGE
60	View of Static Load Test Setup	89
61	Finite Element Break-up 90 Element	90
62	Inducer Static Load Stresscoat Patterns	91
63	Inducer Vibratory Load Stresscoat Patterns	101
64	Schematic of Water Flow Loop	110
65	Performance Pressure Instrumentation Locations	114
66	View of Inducer After Machining and Before Installation of Pressure Tubing	118
67	View of Temperature Compensation Modules in Inducer Hub	118
68	Exploded View of Inducer and Pressure Scanning Valve	119
69	View of Inducer Installed in Test Rig	119
70	Overall View of Test Rig	120
71	View of Strain Gaged Inducer Prior to Test	121
72	Comparison of Integrated and Flowmeter Measured Flow at Rotor Exit	125
73	Radial Distribution of Inlet Flow Angle C = 0.061 in. (0.155 cm)	130
74	Critical Flow Coefficient vs Tip Blade Angle	131
75	Predicted Critical Flow Coefficient Based on Potential Flow Theory	133
76	Radial Distribution of Inlet Flow Parameters U_T = 150 ft/sec (45.6 m/sec), NPSH = 106 ft (32.3 m)	137
77	Noncavitating Performance - C = 0.011 in. (0.028 cm)	139
78	Radial Distribution of Discharge Flow Parameters C = 0.011 in. (0.028 cm), U_T = 150 ft/sec (45.6 m/sec), NPSH = 106 ft (32.3 m)	140
79	Effect of Tip Clearance on Performance [U_T = 150 ft/sec (45.6 m/s), NPSH = 106 ft (32.3 m)]	142

ILLUSTRATIONS (Continued)

FIGURE		PAGE
80	Cavitating Performance [C = 0.061 in. (0.155 cm), U_T = 150 ft/sec (45.6 m/sec)]	143
81	Oscillograph Trace of Pressure Scanning Valve Transducer Output	156
82	Blade Transducer Spectrum Analysis	158
83	Housing Transducer Spectrum Analysis	159
84	Oscillograph Trace of Housing Transducer Output, PVW-11 Test 4.02-1	160
85	Summary of Performance Data for Operational Tests (Noncavitating)	160
86	Summary of Performance Data for Operational Tests (Cavitating)	161
87	Noncavitating Blade Pressure Distribution (U_T = 150 ft/sec (45.6 m/sec), NPSH - 106 ft (32.3 m))	165
88	Noncavitating Blade Pressure Distribution (U_T = 120 ft/sec (37.5 m/sec), NPSH = 106 ft (32.3 m))	167
89	Cavitating Blade Pressure Distribution (U_T = 150 ft/sec (45.6 m/sec))	171
90	102 Element Break-up of Inducer Blade for Stress Analysis	178
91	Measured and Predicted Effective Stresses for Leading Edge Static Loading	179
92	Measured and Predicted Effective Stresses for Midchord Static Loading	180
93	116-Element Break-up of Inducer Blade for Stress Analysis	181
94	Measured and Predicted Effective Stresses for Trailing Edge Static Loading	182
95	Deflection of Inducer Blade Under Static Load	182

ILLUSTRATIONS (Continued)

FIGURE		PAGE
96	127 Element Break-up of Inducer Blade for Stress Analysis	184
97	Pressure Load Distribution used for Input to Inducer Stress Program - Point 2	185
98	Pressure Load Distribution used for Input to Inducer Stress Program - Point 8	186
99a	Measured and Predicted Effective Stresses - Operational Test Point 1	187
99b	Measured and Predicted Effective Stresses - Operational Test Point 2	187
99c	Measured and Predicted Effective Stresses - Operational Test Point 3	188
100	Distribution of Stress with Radius at Leading Edge - Point 1	188
101	Measured and Predicted Effective Stresses - Operational Test Point 5	190
102	Measured and Predicted Effective Stresses - Operational Test Point 8	191
103	Measured and Predicted Relative Vibratory Stress Contours - First Mode	193
104a	Measured and Predicted Relative Vibratory Stress Contours - Second Mode, Predicted	195
104b	Measured and Predicted Relative Vibratory Stress Contours - Second Mode, Measured	196
105a	Measured and Predicted Relative Vibratory Stress Contours - Third Mode, Predicted	197
105b	Measured and Predicted Relative Vibratory Stress Contours - Third Mode, Measured	198
106	Adjusted Measured Relative Vibratory Stress Contours - Third Mode	199
107a	Measured and Predicted Vibratory Stress Contours - Fourth Mode, Predicted	200

ILLUSTRATIONS (Continued)

FIGURE		PAGE
107b	Measured and Predicted Vibratory Stress Contours - Fourth Mode, Measured	201
108	Adjusted Measured Relative Vibratory Stress Contours - Fourth Mode	202
109	Geometry for Deriving $[R_1]$	244
110	Geometry for Deriving $\left\{\Psi_N\right\}$	248
111	Geometry for Deriving $\left\{\Psi\right\}$	249
112	Geometry of Triangular Element With Linearly Varying Thickness	250
113	Generalized Nodal Local Membrane Displacements and Forces on Flat Triangular Element	252
114	Generalized Nodal Bending Displacements and Forces on Flat Triangular Element	255
115	Generalized Nodal Bending Displacements and Forces on Flat Triangular Element	257
116	Geometry of Rotating Triangular Element	259
117	Definition of Quasi-Normal Coordinate System	265

TABLES

TABLE		PAGE
1	Modes and Natural Frequencies of Cantilevered Plate	71
2	Mode Shapes and Natural Frequencies of 6-Degree (0.105-rad) Inducer	73
3	Basic Inducer Design Parameters	76
4	Static Strain and Stress, 300 lb (1335N) Concentrated Load at Leading Edge (Element 6)	92
5	Static Strain and Stress, 300 lb (1335N) Concentrated Load at Midchord (Element 48)	94
6	Static Strain and Stress, 300 lb (1335N) Concentrated Load at Trailing Edge (Element 90)	96
7	Calculation of Effective Stresses	98
8	Deflection Normal to Blade - 200 lb (890N) Concentrated Load	99
9	Inducer Resonant Frequencies and Node Locations	100
10	Vibratory Strain and Stress	105
11	Performance Test Instrumentation	112
12	Pressure Test Instrumentation	116
13	Performance Data Reduction Equations	123
14	Summary of Performance Tests	127
15	Comparison of Task III, Acosta, and NASA Series Inducers	132
16	Summary of Strain Tests	144
17	Noncavitating Statis Strain and Stress NPSH = 106 ft, 32.3 M	145
18	Cavitating Static Strain and Stress, U_T = 150 ft/sec, 46.7 m/s	146
19	Noncavitating Vibratory Strain and Stress, NPSH = 106 ft, 32.3 m	147
20	Cavitating Vibratory Strain and Stress U_T = 150 ft/sec, 45.6 M/s	149

TABLES (Continued)

TABLE		PAGE
21	Summary of Pressure Tests	150
22	Noncavitating Pressure Distribution U_T = 150 ft/sec, (45.6 m/s) NPSH = 106 ft (32.3m).	152
23	Cavitating Pressure Distribution U_T = 150 ft/sec (45.6 m/s).	154
24	Noncavitating Hub Static Pressures NPSH = 106 ft (32.3 m)	157
25	Operating Points used in Computer Program Development	161
26	Comparison of Values of Maximum Stress.	177
27	Effect of Speed on Blade Stress Distribution ($\bar{\Phi}$ = 0.09)	189
28	Predicted and Experimental Natural Frequencies. . . .	192

SUMMARY

Inducers are widely used in rocket engine turbopumps to prevent cavitation in the pump main stages, thereby permitting higher turbopump operating speeds and/or reduced pump inlet pressure. In the design of an inducer, hydrodynamic performance can be accurately predicted from empirical loss and deviation data. The prediction of operating stresses presents a problem, however, because (1) there is a lack of information on blade pressure loading and (2) the complexity of the inducer blade shape prevents simple steady and vibratory stress analysis. Consequently, inducer mechanical design is usually based on several approximations, with liberal safety factors being applied. This approach results in relatively heavy inducers with undesirably thick blades.

The inducer load and stress study was undertaken to provide analytic tools, in the form of computer programs, for the prediction of (1) design and off-design hydrodynamic blade loading under cavitating and noncavitating conditions, (2) blade stresses due to hydrodynamic and centrifugal loading, and (3) blade resonant frequencies and relative stress distribution. The study consisted of (1) a literature survey to establish the current state-of-the-art, (2) formulation of computer programs and correlation with existing data, (3) design and fabrication of a test inducer and test rig, (4) a test program in which blade pressures, resonant frequencies, and stresses were measured and compared with predictions, and (5) development of the computer programs based on the test results.

Existing methods were selected from the literature survey and used as a basis for computer programs to predict inducer blade pressures and stresses. Inducer internal flow was calculated from a mean streamline analysis using finite increments. Stress and vibration characteristics were calculated using a matrix analysis of finite triangular elements.

Computer program predictions were compared with experimental data or exact solutions for inducer cavitating and noncavitating performance, inducer resonant frequencies, cantilevered plate resonant frequencies, inducer stress (bladder between blades), and flat plate stress. The correlation was satisfactory in all cases.

An inducer and test rig were designed with provisions for measurement of blade surface pressures and steady and vibratory strains. The inducer was tested statically and in a closed water loop and the resultant data were compared with values predicted by the computer programs. Minor refinements were made to the programs as a result of the correlation.

SECTION I
INTRODUCTION

Inducers are used as the first stage in liquid rocket engine turbopumps because of the weight reduction and performance gains they offer. Inducers can operate at low inlet pressures, reducing the required propellant tank pressure. Low tank pressures mean lighter propellant tanks. At the same time, the inducer supplies the main stage of the turbopump with a much higher pressure than is possible by tank pressurization, thus allowing the turbopumps to operate at much higher speeds without cavitating. Higher turbopump speeds mean lighter and more efficient pumps. As might be expected, the inducer must pay the penalty for the advantages realized by the engine system. Because of the low tank pressures, the inducer must operate almost continuously in a state of partial cavitation while still providing the necessary head rise. When operating with inlet pressures high enough to prevent cavitation, blade steady stresses become severe. As inlet pressure is lowered and a vapor cavity forms, the steady stresses are reduced. However, the collapse of the vapor cavity is often violent and unstable, resulting in fluctuating blade loads that can cause blade fatigue failure.

Inducer hydrodynamic design has been refined through the correlation of empirical data with design theory to the point where excellent performance, i.e., head rise, efficiency and suction capabilities, can be accurately predicted and achieved. However, in the area of mechanical or structural design, the state-of-the-art has not kept pace, and it is this lack of advance that may limit further improvements in hydrodynamic performance. The reasons for this are (1) the inability of existing design tools to accurately predict the blade loadings that occur in the inducer from pressure and centrifugal forces and (2) the absence of a satisfactory method of predicting the stresses that result even when these forces are known. As a consequence, the inducer blades must be designed conservatively, i.e., overly thick, to ensure that failure will not occur during engine operation. The blade thickness directly affects the blockage in the inducer inlet and is detrimental to inducer suction performance.

It was this deficiency in rocket engine inducer design that led to the initiation of Contract NAS3-11216, "Study of Inducer Loads and Stresses." The objective of this contract work was to develop computer programs that could accurately predict inducer blade pressure distributions and resonant frequencies, along with their resultant stresses. The combined analytical and experimental effort was divided into the following six tasks:

I. Literature Survey
II. Formulations of Analytical Models and Computer Programs
III. Hydrodynamic and Mechanical Design of Test Inducer
IV. Detailed Design of Test Inducer
V. Fabrication of Test Hardware
VI. Experimental Testing and Computer Program Verification.

This final report covers all of the work performed under the contract. The analytical and experimental program and its results are discussed in detail in Volume I and computer program user's information is presented in Volume II.

SECTION II
TECHNICAL PROGRAM

A. TASK I - LITERATURE SURVEY

1. General

A literature survey was conducted to determine the current state-of-the-art in the following aspects of inducer structural design:

1. Methods used in the prediction of design and off-design hydrodynamic loading under cavitating and noncavitating conditions

2. Methods used in the prediction of stresses due to hydrodynamic and centrifugal loading

3. Methods used in the prediction of inducer blade resonant frequencies and associated stress distributions

A method was selected from each category to serve as a basis for the computer programs to be formulated in Task II. The selection was based on the following criteria:

1. Comprehensiveness - ability to account for important physical characteristics (geometric and hydrodynamic)

2. Simplicity - practical design tool

3. Success of similar methods in other applications

4. Availability of empirical substantiation.

As will be noted in the subsequent discussion, it became necessary or desirable to modify some methods and combine attractive features of others to more adequately satisfy these criteria.

The literature survey was conducted through the library facilities of United Aircraft Corporation and the Defense Documentation Center. From these sources, approximately 1800 abstracts were collected, of which over 100 were found to be pertinent to the work requirements of the program. These selected abstracts were categorized and are presented in Appendix A under the following main headings.

Section 1 - Blade Hydrodynamic Loading Under Cavitating and Noncavitating Conditions

Section 2 - Blade Stresses (Stresses in Curved Plates)

Section 3 - Blade Vibrations (Vibrations of Curved Plates)

Resumes of those articles from which material was drawn are presented in Appendix B. The methods evaluated are discussed in the following paragraphs.

2. Hydrodynamic Loading of Inducer Blades

Exact, approximate, and experimental methods can be used in defining flow through inducer passages. Examples of each of these methods are presented below.

a. Exact Methods

Exact methods may employ conformal mapping techniques for solution of the exact potential flow equations. This type solution is for ideal or no-loss flow and normally is solved only for a two-dimensional flow field. Examples of solutions to specific cases have been presented by several authors. Exact solutions for single-phase flow between flat plate cascades was presented by von Karman and Burgers (Reference 1). Stripling and Acosta (Reference 2) extended the potential flow flat plate theory to include the effects of cavitation. Fanti (Reference 3) presents the modified flat plate theory to exactly account for potential flow about airfoils of arbitrary shape in an arbitrary cascade. Jakobsen (Reference 4) presents the most general of the exact cascade flow theory by accounting for varying airfoil shape and complete cavitation. However, he only presents solutions for flat plates and circular arc airfoils.

b. Approximate Methods

The term "approximate method" used here refers to methods that give an approximate analytical description of a three-dimensional flow field. These methods could be divided into two subgroups referred to as three-dimensional and quasi-three-dimensional methods. A three-dimensional approximate method may employ a numerical relaxation or finite difference solution of the potential flow equations. A quasi-three-dimensional solution may involve either a two-dimensional finite difference solution to the basic flow equations with an assumed solution in the third dimension or a one-dimensional solution with assumed solutions in the other two dimensions.

The finite difference solution of the basic flow equations is a standard method. This type solution has been used by Stanitz (Reference 5), Stockman (Reference 6), and Cooper (Reference 7) among others. Stanitz and Stockman present quasi-three-dimensional solutions whereas Cooper presents both three-dimensional and quasi-three-dimensional solutions. Loss calculations can easily be incorporated into methods involving a finite difference solution of a potential flow field. This type solution applies equally well to either cavitating or noncavitating flow.

The most general type solution between the exact and approximate solutions is the three-dimensional approximate solution because of its ability to describe completely a flow field in three dimensions, including the effects of three-dimensional flow, cavitation and flow losses. It was found, however, in Reference 7 that use of a three-dimensional approximate model (referred to as "exact" in that reference) required such large quantities of computer time that it would not be practical to consider

it for use in the present inducer stress design system. A quasi-three-dimensional solution was found to execute much more rapidly on the computer, as stated in Reference 7. It is noted, however, that in models such as this one, flow incidence effects on blade loading in the region of the blade leading edge have not always been properly considered.

Therefore, in the hydrodynamic portion of the Task II effort the quasi-three-dimensional analysis was used for defining the flow field within the inducer passage while using the results of exact potential flow solutions for defining the flow field on and near the blade leading edge. The complete hydrodynamic model will solve both cavitating and noncavitating flow problems accounting for leading edge/flow incidence effects and internal flow losses.

c. Experimental Methods

Experimental methods in general rely heavily on particular test results for use in analysis. Although these techniques are generally less complex in nature, their uses are restricted to specific machines and flow conditions. Because of these restrictions these methods were not considered for use as prediction methods in this program.

3. Stresses and Vibrations in Inducer Blades

Stresses and vibrations in inducers with idealized geometry such as constant helix angle, hub diameter, and blade thickness can probably be determined by classical methods similar to those discussed by Wan (Reference 8), Reissner (Reference 9), and Knowles (Reference 10). Varying geometry that is used in conventional inducers would prevent the use of classical methods because of the increase in the number of variables, and approximate numerical methods are the only practical alternative. A survey of the literature indicates that matrix analysis of finite elements should be applicable to the inducer problem, using existing digital computer techniques.

In the finite element analysis, the object is divided into polygonal elements, usually rectangles or triangles, and internal distributed forces are replaced by statically equivalent forces at element nodes. By selection of appropriate displacement polynomials, the stiffness matrix, which associates the nodal forces with nodal displacements, can be obtained. This matrix depends upon the geometry of the element, and for the inducer, selection of a base element in the shape of a flat triangle would be practical. The change in the directions of the normals of these base elements will then account for blade curvature. Techniques for handling triangular elements that are variable in direction are discussed by Argyris for elements under membrane loading (Reference 11) and McGrattan and North (Reference 12). Although the latter paper involves vibrations, its application to elements in three dimensions is pertinent to the inducer stress program.

a. Stresses in Inducer Blades

Stiffness matrices for triangles can be obtained by direct methods, as discussed by Turner, Clough, and Topp (Reference 13), or by conventional strain energy methods as discussed by Utku (Reference 14) and others. An analytical expression for the stiffness matrix of an arbitrarily shaped triangle is very cumbersome and it is more practical to obtain its numerical elements on a computer by consideration of the strain energy. This matrix will yield the relation between nodal forces and displacements associated with the triangle. Because of blade curvature, normals of the base triangular elements will not lie in the same direction and the stiffness matrices must be transformed to correspond to a common direction. This technique is discussed in detail in Reference 11. After they are transformed, the summation of nodal forces to zero and the equating of nodal displacements at common nodes yields a set of simultaneous displacement equations. The values for displacements are then used to determine stresses. External load conditions in this instance are pressure loading and centrifugal loading.

b. Vibrations of Inducer Blades

After the stiffness matrix is obtained, the frequency equation and nodes can be obtained by consideration of the matrix equation of motion as discussed by McGrattan and North (Reference 12). This will involve a determination of the flexibility matrix, which can be obtained by inversion of the stiffness matrix on the computer.

Similar methods have been used by other divisions of United Aircraft Corporation to calculate frequencies and node shapes for radial impellers. Results agree well with experimental test data.

B. TASK II - FORMULATION OF COMPUTER PROGRAMS

1. Hydrodynamic Computer Program

a. Introduction

To predict inducer blade stresses under cavitating and noncavitating conditions, it is first necessary to obtain the pressure distribution on the surfaces of the blades. The pressure differential across the blade causes a normal force called the hydrodynamic loading. If this information is available from tests, then the hydrodynamic loading can be combined with the centrifugal loading on the blades to predict the blade stresses.

This test information is usually not available. It is known, however, that a large proportion of the blade stress in inducers is caused by the hydrodynamic loading. Therefore, it is essential that accurate methods for predicting the blade hydrodynamic loadings be used. As a part of Task II, a computer program for the prediction of hydrodynamic loading, under cavitating and noncavitating conditions, was formulated and programed.

As a result of continuing refinement of the computer program during the course of the contract effort, the following program subroutines and calculations have been added or modified:

1. Loss and Blockage Model
2. Cavity Model
3. Loading Subroutine
4. Exit Deviation Model
5. Inlet Station Calculations
6. Exit Station Calculations

To avoid confusion, the relations presented in this section pertain to the present formulation of the Hydrodynamic program. Differences between the formulation of models as they existed at the end of Task II (see Reference 15) and the present models are discussed in Section II, Task VI.

b. Description of Analytical Model

The basic flow model selected as a result of the Task I literature survey is a mean streamline, two-dimensional meridional flow model. It is assumed that the average flow conditions in the blade-to-blade space can be represented on a meridional surface so that only a two-dimensional, streamline balancing relaxation analysis is required to establish mean velocities, pressures, and flow angles.

However, in the basic model two important non-ideal flow effects are included, both of which greatly affect the flow field. These are the viscosity of the fluid and the vaporization of the fluid when the local static pressure reaches saturation pressure.

The viscous effects are accounted for using a two-dimensional boundary layer model. The boundary layer analysis determines the amount of flow blockage and momentum defect due to diffusion and to viscous shear forces at the blade surfaces and on the hub and shroud walls. The boundary layer blockage causes the meridional velocity to increase and reduces the work capability of the inducer. The momentum defect causes the mass-average total pressure to be reduced. Thus, the viscosity of the fluid affects both the head input and head output. The presence of a boundary layer and its effect on the second non-ideal fluid characteristic, the formation of a vapor cavity, are also accounted for in the cavity model.

Formation of a vapor cavity occurs when the local static pressure reaches saturation pressure. In the selected model, it is assumed that the fluid will vaporize whenever the fluid reaches some critical value of pressure. Furthermore, this value is assumed to be constant and equal to the equilibrium saturation pressure of the bulk fluid at the inlet to the inducer. The effects of transient heat transfer processes or of local subcooling of the liquid on cavitation are not considered. At the inducer inlet a finite vapor cavity is assumed to occur over some finite distance along the blade. This assumption is consistent with the model

of Stripling and Acosta (Reference 2). The assumption is made that the liquid and vapor are separated by centrifugal effects both in the meridional surface and in the blade-to-blade surface (due to flow curvature). Thus, the cavitation model incorporates the concept of a distinct vapor cavity displacing an otherwise incompressible liquid (see figure 1). Because the vapor merely displaces the liquid in the flow model it is assumed that the actual blade can be replaced by a pseudo-blade made up of the real blade plus the vapor cavity. The real blade angle is replaced by an effective angle, i.e., the average of the blade metal angle and the angle of the surface of discontinuity between the vapor and the liquid. Because of the formation of the cavity the mean flow angle will be different from the mean angle of the pseudo-blade. Other real fluid effects which influence this difference or "deviation" result from the leading edge incidence, trailing edge unloading (commonly called the exit deviation), and the inability of the fluid to follow exactly a curved path due to its inertia. These effects are combined to form the total deviation or simply, the deviation.

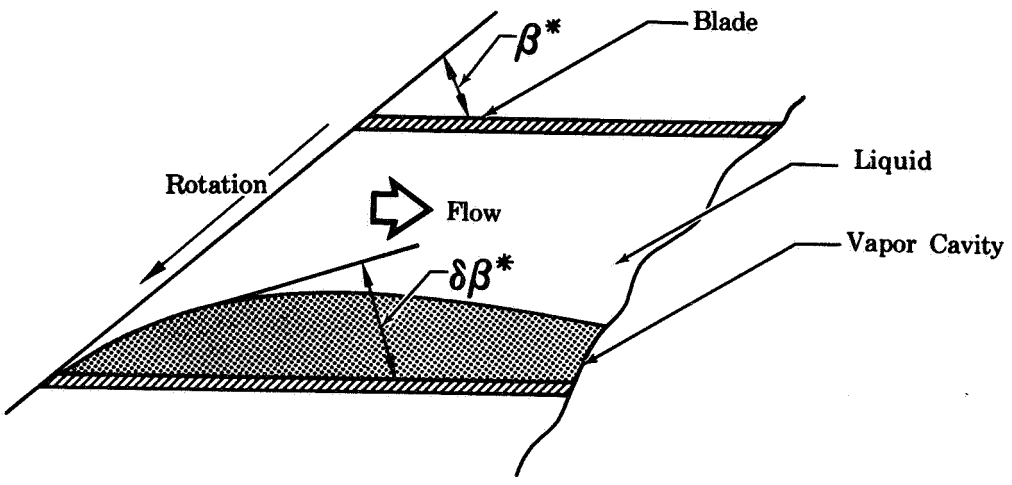

Figure 1. Distinct Vapor Cavity Forms During Cavitation FD 25645B

c. Discussion of Basic Relations

(1) Geometric Relations

The information about the geometry of the inducer required to begin the analysis includes the flowpath inner and outer radii versus axial distance and some description of the blade angle (β^*) and thickness (t) distributions. In the model selected, it is assumed that one surface of the inducer blade is generated by a straight line (generatrix) passing through the hub and tip radii given previously. The other surface is assumed to be generated by a straight line inclined at some angle (γ - the taper angle) and displaced some distance (the blade thickness) with respect to the other generatrix (figure 2). To allow for nonradial element

blading, it is assumed that the product of radius (R) times the tangent of the blade angle varies linearly between the values for the hub and tip. Thus,

$$R \tan \beta^* = R_T \tan \beta_T^* - \frac{R_T - R}{R_T - R_H} \left[R_T \tan \beta_T^* - R_H \tan \beta_H^* \right]$$

from which the local value of β^* can be found for any value of R.

The local blade thickness may be obtained from the given blade tip thickness (t_T) and the taper angle (γ):

$$t = t_T + \gamma(R_T - R)$$

where γ is assumed to be a small angle.

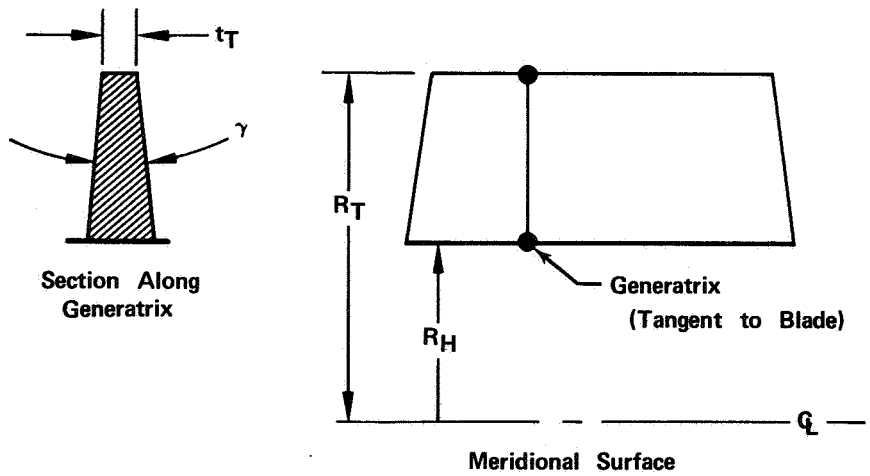

Figure 2. Thickness Distribution of Typical Blade FD 25872B

The distance between surfaces of adjacent blades (measured in the circumferential direction) is given by

$$\tau = \frac{2\pi R}{N_b} - \frac{t}{\sin\beta^*}$$

where τ is the tangential spacing and N_b is the number of blades.

Although the flow in an inducer is primarily axial, the hub or tip contour often has a varying radius. The streamlines then may be forced to change radius and, because of the inducer rotation about its axis, Coriolis forces will cause blade pressure loading. The angle (ψ) of a stream tube between two stations is found by dividing the radial displacement by the axial displacement.

$$\psi = \tan^{-1}\left(\frac{\Delta R}{\Delta Z}\right)$$

(2) Flow Relations

The velocity diagram at any point in the flow is shown in figure 3. From trigonometry

$$W = Vm/\sin\beta$$

$$W_u = W \cos\beta$$

$$V_u = U - W_u$$

$$\alpha = \text{Arc tan } (V_m/V_u)$$

$$V = V_m/\sin\alpha$$

The relative flow angle (β) is found from the blade angle and the deviation angle at any point

$$\beta = \beta^* - \text{deviation}$$

The meridional flow velocity (Vm) is found from the volumetric flow (Q) and the flow area normal to the meridional flow direction (A)

$$Vm = Q/A$$

where

$$A = \tau_\ell \, (\Delta y) \cos\psi$$

and τ_ℓ is that portion of the circumferential distance between two blades that is occupied by liquid, and Δy is the radial distance between streamlines (see figure 4). The value of τ_ℓ is obtained by adjusting the tangential blade spacing (τ) by the boundary layer displacement thickness (δ^*) and the vapor cavity height (b), measured circumferentially.

$$\tau_\ell = \tau - \frac{\delta^*}{\sin\beta^*} - b$$

However, if a cavity does not exist on the blade surface the expression for τ_ℓ becomes:

$$\tau_\ell = \tau - \frac{2\delta^*}{\sin\beta^*}$$

Blockage due to hub and shroud surface boundary layers is accounted for by reducing the hub and tip stream tube heights (Δy) by their respective displacement thickness, δ^*:

$$\Delta y = \Delta y - \frac{\delta^*}{\cos\psi}$$

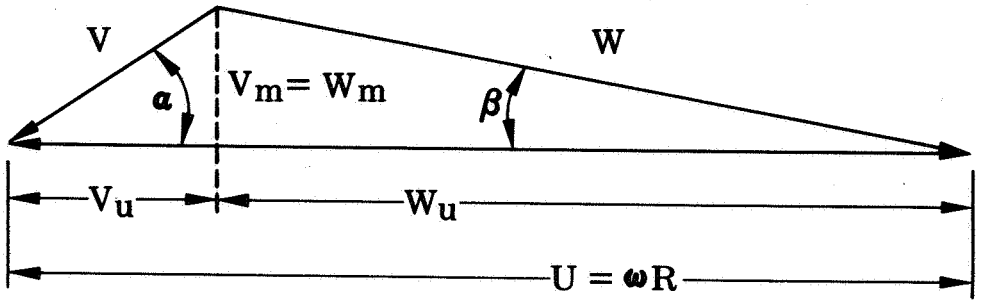

Figure 3. Typical Velocity Diagram FD 25809A

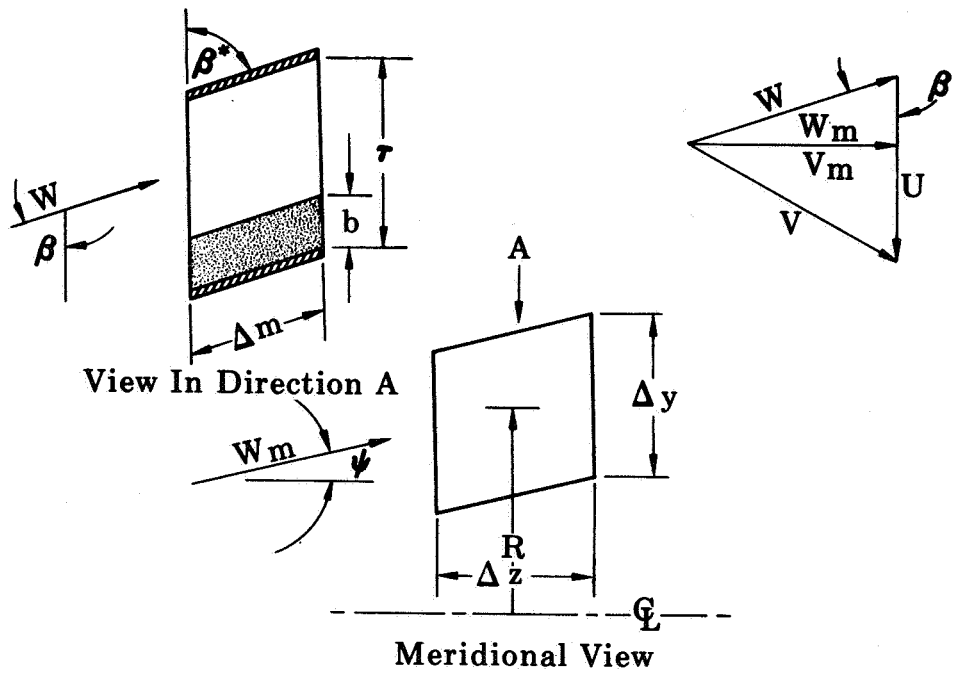

Figure 4. Schematic of Flow Passage FD 25644B

(3) Deviation

(a) Fluid Inertia Model

It is assumed that the flow will tend to follow the mean direction of the passage formed by the blades or the pseudo-blades (where a cavity exists). Because of fluid inertia, however, changes of angle at the leading and trailing edges resulting from leading edge incidence and trailing edge unloading cannot take place discontinuously. The distribution of the deviation angle assumed is related to a steady , 2-dimensional, irrotational flow model. The expressions defining this steady 2-dimensional irrotational flow are:

$$\frac{\partial u}{\partial x} + \frac{\partial v}{\partial y} = 0 \qquad \text{equation of continuity}$$

$$\frac{\partial u}{\partial y} - \frac{\partial v}{\partial x} = 0 \qquad \text{condition of irrotationality}$$

where velocities u and v and coordinates x and y are shown on figure 5. Differentiating the first expression with respect to y and the second with respect to x and subtracting yields:

$$\frac{\partial v^2}{\partial x^2} + \frac{\partial v^2}{\partial y^2} = 0$$

The general solution to this equation is

$$v = \sum_i e^{\pm k_i x} \left[A_i \sin (k_i y) + B_i \cos (k_i y) \right]$$

Satisfying the following boundary conditions

at $y = 0$, $v = 0$
at $y = \tau_n$, $v = 0$
at $x = \infty$, $x = 0$

and evaluating the resulting expression at mid-channel $(\frac{y}{\tau_n}) = 1/2$ gives:

$$v = \sum_{k=1,2...} e^{-k\pi \frac{x}{\tau_n}} A_i \sin \frac{k\pi}{2}$$

Note that when k is an even integer the series term goes to zero.

Considering only the first finite term of the series as being significant results in

$$v = A_1 e^{-\frac{\pi x}{\tau_n}}$$

Relation of the transverse velocity (v) to the inducer inlet relative velocity triangle is shown in figure 5. Using this relation for the transverse velocity the following expression for local fluid deviation results:

$$\tan \delta = \frac{A_1}{W_m} \frac{\sin \beta^* \; e^{-\frac{\pi x}{\tau_n}}}{1 + \frac{A_1}{W_m} \frac{\sin \beta^*}{\tan \beta^*} \; e^{-\frac{\pi x}{\tau_n}}}$$

Applying the boundary conditions:

at $x = 0$ $\quad \tan \delta = \tan \delta o$

at $x = \infty$ $\quad \delta_I = 0$

yields

$$\tan \delta_I = \frac{\tan \delta o \; e^{-\frac{\pi \Delta m}{\tau_n}}}{1 - \frac{\tan \delta o}{\tan \beta^*} \left(1 - e^{-\frac{\pi \Delta m}{\tau_n}} \right)}$$

where δo = initial incidence = $\beta^* - 1/2 \; \delta\beta^* - \beta'$

Δm = incremental distance along the blade

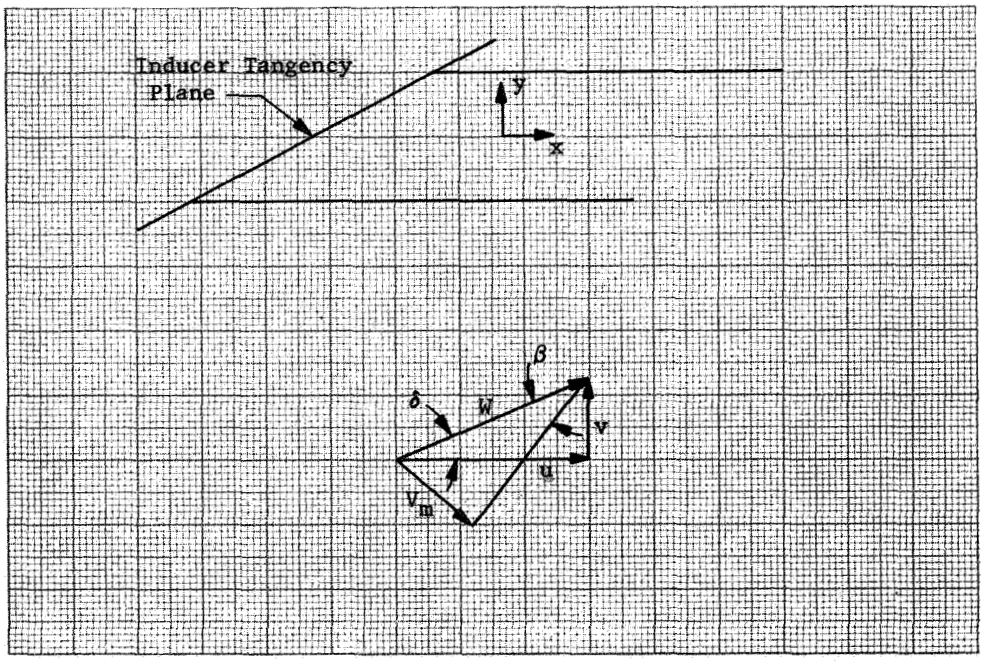

Figure 5. Inducer Velocity Diagram

DF 85036

An illustration of the effect of this inertial lag on deviation is shown in figure 6. The deviation due to incidence is shown to be removed before a distance of one blade gap.

If the blade angle varies in the flow direction the deviation at each station can be found by treating Δm as the distance between stations and δo as the value of deviation at the previous station.

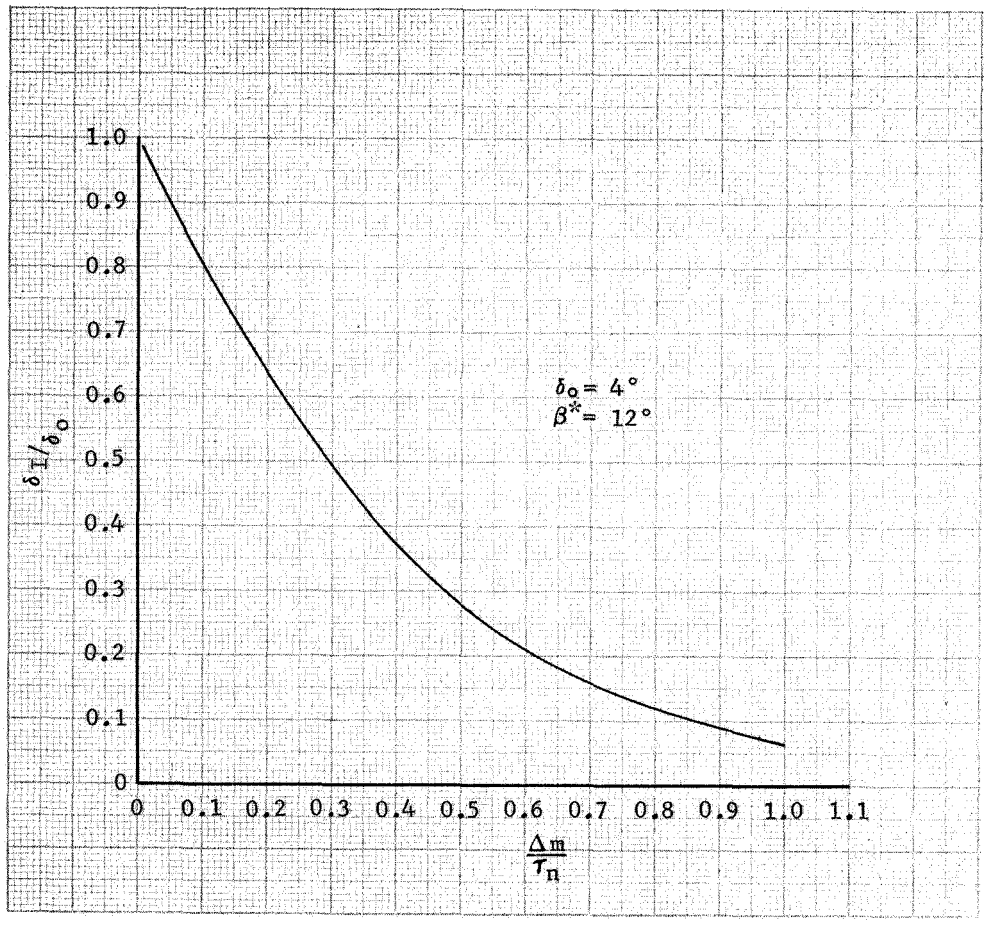

Figure 6. Effect of Inertial Lag On Deviation Due to Incidence DF 85035

(b) Trailing Edge Deviation

The value of exit deviation angle (δ_e), resulting from circulation about the hydrofoils in cascade, is found by using an empirical formula similar to Carter's rule. In the present model, for a given blade geometry the exit deviation is proportional to the blade camber plus inlet incidence, i.e., where ξ = blade camber = $\beta^*_e - \beta^*_o$

$$\frac{\delta_e}{(\xi + i')} = \frac{\delta_e}{(\beta^*_e - \beta_o)} = \text{Constant}$$

where β_e^* is the blade exit angle and β_o is the fluid inlet angle. The constant is assumed to be a function of blade solidity (σ or chord/gap ratio) as normally defined by Carter's rule:

$$\frac{\delta_e}{(\beta_e^* - \beta_o)} = \frac{C_e}{\sqrt{\sigma}}$$

For inducers, C_e is primarily a function of blade angle. From Reference 16 a value of $C_e = 0.28$ was determined, which is consistent with the magnitude from previous empirical correlations for cascades with high stagger angles (Reference 17, 18). If the inducer has cambered blades, an equivalent stagger angle is calculated from inlet and exit values of blade angle.

Upstream of the trailing edge the deviation due to trailing edge unloading (or circulation) is assumed to approach the exit value exponentially, similar to the distribution of deviation due to leading edge incidence given earlier (figure 6).

(c) Deviation Due to Cavitation

In the concept of the selected model, cavitation causes a change in the "effective" blade angle. In this sense, the cavity forms part of a pseudo-blade rather than causing deviation, i.e.,

$$\beta^*\text{eff} = \beta^* - \frac{\delta\beta^*}{2}$$

where $\delta\beta^*$ is the slope of the vapor cavity surface relative to the real blade. However, for reference purposes this deviation is considered as a part of the total deviation:

$$\text{Deviation} = \beta^* - \beta = \delta_I + \delta_e + \frac{\delta\beta^*}{2}$$

(4) Radial Equilibrium

The flow in the inducer must satisfy equilibrium of radial momentum. The static pressure (P) within each streamtube is found from the Bernoulli equation

$$P = P_{rel} - \frac{\rho}{2g}W^2$$

where P_{rel} is the local total relative pressure in the core flow and ρ is the fluid density.

The radial gradient of static pressure for each streamtube can be found from conservation of momentum in the radial direction. There are two effects causing a radial pressure gradient - first, the rotation of the inducer causes a centrifugal pressure gradient

$$\left(\frac{dP}{dr}\right)_1 = \frac{\rho}{g}\frac{(V_u)^2}{R}$$

Secondly, the change in radial velocity (i.e., streamline curvature and radial acceleration) causes a radial pressure gradient:

$$\left(\frac{dP}{dr}\right)_2 = \frac{\rho}{g}\left[V_m^2 \frac{d\psi}{dZ}(\cos\psi)^2 + V_m \sin\psi \cos\psi \frac{dV_m}{dZ}\right]$$

where dZ is the element of axial length. The total pressure gradient is, therefore:

$$\frac{dP}{dr} = \left(\frac{dP}{dr}\right)_1 + \left(\frac{dP}{dr}\right)_2$$

Radial equilibrium is evaluated halfway between axial stations, since the streamline curvature and acceleration are calculated for the change from station-to-station. At the leading edge and far downstream of the inducer, only simple radial equilibrium is used, i.e., $(dP/dr)_2 = 0$.

(5) Streamline Relaxation

The radial position of each streamline at each axial station is determined by satisfying the condition of radial equilibrium with the least error or by an error less than some tolerance level. The error in local static pressure gradient is found by comparing the calculated dP/dr with the finite difference value determined from adjacent streamtubes:

$$E = \frac{\Delta P}{\Delta r} - \frac{dP}{dr}$$

where

$$\Delta P = P_{(i)} - P_{(i-1)}$$

and

$$\Delta r = R_{(i)} - R_{(i-1)}$$

The errors of all streamtubes are computed and minimized by iterating on the position of the streamlines. The positions (in percent of passage height) are corrected by a small incremental step in the direction determined by the error in pressure gradients of the streamtubes above and below each streamline. The size of the incremental correction is reduced after a fixed number of iterations to improve the accuracy. A limit is placed on the total number of iterations to limit computing time.

(6) Blade Loading

After the radial positions of the streamlines are located through the relaxation procedure, the meridional solution at the axial station is completely determined. Then it is possible to superimpose a solution for pressure differential across the blade. Two methods of superposition of this solution are available: in the tangential direction and in the direction normal to the blades. Both methods of analysis were evaluated.

(a) Tangential or Circumferential Loading Method

The blade pressure loading, ΔP_b, is found from conservation of angular momentum of the fluid between any two axial stations. The blade pressure force in the tangential direction is:

$$F = (\Delta P_b)(\Delta y \cos \psi)(\Delta m \sin \beta^*) N_b = (\Delta P_b)(\Delta y)(\Delta Z)(N_b)$$

where Δm is the element of length along the blade

$$\Delta m = \Delta Z / (\cos \psi \sin \beta^*)$$

The moment arm is the radius R. Therefore, the torque is:

$$T = F \cdot R = (\Delta P_b) \ (\Delta y \cos \psi) \ (\Delta m \sin \beta^*) \ (N_b) \ (R)$$

From Euler's turbomachinery equation, the change in fluid angular momentum is equal to this torque

$$\dot{m} \cdot \Delta(RV_u) = T$$

The continuity of mass is given by

$$\dot{m} = \rho(\Delta y \cos \psi) \ (\tau_\ell \sin \beta) \ (W) \ (N_b)$$

Substituting for $\dot{m}$ and T, the momentum equation reduces to

$$\Delta P_b = \frac{\rho W \tau_\ell}{R} \cdot \frac{\sin \beta}{\sin \beta^*} \cdot \frac{\Delta(RV_u)}{\Delta m}$$

If the increment Δm is taken small enough,

$$\frac{\Delta(RV_u)}{\Delta m} \approx \frac{d(RV_u)}{dm} = V_u \frac{dR}{dm} + R\frac{dV_u}{dm}$$

Substituting $V_u = \omega R - W \cos \beta$

and

$$\frac{dV_u}{dm} = \frac{\omega dR}{dm} + W \sin \beta \frac{d\beta}{dm} - \cos \beta \frac{dW}{dm}$$

then

$$\frac{d(RV_u)}{dm} = (2\omega R - W \cos \beta) \frac{dR}{dm} + WR \sin \beta \frac{d\beta}{dm} - R \cos \beta \frac{dW}{dm}$$

and

$$\Delta P_b \approx \frac{\rho W \tau \ell}{R} \cdot \frac{\sin \beta}{\sin \beta^*} \left[2\omega R \frac{dR}{dm} - W \cos \beta \frac{dR}{dm} + WR \sin \beta \frac{d\beta}{dm} - R \cos \beta \frac{dW}{dm} \right]$$

Factoring out $\sin \beta$ and noting that

$$\frac{1}{\sin \beta} \frac{dR}{dm} = \sin \psi$$

and dividing through by the relative dynamic pressure (Q_D)

where

$$Q_D = \frac{\rho W^2}{2g}$$

then, $$\frac{\Delta P_b}{Q_D} = \frac{2 \tau \ell \sin^2 \beta}{\sin \beta^*} \left[\frac{2 \omega \sin \psi}{W} - \frac{\cos \beta \sin \psi}{R} + \frac{d\beta}{dm} - \frac{\cot \beta}{W} \frac{dW}{dm} \right]$$

The first term inside the brackets represents the blade loading caused by Coriolis forces. The second term derives from curvature of the flow in absolute space about the axis at constant relative angle (β). The third term represents the contribution of flow curvature due to the rate of change of the relative flow direction. The last term is the contribution of mean diffusion to the <u>tangential</u> loading ΔP_b. For inducers with low blade camber ($d\beta/dm \approx 0$) and axial flow ($\sin \psi \approx 0$), the last term will dominate and primarily determine the blade hydrodynamic loading.

For small blade angles the circumferential distance between blades over which this loading is applied is large. This effect, coupled with the high sensitivity of the loading gradient to errors in calculation of the mean diffusion term, due to the use of finite differences, can result in large variations and inaccuracies in the blade pressure loading.

(b) Normal Loading Method

Normal loadings are expressed in the same form as the tangential loadings and are comprised of the same terms, with the exception of the contribution resulting from diffusion in the direction of flow (i.e., $\frac{\cot \beta}{W} \frac{dW}{dm}$). This term, being a gradient in the flow direction and therefore in the blading direction, cannot have a component normal to the blade and hence cannot contribute to the normal loading.

$$\frac{\Delta P_{bn}}{Q_D} = \frac{2\tau \ell \sin^2 \beta}{\sin \beta^*} \left[\frac{2\omega \sin \psi}{W} - \frac{\cos \beta \sin \psi}{R} + \frac{d\beta}{dm} \right]$$

Although calculation of normal loadings alleviates the disadvantages inherent with the tangential blade pressure loadings, they do possess some undesirable features. To apply normal loadings the mid-channel flow properties and characteristics must be known at all points normal to the surface on which the pressure is to be calculated. The inlet and exit flow sections of cascades have portions of flow surfaces which are referred to as uncovered (no channel exists) as shown in figure 7.

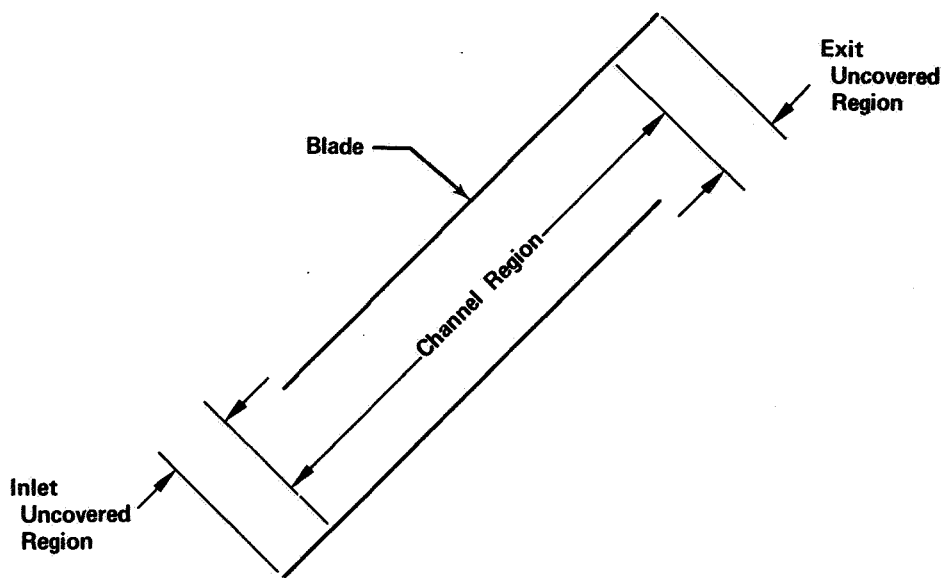

Figure 7. Schematic Cascade Section For Normal Loading Analysis

FD 48162

1 Inlet Uncovered Region

The streamtube axial velocity is assumed constant between the inlet station and blade leading edge. The relative velocity is assumed to vary exponentially over this region with a distribution similar to that discussed in Section (3) (a) and is calculated by:

$$W_o = W_{LE} - (W_o - W_{LE})e^{\left(m - \frac{\tau \cos \beta^*_o}{2}\right)\frac{N_b}{R \sin \beta^*_o}}$$

where subscripts indicate values at the inlet (upstream) and blade leading edge stations.

The blade pressure loading due to flow curvature in the plane of the cascade predominates, resulting in the following expression for normal loading (ΔP_{bn}) over the inlet uncovered region.

$$\Delta P_{bn} = -\frac{\pi \rho}{g} \frac{V_{m_o}}{\cos \beta} \frac{\sin^2 \beta}{\sin^2 \beta^*} (W_o - W_{LE})e^{\left(m - \frac{\tau \cos \beta^*_o}{2}\right)\frac{N_b}{R \sin \beta^*_o}}$$

As illustrated in figure 7 the loadings calculated in this manner apply only to the blade suction surface at the cascade.

Inlet relative total pressure is assumed constant for the streamtubes over the uncovered inlet region. Streamtube static pressure therefore is calculated by:

$$P = P_{rel} - \frac{\rho}{2g} W^2$$

and suction surface pressure is expressed as

$$P_s = P - \frac{\Delta P_{bn}}{2}$$

2 Exit Uncovered Region

The exit uncovered region is analyzed in a similar manner. The exit station axial velocity is assumed constant over the region and the relative velocity is expressed by:

$$W = W_e - (W_e - W_{TE})e^{-\left[(m_{TE} - m) - \frac{\tau \cos \beta^*_e}{2}\right]\frac{N_b}{R \sin \beta^*_e}}$$

where subscripts indicate values at blade trailing edge and exit (downstream) stations.

In the exit region, as in the inlet region, the flow curvature term is the dominant term in the normal loading calculation. The expression used in the calculation of the normal loading is:

$$\Delta P_{bn} = \pi \frac{\rho}{g} \frac{V_{m_e}}{\cos\beta} \frac{\sin^2\beta}{\sin\beta^*_e} (W_e - W_{TE})_e^{-\left[(m_{TE} - m) - \frac{\tau\cos\beta^*_e}{2}\right]\frac{N_b}{R\sin\beta^*_e}}$$

Relative pressure downstream of the inducer is assumed constant for the streamtube over the uncovered exit region. Streamtube static pressure is written as:

$$P = P_{rel_e} - \frac{\rho}{2g} W^2$$

where P_{rel_e} is the total relative pressure at the exit station and includes the effects of wake mixing losses.

Pressure surface pressure over this exit uncovered region is calculated by:

$$P_p = P + \frac{\Delta P_{bn}}{2}$$

3 Channel Region

The flow conditions within the blading passage are calculated as described in Section II, B1c(2). Values of streamtube pressure and normal loading as calculated in the main program are stored and are curve fit as a function of blade length in the blade pressure loading subroutine. These data are called as required to calculate suction and pressure surface pressures at locations circumferentially opposite each other as shown in figure 8.

Combining the uncovered and covered methods of calculating blade surface pressures makes possible the calculation of blade pressure loadings at any point within the inducer.

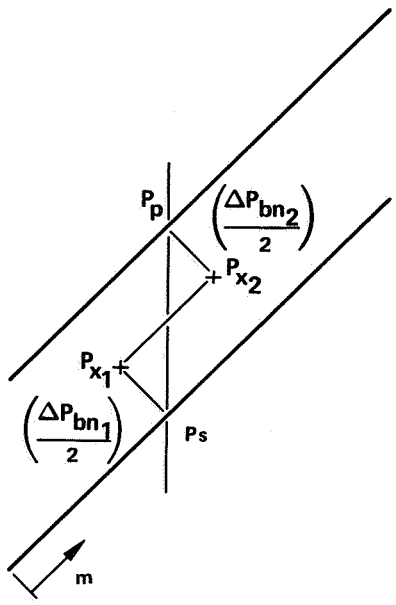

$$\Delta P_b = \left(P_{x_2} + \frac{\Delta P_{bn_2}}{2}\right) - \left(P_{x_1} - \frac{\Delta P_{bn_1}}{2}\right)$$

Figure 8. Conversion of Blade Normal Loading to Blade Circumferential Loading FD 48161

(7) Inlet Calculations

(a) Radial Variation of Inlet Conditions

Special inlet calculations are required to establish streamline locations, incidence angles, and other relative inlet calculations. The inlet routine accepts radial variations in total pressure, axial velocity and prewhirl angle.

The inlet annulus is divided into equal area streamtubes. The volumetric flow rate for each streamtube is found from

$$Q = V_m \cdot A$$

(b) Blade Leading Edge Sweep

The leading edge of the inducer blade is often swept to reduce blade root maximum stress and to improve cavitating performance. Provisions for analyzing inducers with swept leading edges are included.

Blade leading edge sweep is described (geometrically) in the R-Z (meridional) plane by a third order polynominal in R with constant coefficients. Radial leading edge inducers are described by setting each of these coefficients to zero.

The method of flow analysis employed for the swept and unswept leading edge cases is the same. That is, the flow is analyzed along radial generator lines. The fluid is assumed to possess inlet angular momentum at all points along a generator which lay outside of the inducer. Corrections for blade and blade boundary layer blockage are made where applicable. Streamline relaxation and all flow calculations are handled the same as for the unswept leading edge case.

(8) Exit Calculations

Because of boundary layer and blade thickness, wakes will exist at the exit of the inducer. These wakes mix out a short distance downstream of the inducer causing the average axial velocity to decrease due to reduced blockage. This diffusion will cause some redistribution of exit flow conditions.

An exit station downstream of the blade trailing edge is included to evaluate these effects and to provide exit pressures and velocities for performance evaluation. Streamline locations are defined by satisfying simple radial momentum, i.e., $(dp/dr)_2 = 0$. (See paragraph 1c4.)

(9) Performance Calculations

The overall performance calculations include mass average and radial distribution of performance parameters such as work input, head rise, and efficiency. Other pertinent parameters, such as NPSH, Reynolds Number, suction specific speed, flow coefficient, and head coefficient are included in these calculations.

(10) Boundary Layer Calculations

A two-dimensional, turbulent, incompressible boundary layer model including the effects of pressure gradient, is employed for calculating the boundary layer growth on all surfaces. A finite difference solution of the integral momentum equation and the shape factor equation of Garner (Reference 19) is used.

$$\frac{d\theta}{dm} = \frac{C_f}{2.0} - (H + 2.0)\,\frac{\theta}{W}\,\frac{dW}{dm}$$

$$\frac{\theta dH}{dm} = \frac{5_e^{(H - 1.4)}}{Re_\theta^{1/6}} \left[- Re_\theta^{1/6}\,\frac{\theta}{W}\,\frac{dW}{dm} - 0.0135\,(H - 1.4) \right]$$

where

θ = momentum thickness
H = shape factor
C_f = friction factor
Re_θ = Reynolds Number

A forward integration technique is employed in solution of these equations.

Skin friction coefficient (C_f) is determined using the Ludwig-Tillman equation

$$C_f = 0.246(10)^{-0.678H}(Re_\theta)^{-0.268}$$

The Reynolds Number (Re_θ) is defined as

$$Re_\theta = \frac{\theta W}{\nu}$$

where ν is the fluid kinematic viscosity.

Boundary layer displacement thickness (δ^*) is determined from the shape factor (H) and the momentum thickness (θ) by

$$\delta^* = (H)(\theta)$$

It is assumed that there is little secondary flow in the inducer so that migration of the boundary layer flow from the pressure surface to the suction surface is not significant.

(11) Loss System

The assumed loss system model makes use of the fact that the momentum thickness, as calculated in the boundary layer model discussed above, includes the streamtube momentum defect resulting from both skin friction and streamtube diffusion. This momentum defect is converted to a total pressure loss in the relative frame of reference by mixing out the boundary layer momentum thickness through a momentum mixing process. The resulting loss in mass average total relative pressure (PO_{rel}) for the blade boundary layers is

$$\Delta PO_{rel} = P_{rel} - PO_{rel}$$

$$\frac{\Delta PO_{rel}}{Q_D} = \frac{4\theta}{\tau \sin\beta^*}$$

The loss for the hub and shroud stream tubes is calculated in a similar manner.

Boundary layer analyses performed on typical inducers indicate that the flow within an inducer is not fully developed (i.e., the boundary layer thickness does not comprise the complete blading passage). This allows the constant momentum mixing of the boundary layers for calculating losses in streamtube total relative pressure as discussed above.

On that portion of the surfaces where cavitation is present, the boundary layer is assumed to be contained in the cavity. Therefore, no additional momentum defect is accounted for, so the equation becomes

$$\frac{\Delta PO_{rel}}{Q_D} = \frac{2\theta}{\tau \sin\beta^*}$$

the end wall boundary layers are accounted for by an additional defect term.

$$\frac{\Delta PO_{rel}}{Q_D} = \frac{4\theta}{\tau \sin\beta^*} + \frac{2\theta}{\Delta y}$$

(12) Cavitation Model

(a) Description

The present flow model for cavitation incorporates the concept of a distinct vapor cavity forming on the suction surface of the blade and attached at the leading edge (figure 1). This cavity tends to act as a pseudo-blade, displacing the flow and allowing it to turn more gradually. It is the more gradual turning that allows the pressure at the vapor liquid interface (i.e., the "Suction Surface" of the pseudo-blade) to be equal to the saturation pressure. If the inlet pressure decreases, then the cavity will grow to form a shape such that the suction surface pressure will always equal saturation pressure.

Several two-dimensional, free streamline, potential flow (nonviscous) models exist which predict vapor cavity growth as a function of inducer inlet geometry and operating conditions. The models of Stripling and Acosta (Reference 2) and Jakobsen (Reference 4) apply conformal mapping for their solution. Whereas, the model of Stripling and Acosta can be applied only to two-dimensional flat plate cascades, the method of Jakobsen applies to cambered blades as well. However, Reference 4 presents the solutions only for flat plate and circular arc cascades.

Although these idealized models lend much insight into the effects of blading geometry and operating conditions on vapor cavity growth, they do not include real effects resulting from viscous, three-dimensional flow. Viscous effects influence cavity growth through boundary layer blockage (δ^*) and drag forces (F_D). Three-dimensional effects result from centrifugal forces, streamline relocation, and changes in passage width.

The models of Stripling and Acosta and Jakobsen, although employing conformal transformation techniques to arrive at a solution for the vapor cavity shape, solve basic flow relationships. This was pointed out in Reference 2 where it was noted that the maximum height of the two-dimensional cavity could be calculated from one-dimensional conservation of momentum parallel to the blades. This suggestion has been used in formulating a cavity model during the Task VI effort which satisfies the same basic flow relations. Significantly, it includes viscous and three-dimensional effects.

Solution for cavity height is based on momentum considerations and is possible by relating the mean angle of the flow (relative to the blade) to the blade angle. The adoption of this approach makes it possible to use finite differences so that real fluid effects can be included.

The finite cavity which occurs within the inducer is generated such that conservation of momentum in the through flow direction (parallel to the blades) is at all times satisfied. Interdependence between the cavity shape (height, b, and slope, $\delta\beta^*$) and the radial streamline location requires an iterative procedure for solution. The forces associated with generation of the cavity are discussed below. These forces include both those encountered in a two-dimensional potential flow analysis and those resulting from three-dimensional and viscous effects.

An element of fluid existing in a blading passage with a vapor cavity is shown in figure 9.

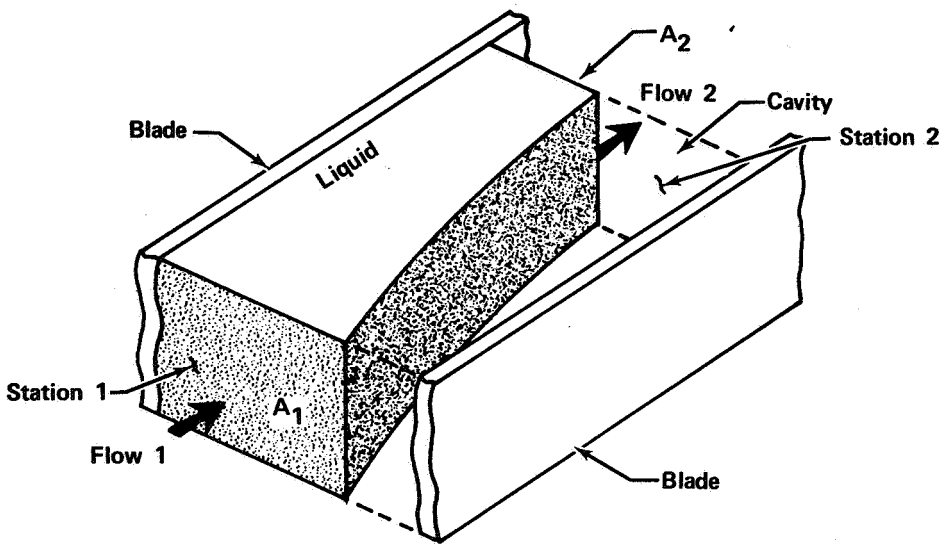

Figure 9. Fluid Element with Vapor Cavity FD 38381

A momentum balance between stations 1 and 2 in the blading through flow direction gives

$$M_1 = M_2 + \Delta M$$

where M_1 and M_2 are the liquid through-flow momenta (mass flow rate times velocity) at stations 1 and 2. ΔM represents the change in momentum of the liquid between stations 1 and 2 and is comprised of shear or drag forces (F_D), normal or pressure forces (F_p), and a body force (F_C) due to centrifugal effects.

$$\Delta M = F_D + F_p + F_C$$

(b) Derivation of Forces

(1) Shear Forces

Shear forces result from a shear stress acting over some finite area. For a general streamtube element as shown in figure 10, four surface areas exist over which shear stresses may act. Surfaces 2 and 3 are the streamtube interfaces between the lower and upper streamtubes with the exception of the special cases where the streamtube being analyzed is either the hub or shroud stream tube, Surfaces 4 and 1 are the blade liquid and liquid-cavity interfaces respectively.

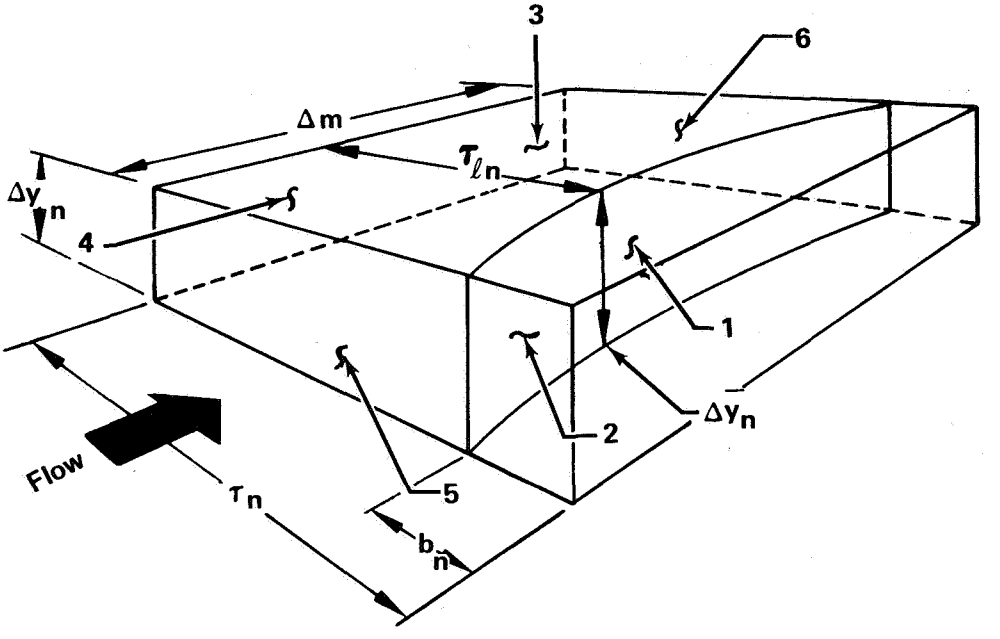

Figure 10. Surfaces of Fluid Element FD 38382B

Shear stresses existing between adjacent streamtubes and along the liquid-cavity interface are assumed to be small with respect to the shear stresses that exist between liquid and inducer surfaces. Therefore, no contribution is made to the total shear force on the liquid element from surfaces 1, 2, and 3. The total shear force for the liquid element is

$$F_D = (\epsilon)(\Delta m)(\bar{\Delta y}_n)$$

where Δm is the liquid element length in the direction of the flow, ϵ is the shear stress, and Δy_n is the element height measured normal to the through flow direction. The bar (-) indicates average values between station 1 and 2. Using the expression for shear stress:

$$\epsilon = C_f \frac{\rho W^2}{g}$$

and defining Δy_n as $\Delta y_n = \Delta y \cos\psi$ allows the shear force to be expressed by

$$F_D = (C_f)\left(\frac{\rho W^2}{2g}\right)(\Delta m) \quad \Delta\bar{y} \cos\bar{\psi}$$

An additional wetted surface exists for each of the hub and shroud streamtubes from which shear forces are generated. This shear force is expressed as:

$$F_D = (C_f)\left(\frac{\rho W^2}{2g}\right)(\Delta m)(\bar{\tau}_{\ell n})$$

where $\tau_{\ell n}$ is the fluid element width measured normal to the blading surface and is expressed by:

$$\tau_{\ell n} = (\tau_\ell)(\sin\beta^*)$$

This additional shear force is combined with the blade shear force to give a total force of:

$$F_D = (C_f)\left(\frac{\rho W^2}{2g}\right)(\Delta\bar{y} \cos\bar{\psi} + \bar{\tau}_\ell \sin\bar{\beta}^*) \quad (\Delta m)$$

for the hub and shroud streamtubes.

(2) Pressure Forces

Surface pressure forces or normal forces result from a static pressure acting over a finite area. For a general liquid element it is possible for normal forces to occur on all six element surfaces.

Consider first surfaces 2 and 3 from figure 10. A side view of the liquid element is shown in figure 11. This figure is an illustration of the effect of streamtube convergence. Normal areas for surfaces 2 and 3 result from projections of these planes into a plane perpendicular to the through flow direction. These areas are combined and are represented by:

$$A_n = (\Delta y_{n1} - \Delta y_{n2})\bar{\tau}_\ell \sin\bar{\beta}^*$$

The pressure acting over this surface is assumed to be the average streamtube pressure $(\bar{P})$ between stations 1 and 2. Therefore, the pressure force resulting from streamline relocation is represented by

$$F_{PSC} = (\bar{P})(\Delta y_{n1} - \Delta y_{n2})(\bar{\tau}_\ell \sin\bar{\beta}^*)$$

The other normal or pressure forces are represented in a similar manner. Figure 12 illustrates the forces resulting from cavity growth and blade passage convergence on the liquid element. The pressure force resulting from the formation of the vapor cavity is represented by

$$F_{PC} = (P_{SAT})(\Delta b_n)\Delta\bar{y} \cos\bar{\psi}$$

where P_{SAT} is the fluid saturation pressure and Δb_n is the change in normal vapor cavity height between stations 1 and 2.

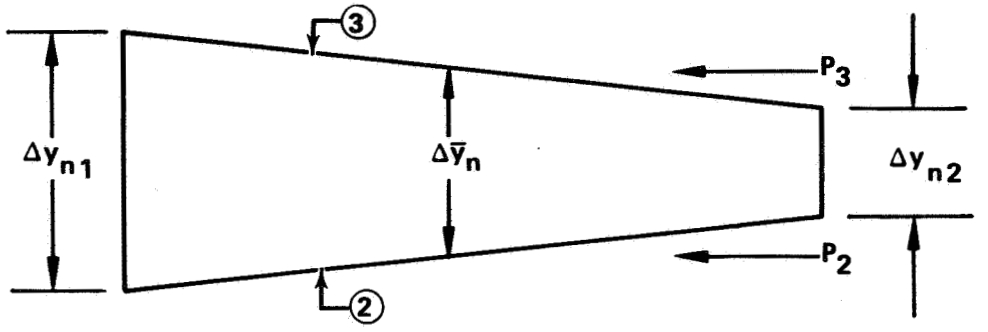

Figure 11. Pressure Force Due to Streamtube Convergence FD 38379B

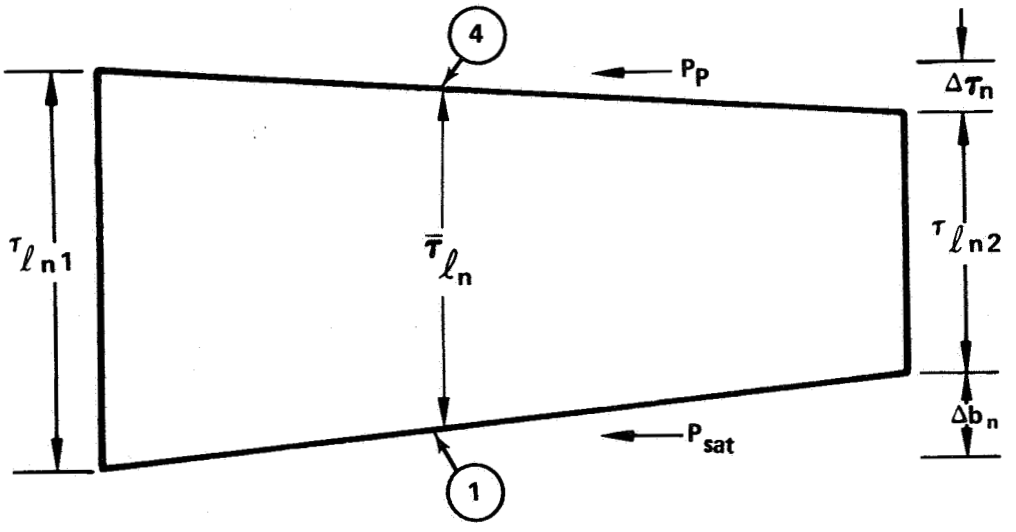

Figure 12. Pressure Force Due to Cavity Growth and Passage Convergence FD 38383B

The pressure force resulting from the change in blade passage width is represented by

$$F_{P\Delta\tau} = (\bar{P})(\Delta\tau_n)\ \Delta\bar{y}\ \cos\bar{\psi}$$

where $\Delta\tau_n$ is the change in blade passage width, and the pressure on the blade pressure surface (P_p) is assumed to be approximately equal to $\bar{P}$. The pressure forces on surfaces 5 and 6 (figure 10), which are the flow areas at each end of the liquid element and are by definition normal to the through flow direction, are expressed as

$$F_{P1} = P_1(\tau_{\ell_1}\ \sin\beta_1^*)\ \Delta y_1\ \cos\bar{\psi}$$

and

$$F_{P2} = P_2(\tau_{\ell_2} \sin \beta_2^*) \Delta y_2 \cos \bar{\psi}$$

where P_1 and P_2 are the inlet and exit streamtube element static pressures.

(3) Centrifugal Force

In inducer flow, the liquid element of mass (m) is moving at some finite tangential velocity (Vu) resulting in a radial or centrifugal force acting on the liquid element.

$$F_R = \frac{m}{g} \frac{Vu^2}{R}$$

If this element is not traveling parallel to the axis of rotation, as illustrated in figure 13, a component of this centrifugal force will act along the through flow direction. This force can be written as:

$$F_C = \frac{m}{g} \frac{Vu^2}{R} \sin \psi$$

or

$$F_C = \frac{\rho}{g} (\tau_{\ell}^{-} \sin \bar{\beta}^*) \Delta y \cos \bar{\psi} (R_2 - R_1) \frac{\overline{Vu}^2}{\bar{R}}$$

where $\overline{Vu}$ and $\bar{R}$ are the average fluid element tangential velocity and radius and $(R_2 - R_1)$ represents the net radial relocation of the streamtube element.

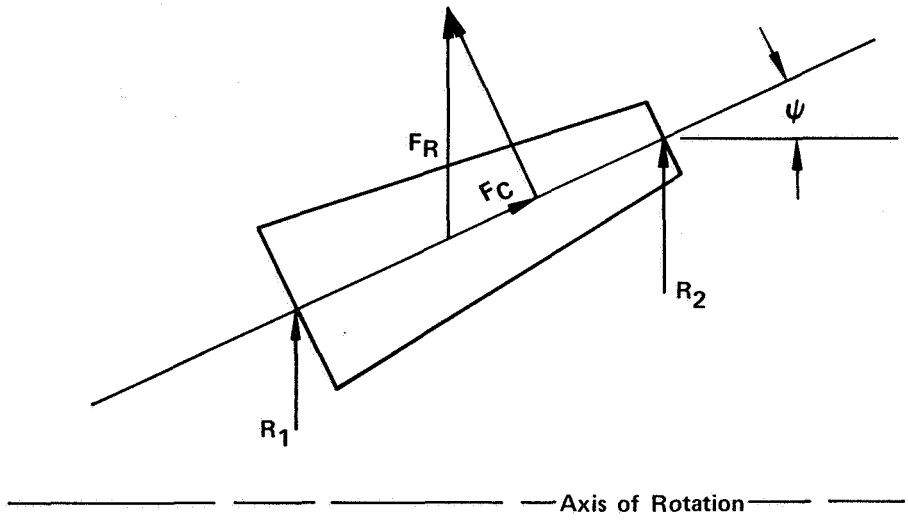

Figure 13. Centrifugal Force on Liquid Element FD 38380

(4) Summary of Forces

The following is a summary of the forces discussed:

$$F_D = C_f \left(\frac{\rho W^2}{2g}\right)\left(\frac{\Delta\bar{y}\cos\bar{\psi}}{\bar{\psi}} + \bar{\tau}_\ell \sin\bar{\beta}^*\right)(\Delta m)$$ Drag Force (general element)

$$F_{PSC} = (\bar{P})\ (\Delta y_{n1} - \Delta y_{n2})\ (\bar{\tau}_\ell \sin\bar{\beta}^*)$$ Pressure Force (streamline convergence)

$$F_{PC} = P_{SAT}\ (\Delta b_n)\ \Delta\bar{y}\cos\bar{\psi}$$ Pressure Force (cavity)

$$F_{P\Delta\tau} = (\bar{P})\ \frac{\Delta\bar{y}\cos\bar{\psi}}{\bar{\psi}}\ (\Delta\tau_n)$$ Pressure Force (change in blade passage width)

$$F_{P1} = P_1\ (\tau_{\ell 1} \sin\beta_1^*)\ \Delta y_1 \cos\bar{\psi}$$ Pressure Force (inlet)

$$F_{P2} = P_2\ (\tau_{\ell 2} \sin\beta_2^*)\ \Delta y_2 \cos\bar{\psi}$$ Pressure Force (exit)

$$F_C = \frac{\rho}{g}\ (\tau_\ell \sin\bar{\beta}^*)\ \Delta\bar{y}\cos\bar{\psi}\ (R_2 - R_1)\ \frac{\bar{V}_u^{\,2}}{\bar{R}}$$ Centrifugal Force

Assuming that the pressures acting in the direction of the flow are positive, the forces are summed and set equal to the change in through flow momentum,

$$F_{P1} + F_C - F_{P2} - F_{PSC} - F_{P\Delta\tau} - F_D - F_{PC} =$$

$$\frac{\dot{m}}{g}\left[W_2 \cos\delta_2 - W_1 \cos\delta_1\right]$$

where $\dot{m}$ is the streamtube mass rate of flow and δ is the deviation angle. Adjustments are made to the cavity slope ($\delta\beta^*$) and height (b) at each station such that the above expression is satisfied for a given streamline location and streamtube shape. This technique is repeated for each streamtube in the inducer analysis at successive stations resulting in definition of the cavity shape. To arrive at the correct cavity shape within an inducer, equilibrium of both through flow and radial momentum must be satisfied. Stipulation of these conditions assures that the proper cavity shape and streamline location are achieved.

(c) Cavity Collapse

The cavity is allowed to grow until its slope ($\delta\beta^*$) becumes zero (parallel to the blade suction surface) indicating that it has reached

its maximum height. Then it is assumed that the cavity collapses in a turbulent wake. This causes a sudden expansion of the liquid flow and results in a loss of total pressure as well as a rise in static pressure. These values are found by specifying a rate of collapse (i.e., wake mixing) and solving for static and total pressure from the equations for continuity of mass and momentum. The loss in total relative pressure (cavity dump loss) is expressed as

$$\Delta P_D = \frac{\rho}{2g}\left[W'\left(1 - \frac{W}{W'}\right)\right]^2 + (\bar{P} - P_{SAT})\left[1 - \frac{W}{W'} - \left(\frac{(\tau_\ell + \tau'_\ell)(\Delta y + \Delta y')}{2\tau_\ell\,\Delta y}\right)\right]$$

The prime refers to values at the previous station.

Figure 14 shows a typical cavity collapse. Point (a) corresponds to the point of maximum cavity height, point (b) represents the complete collapse of the cavity, and $_w$ is the angle of collapse. The cavity collapse angle is a function of the maximum normal cavity height and varies inversely with this cavity height. The relationship between collapse angle and normal cavity height was established during Task VI. By calculating the angle needed to predict the correct cavity lengths for selected conditions, and by curve fitting these angles as a function of maximum cavity height, the collapse angles were determined.

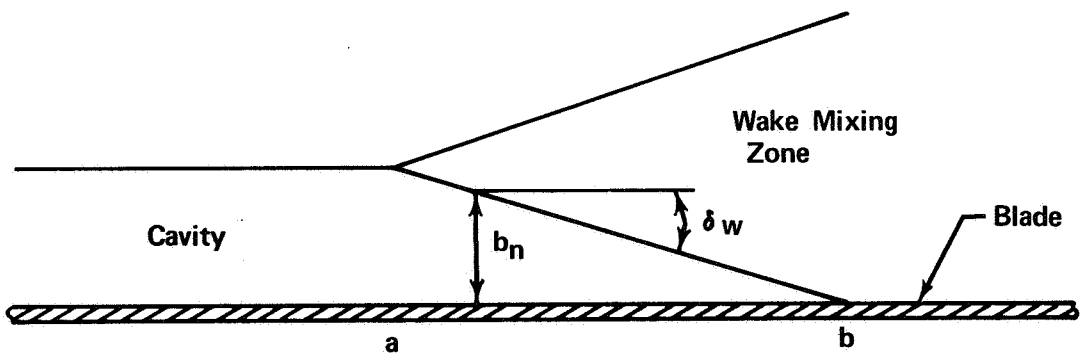

Figure 14. Typical Cavity Collapse FD 48163

d. Typical Results of Analyses

(1) Test Cases

In this section, typical results from the hydrodynamic analysis program are presented for four separate test cases. Two of the test cases were used for verification of the flow model operating under non-cavitating conditions, and the other two test cases were used in evaluating the model during cavitating operation. These test cases were as follows:

Noncavitating

- Paddle wheel
- NASA 12-deg (0.21-rad) helical inducer (NASA TND-1170)

Cavitating

- Cavitating flat plate cascade
- NASA 12-deg (0.21-rad) helical inducer (NASA TND-1170)

(2) Noncavitating Test Cases

(a) Paddle Wheel

This test case was selected to study a simplified geometry that would allow solution of the radial momentum differential equation by direct integration, resulting in an exact expression for the radial distributions of static pressure and axial velocity. Geometry and operating conditions for this test case are shown in figure 15.

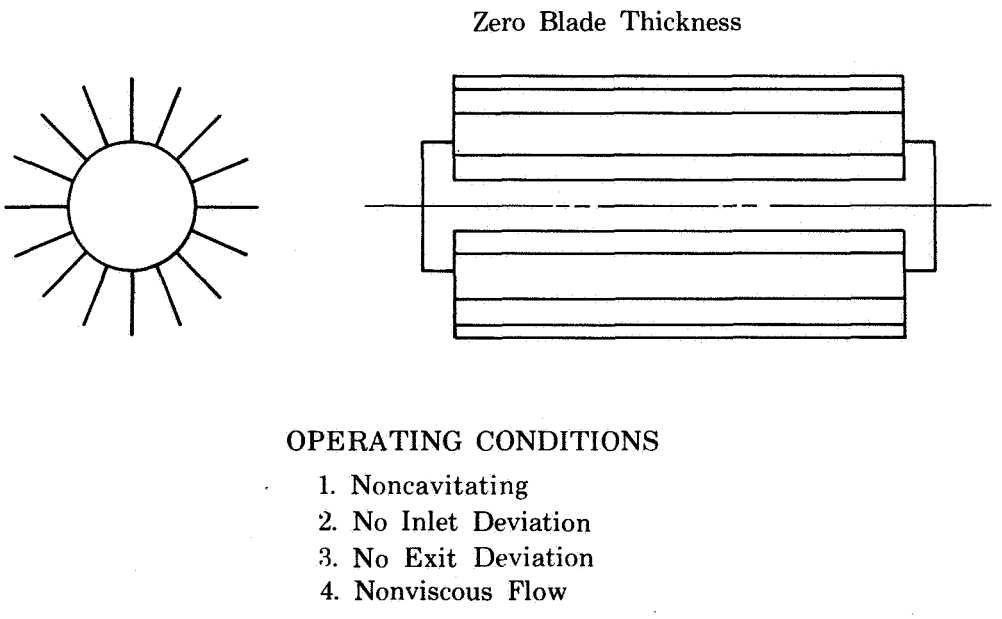

Figure 15. Paddle Wheel Geometry and Operating Conditions FD 25899

A comparison of the exact analytical and program calculated radial pressure profile is shown in figure 16. The program results are shown to be in complete agreement with the exact analytical solution. Verifying that the streamline balance procedure as used by the hydrodynamic program operates as desired in satisfying radial equilibrium.

The criteria for program convergence which assures the correct streamline position and streamtube properties are based on satisfying radial momentum. The error in streamline location at any time during the program relaxation process is defined by:

$$\text{Error} = \frac{\Delta p}{\Delta r} - \frac{dp}{dr}$$

where dp/dr is the radial pressure gradient required to satisfy radial momentum and $\Delta p/\Delta r$ is the pressure gradient which exists between adjacent streamtubes for given streamline locations. The streamline positions are relaxed until their locations satisfy radial momentum.

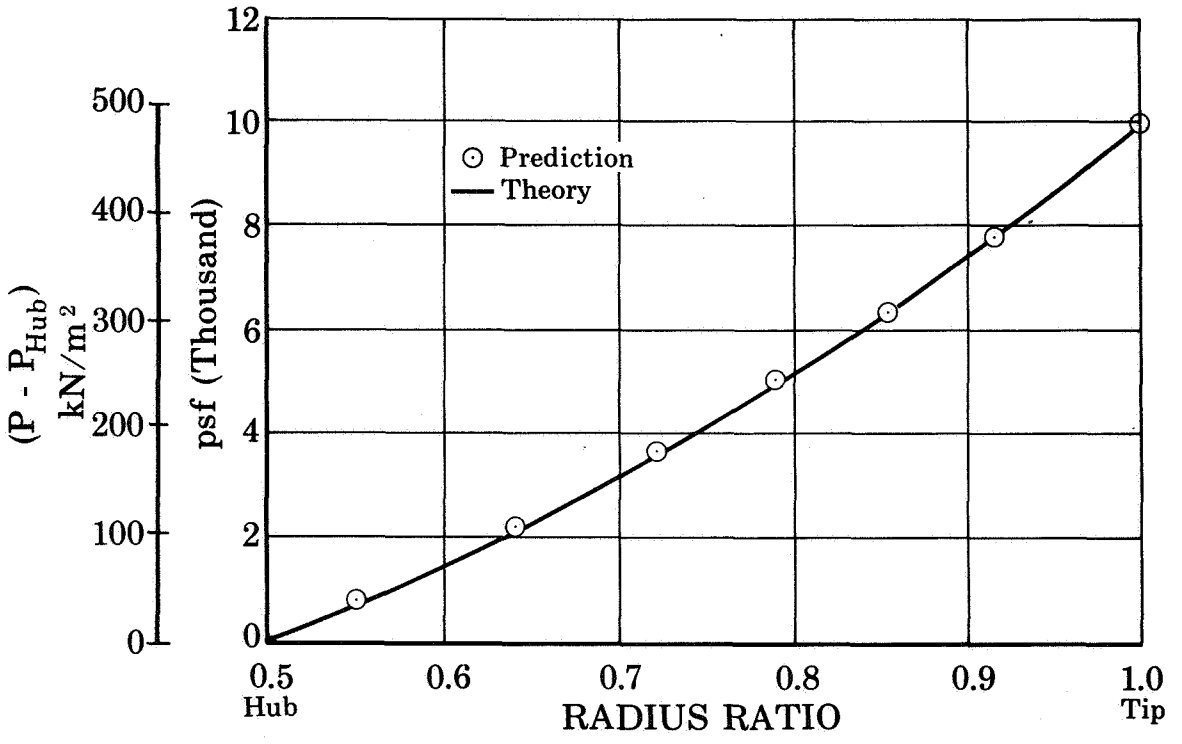

Figure 16. Paddle Wheel Test Case - Radial Equilibrium FD 25397

(b) NASA 12-deg (0.21-rad) Inducer (NASA TND-1170)

Use of this inducer as a test case to aid in program checkout was based upon the availability of an extensive amount of noncavitating test data. This inducer is also reasonably representative of most inducer designs and, therefore, would provide a sufficiently rigorous checkout of the program's capability.

Inducer performance was investigated for several inlet flow coefficients at noncavitating inlet conditions. Comparisons between analytically predicted and experimental results are shown.

1 Head vs Flow

A head-flow curve, plotted as head coefficient as a function of flow coefficient, is shown in figure 17. Close agreement between the experimental and program predicted results is shown.

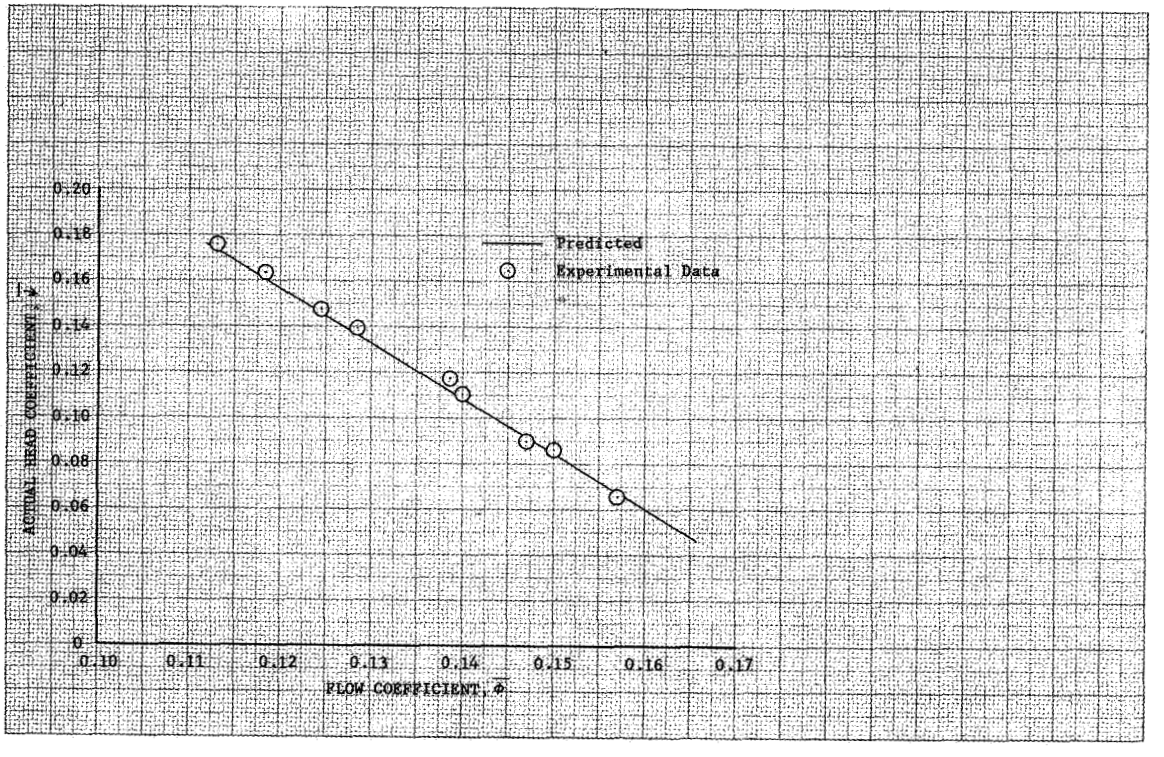

Figure 17. Comparison of Predicted and Actual Head-Flow Coefficient for NASA 12-deg Inducer DF 85015

2 Ideal Head and Head Loss vs Flow

Accurate prediction of actual head coefficient is dependent upon accurate prediction of both ideal head rise and head loss. Figures 18 and 19 show the comparison between predicted and experimental results for ideal head rise and head loss respectively as a function of inlet flow coefficient.

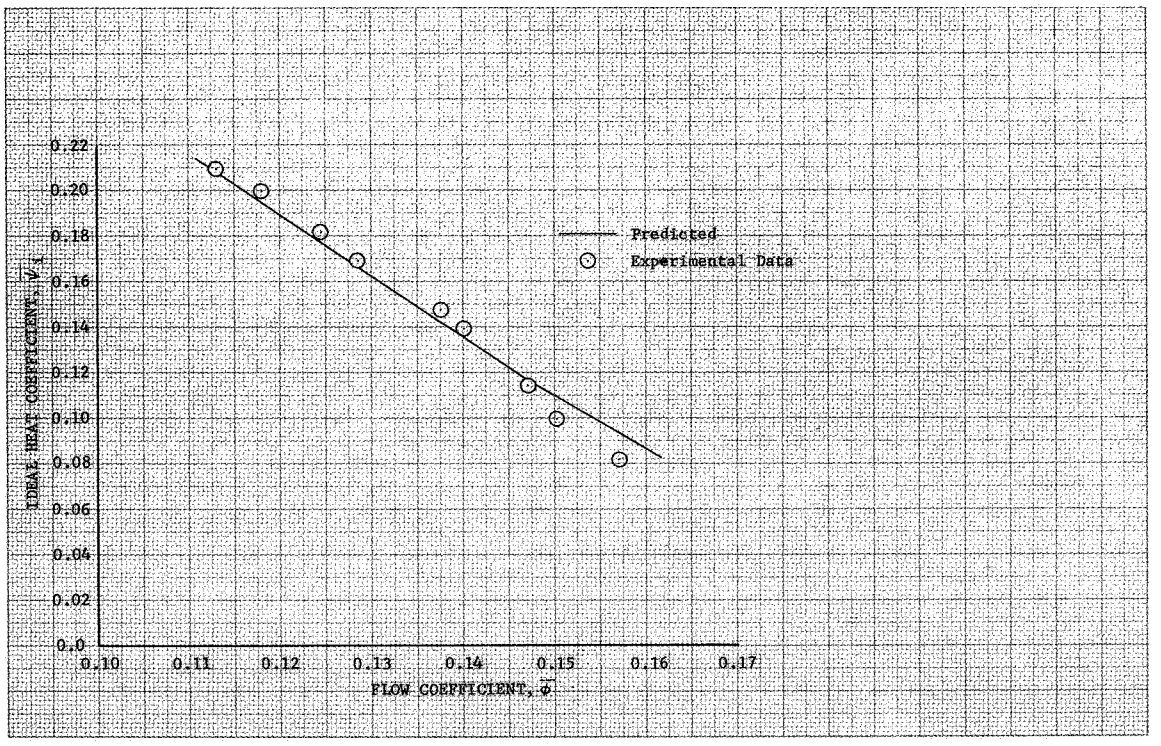

Figure 18. Comparison of Predicted and Actual Ideal Head Coefficient for NASA 12-deg Inducer DF 85014

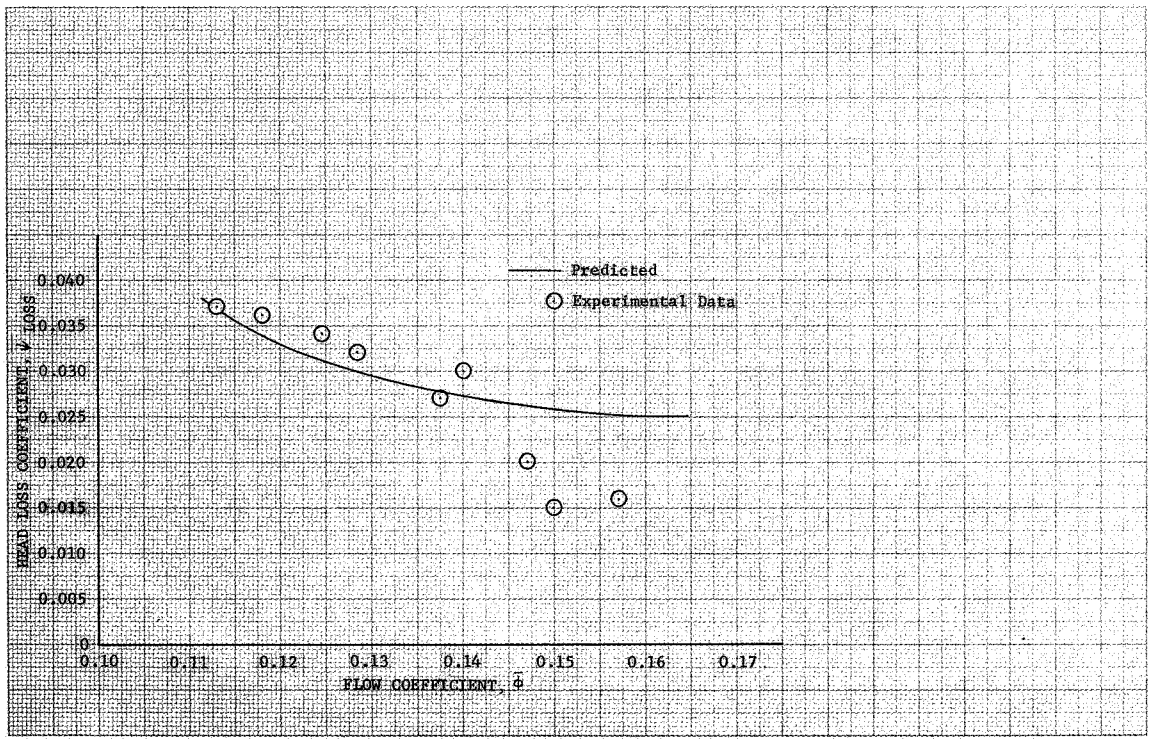

Figure 19. Comparison of Predicted and Actual Head Loss Coefficient for NASA 12-deg Inducer DF 85013

Again, good agreement was achieved thus confirming the accuracy observed in prediction of actual head coefficient (figure 17).

3 Efficiency vs Flow

If ideal head rise and head loss are predicted correctly, not only will actual head rise be accurately predicted but efficiency as well. This is shown in figure 20.

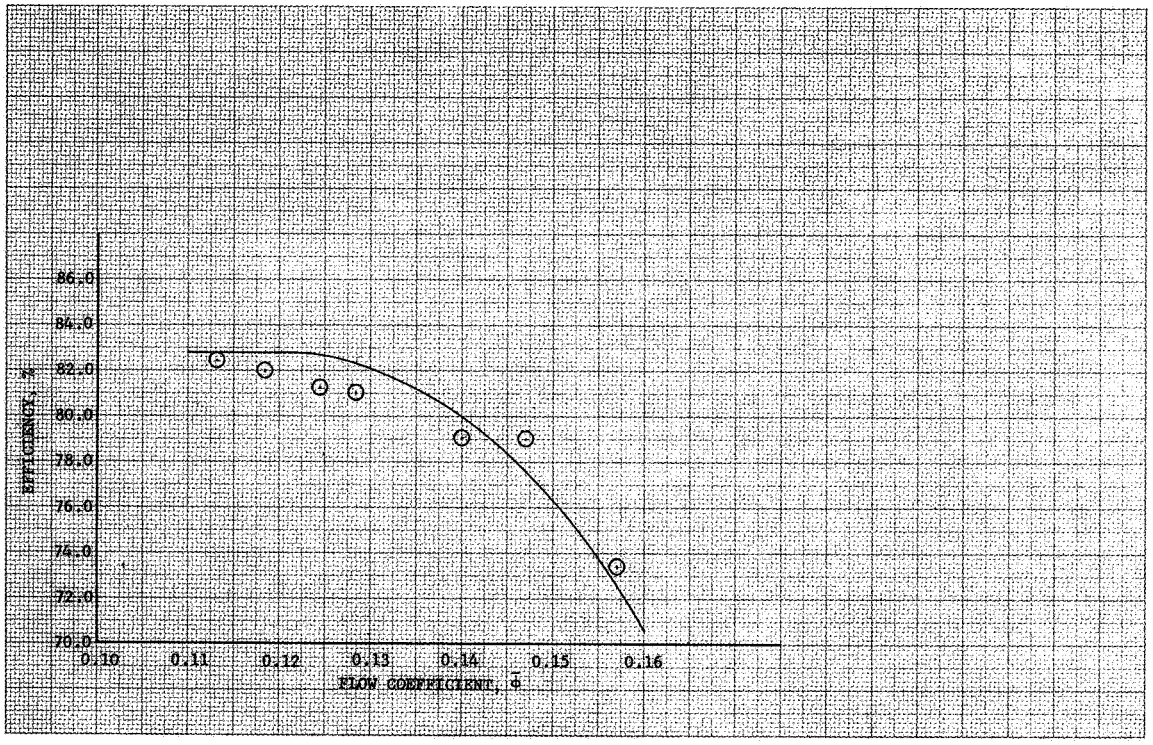

Figure 20. Comparison of Predicted and Actual Efficiency for NASA 12-deg Inducer DF 85012

(3) Cavitating Test Case

(a) Cavitating Flat Plate Cascade

Stripling and Acosta (Reference 2) formulated a two-dimensional inviscid potential flow model for calculating the cavity shape along a zero thickness flat plate cascade of arbitrary stagger angle and inlet conditions. The cavity model used in the present hydrodynamic program (discussed in Section B) can be reduced to a two-dimensional inviscid flow model by eliminating blade thickness, shear forces (viscous effects), and streamline relocation.

This was done by inputting to the program

(1) Zero tip thickness $t_T = 0.0$

(2) Zero taper angle $\gamma = 0.0$

(3) Zero viscosity $\mu = 0.0$

(4) A high hub-to-tip ratio $R_H \approx R_T$

and modifying the source deck to bypass the streamline iteration so that the distance between streamlines remained constant.

The blading geometry and inlet conditions discussed by Stripling and Acosta in Reference 2 were analyzed and the results compared with those presented in their paper. As shown in figure 21, the cavity shape as predicted using the new model for the special, inviscid, two-dimensional, zero blade-thickness case, agrees almost exactly with that predicted by the method of Stripling and Acosta.

(b) NASA 12-deg (0.21-rad) Inducer (Cavitating)

The overall head rise of an inducer operating under varying flow conditions (cavitating and noncavitating) can be recorded in nondimensional form. Figure 22 shows a comparison between test data and computer program results for the cavitating performance of the NASA 12-deg (0.21 rad) inducer recorded in the form ψ/ψ (noncavitating) as a function of cavitation parameter, k. The predicted effect of reducing k on inducer head rise and the predicted point of complete head breakdown agree closely with the experimental data.

2. Stress and Vibration Computer Programs

a. Introduction

Computer programs for determining stress and vibratory characteristics in three-dimensional inducer blades have been developed.

The programs are based on the matrix displacement method using discrete flat triangular elements to define the blade surface.

The inducer blade middle surface is generated by a skewed line that moves at a fixed distance from the axis of the inducer. The numerical (x,y,z) coordinates of this surface are thus directly defined by the wrap angle θ and elevation of the generating line. This surface is then replaced by flat triangular elements that are joined at the vertices or nodes that lie on the surface. The curvature of the surface is thus approximated by the change in direction of the normals to the triangular elements. Each element has a local rectangular coordinate system $(\bar{x},\bar{y},\bar{z})$ associated with it. Displacement functions, which are expressed in terms of local coordinates, yield stiffness, centrifugal load, pressure load, and inertia matrices expressed in terms of generalized nodal forces and generalized nodal displacements.

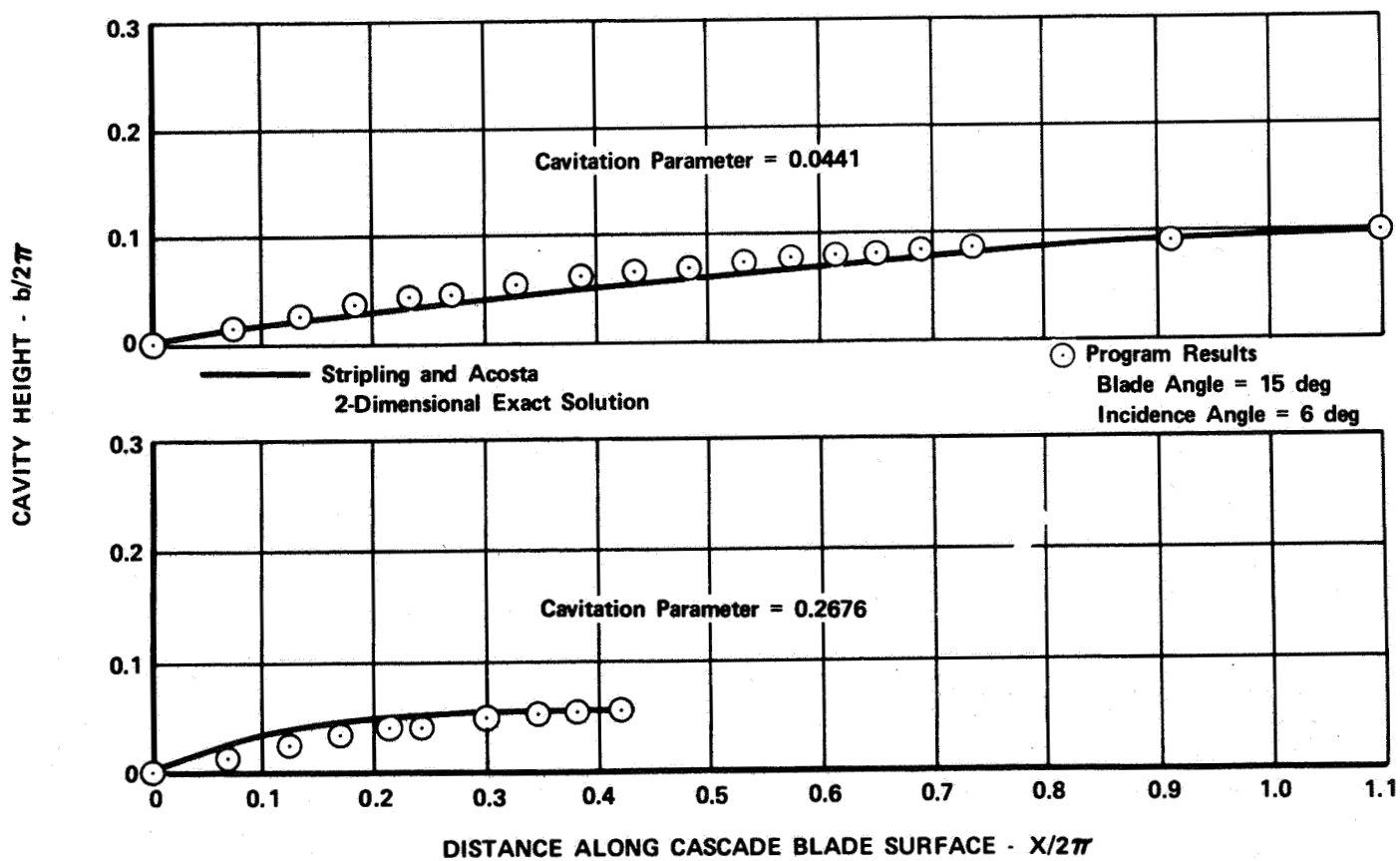

Figure 21. Comparison of Cavity Height Prediction

FD 38276A

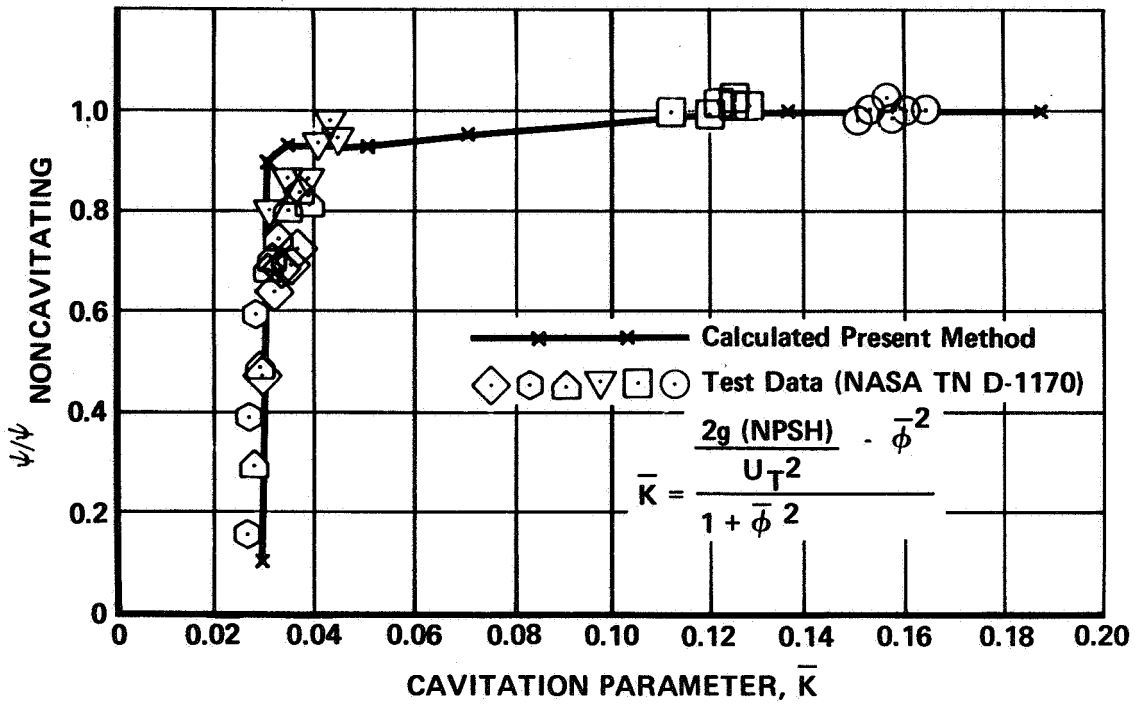

Figure 22. Comparison of Credited and Actual Suction Performance for NASA 12-Deg Inducer FD 40423

For the stress program, these matrices are first transformed to a common rectangular coordinate system. Assembly of these matrices, by satisfying compatibility and equilibrium at common nodes and boundary conditions, yields a set of simultaneous equations with nodal displacements as unknowns. Displacements that satisfy this set of equations are then used to calculate stresses.

The vibration program is handled differently than the stress program because only 50 degrees of freedom can be handled by an existing latent root or eigen-value program. This allows a breakup of only eight free nodes each of which has six degrees of freedom. For this reason, the number of degrees of freedom per free node was reduced to one by first assuming that the dominant displacement is normal to the surface and then using matrix condensation techniques. In this instance, local stiffness and inertia matrices were transformed to a rectangular coordinate system in which the normal direction at a node is in the mean direction of the normals of a set of triangular elements which have common vertices at a node. Assembly of these matrices by satisfying nodal compatibility and equilibrium followed by a matrix condensation yields frequency equations from which frequency and mode shapes are obtained.

b. Derivations of Basic Relations

The derivations of the various relations, in matrix form, that are used in the analytical models for the stress and vibration programs are discussed in Appendix D in the sequence outlined below. They are separated into relations that are common to both the stress and vibration programs and those that apply specifically to only one of the programs.

Both Programs

(1) Direction Cosine Matrix $\left[R_1\right]$

(2) Nodal Coordinate Matrix $\left\{\bar{\Psi}_N\right\}$

(3) Triangular Surface Coordinate Matrix $\left\{\Psi\right\}$

(4) Thickness Matrix Relation

(5) Membrane Stiffness Matrix $\left[\bar{K}_M\right]$

(6) Bending Stiffness Matrix $\left[\bar{K}_B\right]$

Stress Program

(7) Pressure Force Matrix $\left\{\bar{F}_p\right\}_N$

(8) Centrifugal Force Matrix $\left\{\bar{F}_c\right\}_N$

(9) Approximate Centrifugal Force Matrix $\left\{F_c\right\}_N$

Vibration Program

(10) Membrane Inertia Matrix $\left[\bar{M}_M\right]$

(11) Bending Inertia Matrix $\left[\bar{M}_B\right]$

(12) Normal Direction Cosine Matrix $\left[R_1\right]_n$

(13) Relative Vibratory Bending Stress Matrix $\left\{\bar{\sigma}_B\right\}$

c. Description of Analytical Model

(1) Blade Generation

A typical inducer is shown in figure 23. The inducer blade is normally machined by a straight milling cutter whose axis is tilted and may pass at a fixed distance from the axis of the inducer while the inducer blank advances and rotates at the desired lead. The middle surface of the inducer blade is used for purposes of analysis and geometric parameters that define the right-handed (x,y,z) coordinates of the surface are hub radius R_H, off-set radius, R_G, tilt angle λ, lead height z_H, radius R along projection of generator, and wrap angle θ as shown in figure 24.

The (x,y,z) coordinates in terms of these parameters are:

$$x = R_G \cos \theta - R \sin \theta$$

$$y = R_G \sin \theta + R \cos \theta$$

$$z = z_H + (R - R_H) \tan \lambda$$

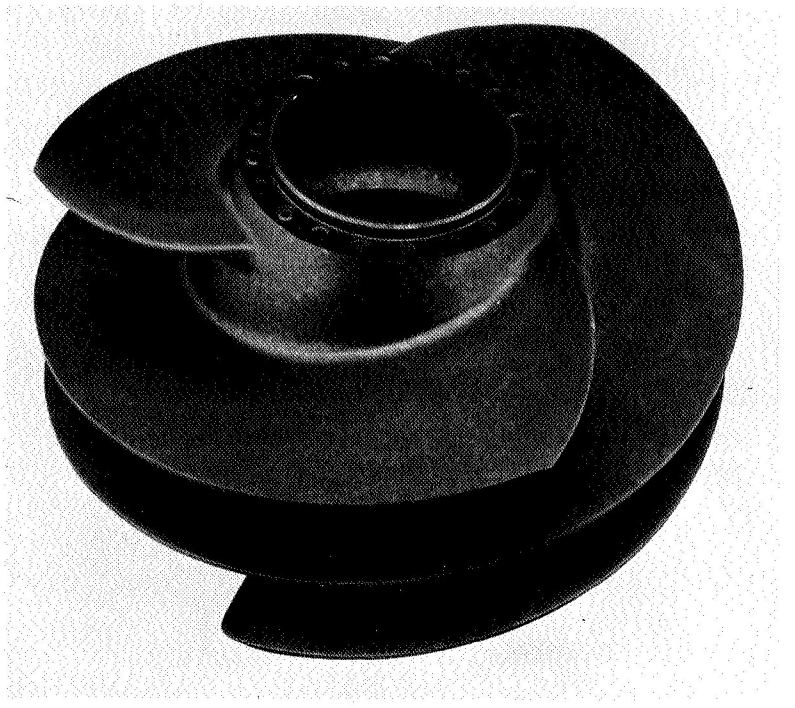

Figure 23. Turbopump Inducer FE 100920

(2) Finite Element Breakup

The use of discrete triangular elements for the stress analysis of three dimensional surfaces is discussed by Argyris, Cheung, Petyt, Zienkiewicz and others. In this instance, the surface is replaced by flat triangular elements that are joined at the vertices or nodes which lie on the original surface. Such analysis requires that the coordinates of the node be expressed in a common and local rectangular coordinate system. A right hand local system was chosen so that the base of each triangle lies on a generating line which defines the $\bar{x}$ axis while the third vertex lies on an adjacent generator. The $\bar{y}$ axis lies in the plane of the triangle in a right-hand sense as shown in figure 25. In this manner the coordinates of the nodes of each triangle are well defined because they always lie on generating lines whose coordinates are known.

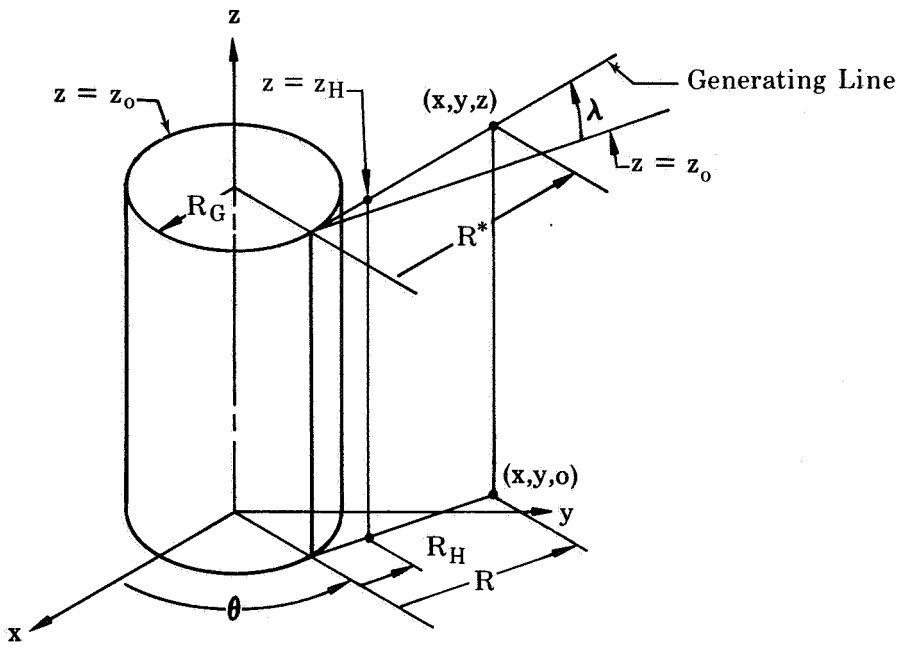

Figure 24. Geometric Parameters of Middle Surface of Inducer Blade FD 25602A

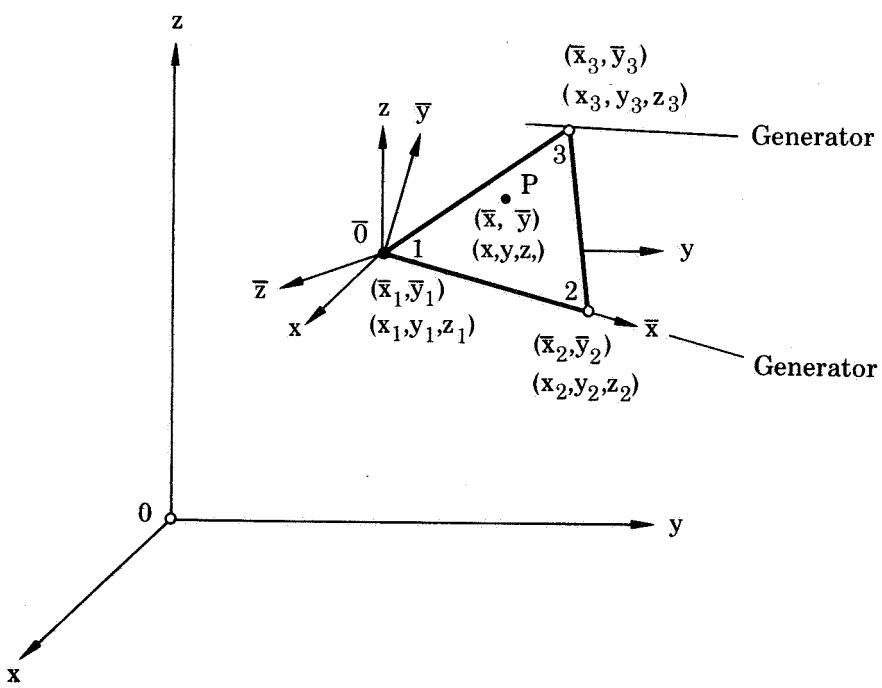

Figure 25. Local ($\bar{x}$, $\bar{y}$, $\bar{z}$) and Common (x, y, z) Rectangular Coordinate System for Triangular Element FD 25629

Nodal points are equally spaced on a generator between the hub radius R_H^* and tip radius R_T^* and establish the triangulation of the inducer blade as shown in figure 26. The common coordinates of the vertices are then used to calculate the direction cosine matrix $[R_1]$ as described in Appendix D. This matrix establishes the relation between the directions of the local coordinate axes relative to the common coordinate axes for each element and is defined as:

$$\left[R_1\right] = \begin{bmatrix} \cos(x,\bar{x}) & \cos(x,\bar{y}) & \cos(x,\bar{z}) \\ \cos(y,\bar{x}) & \cos(y,\bar{y}) & \cos(y,\bar{z}) \\ \cos(z,\bar{x}) & \cos(z,\bar{y}) & \cos(z,\bar{z}) \end{bmatrix}$$

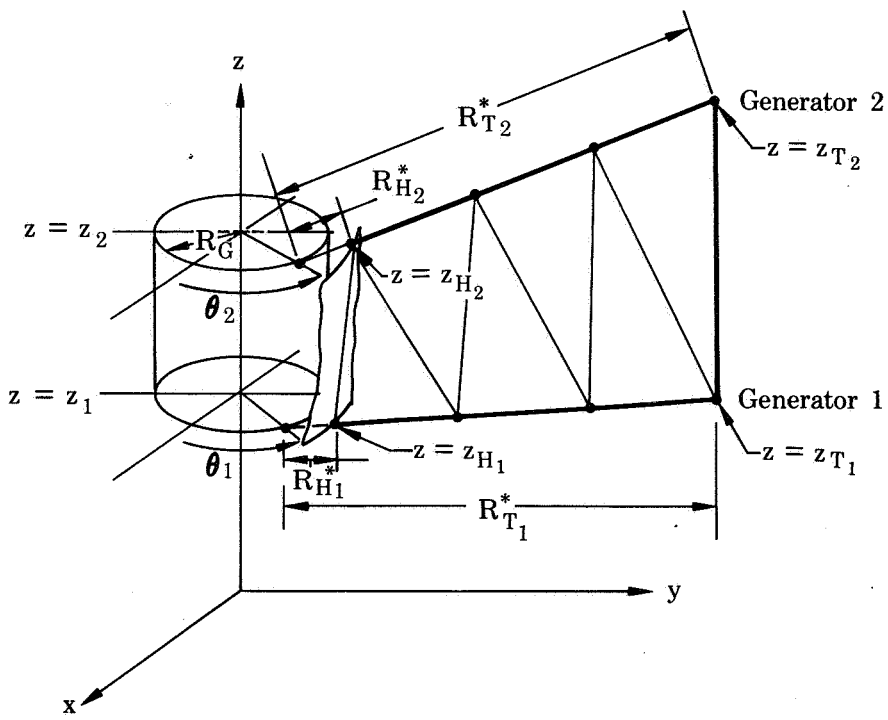

Figure 26. Triangulation of Inducer Blade FD 25630A

This matrix is used later for transforming stiffness and mass matrices and is used to calculate the local nodal coordinates by the following relations:

$$\left\{\bar{\Psi}_1\right\} = \begin{Bmatrix} \bar{x}_1 \\ \bar{y}_1 \\ \bar{z}_1 \end{Bmatrix} = \left\{0\right\}$$

$$\left\{\bar{\Psi}_2\right\} = \begin{Bmatrix} \bar{x}_2 \\ 0 \\ 0 \end{Bmatrix} = \left[R_1\right]^T \begin{Bmatrix} x_2 - x_1 \\ y_2 - y_1 \\ z_2 - z_1 \end{Bmatrix}$$

$$\left\{\bar{\Psi}_3\right\} = \begin{Bmatrix} \bar{x}_3 \\ \bar{y}_3 \\ 0 \end{Bmatrix} = \left[R_1\right]^T \begin{Bmatrix} x_3 - x_1 \\ y_3 - y_1 \\ z_3 - z_1 \end{Bmatrix}$$

or in matrix form:

$$\left\{\bar{\Psi}_N\right\} = \left[R_1\right]^T \left\{\Psi_N - \Psi_1\right\}$$

where

$$\left\{\Psi_N\right\} = \begin{Bmatrix} x_N \\ y_N \\ z_N \end{Bmatrix} \quad N = 1,2,3$$

(3) Displacement Functions for Triangular Elements

The use of triangular elements for finite element analysis is discussed extensively by Argyris, Cheung, Clough, Hermann, Melosh, Petyt, Tocher, Utku, Zienkiewicz, and others. Methods which are directly applicable to the three-dimensional inducer problem are discussed by Argyris, Cheung, Petyt, and Zienkiewicz.

The accuracy of the displacement method depends upon the selection of an appropriate displacement function; polynomial functions usually being the most appropriate.

For the triangular element under in-plane membrane loading the expressing of local membrane displacements $\bar{u}$ and $\bar{v}$ as linear functions of $\bar{x}$ and $\bar{y}$ yields a uniform strain field in the triangular element. Such a function provides compatibility at the interface between adjacent elements and involves six coefficients that are determined in terms of the six nodal displacements and six nodal coordinates of the vertices of the triangle. Linear displacement functions are used in the derivation of the membrane stiffness matrix $[\bar{K}_M]$ and the membrane inertia matrix $[\bar{M}_M]$ in paragraphs (5) and (10) of Appendix D, respectively.

An appropriate displacement function for triangular elements under bending is more difficult to set up because in addition to a lateral deflection, $\bar{w}$, there are rotations, $\bar{\theta}_x$ and $\bar{\theta}_y$. Thus, there will be nine nodal displacements for each triangular element. If a cubic polynomial

deflection function with terms like; const.-, $\bar{x}$, $\bar{y}$, $\bar{x}^2$, $\overline{xy}$, $\bar{y}^2$, $\bar{x}^3$, $\bar{x}^2\bar{y}$, $\overline{xy}^2$, $\bar{y}^3$, is selected, one of the 10 terms will have to be deleted because only nine conditions can be satisfied, and hence the displacement function can have only nine coefficients. Although compatibility of edge displacement and slope in the direction of edges at an interface exists for the cubic displacement function, there is no guarantee that the normal slope in a direction perpendicular to the edges is continuous. It is not known how much error will be caused by such nonconformity. Clough, Zienkiewicz, and others discuss methods of obtaining conforming displacement functions but they are too complicated for use in the inducer program.

The Adini polynominal displacement function

$$\bar{w} = \bar{a}_1 + \bar{a}_2\bar{x} + \bar{a}_3\bar{y} + \bar{a}_4\bar{x}^2 + \bar{a}_5\bar{y}^2 + \bar{a}_6\bar{x}^3 + \bar{a}_7\bar{x}^2\bar{y} + \bar{a}_8\bar{x}\bar{y}^2 + \bar{a}_9\bar{y}^3.$$

where the uniform twist term, $\bar{x}\bar{y}$, in the 10 term cubic polynominal is omitted to maintain symmetry, as discussed by Clough, has been used successfully in other applications and as a result was employed in the inducer program.

(4) Effective Stress Criteria

The use of radial, tangential, and shear stresses individually for design purposes is meaningless because the interaction of these stresses can cause a failure mode which would not be apparent if the stresses were used individually. For this reason a provision has been made in the program to calculate an effective stress, based on combined stresses, which can be compared to the allowable uniaxial stress obtained from conventional test specimens. Generally, when the effective stress exceeds the allowable stress, failure is possible due to the initiation of plastic flow. Experiments indicate that an effective stress based on the energy of distortion theory is applicable. This effective stress $\bar{\sigma}_e$ in terms of the principal stresses $\bar{\sigma}_x$ and $\bar{\sigma}_y$ as used in the programs is

$$\bar{\sigma}_e = \sqrt{\bar{\sigma}_x^{\,2} + \bar{\sigma}_y^{\,2} - \bar{\sigma}_x\bar{\sigma}_y}$$

Although the effective stress does not exist physically, its distribution over the inducer blade, based on the combining of theoretical and measured stresses, will indicate areas of distress wherever its value exceeds the allowable.

It should be noted that if membrane stresses exist the total stress at the centroid on the top surface of an element can differ from that at the centroid on the bottom of the same element. For this reason the program calculates centroidal stresses at the top, middle, and bottom surface of each element. When membrane stresses are negligible the effective stresses at the top and bottom surfaces of an element are equal and the true stresses differ in sign only.

d. Methods of Analysis

(1) Stress Program

(a) Forces and Displacements

The matrix displacement method using discrete triangular elements is used for these programs. In this method generalized nodal forces are expressed as linear functions of generalized nodal displacements in matrix form. These matrices are derived in paragraph B2d, below, and are determined for triangular elements in the local coordinate system. The force and displacement systems are right-handed, and the components are shown in figures 27 and 28. Moments and rotations are treated as vectors in the same manner as forces and displacements, as is done by Petyt and Zienkiewicz. This prevents confusion when transforming matrices to a rotated coordinate system. The matrix relation for the local system is then:

$$\left\{\bar{F}\right\}_N = \underset{(15 \times 1)}{\begin{bmatrix} \bar{F}_{\bar{x}_1} \\ \bar{F}_{\bar{y}_1} \\ \bar{F}_{\bar{x}_2} \\ \bar{F}_{\bar{y}_2} \\ \bar{F}_{\bar{x}_3} \\ \bar{F}_{\bar{y}_3} \\ \hline \bar{F}_{\bar{z}_1} \\ \bar{M}_{\bar{x}_1} \\ \bar{M}_{\bar{y}_1} \\ \bar{F}_{\bar{z}_2} \\ \bar{M}_{\bar{x}_2} \\ \bar{M}_{\bar{y}_2} \\ \bar{F}_{\bar{z}_3} \\ \bar{M}_{\bar{x}_3} \\ \bar{M}_{\bar{y}_3} \end{bmatrix}_N} = \underset{(15 \times 15)}{\left[\begin{array}{c|c} \left[\bar{K}_M\right] & 0 \\ (6x6) & (6x9) \\ \hline 0 & \left[\bar{K}_B\right] \\ (9x6) & (9x9) \end{array}\right]} \underset{(15 \times 1)}{\begin{bmatrix} \bar{u}_1 \\ \bar{v}_1 \\ \bar{u}_2 \\ \bar{v}_2 \\ \bar{u}_3 \\ \bar{v}_3 \\ \hline \bar{w}_1 \\ \bar{\theta}_{\bar{x}_1} \\ \bar{\theta}_{\bar{y}_1} \\ \bar{w}_2 \\ \bar{\theta}_{\bar{x}_2} \\ \bar{\theta}_{\bar{y}_2} \\ \bar{w}_3 \\ \bar{\theta}_{\bar{x}_3} \\ \bar{\theta}_{\bar{y}_3} \end{bmatrix}_N} = \left[\bar{K}\right]\left\{\bar{\delta}\right\}_N$$

where $\left[\bar{K}_M\right]$ and $\left[\bar{K}_B\right]$ are the local membrane and bending stiffness matrices whose composite form is $\left[\bar{K}\right]$, and $\left\{\bar{F}\right\}_N$ and $\left\{\bar{\delta}\right\}_N$ are generalized nodal force and displacement column matrices or vectors. Displacements and moments in the local $\bar{z}$ direction are assumed zero as is discussed by Zienkiewicz. These terms, however, will appear in this common system and are retained for convenience.

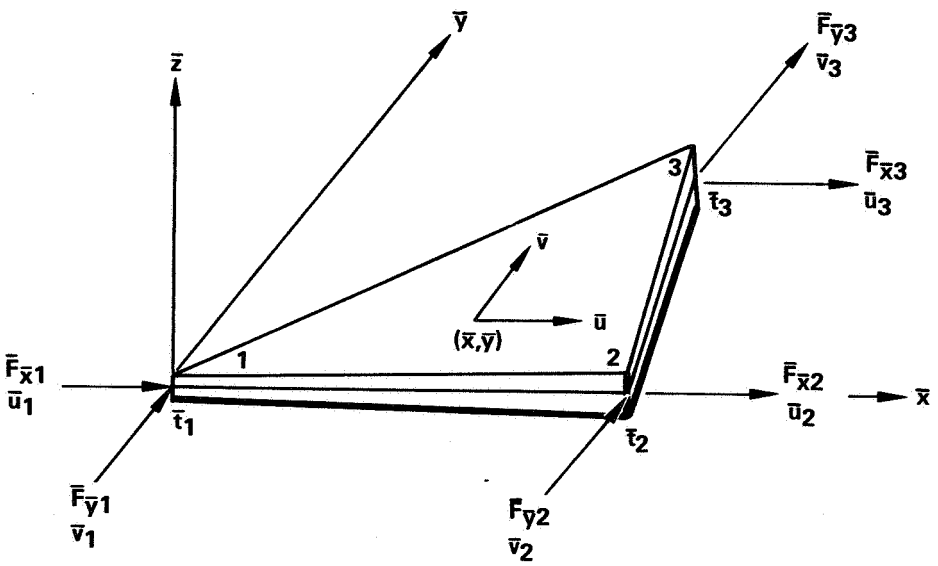

Figure 27. Generalized Nodal Local Membrane Displacements and Forces on Flat Triangular Element FD 25631A

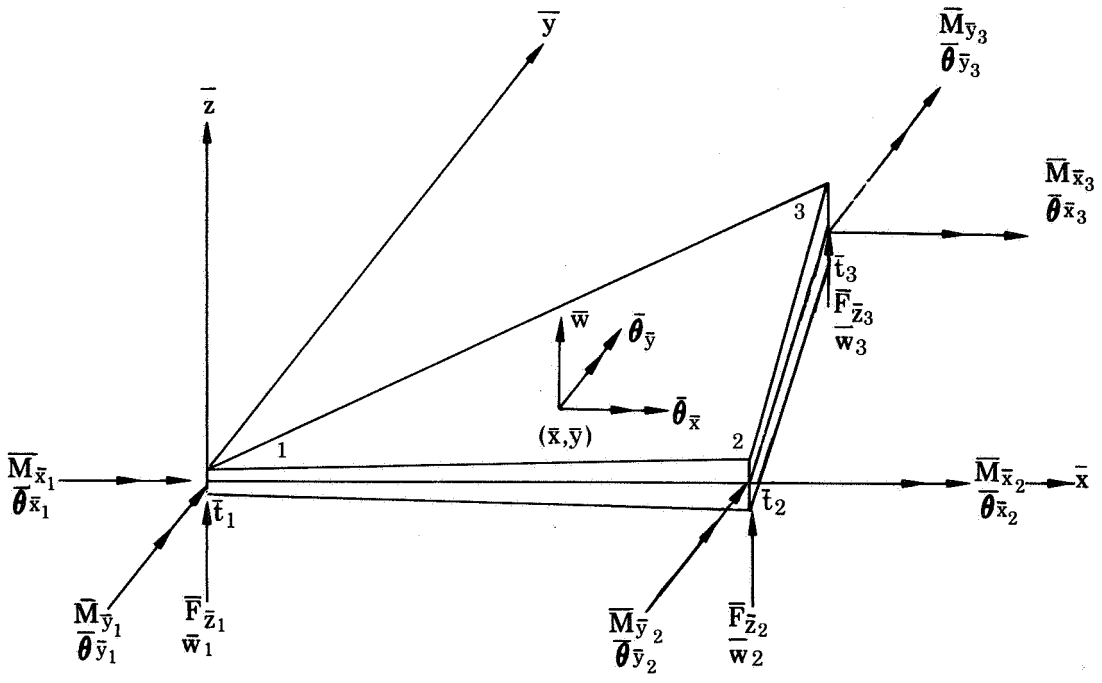

Figure 28. Generalized Nodal Bending Displacements and Forces on Flat Triangular Element FD 25652A

Generalized nodal pressure force matrices $\left\{\bar{F}_p\right\}_N$ and generalized nodal centrifugal forces matrices $\left\{\bar{F}_c\right\}_N$, which are derived in Appendix D, are also column matrices or vectors of the same order as $\left\{\bar{F}\right\}_N$. With these forces acting the general nodal force-displacement relation for a triangular element in local coordinates is:

$$\left\{\bar{F}\right\}_N = \left[\bar{K}\right]\left\{\bar{\delta}\right\}_N - \left\{\bar{F}_p\right\}_N - \left\{\bar{F}_c\right\}_N \tag{1}$$

To solve the three-dimensional stress problem, all generalized forces and displacements in this local system must be broken into components along the axes in the common system. This is accomplished by applying the direction cosine matrix $\left[R_1\right]$ to triplets of generalized forces and displacements in the local system. Because there are 6 degrees of freedom per node the stiffness matrix for a triangular element will be of order (18 x 18) and the generalized force and displacement matrices will be of order (18 x 1). To make the local matrices compatible, they must be of the same order. This is accomplished by placing zeros in appropriate positions; $\left\{\bar{F}_p\right\}_N$ and $\left\{\bar{F}_c\right\}_N$ are also expressed as an (18 x 1) column matrix by inserting zeros in appropriate locations.

$$
\underset{(18 \times 1)}{\begin{bmatrix} \bar{F}_{\bar{x}_1} \\ \bar{F}_{\bar{y}_1} \\ \bar{F}_{\bar{x}_2} \\ \bar{F}_{\bar{y}_2} \\ \bar{F}_{\bar{x}_3} \\ \bar{F}_{\bar{y}_3} \\ \hline \bar{F}_{\bar{z}_1} \\ \bar{M}_{\bar{x}_1} \\ \bar{M}_{\bar{y}_1} \\ \bar{F}_{\bar{z}_2} \\ \bar{M}_{\bar{x}_2} \\ \bar{M}_{\bar{y}_2} \\ \bar{F}_{\bar{z}_3} \\ \bar{M}_{\bar{x}_3} \\ \bar{M}_{\bar{y}_3} \\ \hline \bar{M}_{\bar{z}_1} \\ \bar{M}_{\bar{z}_2} \\ \bar{M}_{\bar{z}_3} \end{bmatrix}_N}
=
\underset{(18 \times 18)}{\left[\begin{array}{c|c} \underset{(6 \times 6)}{\left[\bar{K}_M\right]} & 0 \\ \hline \text{SYMMETRIC} & \underset{(9 \times 9)}{\left[\bar{K}_B\right]} \end{array}\right]}
\underset{(18 \times 1)}{\left[\begin{array}{c} \bar{u}_1 \\ \bar{v}_1 \\ \bar{u}_2 \\ \bar{v}_2 \\ \bar{u}_3 \\ \bar{v}_3 \\ \hline \bar{w}_1 \\ \bar{\theta}_{\bar{x}_1} \\ \bar{\theta}_{\bar{y}_1} \\ \bar{w}_2 \\ \bar{\theta}_{\bar{x}_2} \\ \bar{\theta}_{\bar{y}_2} \\ \bar{w}_3 \\ \bar{\theta}_{\bar{x}_3} \\ \bar{\theta}_{\bar{y}_3} \\ \hline \bar{\theta}_{\bar{z}_1} \\ \bar{\theta}_{\bar{z}_2} \\ \bar{\theta}_{\bar{z}_3} \end{array}\right]_N}
\qquad (2)
$$

The order of the elements in the local generalized force and displacement column matrices are then changed to be compatible with that of the direction cosine matrix $\left[R_1\right]$. Under this re-ordering, the relation between the generalized force and displacement column matrices in the common system and the local system is

$$
\underset{(18\times 1)}{\begin{bmatrix} F_{x_1} \\ F_{y_1} \\ F_{z_1} \\ F_{x_2} \\ F_{y_2} \\ F_{z_2} \\ F_{x_3} \\ F_{y_3} \\ F_{z_3} \\ M_{x_1} \\ M_{y_1} \\ M_{z_1} \\ M_{x_2} \\ M_{y_2} \\ M_{z_2} \\ M_{x_3} \\ M_{y_3} \\ M_{z_3} \end{bmatrix}_N}
,
\underset{(18\times 1)}{\begin{bmatrix} u_1 \\ v_1 \\ w_1 \\ u_2 \\ v_2 \\ w_2 \\ u_3 \\ v_3 \\ w_3 \\ \theta_{x_1} \\ \theta_{y_1} \\ \theta_{z_1} \\ \theta_{x_2} \\ \theta_{y_2} \\ \theta_{z_2} \\ \theta_{x_3} \\ \theta_{y_3} \\ \theta_{z_3} \end{bmatrix}_N}
=
\underset{(18\times 18)}{\begin{bmatrix} \left[R_1\right] & & & & & 0 \\ & \left[R_1\right] & & & & \\ & & \left[R_1\right] & & & \\ & & & \left[R_1\right] & & \\ & & & & \left[R_1\right] & \\ \text{SYMMETRIC} & & & & & \left[R_1\right] \end{bmatrix}}
\underset{(18\times 1)}{\begin{bmatrix} \bar{F}_{x_1} \\ \bar{F}_{y_1} \\ \bar{F}_{z_1} \\ \bar{F}_{x_2} \\ \bar{F}_{y_2} \\ \bar{F}_{z_2} \\ \bar{F}_{x_3} \\ \bar{F}_{y_3} \\ \bar{F}_{z_3} \\ \bar{M}_{x_1} \\ \bar{M}_{y_1} \\ \bar{M}_{z_1} \\ \bar{M}_{x_2} \\ \bar{M}_{y_2} \\ \bar{M}_{z_2} \\ \bar{M}_{x_3} \\ \bar{M}_{y_3} \\ \bar{M}_{z_3} \end{bmatrix}_N}
,
\underset{(18\times 1)}{\begin{bmatrix} \bar{u}_1 \\ \bar{v}_1 \\ \bar{w}_1 \\ \bar{u}_2 \\ \bar{v}_2 \\ \bar{w}_2 \\ \bar{u}_3 \\ \bar{v}_3 \\ \bar{w}_3 \\ \bar{\theta}_{x_1} \\ \bar{\theta}_{y_1} \\ \bar{\theta}_{z_1} \\ \bar{\theta}_{x_2} \\ \bar{\theta}_{y_2} \\ \bar{\theta}_{z_2} \\ \bar{\theta}_{x_3} \\ \bar{\theta}_{y_3} \\ \bar{\theta}_{z_3} \end{bmatrix}_N}
$$

or, in matrix notation

$$\left\{F\right\}_N = \left[R_6\right]\left\{\bar{F}\right\}_N \tag{3}$$

$$\left\{\delta\right\}_N = \left[R_6\right]\left\{\bar{\delta}\right\}_N \tag{4}$$

The general force-displacement matrix relation for a triangular element in the common system is obtained conventionally by transforming (1) using (3) and (4) from which

$$\left\{\bar{F}\right\}_N = \left[R_6\right]^T \left\{F\right\}_N \text{ and } \left\{\bar{\delta}\right\}_N = \left[R_6\right]^T \left\{\delta\right\}_N$$

Then (1) transforms from

$$\left\{\bar{F}\right\}_N = \left[\bar{K}\right]\left\{\bar{\delta}\right\}_N - \left\{\bar{F}_p\right\}_N - \left\{\bar{F}_c\right\}_N$$

to

$$\left[R_6\right]^T \left\{F\right\}_N = \left[\bar{K}\right]\left[R_6\right]^T \left\{\delta\right\}_N - \left[R_6\right]^T \left\{F_p\right\}_N - \left[R_6\right]^T \left\{F_c\right\}_N$$

or

$$\left\{F\right\}_N = \left[R_6\right]\left[\bar{K}\right]\left[R_6\right]^T \left\{\delta\right\}_N - \left\{F_p\right\}_N - \left\{F_c\right\}_N$$

Thus, the general force-displacement matrix relation for a triangle in the common system is expressed by

$$\left\{F\right\}_N = \left[K\right]\left\{\delta\right\}_N - \left\{F_p\right\}_N - \left\{F_c\right\}_N \tag{5}$$

where the elements on the right side are obtained directly from the local system properties by the relations

$$\left\{F_p\right\}_N = \left[R_6\right]\left\{\bar{F}_p\right\}_N$$

$$\left\{F_c\right\}_N = \left[R_6\right]\left\{\bar{F}_c\right\}_N$$

$$\left[K\right] = \left[R_6\right]\left[\bar{K}\right]\left[R_6\right]^T$$

The generalized nodal displacement matrix relation for the triangulated surface was assembled by considering a representative node that is common to neighboring triangular elements as shown in figure 29. Because each node has 6 degrees of freedom there will be 6n degrees of freedom for a system with n free nodes. Thus all column matrices will be of order (6n x 1) and the stiffness matrix will be of order (6n x 6n). The operations that yield the displacement matrix relation are:

1. Add the elements of $\left\{F_p\right\}_N$ and $\left\{F_c\right\}_N$ which are associated with a common node. This yields the system matrices $\left\{F_p\right\}_T$ and $\left\{F_c\right\}_T$
2. Sum all of the elements of $\left\{F\right\}_N$ which are associated with a common node to zero in order to satisfy internal nodal equilibrium

3. Equate generalized displacements of vertices that have a common node.

4. Add elements of stiffness matrices which are associated with a common node. This will yield the system stiffness matrix $\left[K\right]_T$.

The generalized displacement matrix equation for the system is then

$$\left[K\right]_T \left\{\delta\right\}_N - \left\{F_p\right\}_T - \left\{F_c\right\}_T = \left\{0\right\} \tag{6}$$

The solution to this set of simultaneous equations yields the generalized nodal displacements $\left\{\delta\right\}_N$. These are then transformed back to the local system by

$$\left\{\bar{\delta}\right\}_N = \left[R_6\right]^T \left\{\delta\right\}_N$$

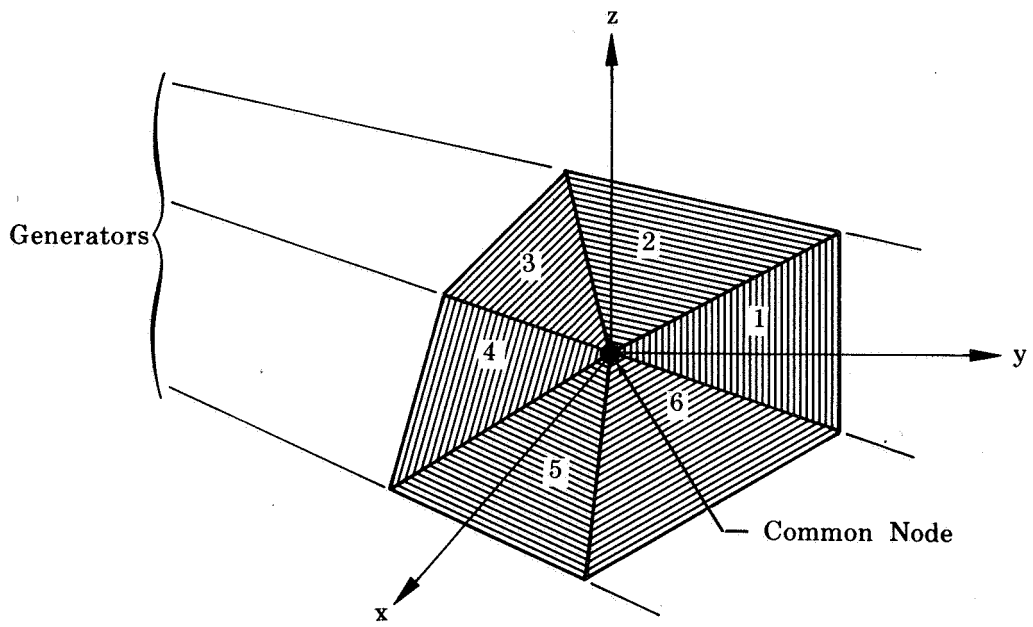

Figure 29. Common Node of 6 Neighboring Triangles FD 25667A

(b) Stresses

The membrane stress matrix and bending moment matrix in the local system are then given by

$$\left\{\bar{\sigma}_M\right\} = \begin{Bmatrix} \bar{\sigma}_{\bar{x}\bar{x}} \\ \bar{\sigma}_{\bar{y}\bar{y}} \\ \bar{\tau}_{\bar{x}\bar{y}} \end{Bmatrix}_M = \left[\bar{E}_M\right]\left[\bar{W}_M\right]\left[\bar{A}_M\right]_N^{-1} \left\{\bar{\delta}_M\right\}_N$$

$$\left\{\bar{M}\right\} = \begin{Bmatrix} \bar{M}_{\bar{x}} \\ \bar{M}_{\bar{y}} \\ \bar{M}_{\bar{x}\bar{y}} \end{Bmatrix}_B = \bar{D} \left[\bar{V}_{B_1}\right]\left[\bar{E}_B\right]\left[\bar{A}_B\right]_N^{-1} \left\{\bar{\delta}_B\right\}_N$$

with the symbols defined in Appendix D. The bending moments are linear functions of $\bar{x}$ and $\bar{y}$ and are evaluated at the centroid C to yield the centroidal bending stresses.

$$\left\{\bar{\sigma}_B\right\} = \begin{Bmatrix} \bar{\sigma}_{\bar{y}} \\ \bar{\sigma}_{\bar{x}} \\ \bar{\tau}_{\bar{x}\bar{y}} \end{Bmatrix}_B = \frac{\left\{6\ \bar{M}_c\right\}}{\bar{t}_c^{\,2}}$$

(c) Development of Subsystems

The direct solution of the set of simultaneous equations (6) is time-consuming and uneconomical when a large number of unknowns is involved. For this reason, the execution time was reduced by subsystem analysis. This was accomplished by providing an option to divide the system into subsystems as shown in figure 30. Each subsystem has common boundary nodes a and internal nodes b. The internal nodes include all nodes that do not lie on a common boundary. The general force-displacement relation for each subsystem is of the form (5) and becomes

$$\left\{F\right\}_{N^{ss}} = \left[K\right]_{ss}\left\{\delta\right\}_{N^{ss}} - \left\{F_p\right\}_{N^{ss}} - \left\{F_c\right\}_{N^{ss}}$$

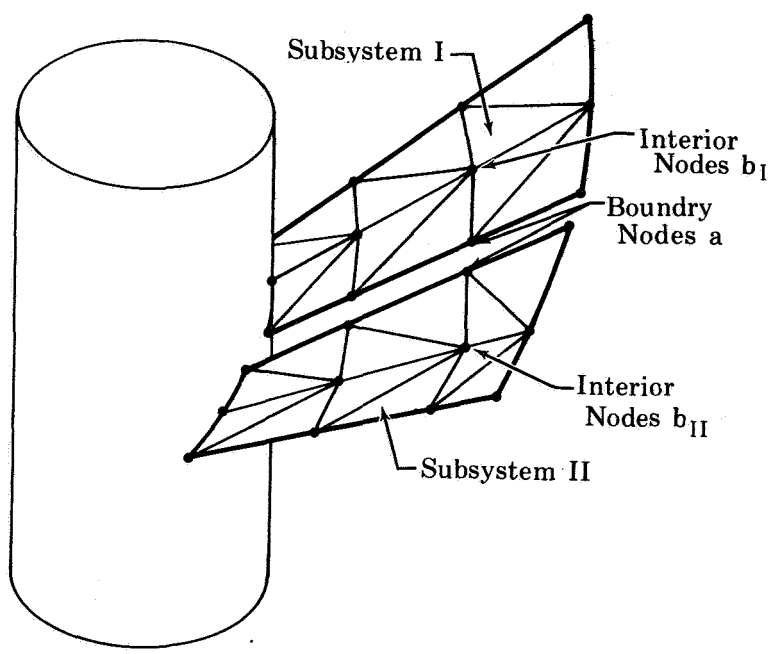

Figure 30. Division of System Into Subsystems FD 25668A

Then, the subsystem matrix was partitioned to separate boundary nodes from internal nodes in the following manner since the summation of nodal forces at internal points is zero.

$$\left\{F\right\}_{N^{ss}} = \left\{\begin{matrix} F_a \\ 0 \end{matrix}\right\}_{N^{ss}} = \left[\begin{matrix} K_{aa} & K_{ab} \\ K_{ba} & K_{bb} \end{matrix}\right] \left\{\begin{matrix} \delta_a \\ \delta_b \end{matrix}\right\}_N - \left\{\begin{matrix} F_{pa} \\ F_{pb} \end{matrix}\right\}_N - \left\{\begin{matrix} F_{ca} \\ F_{cb} \end{matrix}\right\}_N$$

This partitioning yields two matrix equations

$$\begin{aligned} \left[K_{aa}\right]\left\{\delta_a\right\}_N + \left[K_{ab}\right]\left\{\delta_b\right\}_N - \left\{F_{pa}\right\}_N - \left\{F_{ca}\right\}_N &= \left\{F_a\right\}_N \\ \left[K_{ba}\right]\left\{\delta_a\right\}_N + \left[K_{bb}\right]\left\{\delta_b\right\}_N - \left\{F_{pb}\right\}_N - \left\{F_{cb}\right\}_N &= 0 \end{aligned} \qquad (7)$$

By eliminating the internal nodal deflections $\left\{\delta_b\right\}_N$ from the expressions, the generalized boundary force $\left\{F_a\right\}_N$ in terms of the generalized boundary deflection and the internal properties of the subsystem is obtained. Thus,

$$\begin{aligned} \left\{F_a\right\}_{N^{ss}} = &\left[K_{aa} - K_{ab}K_{bb}^{-1}K_{ba}\right]\left\{\delta_a\right\}_N \\ &- \left[F_{pa} - K_{ab}K_{bb}^{-1}\left\{F_{pb}\right\}\right]_N \\ &- \left[F_{ca} - K_{ab}K_{bb}^{-1}\left\{F_{cb}\right\}\right]_N \end{aligned}$$

At the boundaries common to the subsystems, the displacements $\left\{\delta_a\right\}_N$ are equated and forces $\left\{F_a\right\}_N$ are summed to zero. This yields a set of simutaneous equations with the boundary displacements $\left\{\delta_a\right\}_N$ as unknowns. These equations are solved for $\left\{\delta_a\right\}_N$, and $\left\{\delta_b\right\}_N$ is then found from (7) by

$$\left\{\delta_b\right\}_N = \left[K_{bb}\right]^{-1}\left[-\left[K_{ba}\right]\left\{\delta_a\right\}_N + \left\{F_{pb}\right\}_N + \left\{F_{cb}\right\}_N\right]$$

Execution times on this program have been reduced by a factor of up to 25 by means of this technique.

(2) Vibration Program

For the vibration program, the surface of the inducer is triangulated in the same manner as the stress program and the same local stiffness matrices $\left[\bar{K}_M\right]$ and $\left[\bar{K}_B\right]$ are used. In addition to these matrices the triangular elements have local membrane inertia matrices $\left[\bar{M}_M\right]$ and bending inertia matrices $\left[\bar{M}_B\right]$, which are defined in Appendix D. The associated local nodal inertia force matrix, assuming harmonic vibrations of frequency ω and amplitudes $\left\{\bar{q}\right\}_N$ is similar to (2) and is

$$
\begin{bmatrix}
\bar{F}_{\bar{x}_1} \\ \bar{F}_{\bar{y}_1} \\ \bar{F}_{\bar{x}_2} \\ \bar{F}_{\bar{y}_2} \\ \bar{F}_{\bar{x}_3} \\ \bar{F}_{\bar{y}_3} \\ \hline \bar{F}_{\bar{z}_1} \\ \bar{M}_{\bar{x}_1} \\ \bar{M}_{\bar{y}_1} \\ \bar{F}_{\bar{z}_2} \\ \bar{M}_{\bar{x}_2} \\ \bar{M}_{\bar{y}_2} \\ \bar{F}_{\bar{z}_3} \\ \bar{M}_{\bar{x}_3} \\ \bar{M}_{\bar{z}_3} \\ \hline \bar{M}_{\bar{z}_1} \\ \bar{M}_{\bar{z}_2} \\ \bar{M}_{\bar{z}_3}
\end{bmatrix}_N
= -\omega^2
\left[\begin{array}{c|c}
\left[\bar{M}_M\right] & 0 \\ \hline
\multicolumn{2}{c}{\text{SYMMETRIC}} \quad \left[\bar{M}_B\right]
\end{array}\right]
\begin{bmatrix}
\bar{u}_1 \\ \bar{v}_1 \\ \bar{u}_2 \\ \bar{v}_2 \\ \bar{u}_3 \\ \bar{v}_3 \\ \hline \bar{w}_1 \\ \bar{\theta}_{\bar{x}_1} \\ \bar{\theta}_{\bar{y}_1} \\ \bar{w}_2 \\ \bar{\theta}_{\bar{x}_2} \\ \bar{\theta}_{\bar{y}_2} \\ \bar{w}_3 \\ \bar{\theta}_{\bar{x}_3} \\ \bar{\theta}_{\bar{y}_3} \\ \hline \bar{\theta}_{\bar{z}_1} \\ \bar{\theta}_{\bar{z}_2} \\ \bar{\theta}_{\bar{z}_3}
\end{bmatrix}_N
= -\omega^2 \left[\bar{M}\right] \left\{\bar{q}\right\}_N
$$

It was now assumed that the vibration of the inducer blade is normal to the inducer surface. For this reason a right-handed rectangular coordinate system different from the common system used in the stress program was adopted and is shown in figure 31. The z axis of this system is in the mean direction of the four normals to triangular elements that have common vertices at a node and a common generator, and the x axis is in the direction of the generator.

The directions of the normals are obtained from the direction cosine matrix $\left[R_1\right]$. Because the y axis is normal to the x axis, the direction of y is established, resulting in a new direction cosine matrix $\left[R_1\right]_n$ as defined in Appendix D. The generalized inertia force matrix relation for a triangular element in the quasi-normal system is obtained in the same manner as the generalized static force-displacement matrix (2).

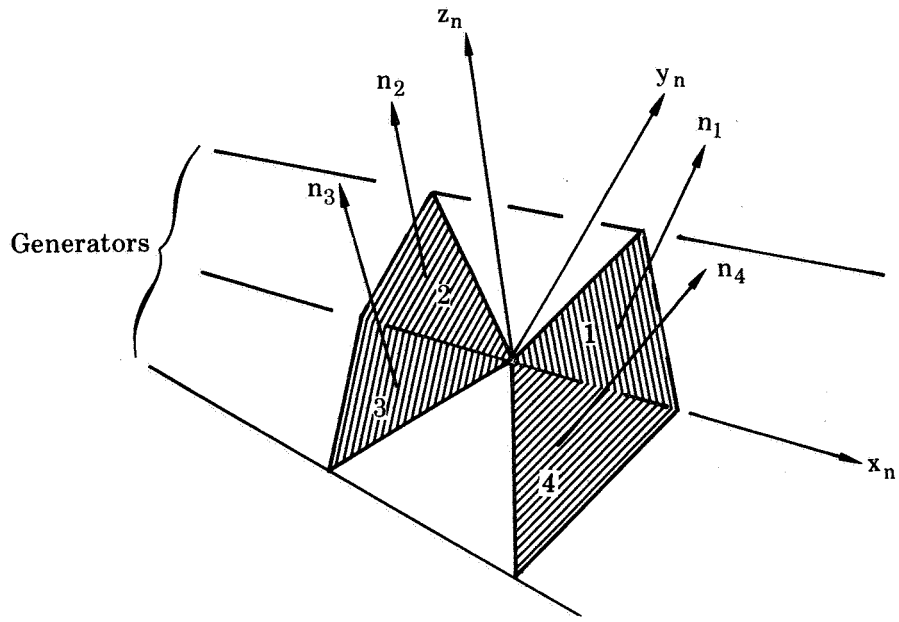

Figure 31. Definition of Quasi-Normal Coordinate System FD 25669A

$$\left\{\bar{F}\right\}_N = -\omega^2 \left[\bar{M}\right] \left\{\bar{q}\right\}_N \tag{8}$$

From (3) and (4)

$$\left\{\bar{F}\right\}_N = \left[R_6\right]_n^T \left\{F\right\}_N \text{and} \quad \left\{\bar{q}\right\}_N = \left[R_6\right]_n^T \left\{q\right\}_N$$

Then (8) transforms to

$$\left[R_6\right]_n^T \left\{F\right\}_N = -\omega^2 \left[\bar{M}\right] \left[R_6\right]_n^T \left\{q\right\}_N$$

or

$$\left\{F\right\}_N = -\omega^2 \left[R_6\right]_n \left[\bar{M}\right] \left[R_6\right]_n^T \left\{q\right\}_N$$

Thus, the generalized inertia force matrix relation for a triangular element in the quasi-normal system is expressed by

$$\left\{F\right\}_N = -\omega^2 \left[M\right] \left\{q\right\}_N$$

where $\left\{F\right\}_N$, $\left[M\right]$ and $\left\{q\right\}_N$ are referred to the quasi-normal system

and the mass matrix $\left[M\right]$ is defined by

$$\left[M\right] = \left[R_6\right]_n \left[\bar{M}\right] \left[R_6\right]_n^T$$

The stiffness and mass matrices are now assembled in the same manner that was used in the stress program. Elements of stiffness and mass matrices, which are associated with a common node, are added and displacements at common nodes are equated. The matrix equation of motion of free nodes of the system is then

$$\left\{F\right\}_N = \left[- \omega^2 \left[M\right]_T + \left[K\right]_T \right] \left\{q\right\}_N = \left\{0\right\}$$

The associated eigen-value equation is then

$$\left| - \omega^2 \left[I\right] \left[M\right]_T + \left[K\right]_T \right| = 0$$

Because each free node has six degrees of freedom, the eigen-value matrix will be of order (6n x 6n) for a system with n free nodes. This allows only eight free nodes to describe the inducer geometry because the capacity of an existent IBM 360 eigen-value program is limited to 50 eigen-values. Because eight free nodes are insufficient to describe a typical inducer, the number of degrees of freedom per node was reduced to one by matrix condensation techniques following a procedure recommended by Guyan*. This is accomplished by rearranging and partitioning by which the nodal force-displacement relation can be expressed in the matrix form

$$\underset{(6n \times 1)}{\left\{F\right\}_N} = \left[\begin{array}{cc|c} \underset{(n \times n)}{\left[A\right]} & \underset{(n \times 2n)}{\left[C\right]^T} & \\ \underset{(2n \times n)}{\left[C\right]} & \underset{(2n \times 2n)}{\left[B\right]} & \underset{(3n \times 3n)}{\left[E\right]^T} \\ \hline & \underset{(3n \times 3n)}{\left[E\right]} & \underset{(3n \times 3n)}{\left[D\right]} \end{array}\right] \left[\begin{array}{c} w \\ \theta x \\ \theta y \\ \hline u \\ v \\ \theta z \end{array}\right]_N \begin{array}{l} (3n \times 1) \\ \\ \\ \\ (3n \times 1) \end{array}$$

It is now assumed that if the plate vibrates normally to the surface u, v, and θ_z are zero. This can be accomplished by deleting the rows and columns containing the matrices $\left[D\right]$, $\left[E\right]$, and $\left[E\right]^T$. After deletion and further partitioning, the nodal force-displacement matrix relation is

$$\underset{(3n \times 1)}{\left\{F\right\}_N} = \left[\begin{array}{c} F_1 \\ \hline F_2 \end{array}\right] \begin{array}{l} (n \times 1) \\ \\ (2n \times 1) \end{array} = \left[\begin{array}{c|c} \underset{(n \times n)}{\left[A\right]} & \underset{(n \times 2n)}{\left[C\right]^T} \\ \hline \underset{(2n \times n)}{\left[C\right]} & \underset{(2n \times 2n)}{\left[B\right]} \end{array}\right] \left[\begin{array}{c} w \\ \hline \theta x \\ \theta y \end{array}\right]_N \begin{array}{l} (n \times 1) \\ \\ (2n \times 1) \end{array}$$

Letting $F_2 = 0$ for condensation as recommended by Guyan yields two matrix equations

$$\left\{F_1\right\}_N = \left[A\right]\left\{w\right\}_N + \left[C\right]^T \left\{\theta\right\}_N$$

$$\left\{0\right\} = \left[C\right]\left\{w\right\}_N + \left[B\right]\left\{\theta\right\}_N$$

*See Appendix A, section 3.

where

$$\left\{\theta\right\}_N = \left\{\begin{matrix}\theta x \\ \theta y\end{matrix}\right\}_N$$

Eliminating θ

$$\left\{F\right\}_N = \left[\begin{array}{c|c} \left[A\right] & \left[C\right]^T \\ \hline \left[C\right] & \left[B\right] \end{array}\right] \left[\begin{array}{c} \left\{w\right\}_N \\ \hline -\left[B\right]^{-1}\left[C\right]\left\{w\right\}_N \end{array}\right] \tag{9}$$

or

$$\underset{(n \times 1)}{\left\{F\right\}_N} = \underset{(n \times n)}{\left[\left[A\right] - \left[C\right]^T \left[B\right]^{-1} \left[C\right]\right]} \underset{(n \times 1)}{\left\{w\right\}_N} = \left[K\right]^* \left\{w\right\}_N \tag{10}$$

Thus, the reduced stiffness matrix is

$$\left[K\right]^* = \left[\left[A\right] - \left[C\right]^T \left[B\right]^{-1} \left[C\right]\right]$$

This operation reduces the number of degrees of freedom to n while still retaining the physical properties of the original system. Examination of (9) and (10) indicates that it amounts to a coordinate transformation as discussed by Guyan, i.e.

$$\left\{q\right\}_N = \left\{\begin{matrix} w \\ \hline \theta \end{matrix}\right\}_N = \left[T\right] \left\{w\right\}_N$$

where

$$\left[T\right] = \left[\begin{matrix} I \\ -B^{-1}C \end{matrix}\right]$$

Thus, if the internal strain energy is to be preserved under this transformation

$$U = \frac{1}{2}\left\{q\right\}_N \left[K\right] \left\{q\right\}_N = \frac{1}{2}\left\{w\right\}_N \left[T\right]^T \left[K\right] \left[T\right]\left\{w\right\}_N = \frac{1}{2}\left\{w\right\}_N \left[K\right]_T^* \left\{w\right\}_N$$

Thus, the reduced system stiffness matrix is of the form

$$\left[K\right]_T^* = \left[T\right]^T \left[K\right]_T \left[T\right]$$

The kinetic energy must also be preserved under this transformation. Thus,

$$T = \frac{1}{2}\left\{\dot{q}\right\}_N \left[M\right]\left\{\dot{q}\right\}_N = \frac{1}{2}\left\{\dot{w}\right\}_N \left[T\right]^T \left[M\right]\left[T\right]\left\{\dot{w}\right\}_N = \frac{1}{2}\left\{\dot{w}\right\}_N \left[M\right]^* \left\{\dot{w}\right\}_N$$

The reduced system mass matrix is then

$$\left[M\right]_T^* = \left[T\right]^T \left[M\right]_T \left[T\right]$$

Using these reduced matrices, the equation of motion becomes

$$\left[- \omega^2 \left[M\right]_T^* + \left[K\right]_T^* \right] \left\{w\right\}_N = \left\{0\right\}$$

The associated eigen-value equation then involves only n degrees of freedom and is

$$\left| - \omega^2 \left[I\right] + \left[M\right]_T^{*-1} \left[K\right]_T^* \right| = 0$$

e. Discussion of Typical Results of Analyses

The initial test cases for the stress and vibration computer programs were run on flat surfaces using a special matrix. This was done in order to obtain two-dimensional solutions that could be compared with known two-dimensional solutions. Flat plate geometries cannot be run with the existing three-dimensional program because the matrix becomes singular. For this reason all of the test cases except the rotating disc were re-run by programming the surface so that it was slightly warped out of plane. The results of these re-runs agreed just as close to the theoretical values for flat plates as did the first flat plate runs.

(1) Stress Program

(a) Sectors

Test cases were run on 45 degree flat sectors with 9 (figure 32a) and 30 (figure 32b) free nodes under uniform transverse loading and centrifugal loading. There was a decided improvement in the accuracy of predicted radial deflection for the centrifugal load case in going from 9 to 30 nodes as is shown in figure 33. Radial membrane stresses on interior triangular elements just about straddled the estimated stress curve when they were plotted for the centroid* of the appropriate triangle as is shown in figure 34. Approximate stresses and deflections were estimated by direct integration assuming that the radial pull is independent of polar angle. Averaging the stresses at each node by averaging the stresses in the triangles immediately surrounding a node also agreed fairly well with the estimated curve as is shown in figure 35.

The predicted displacements under bending load also were improved in going from 9 to 30 nodes as is shown in figure 36. Radial bending stresses on interior triangular elements also straddled the estimated curve as is shown in figure 37. These stresses were also averaged at the center nodes and are presented in figure 38. Stresses were obtained from the moment distribution on a cantilever beam of linearly varying width and deflections were approximated by the moment-area method.

* Gerstenkoro presents data at the centroid of triangular elements for the solution of the thick-walled cylinder using finite elements, and Zienkiewicz discusses this and other methods of averaging stresses in triangular elements.

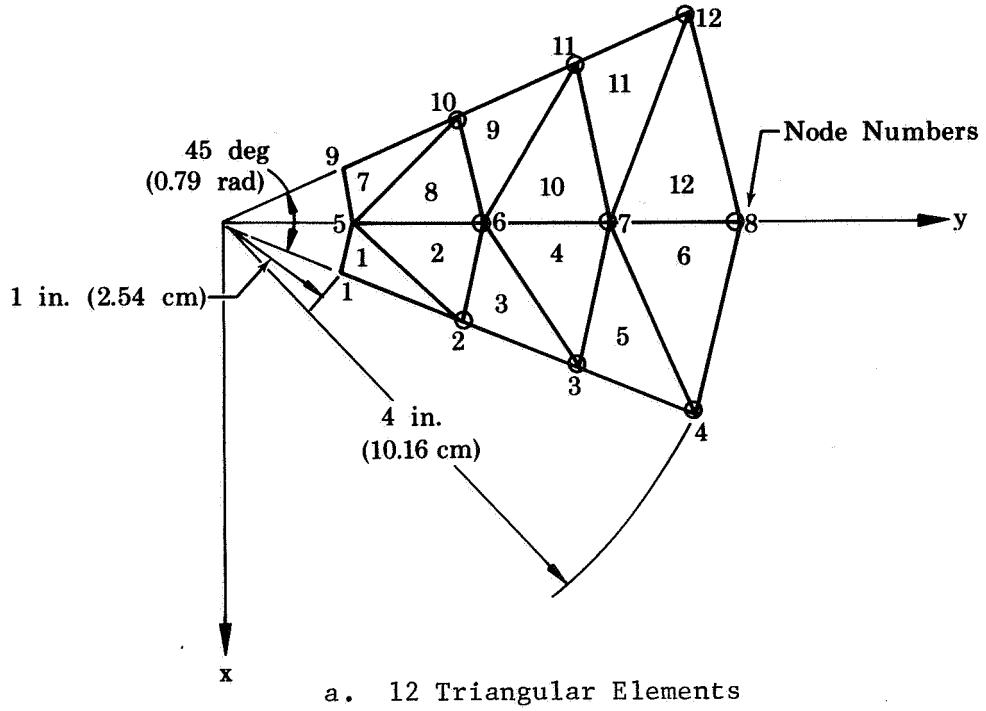

a. 12 Triangular Elements

Figure 32a. Breakup of 45-Degree Sector FD 25670A

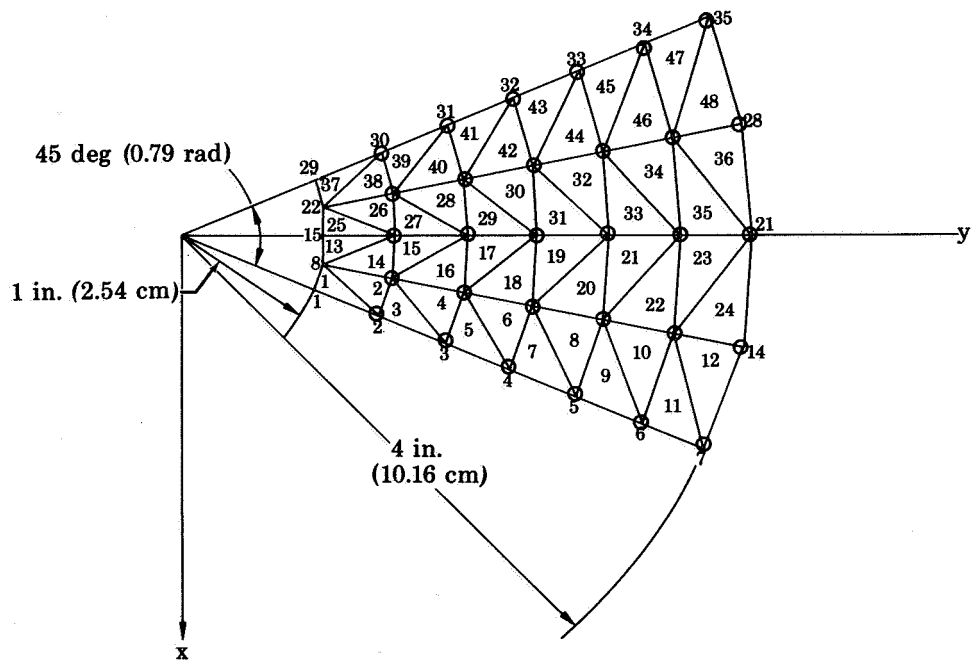

b. 48 Triangular Elements

Figure 32b. Breakup of 45-Degree Sector FD 25672A

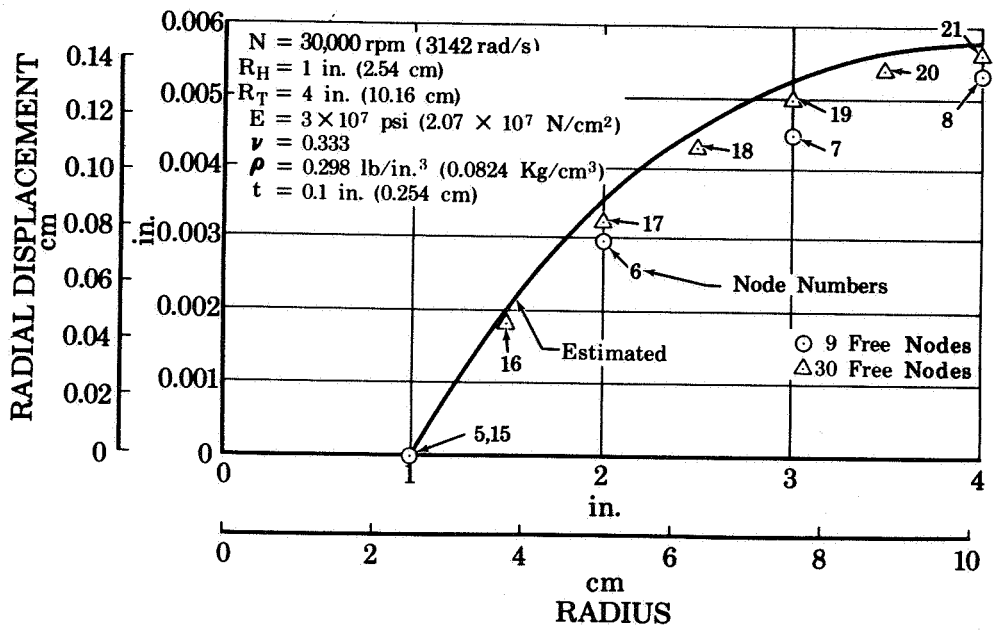

Figure 33. Radial Displacements in Rotating 45-Degree Sector FD 25335C

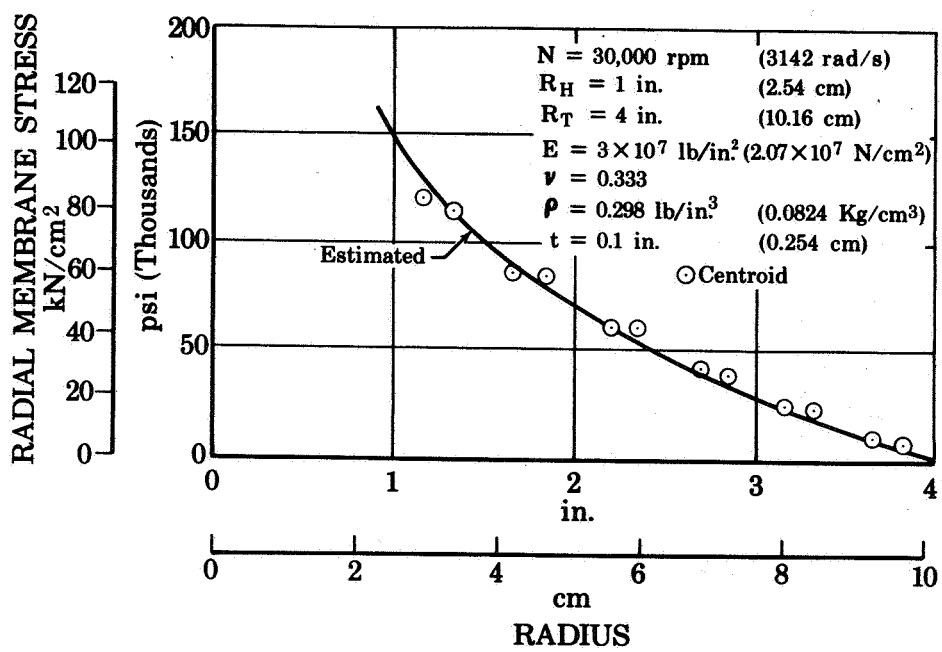

Figure 34. Radial Membrane Stresses in Rotating 45-Degree Sector with 30 Free Nodes FD 25657

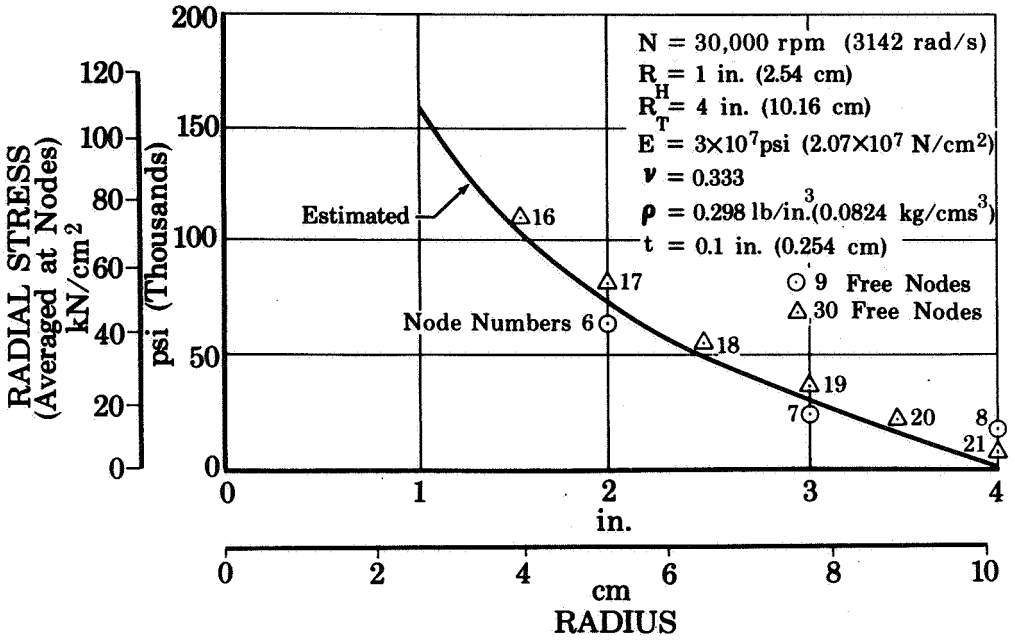

Figure 35. Radial Membrane Stresses in Rotating 45-Degree Sector at Midchord FD 25786B

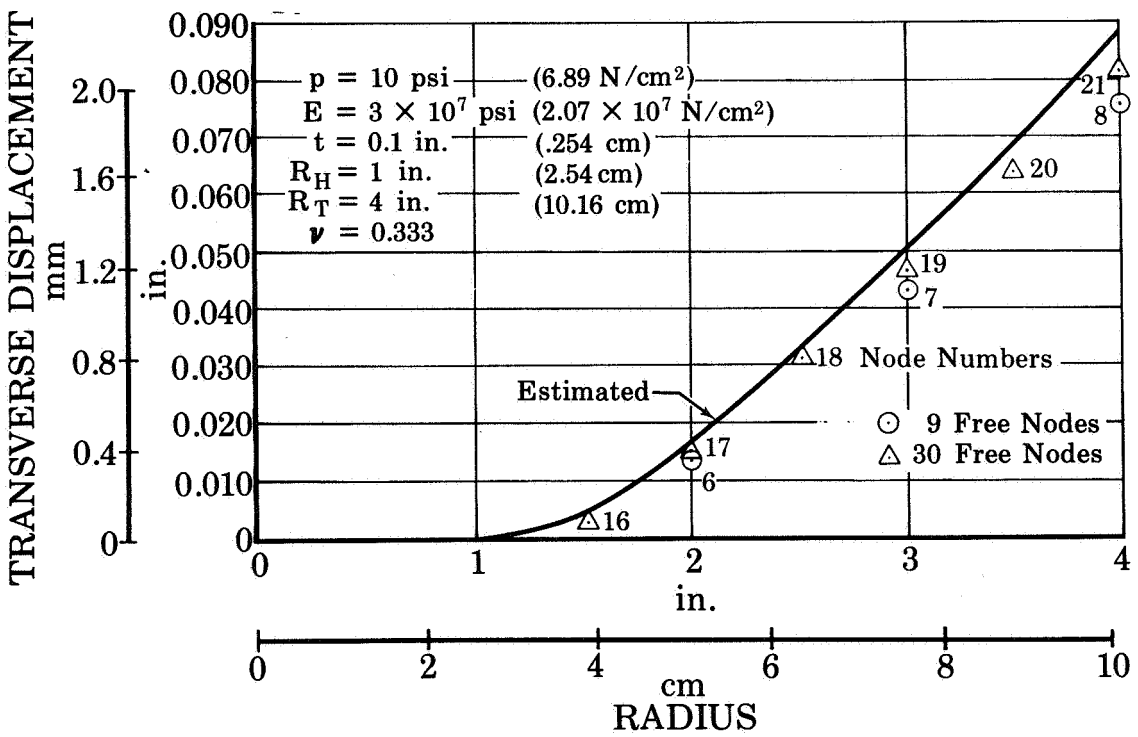

Figure 36. Transverse Midchord Displacement of Uniformly Loaded 45-Degree Cantilevered Sector FD 25787A

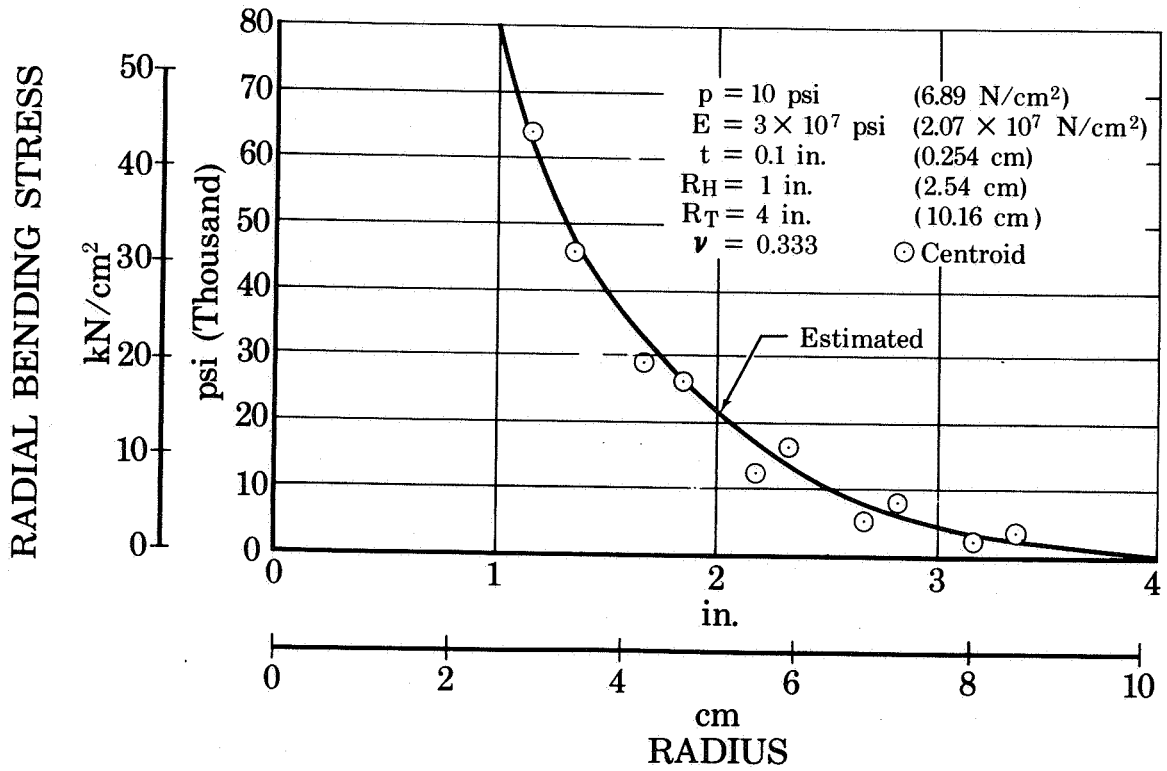

Figure 37. Radial Bending Stresses in Uniformly Loaded 45-Degree Cantilever Sector with 30 Free Nodes FD 25788A

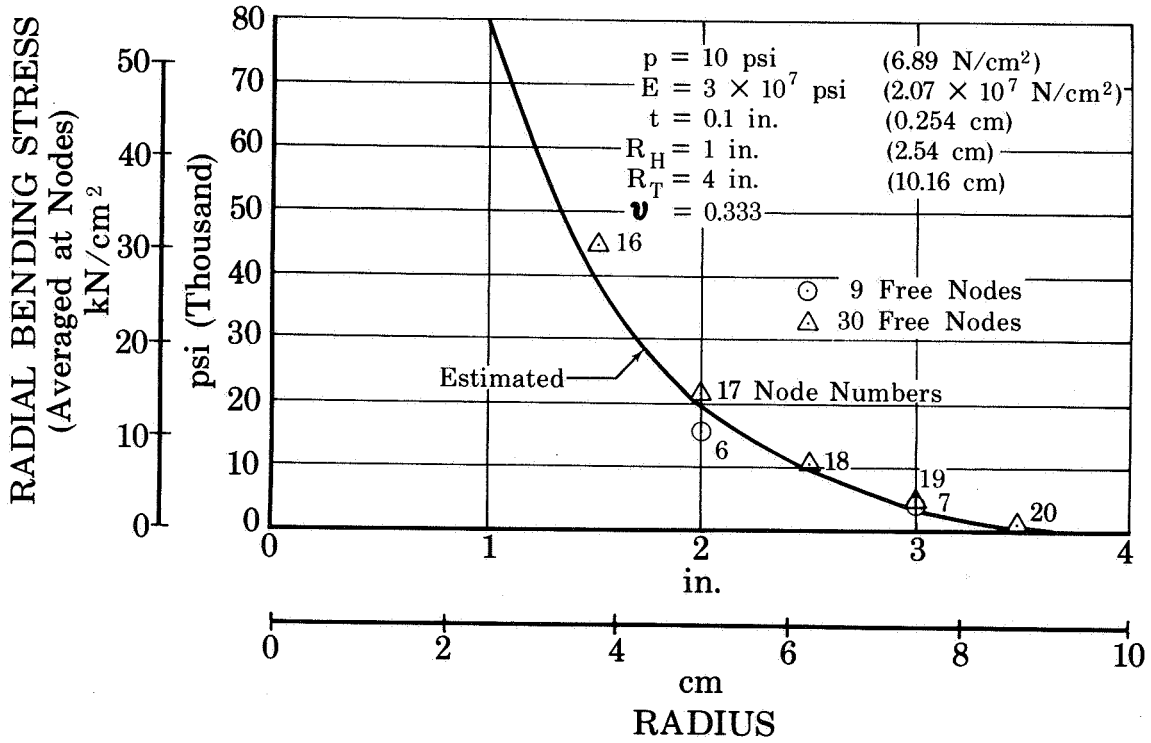

Figure 38. Radial Bending Stresses in Uniformly Loaded 45-Degree Cantilevered Sector [Midchord] FD 25789A

(b) Rectangles

Similar test cases were run on 2 by 3 in. (5.08 by 7.62 cm) rectangles as shown in figures 39 through 43. Good agreement was achieved in all cases. Displacements always agreed better than the stresses.

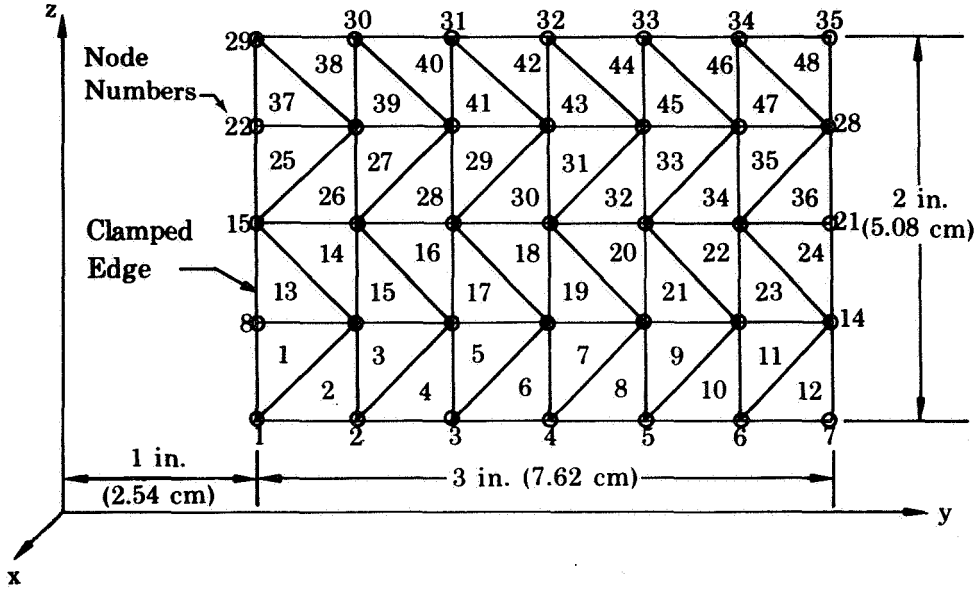

Figure 39. Breakup of 2-inch by 3-inch Rectangle into 48 Triangular Elements and 30 Free Nodes FD 25673A

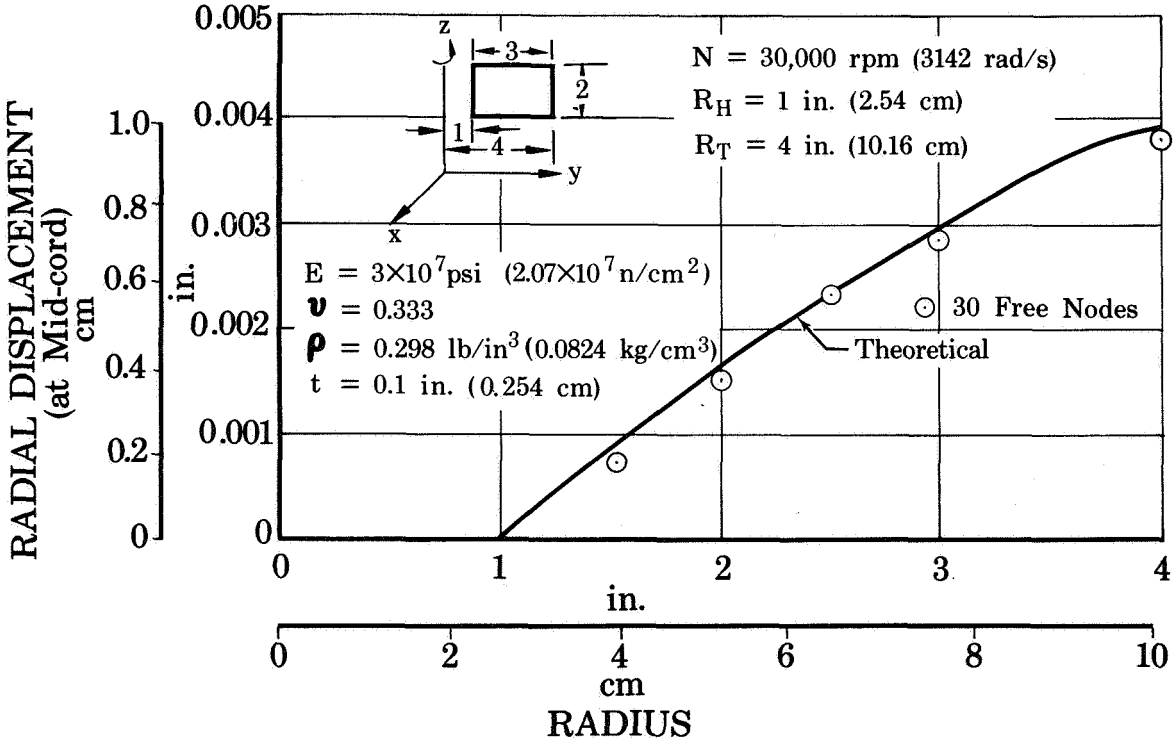

Figure 40. Radial Displacements in Rotating Rectangle with 30 Free Nodes FD 25790

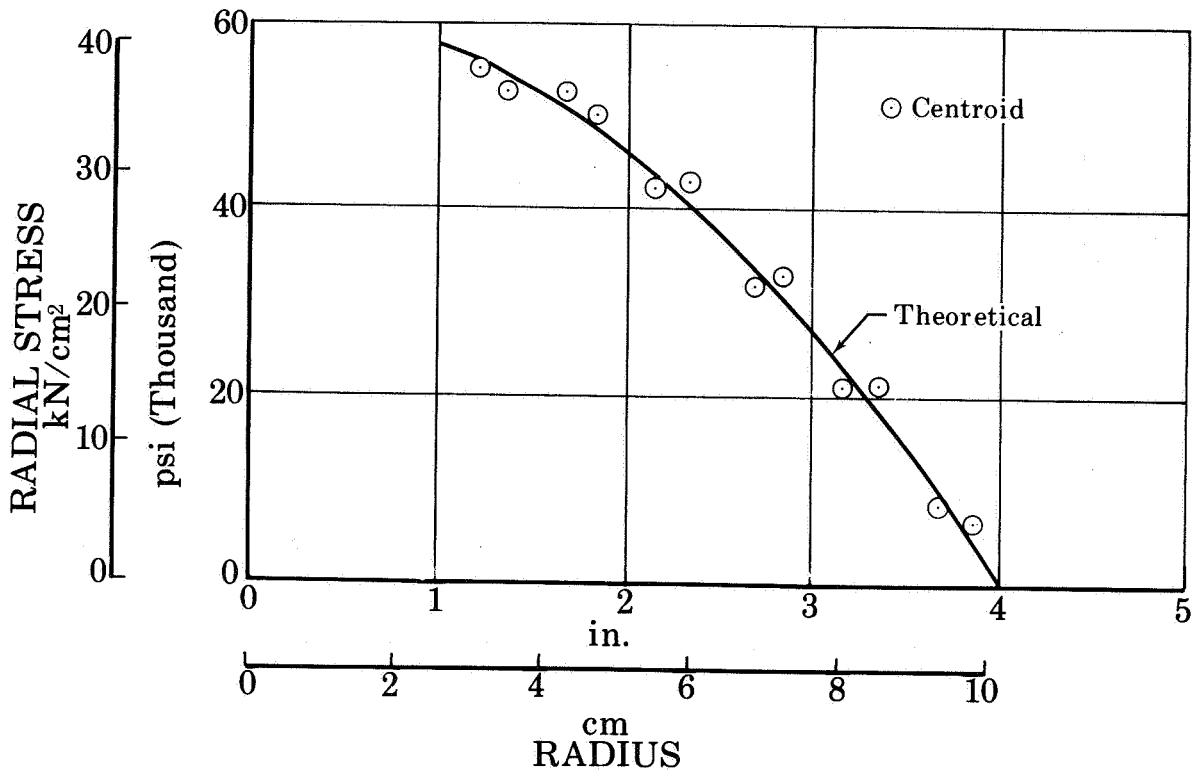

Figure 41. Radial Stresses in Rotating Rectangle with 30 Free Nodes FD 25791

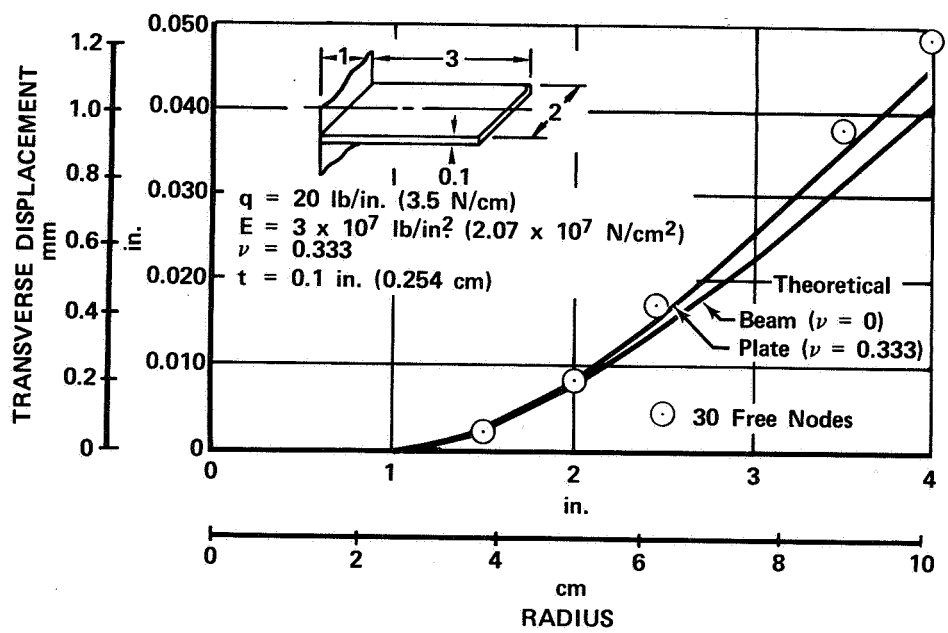

Figure 42. Transverse Midchord Displacement of Uniformly Loaded Cantilever with 30 Free Nodes FD 25792A

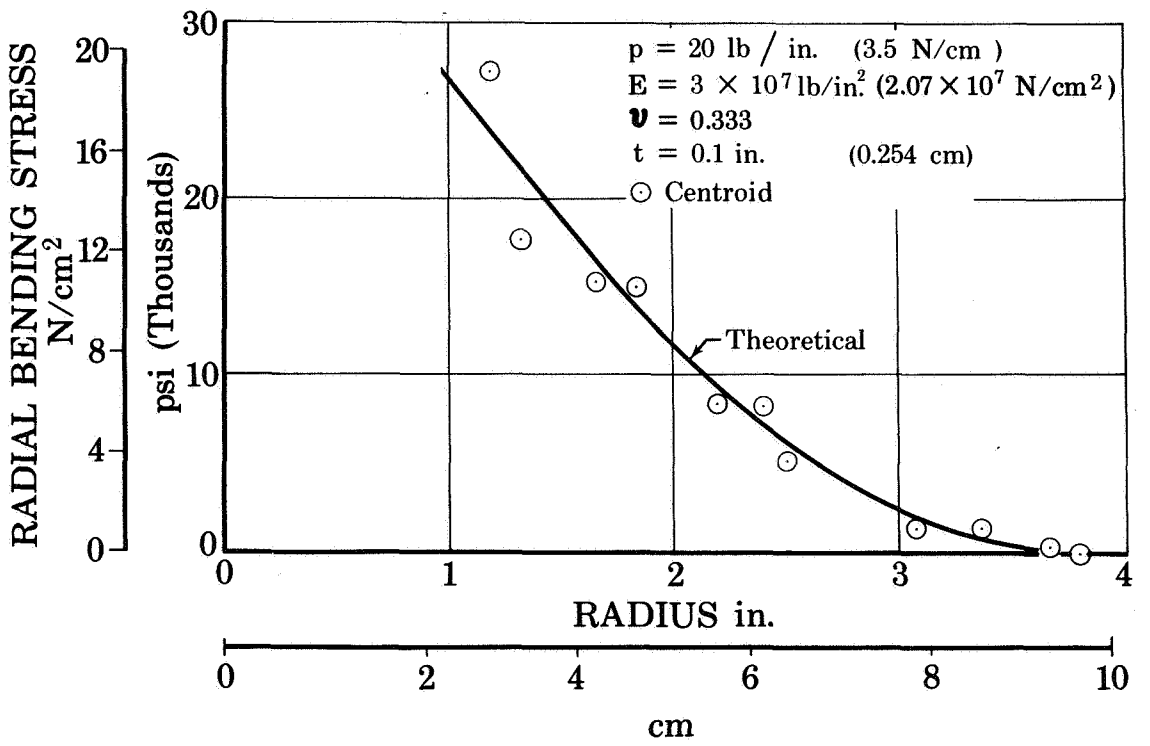

Figure 43. Radial Bending Stress in Uniformly Loaded Cantilever with 30 Free Nodes FD 25793

(c) Circular Disk

A test case for a solid bore spinning disk with 48 free nodes (figure 44) was evaluated next. Displacements again agreed with theoretical results as shown in figure 45. Results were compared with the theoretical plane stress solution for a disk and with results from an existing program which is used by Pratt & Whitney Aircraft for compressor and turbine disk design, with $\nu = 0.300$. Stresses that were averaged at the nodes did not agree as closely as those for sectors and rectangles as is shown in figure 46. Pertaining to stress interpretation in general and figure 46 in particular, stresses at the hub and free edges cannot be evaluated directly because the correct stress gradient cannot be accounted for in a triangle over which the membrane stress is assumed constant or the bending stress is assumed to vary linearly. Such stresses can be obtained by using either extrapolation, smaller elements, or judicious weighing of element stresses as discussed by Zienkiewicz. It is expected that a finer breakup would reduce the error.

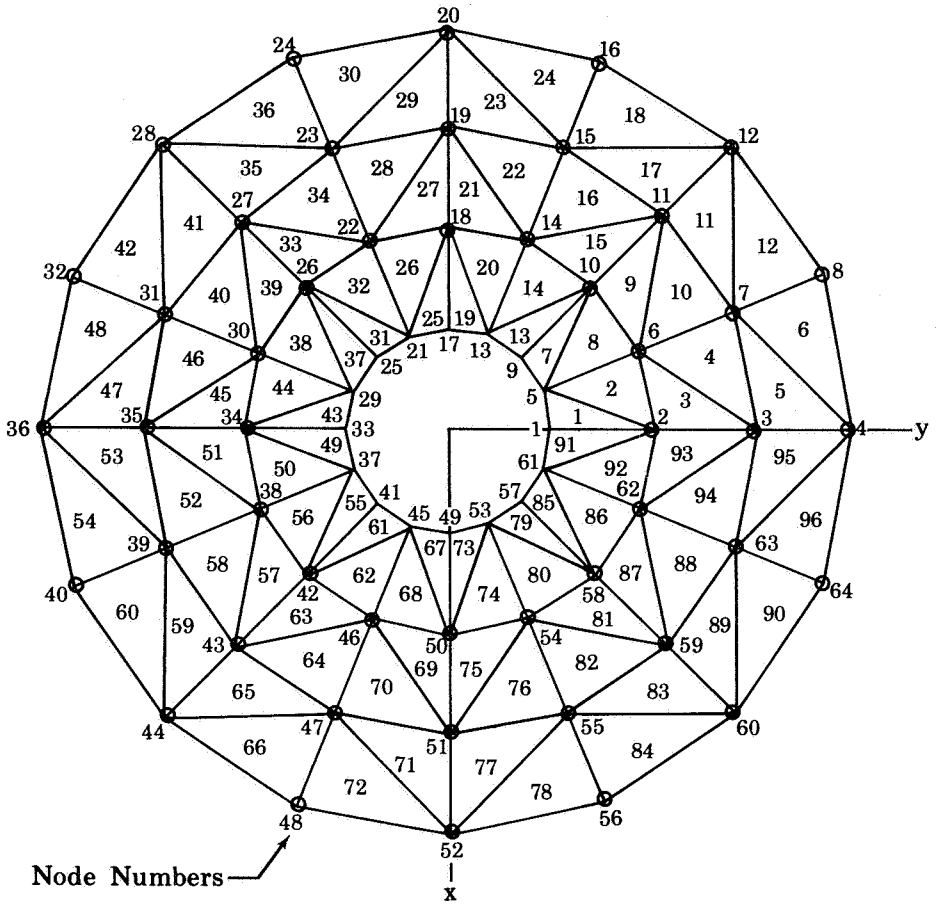

Figure 44. Breakup of Circular Disk into 96 Triangular Elements and 48 Free Nodes FD 25655A

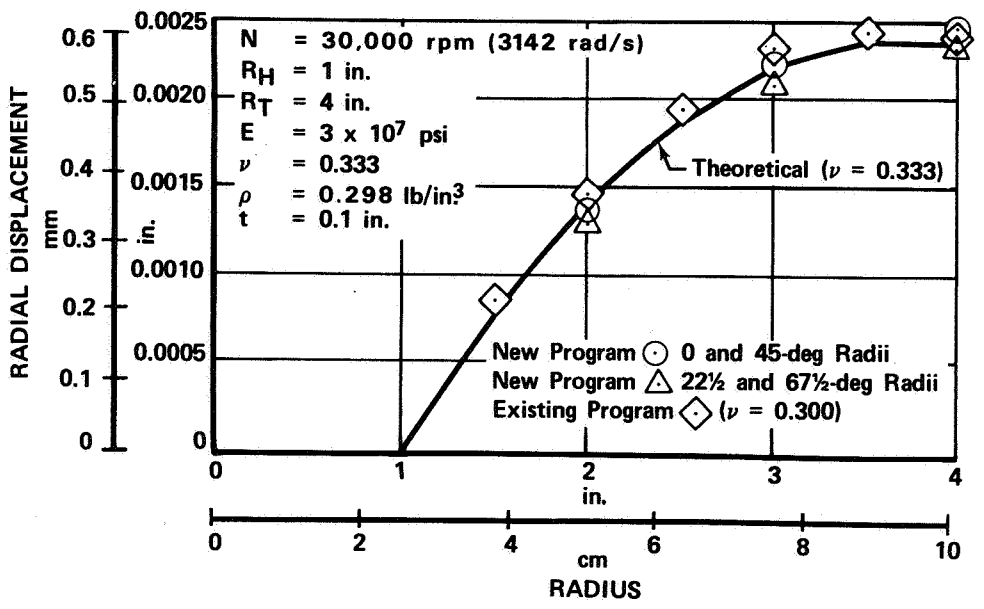

Figure 45. Radial Displacements in 48 Node Spinning Disk FD 25794C

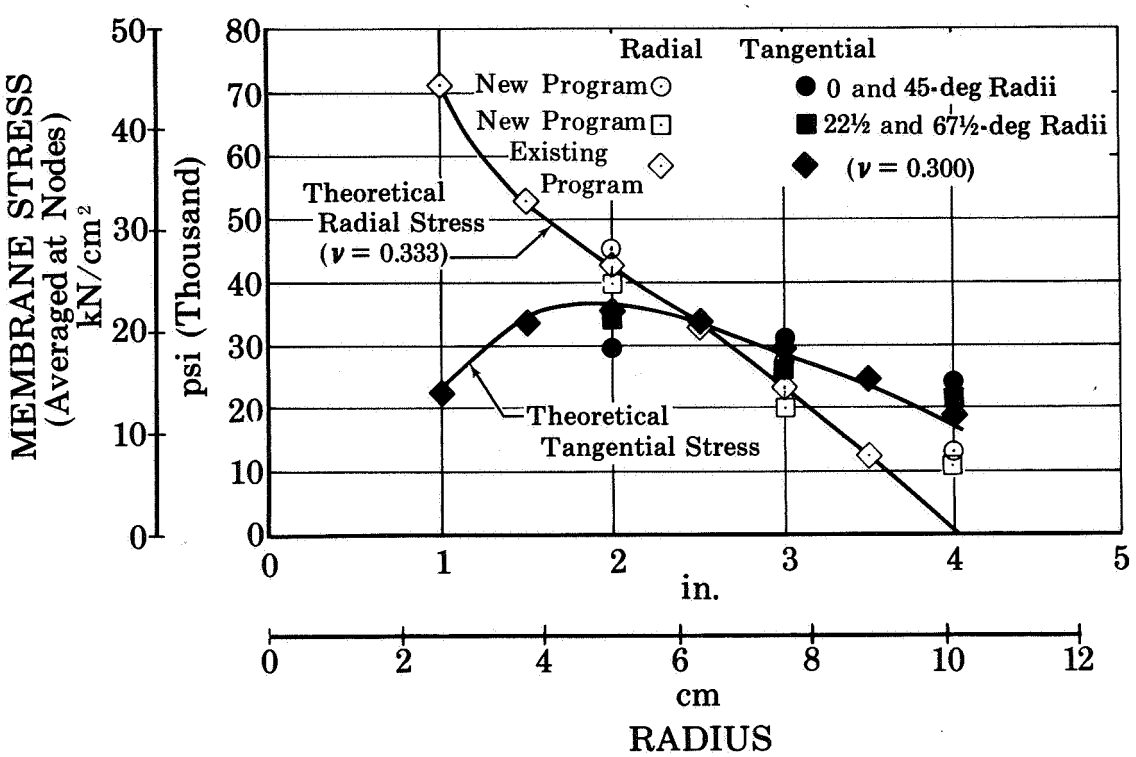

Figure 46. Radial and Tangential Membrane Stresses in 48 Node Spinning Disk FD 25795A

(2) Vibration Program

(a) Rectangular Plate

A test case on a 1 by 2 in. (2.5 bu 5.1 cm) rectangular plate with 40 free nodes (figure 47) yielded the results shown in table 1. Comparison with the first four known mode shapes was in good agreement, as is shown in figure 48. The predicted frequency of the first torsional mode (1/0 mode), however, was high (see table 1).

Table 1. Modes and Natural Frequencies of Cantilevered Plate

Mode	Exact*	Frequencies, cps Existing Program For Flat Plates	Present Program
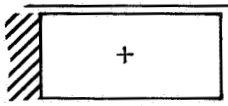 0/0	846	844	720
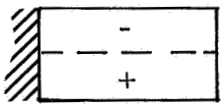 1/0	3,638	3,584	4,942
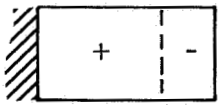 0/1	5,266	5,301	4,513
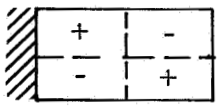 1/1	11,870	11,802	14,648
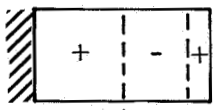 0/2		15,185	12,532
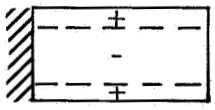 2/0		23,011	21,563
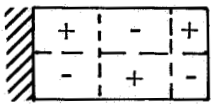 1/2		23,340	25,165
		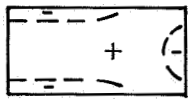 29,469	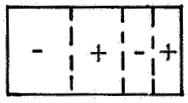 24,459 0/3
		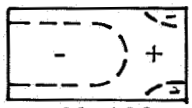 31,190	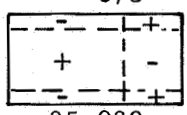 35,039 2/1
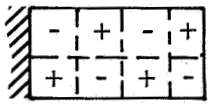 1/3		38,331	38,175

* Refer to Barton in Appendix A

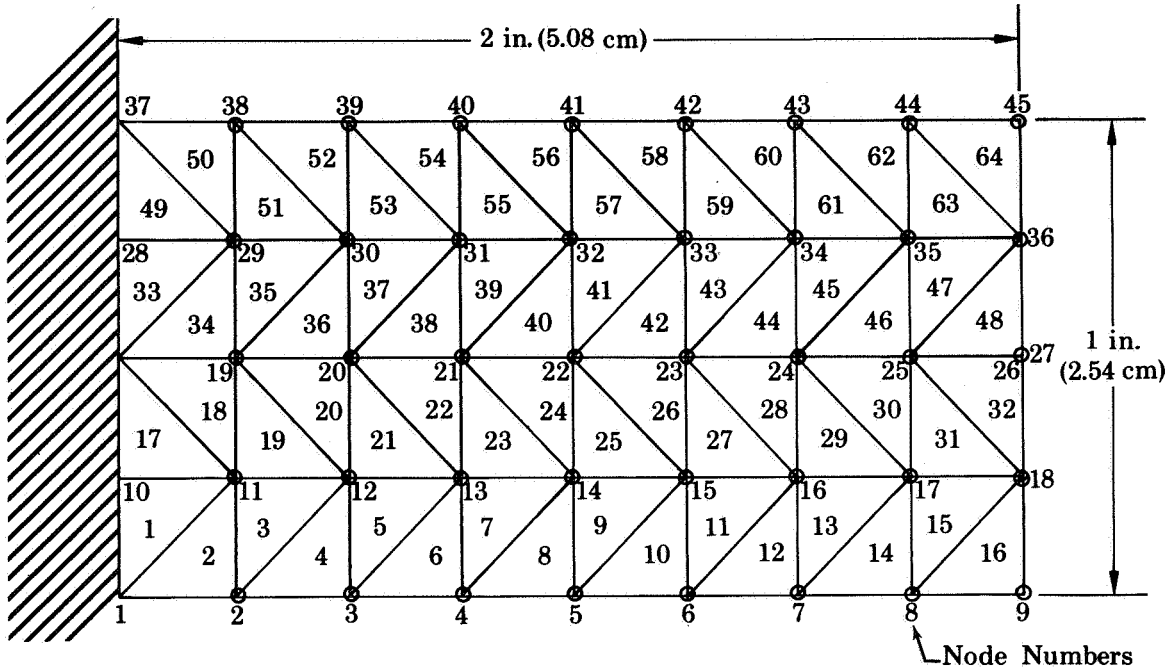

Figure 47. Breakup of 1-inch by 2-inch Rectangular Plate into 64 Triangular Elements and 40 Free Nodes

FD 25656A

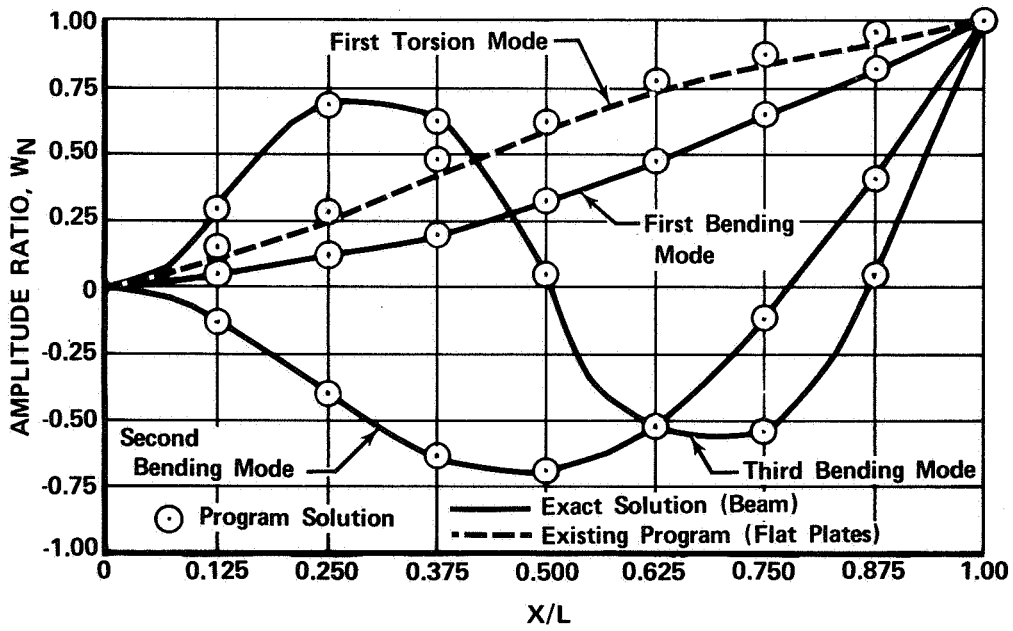

Figure 48. Comparison of Mode Shapes of Cantilever Plate

Figure 49 shows relative centroidal vibratory bending stresses for the same 1 by 2 in. rectangular plate as compared to the theoretical values for a cantilevered beam at the same shape. The agreement is good except near the clamped edge. It is anticipated that this can be improved by the use of more elements.

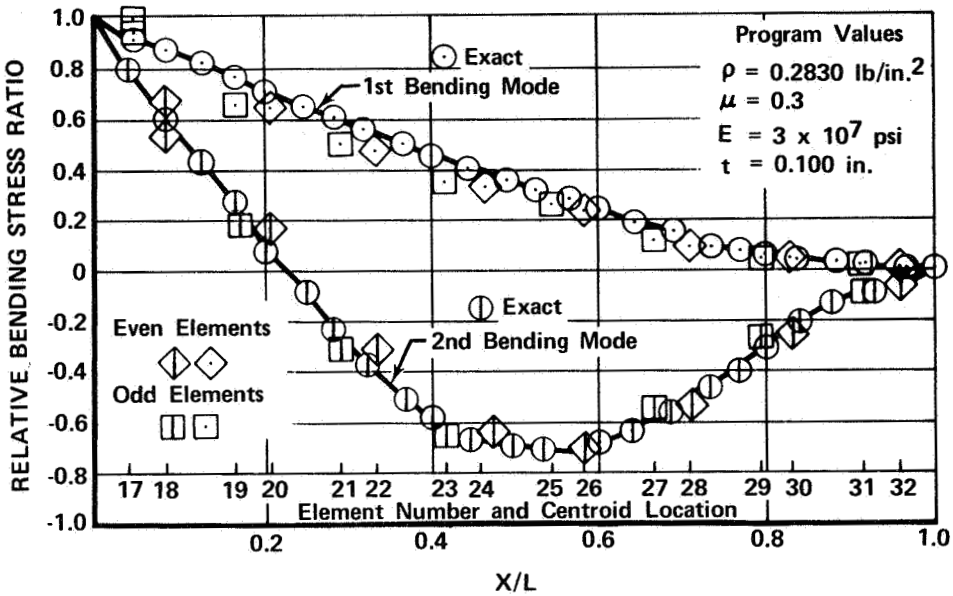

Figure 49. Relative Vibratory Bending Stresses in a Cantilever Beam (2 x 1) FD 48170

(b) Six-Degree Inducer

A test case for an inducer with a 6-degree inlet blade angle and with a 438-degree wrap angle was conducted and results compared with test data as shown in table 2. The results were in fairly good agreement through the fifth mode.

Table 2. Mode Shapes and Natural Frequencies of 6-Degree (0.105-rad) Inducer

Mode	Frequency (cps) Test Data	Frequency (cps) Calculated (Present Program)
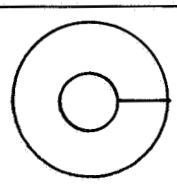 0/0	441	483
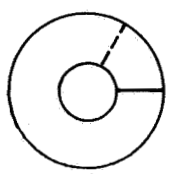 1/0	575	540

Table 2. Mode Shapes and Natural Frequencies of 6-Degree (0.105-rad) Inducer (Continued)

Mode	Frequency (cps) Test Data	Calculated (Present Program)
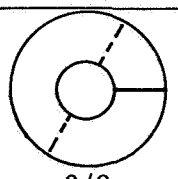 2/0	---	606
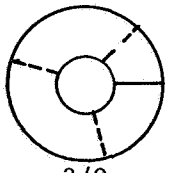 3/0	---	709
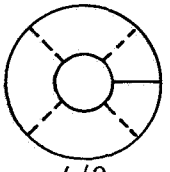 4/0	831	840
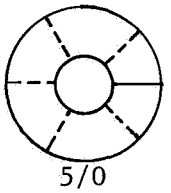 5/0	---	994
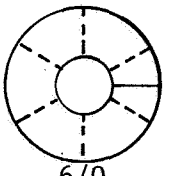 6/0	957	1170

C. TASK III - DESIGN OF TEST INDUCER

1. Inducer Design and Analysis

a. Preliminary Design

(1) Requirements

Task III work requirements called for the preliminary design of an inducer to be instrumented and tested in Task VI, both in static rigs and a water flow loop. Test results were then used in the development of the computer programs formulated in Task II.

The following performance characteristics were established as design goals:

1. Minimum Flow Coefficient (ϕ) - 0.065
2. Minimum Head Coefficient (ψ) - 0.15
3. Minimum Suction Specific Speed (N_{ss}) - 40,000.

During the Task III preliminary design phase, it was found that, to achieve a suction specific speed of 40,000 would require the use of low blade angles and thin blades both of which would limit instrumentation and compromise the acquisition of extensive and accurate test data. Therefore, the blade thickness and inlet angle were selected to provide good instrumentation coverage, and the other inducer parameters varied to obtain maximum suction specific speed.

(2) Selection of Basic Parameters

A three-blade design was selected, and zero blade taper angle was used to provide adequate tip thickness for instrumentation and still maintain low hub blockage for good suction performance. To obtain various hydrodynamic loading conditions, the meridional area was reduced by 15% at the exit, and the blade was cambered by 2 deg at the tip. An inlet tip angle of 8 deg was selected to provide adequate room for instrumentation while maintaining a relatively low angle for good suction performance.

Titanium was selected as the inducer material primarily because of its low modulus of elasticity and high strength-to-weight ratio. The low modulus, which results in a high strain per unit of stress, provides improved accuracy in strain gage testing. The high strength to weight ratio made it possible to design the blade tip to the desired thickness for instrumentation without having to increase the thickness at the hub to obtain the necessary strength.

In addition, because the inducer is overhung on the test rig shaft, the light weight of the titanium eliminated a potential critical speed problem. The oxidation resistance of the titanium further inhanced its selection as the inducer material.

For simplicity and ease of rig modification, a constant OD flowpath was used. A high solidity was specified to obtain a high work level as well as good suction performance. The tip speed was limited to 150 ft/sec (46 m/sec) in an attempt to preclude cavitation damage. A maximum OD and minimum ID were used to provide the largest blade surface for instrumentation. The basic design parameters are listed in table 3.

Table 3. Basic Inducer Design Parameters

		Inlet	Exit
Hub Diameter, in. (cm)		2.8 (7.1)	3.74 (9.5)
Blade Angle-Tip, deg (rad)		8 (0.14)	10 (0.18)
Blade Angle-Hub, deg (rad)		19.35 (0.339)	18.25 (0.318)
Tip Diameter, in. (cm)	7.0 (17.8)		
Blade Thickness, in. (cm)	0.130 (0.330)		
Number of Blades	3		
Flow Coefficient	0.07		
Head Coefficient	0.24		
Suction Specific Speed (100% Head Falloff)	30,000 (min)		
Flow Rate, Gpm (m^3/S)	1060 (0.067)		
Rotor Speed, rpm (rad/s)	4900 (513)		

b. Flow Path and Blading Design

The hub contour and blade angle distribution are shown in figure 50. The tip blade angle was held constant at 8 deg for a tangential gap/chord ratio of approximately one. The blade angle profile from this point to the exit followed a power distribution as shown in figure 50. This blade design is patterned after the "J" blade concept. This design technique, in incorporating a noncambered inlet for a tangential solidity of one, allows the leading edge incidence to be removed before turning the flow in the cambered section of the blade to produce the desired head. In doing this, the blade pressure loading due to leading edge incidence diminishes before the loading due to blade camber begins. This prevents addition of loadings due to incidence and camber near the blade leading edge.

After determination of the blade angle distribution, the channel flow area was held constant so that an acceptable mean line relative velocity profile would be obtained. With flow area and tip diameter constant and the blade angle distribution specified, an approximate hub contour was determined. A test rig requirement that the inducer exit flow be axial resulted in some departure from this desired hub contour.

The mean relative velocity profiles, as determined from the hydrodynamic program, are shown in figure 51. The velocity profiles shown are both smooth and devoid of any excessive diffusion other than in the region of the leading edge, where some rapid diffusion exists. This leading edge diffusion is the result of the rapid turning due to leading edge incidence, and is common to any inducer design. It can be tolerated (if the diffusion velocity ratio is not extremely high) because the boundary layers are still very thin near the leading edge.

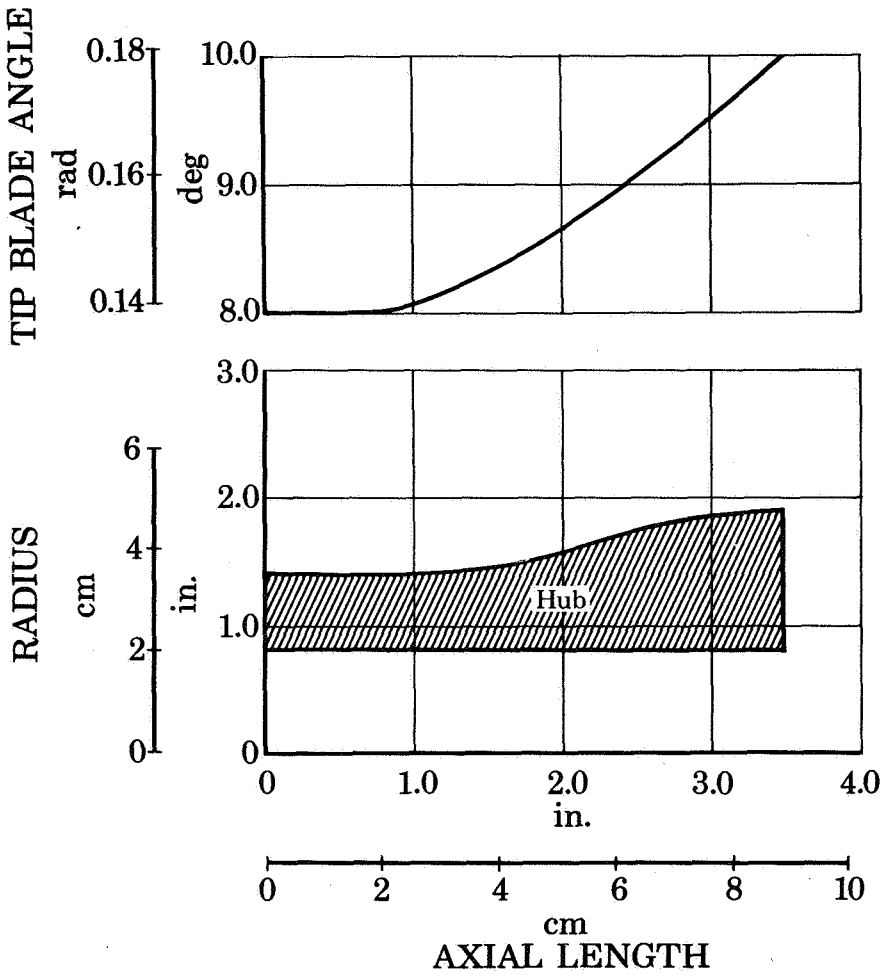

Figure 50. Inducer Flow Path and Blade Angle Distribution FD 25798A

c. Performance and Stress Analysis

The overall performance, hydrodynamic blade loading and stress distribution for the inducer were analyzed using the computer programs originally developed in Task II. While the stress and vibration computer programs have remained unchanged, significant modifications have been made to the hydrodynamic program, as mentioned earlier. The performance, hydrodynamic loading and stress values predicted using the modified program are presented in the Task VI discussion. The original predictions, which were used primarily to assist in locating instrumentation and to assure the safe operation of the inducer from the stress standpoint, are not pertinent to the development of the computer programs and, therefore, are not included in this report. These predicted data were presented in the interim report (Reference 15).

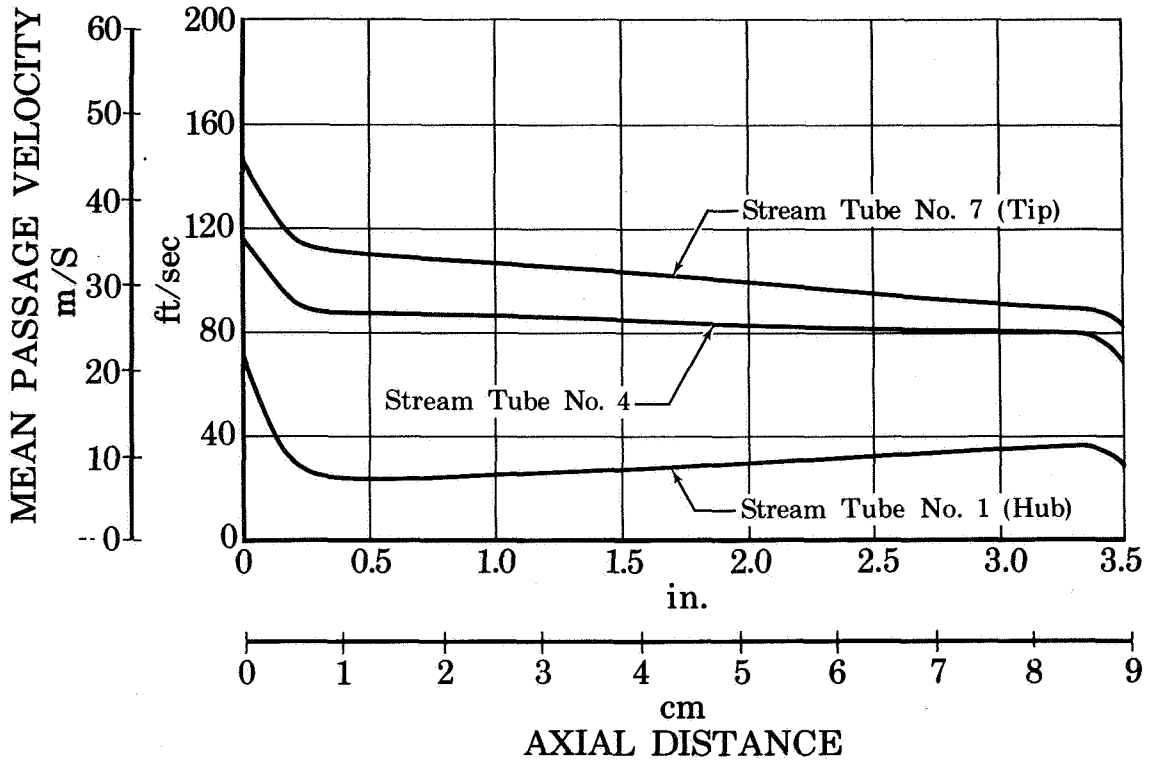

Figure 51. Inducer Mean Passage Velocity Profile FD 25800

2. Instrumentation Design

Blade surface pressure and strain distribution data were required for correlation with computer program predictions. Provisions for these measurements were made during the design stage of the program. Pressure data were to be measured during inducer operation in water, and strain data were to be measured both in static laboratory tests and during operation in water. Because of the unique requirements and critical nature of the instrumentation needed in the test program, a summary of blade data requirements and instrumentation employed is given in the following paragraphs.

a. Blade and Hub Steady Pressures

A pressure scanning valve-transducer assembly* was selected to measure blade and hub steady pressures during inducer flow tests. A photograph of the valve assembly and a schematic which illustrates its operation are shown in figures 52 and 53. The valve rotor rotates in 48 discrete steps so that the collector slot sequentially connects each of 48 sensing ports to a single internally mounted transducer located on the valve centerline. The rotor is driven by a 28-volt solenoid through a ratchet mechanism that causes the valve to index one sensing port each time the solenoid is energized. A switch in the drive train is actuated

*Scanivalve Corporation, San Diego, California, Model 48D9 Special

each time the valve makes one rotation (48 steps) and that signal is used to indicate that the valve is on "home" port. A potentiometer in the drive train also provides a resistance that is proportional to the valve position and can be used as a position indicator.

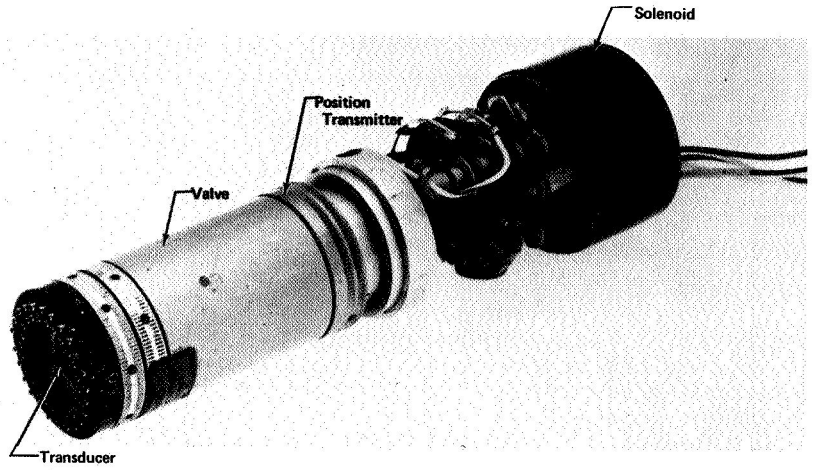

Figure 52. Pressure Scanning Valve - Transducer Assembly FE 94089

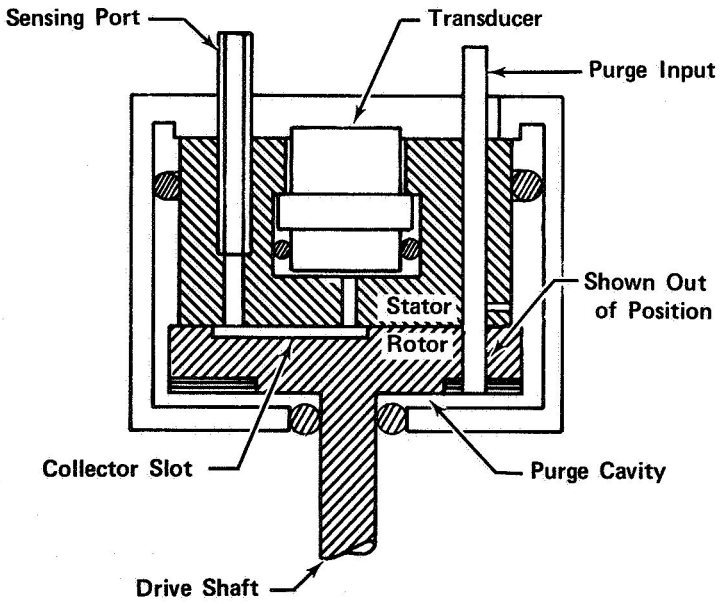

Figure 53. Schematic of Pressure Scanning Valve FD 21392

The valve assembly was installed in the inducer hub as shown in figure 54 and its electrical leads were routed through the drive shaft for connection to a slip ring. Eleven leads were required: four for power and stepping control, three for position indication, and four for the transducer. The inducer drive shaft housed the valve assembly so that the inducer could be removed without disturbing the valve and its electrical connections to the slip ring. Surface pressures were sensed using small-diameter tubing recessed into the blade and drilled at the desired radial location. The pressure tap lines were routed to the front of the inducer and connected to the valve with nylon tubing. Spacers and rubber packings were used to secure the valve assembly radially and axially in the drive shaft.

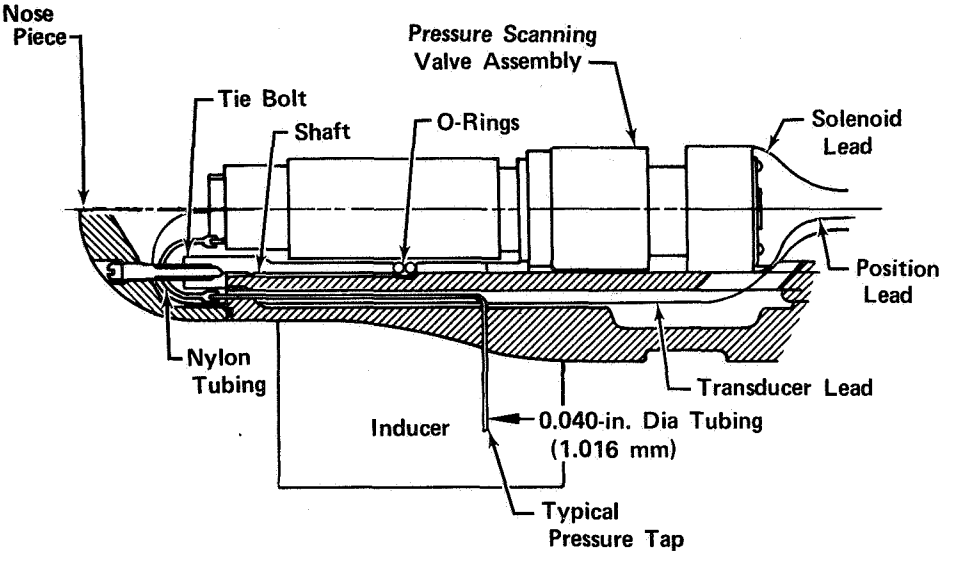

Figure 54. Pressure Scanning Valve in Inducer Hub FD 25812

Since the pressure scanning valve-transducer assembly was located on the inducer centerline and pressure taps were located at some radius on the blades, the pressure sensed by the transducer would be lower than the actual pressure on the blade by the centrifugal pressure of the fluid in the tap line. A correction to the sensed pressure could easily be applied if the fluid in the tap line were of known density. However, the density would not be known if the blade surface pressure was less than the pressure generated by centrifugal force on the column of water. As an example, since blade suction surface pressures could be as low as vapor pressure, water would be forced out of the tap line until the integrated centrifugal pressure equalled the blade pressure. The tap line would then be filled with a combination of water and water vapor with the interface being at an unknown radius. The transducer would sense vapor pressure, and actual blade surface pressure would be indeterminable from the test data.

To circumvent this problem, provisions were made to purge the pressure tap lines with air at a pressure higher than the predicted blade surface pressure. The centrifugal pressure of the air column would be negligible. Purging was accomplished by employing a modified pressure scanning valve which had a hole in its rotor one port ahead of the collector slot, a sealed case cavity, and one sensing port vented to the case cavity. These modifications are shown in figure 53. In operation, a constant pressure purge was applied through the vented sensing port to pressurize the valve case and purge each sensing port through the hole in the rotor just prior to its being connected to the transducer. As long as purge pressure is higher than blade surface pressure, the tap lines are completely filled with air at blade surface pressure and the transducer measures actual blade surface pressure. Purge pressure was limited by valve capabilities which dictated that case pressure not exceed 100 psia (69 N/cm^2) and that case-sensing port differential pressure not exceed 60 psid (41 N/cm^2). These limitations resulted in the loss of some data but the inaccurate points were readily apparent because the transducer measured purge pressure when blade pressure was higher than purge pressure (i.e., the tap line became partly filled with water; centrifugal pressure together with purge pressure, balanced the blade surface pressure).

Forty-eight sensing ports were available on the pressure scanning valve. One of these was used to provide purge pressure and another was left open in the shaft bore, for an ambient reference reading, leaving 46 sensing ports available for pressure measurement. This number was insufficient to fully define the inducer blade pressure distribution; therefore two test series were planned to permit data to be taken at 92 points. The selected points were along two design point streamlines and along the inducer hub as shown in figure 55. Pressure and suction surface taps were alternated to prevent back to back grooves in the blades at 19 angular stations along two of the three inducer blades. Three pressure surface taps (locations 2, 8, and 13) were duplicated on the third blade and read for both test series to insure data continuity.

The nineteen measurement stations were selected to provide fine resolution near the blade leading and trailing edges where pressure should change rapidly, and relatively coarse resolution in the inducer center section where pressures should change slowly.

Pressures along the outer streamline were selected to be measured first, after which the inducer would be removed, outer taps plugged, and new taps installed along the inner streamline.

b. Blade Vibratory Pressures

To obtain blade vibratory pressures provisions were made to install miniature transducers*, one of which is shown in figure 56. The transducers employ a monolithic Wheatstone bridge formed directly on a silicon diaphram. Although the transducers are capable of measuring both steady and vibratory pressures, they were employed for only vibratory measurements in this application. The effects of cementing and centrifugal force would make them less accurate than the pressure scanning valve for steady pressure measurement.

*Kulite Semiconductor Products, Inc. Model LPS 125 - 150

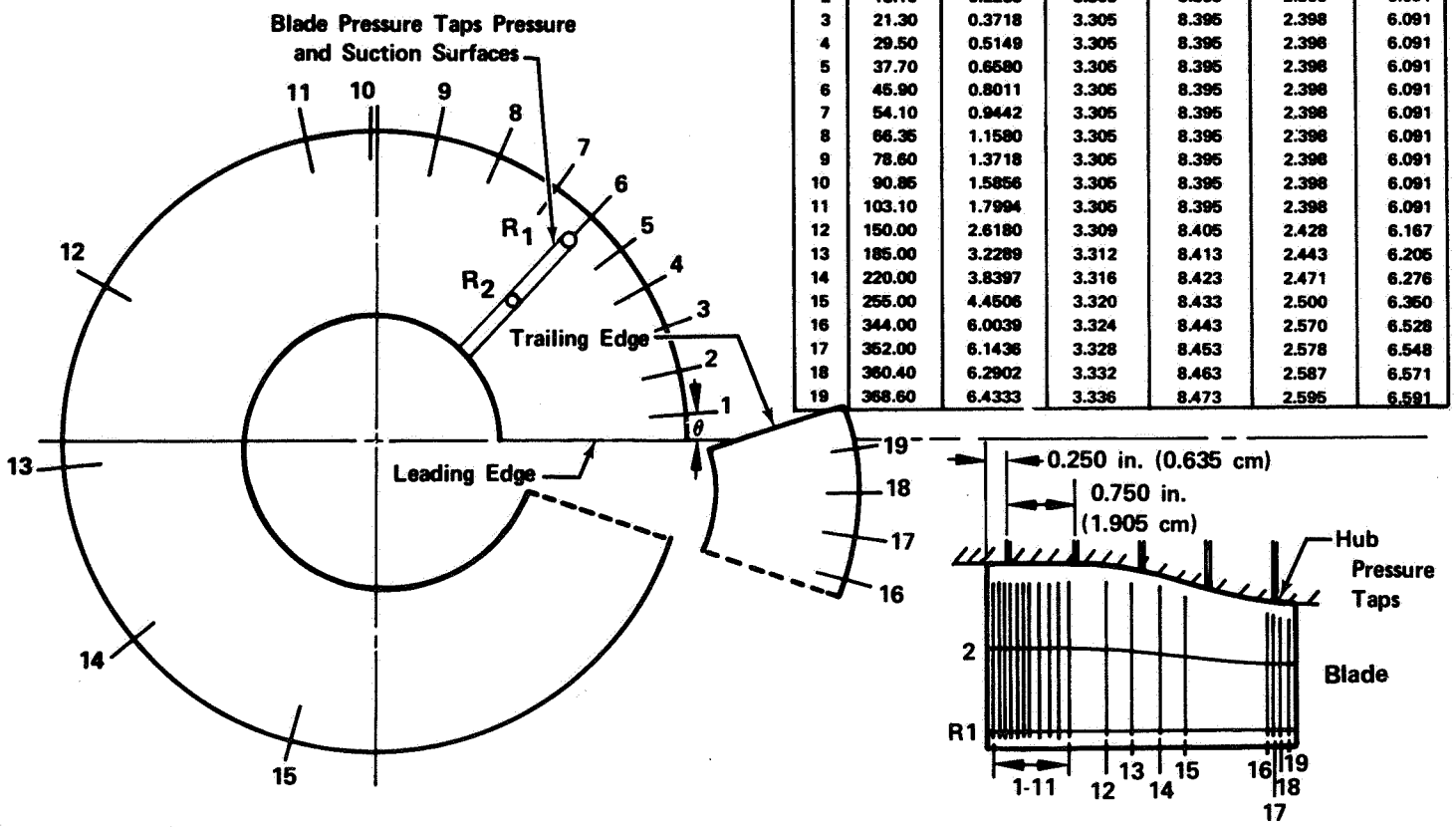

	Angular Location,		Radial Location - R			
			1		2	
	deg	rad	in.	cm	in.	cm
1	4.90	0.0855	3.305	8.395	2.398	6.091
2	13.10	0.2286	3.305	8.395	2.398	6.091
3	21.30	0.3718	3.305	8.395	2.398	6.091
4	29.50	0.5149	3.305	8.395	2.398	6.091
5	37.70	0.6580	3.305	8.395	2.398	6.091
6	45.90	0.8011	3.305	8.395	2.398	6.091
7	54.10	0.9442	3.305	8.395	2.398	6.091
8	66.35	1.1580	3.305	8.395	2.398	6.091
9	78.60	1.3718	3.305	8.395	2.398	6.091
10	90.85	1.5856	3.305	8.395	2.398	6.091
11	103.10	1.7994	3.305	8.395	2.398	6.091
12	150.00	2.6180	3.309	8.405	2.428	6.167
13	185.00	3.2289	3.312	8.413	2.443	6.205
14	220.00	3.8397	3.316	8.423	2.471	6.276
15	255.00	4.4506	3.320	8.433	2.500	6.350
16	344.00	6.0039	3.324	8.443	2.570	6.528
17	352.00	6.1436	3.328	8.453	2.578	6.548
18	360.40	6.2902	3.332	8.463	2.587	6.571
19	368.60	6.4333	3.336	8.473	2.595	6.591

Figure 55. Blade Surface Pressure Tap Locations - Blades

FD 25876B

Figure 56. Miniature Transducer FE 89875

The transducers were located along the outer streamline of a blade suction surface as shown in figure 57. This location was selected to place the transducers in the region of maximum cavitation. The transducers were installed flush with the blade surface and cemented in place.

c. Blade Steady and Vibratory Strain

Three element strain gage rosettes** were incorporated in the design to measure blade steady and vibratory strains. The rosettes were applied to the suction surface of a single blade for laboratory steady and vibratory strain tests. One rosette was located at each of the 64 analytic finite element nodes used in the stress analysis to facilitate the correlation of experimental with predicted data. The use of rosettes instead of single element gages permitted calculation of stress magnitude and direction at each node.

Slip ring capacity (48 channels) limited the number of rosettes that could be read during operational tests to twelve. Rosettes at nodes 1 through 12 were selected to provide data in the region of maximum predicted blade loading. In addition, spare rosettes were added at node 1 of the other two blades to ensure that gage failure did not prevent strain measurements at this critical location and the gage at node 13 was prepared as a spare. Strain instrumentation for operational tests therefore consisted of primary rosettes at nodes 1 through 12, 2 spare rosettes at node 1 and one spare rosette at node 13.

**Baldwin Lima Hamilton Type WA-06-120WR-120

Angular Location, θ		
	deg	rad
1	6.00	0.1025
2	21.30	0.3718
3	37.70	0.6580
4	55.88	0.9753
5	84.37	1.4725
6	111.57	1.9472

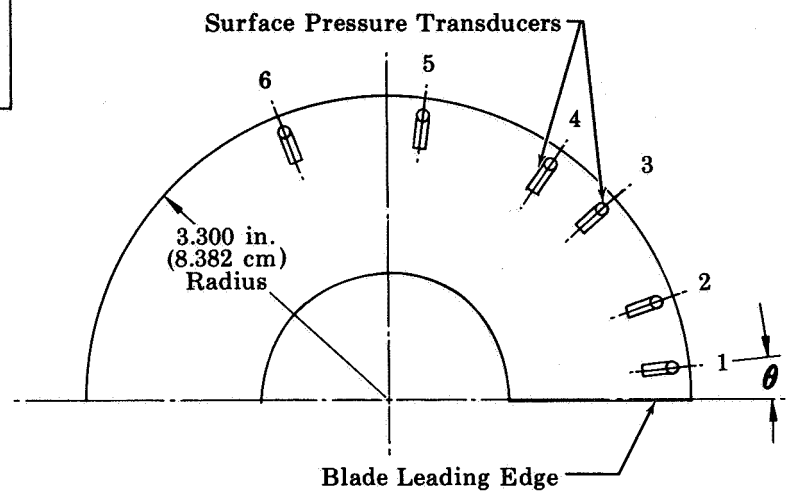

Figure 57. Miniature Transducer Locations - Blade No. 3 FD 25858

3. Test Rig Design

The inducer and instrumentation were designed into a water loop test rig as shown in figure 58. The rig was assembled with the pressure scanning valve and miniature transducers, or with the strain gages, depending on test requirements. Leads were routed through the hollow drive shaft and connected to the slip ring. For performance tests, with no inducer instrumentation, a torquemeter was substituted for the slip ring in the drive train.

The inducer was overhung in the inlet line from a rubber sleeve bearing to provide unobstructed inlet flow. An acrylic plastic sleeve was used to house the inducer to permit observation of cavitating flow. The acrylic sleeve contained provisions for inlet and discharge traverse instrumentation and static pressure measurements along the inducer blade tip. A sealed annulus was provided at the rear of the rig and 0.062 in. (0.158 cm) diameter steel tubing was routed from the annulus to the pressure scanning valve to provide the valve with purge air.

Analytic checks of the rig stresses and rotor dynamics indicated that the design was satisfactory. The rig first critical speed was conservatively calculated as 6200 rpm (649.3 rad/s) neglecting the stiffness of the rubber sleeve bearing. This value was 25% higher than the maximum operating speed of 4900 rpm (513.1 rad/s). All drive train components had a minimim safety factor of 4 considering a maximum torque requirement of 1000 in.-lb (113 cm-N). The standard slip ring shaft was not strong enough to drive the rig so a modified design using a higher strength material was substituted.

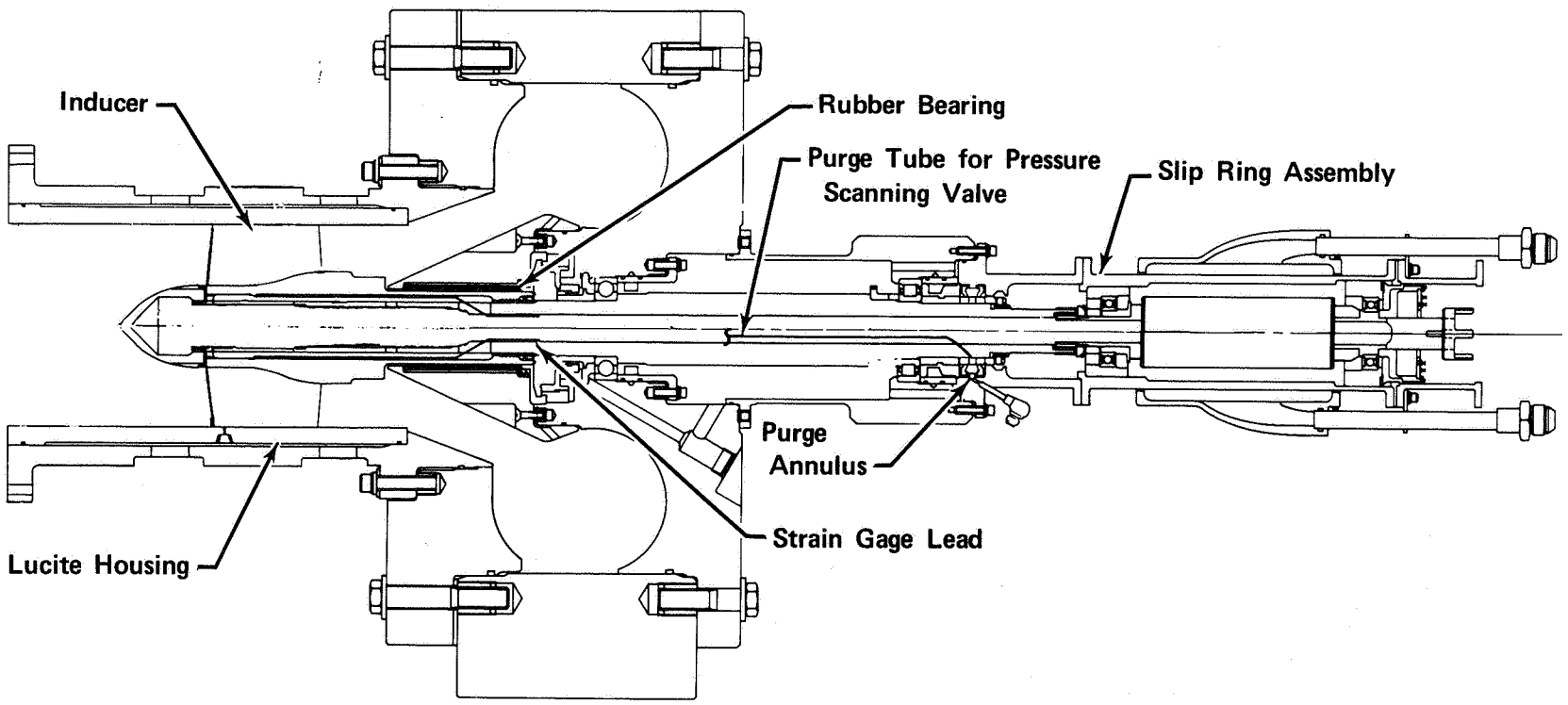

Figure 58. Inducer Test Rig Design

FD 21423

D. TASK IV - DETAIL DESIGN

Detail manufacturing drawings were prepared for new parts required to install the inducer and instrumentation in the water test loop. The areas for which new parts were required are shaded in figure 59.

E. TASK V - FABRICATION

One set of rig parts and two inducers were fabricated with one inducer to be used for pressure testing and one for strain gage testing. Critical dimensions of rig parts were inspected and inducer blade surface coordinates were thoroughly inspected. The inducers were also flourescent-penetrant inspected for cracks.

Critical fit dimensions of all parts were acceptable. Blade and hub surface coordinates for the two inducers deviated from blueprint limits as listed below.

	Pressure Test Inducer		Strain Test Inducer	
	In.	Cm	In.	Cm
Blade Deviation	0.003	0.008	0.004	0.010
Hub Deviation	0.016	0.041	0.004	0.010

These deviations were considered sufficiently small as to have negligible effect on the test data.

F. TASK VI - EXPERIMENTAL TESTING AND COMPUTER PROGRAM DEVELOPMENT

The purpose of this task was to generate experimental data for correlation with, and development of, the computer programs formulated in Task II. To provide the data required to fully substantiate the computer programs (hydrodynamic, stress, and vibration) a three part experimental program was conducted. The three parts consisted of:

1. Static load testing in which a strain-gaged inducer was subjected to steady point loads and strains were measured.

2. Vibration testing to determine blade resonant frequencies and corresponding relative stress distributions.

3. Operational testing in a closed water loop with both blade surface pressures and strains measured.

Data from these tests were correlated with the computer programs and modifications were made to the programs where required to improve accuracy.

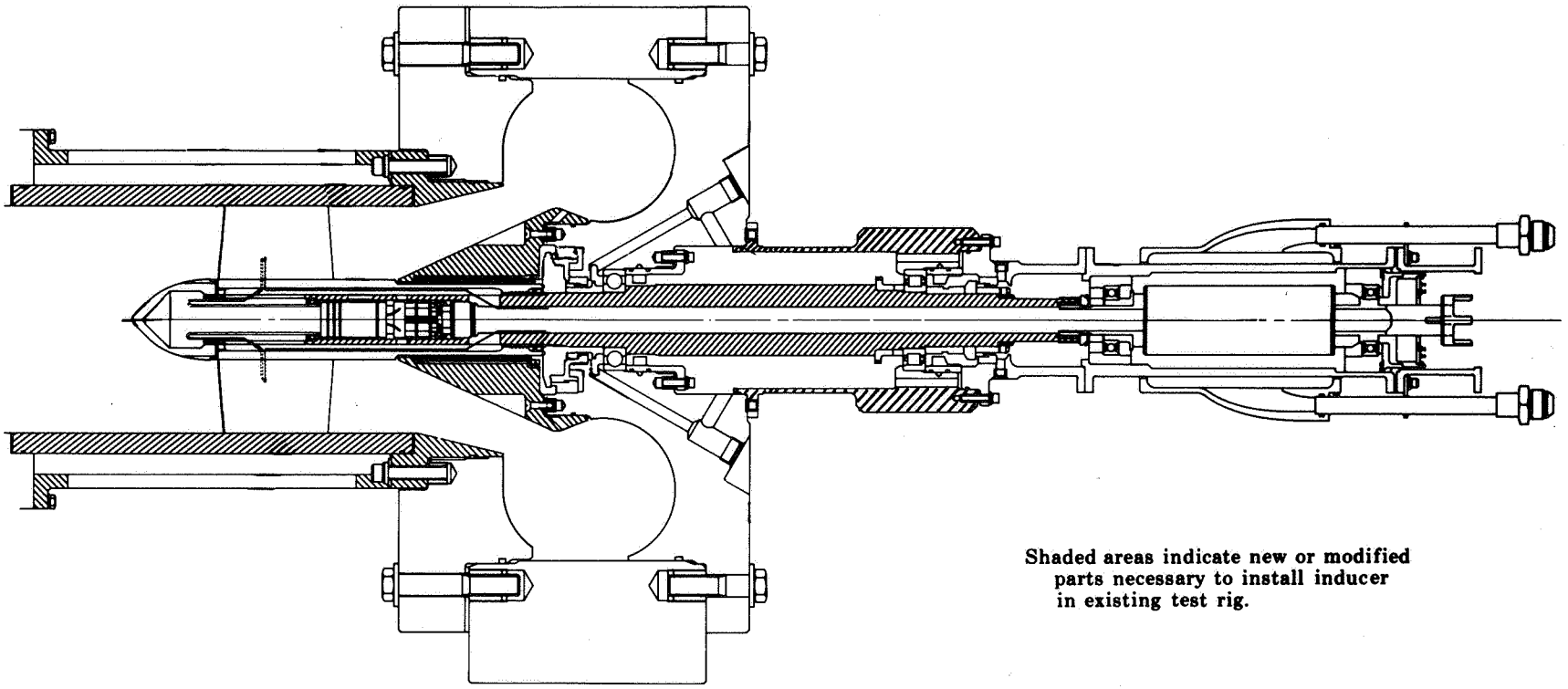

Figure 59. Test Rig Modifications

FD 21423A

The test programs and subsequent data comparison are discussed in the following paragraphs.

1. Static Load Testing

a. Test Procedure

Concentrated static loads were applied to the inducer blade normal to the blade surface and the resulting strain distributions and deflections were measured for correlation with the stress prediction computer program. The loads were applied separately at three angular locations along the blade tip; near the leading edge, at midchord, and near the trailing edge. Strains for each load configuration were measured with strain gages, and deflections were measured with dial indicators set normal to the blade surface.

The test setup for the static load tests is shown in figure 60. Loads were applied by a hydraulic ram to triangular-shaped pads located on the blade surface. The triangular pads correspond to three of the triangular elements (6, 48, 90) used in the analytic program and shown in figure 61. A ball joint was used between the ram and the pads to ensure normal loading. Force applied to the blade was calculated from ram hydraulic pressure and the known dimensions of the lever. Blade instrumentation consisted of 64 strain gage rosettes on the blade suction surface, one at each of the analytic element nodes of figure 61. The rosettes were of the three element stacked type permitting calculation of strain and strain direction at each point. The output of each gage was manually read from a "SR4" readout during tests. Blade deflections were measured at 16 places along the blade tip with dial indicators. The indicators were located to read axial deflection at each of the analytic nodes on the blade tip (nodes 4, 8, 12, ...64).

Preliminary stresscoat tests were conducted to determine the location of maximum strain for each of the load configurations. A 200 lb (890 N) point load was applied in sequence to the suction surface of a stresscoated blade at the centroid of analytic elements No. 6 at the leading edge, No. 48 at midchord, and No. 90 at the trailing edge. The resulting stresscoat patterns on the suction surface are shown in figure 62.

Strain gage rosettes were then installed and loads up to 300 lb (1335 N) in 100 lb (445 N) increments were applied in sequence at the same points previously used for the stresscoat tests. These loads were applied first to the suction, then to the pressure surface so that blade membrane strains could be calculated. Strain data from all gages were recorded for each force increment.

Dial indicators were placed normal to the blade surface along the blade tip and loads were reapplied to the blade suction surface in 50 lb (222 N) increments to a maximum of 200 lb (890 N). Deflection readings were taken at each incremental load.

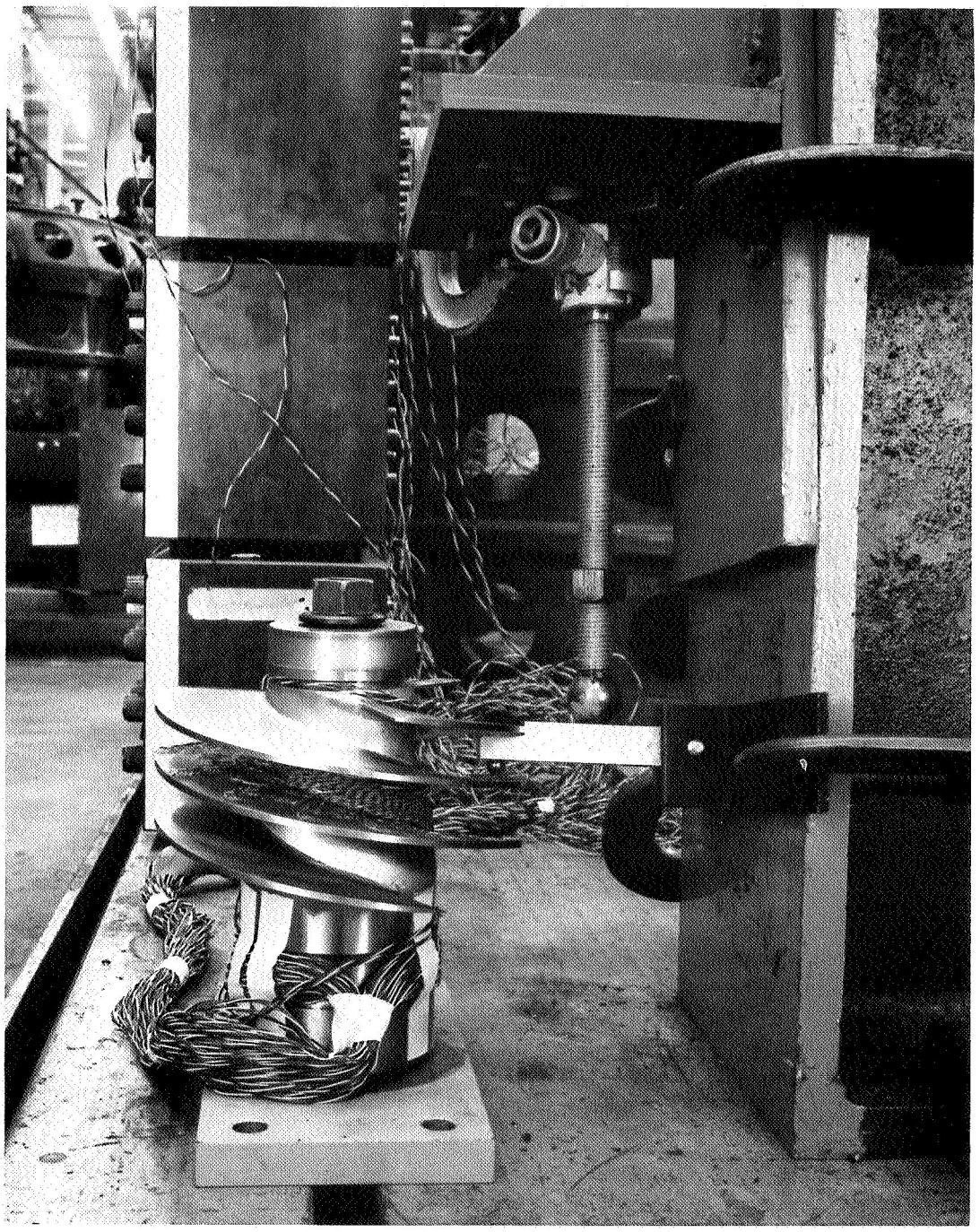

Figure 60. View of Static Load Test Setup FE 88150

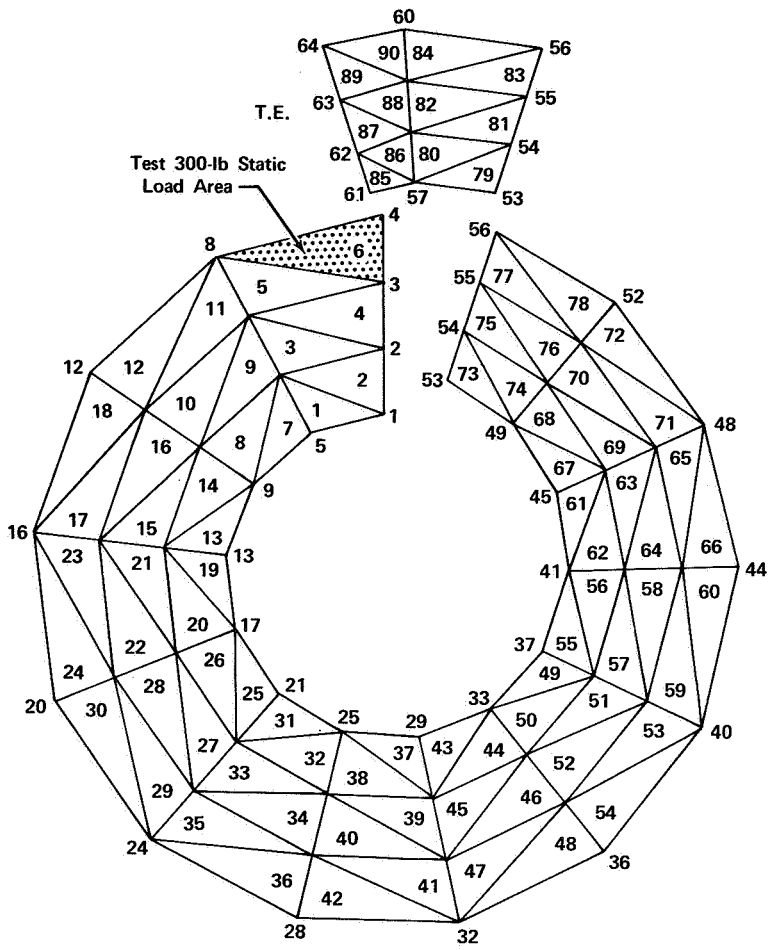

Figure 61. Finite Element Break-up 90 Element

b. Test Results

Strains and deflections increased approximately linearly with the application of incremental loads so that results at maximum load are sufficient to define the test data.

Strain and calculated effective stress data for the six load applications (leading edge, midchord, and trailing edge pressure and suction surfaces) are presented in tables 4, 5, and 6. Effective stress was calculated from the strain measurements using the relations of table 7. Only data at the 16 analytic nodes nearest the applied load are presented in the interest of conciseness. Effective stresses at nodes further removed from the load were less than 8000 psi (5510 N/cm^2) in all cases.

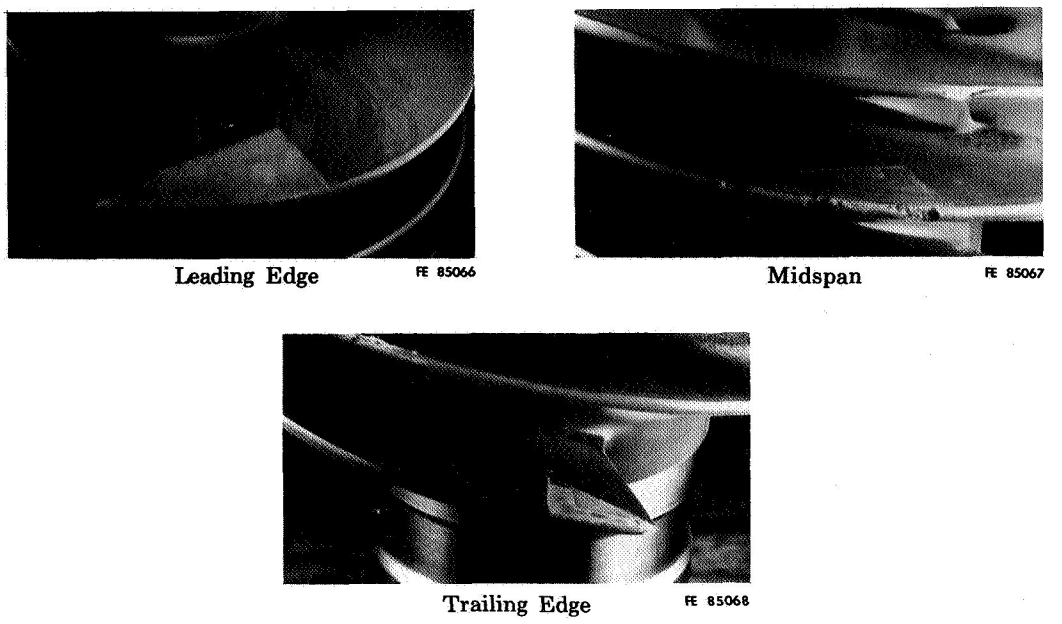

Figure 62. Inducer Static Load Stresscoat Patterns FD 31723

Deflections for the maximum load of 200 lb (890 N) applied to the suction surface at leading edge, midchord, and trailing edge are tabulated in table 8. Data from all dial indicators that showed deflection are listed.

2. Vibration Testing

a. Test Procedure

Vibration tests were conducted to measure inducer blade resonant frequencies and associated relative strain distributions for comparison with computer program predictions.

Shaker table tests were conducted in which the inducer was excited at resonant frequencies and: (1) nodes were located, (2) stresscoat patterns were determined, and (3) strains were measured with strain gages.

The inducer was first excited over a range of frequencies to 4500 Hz. Resonant frequencies within this range were noted by observing the inducer with a strobe light. Node locations at each resonant frequency were determined with the aid of a capacitance type distance probe. Displacements at frequencies higher than the fourth mode were low, however, and only the node termination at the blade tip could be established.

Table 4. Static Strain and Stress, 300 lb (1335 N) Concentrated Load at Leading Edge (Element 6)

Node	Load on Suction Surface				Load on Pressure Surface			
	Radial	Strain, $\epsilon \times 10^6$ 45 deg (0.78 rad)	Tangential	Effective Stress, lb/in.^{2} (N/cm^2)	Radial	Strain, $\epsilon \times 10^6$ 45 deg (0.78 rad)	Tangential	Effective Stress, lb/in.^{2} (N/cm^2)
1	4170	2470	-630	67,800 (46,800)	-3980	-2600	570	-66,000 (-45,600)
2	2900	550	-800	47,700 (32,900)	-2820	- 670	770	-45,900 (-31,700)
3	OPEN	OPEN	OPEN		- 780	330	290	-17,600 (-12,100)
4	OPEN	OPEN	OPEN		OPEN	OPEN	OPEN	
5	2450	670	260	42,400 (29,300)	-2700	- 780	-220	-46,100 (-31,800)
6	1350	- 20	670	33,400 (23,100)	-1370	90	-530	-32,900 (-22,700)
7	110	-300	1260	29,200 (19,500)	- 70	460	-960	-25,800 (-17,800)
8	-530	-190	1760	33,000 (22,800)	440	350	-1350	-27,700 (-19,100)
9	640	200	-50	10,400 (7,170)	- 520	-160	50	-8,400 (-5,800)
10	580	-70	400	16,800 (11,600)	- 360	160	-320	-13,400 (-9,240)

Table 4. Static Strain and Stress, 300 lb (1335 N) Concentrated Load at Leading Edge (Element 6) (Continued)

Node	Load on Suction Surface				Load on Pressure Surface			
	Radial	Strain, $\epsilon \times 10^6$ 45 deg (0.78 rad)	Tangential	Effective Stress, lb/in.^{2} (N/cm^2)	Radial	Strain, $\epsilon \times 10^6$ 45 deg (0.78 rad)	Tangential	Effective Stress, lb/in.^{2} (N/cm^2)
11	-140	-150	810	16,500 (11,400)	200	160	-900	-18,000 (-12,400)
12	-400	180	1320	22,100 (15,300)	410	-200	-1420	-24,000 (-16,600)
13	180	110	-50	3,100 (2,140)	-120	-100	80	-2,700 (-1,860)
14	130	-50	30	3,500 (2,420)	- 80	50	-40	-2,800 (-1,930)
15	-110	-40	300	5,700 (3,940)	120	10	-320	-5,700 (-3,940)
16	-150	120	460	7,500 (5,180)	140	-150	-460	-7,400 (-5,110)

Table 5. Static Strain and Stress, 300 lb (1335 N) Concentrated Load at Midchord (Element 48)

Node	Load on Suction Surface				Load on Pressure Surface			
	Strain, $\epsilon \times 10^6$			Effective Stress, lb/in^2 (N/cm^2)	Strain, $\epsilon \times 10^6$			Effective Stress, lb/in^2 (N/cm^2)
	Radial	45 deg (0.78 rad)	Tangential		Radial	45 deg (0.78 rad)	Tangential	
25	660	670	200	12,500 (8,630)	-600	-590	-170	-11,200 (-7,730)
26	480	930	500	15,000 (10,400)	-470	-830	-440	-13,500 (-9,320)
27	120	660	450	11,000 (7,600)	-120	-570	-370	-9,400 (-6,490)
28	-30	270	170	5,000 (3,450)	40	-220	-120	-4,300 (-2,970)
29	1640	900	120	26,500 (18,300)	-1430	-800	- 90	-23,100 (-15,900)
30	1420	1560	330	28,000 (19,300)	-1260	-1400	-320	-25,000 (-17,300)
31	470	1240	150	21,400 (14,800)	-380	-1050	-160	-17,900 (-12,350)
32	130	640	-190	-14,600 (-10,070)	-100	-480	210	11,900 (8,210)
33	1780	710	80	29,100 (20,100)	-1650	-650	-40	-26,800 (-18,500)

Table 5. Static Strain and Stress, 300 lb (1335 N) Concentrated Load at Midchord (Element 48) (Continued)

Node	Load on Suction Surface				Load on Pressure Surface			
	Strain, $\epsilon \times 10^6$			Effective Stress, lb/in^2 (N/cm^2)	Strain, $\epsilon \times 10^6$			Effective Stress, lb/in^2 (N/cm^2)
	Radial	45 deg (0.78 rad)	Tangential		Radial	45 deg (0.78 rad)	Tangential	
34	1230	310	250	22,400 (15,500)	-1060	-220	-170	-19,400 (-13,400)
35	350	-270	130	12,400 (8,560)	-170	330	- 50	-9,800 (-6,760)
36	-120	-460	370	13,800 (9,520)	70	390	-190	-10,100 (-6,970)
37	530	200	-10	8,500 (5,770)	-480	-130	40	-7,800 (-5,380)
38	520	-60	250	13,500 (9,320)	-380	120	-220	-11,500 (-7,940)
39	-310	90	1070	18,300 (12,600)	290	-70	-950	-16,200 (-11,200)
40	-60	-160	680	14,700 (10,140)	80	160	-600	-13,000 (-8,970)

Table 6. Static Strain and Stress, 300 lb (1335 N) Concentrated Load at Trailing Edge (Element 90)

Node	Load on Suction Surface				Load on Pressure Surface			
	Radial	Strain, $\epsilon \times 10^6$ 45 deg (0.78 rad)	Tangential	Effective Stress, lb/in^2 (N/cm^2)	Radial	Strain, $\epsilon \times 10^6$ 45 deg (0.78 rad)	Tangential	Effective Stress, lb/in^2 (N/cm^2)
52	-40	120	160	2,900 (2,000)	0	-100	-60	-1,800 (-1,240)
53	1680	1360	240	28,000 (19,300)	-1460	-1250	-260	-25,600 (-17,700)
54	1440	2570	1060	41,200 (28,400)	-1460	-2480	-1130	-40,100 (-27,600)
55	170	2020	1470	35,000 (25,200)	-190	-1870	-1490	-32,800 (-22,600)
56	-210	1060	920	20,900 (14,400)	190	-910	-920	-19,000 (-13,100)
57	5220	2390	-60	83,500 (57,600)	-5510	-2730	0	-87,900 (-60,700)
58	2560	2830	580	50,700 (35,000)	-2430	-3300	-1090	-55,200 (-38,100)
59	280	3050	920	54,300 (37,500)	-80	-3870	-1950	-68,200 (-47,100)
60	-390	1440	290	32,400 (22,200)	600	-2100	-1280	-43,000 (-29,700)

Table 6. Static Strain and Stress, 300 lb (1335 N) Concentrated Load at Trailing Edge (Element 90) (Continued)

Node	Load on Suction Surface				Load on Pressure Surface			
	Strain, $\epsilon \times 10^6$			Effective Stress, lb/in^2 (N/cm^2)	Strain, $\epsilon \times 10^6$			Effective Stress, lb/in^2 (N/cm^2)
	Radial	45 deg (0.78 rad)	Tangential		Radial	45 deg (0.78 rad)	Tangential	
61	80	-510	-200	10,100 (6,970)	-760	40	40	-14,800 (-10,200)
62	340	530	10	9,300 (6,420)	980	-560	-410	24,100 (16,600)
63	-720	490	250	-19,300 (-13,300)	1370	-590	-410	31,600 (21,800)
64	-290	40	20	-5,900 (-4,070)	560	-30	0	11,100 (7,660)

Table 7. Calculation of Effective Stresses

Principal stresses were calculated from strain gage data using the following relations:

$$\sigma_{max} = \frac{E}{2}\left[\frac{\epsilon_1 + \epsilon_3}{1 - \mu} + \frac{1}{1 + \mu}\sqrt{(\epsilon_1 - \epsilon_3)^2 + \left[2\epsilon_2 - (\epsilon_1 + \epsilon_3)^2\right]}\right]$$

$$\sigma_{min} = \frac{E}{2}\left[\frac{\epsilon_1 + \epsilon_3}{1 - \mu} - \frac{1}{1 + \mu}\sqrt{(\epsilon_1 - \epsilon_3)^2 + \left[2\epsilon_2 - (\epsilon_1 + \epsilon_2)^2\right]}\right]$$

where:

ϵ_1 = Radial strain gage strain reading

ϵ_2 = 45 deg strain gage strain reading

ϵ_3 = Tangential strain gage strain reading

E = Modulus at elasticity

μ = Poisson's ratio

The effective stress was calculated by the following relation:

$$\sigma_{eff} = \sqrt{\sigma_{max}^2 + \sigma_{min}^2 - \sigma_{max}\,\sigma_{min}}$$

Stresscoat representations of strain distribution were obtained by applying stresscoat, exciting the inducer at a particular vibration mode at sufficient amplitude to break the stresscoat, and photographing the resultant stresscoat pattern. This process was repeated for each of the first four vibration modes.

Relative strain magnitude and distribution were measured with the same three-gage, stacked, strain gage rosettes used in static load tests. The inducer was again excited at each of its first four vibration modes and vibratory strain was manually recorded for each mode. Observed strain readings were limited to 1000 in./in. (17,000 psi, 11,800 N/cm^2) by controlling input vibration amplitude to prevent fatigue failure of the blades during the tests. Even with this limit, a fatigue crack did occur extending approximately one inch from the blade trailing edge at the root during measurement of 3/0 mode strains. The crack was weld repaired prior to completion of 3/0 and 0/0 mode strain measurement.

b. Test Results

Eleven resonant frequencies were noted within the 0-4500 Hz range scanned. The frequencies and node locations at the blade tip are listed in table 9.

Table 8. Deflection Normal to Blade - 200 lb (890 N) Concentrated Load

Load Applied Near Leading Edge of Blade			Load Applied Near Midpoint of Blade			Load Applied Near Trailing Edge of Blade		
Node	Deflection, in.	Deflection, cm	Node	Deflection, in.	Deflection, cm	Node	Deflection, in.	Deflection, cm
3	0.0315	0.0800	20	0.0007	0.0018	52	0.0011	0.0028
4	0.0625	0.1590	24	0.0012	0.0031	56	0.0139	0.0353
8	0.0338	0.0859	28	0.0049	0.0124	60	0.0477	0.1211
12	0.0080	0.0203	32	0.0147	0.0374	64	0.0672	0.1707
16	0.0023	0.0058	36	0.0189	0.0480			
20	0.0012	0.0031	40	0.0075	0.0191			
24	0.0012	0.0031	44	0.0015	0.0038			
			48	0.0006	0.0015			

Table 9. Inducer Resonant Frequencies and Node Locations

Mode	Frequency Hz	No. of Nodes	Node Location at Blade Tip Deg (rad) From LE
0/0	1067	--	At hub-blade interface
1/0	1245	1	56 (0.98)
2/0	1408	2	40, 141 (0.70, 2.46)
3/0	1522	3	34, 111, 193 (0.59, 1.94, 3.37)
4/0	1640	4	29, 93, 173, 277 (0.51, 1.62, 3.02, 4.84)
5/0	1740	5	27, 87, 150, 219, 312 (0.47, 1.52, 2.62, 3.82, 5.44)
6/0	1947	6	24, 76, 133, 192, 252, 339 (0.42, 1.33, 2.32, 3.35, 4.40, 5.91)
7/0	2158	7	23, 67, 118, 171, 226, 308, 341 (0.40, 1.17, 2.06, 2.98, 3.94, 5.37, 5.95)
9/0	2858	9	15, 50, 92, 138, 180, 219, 257, 308, 350 (0.26, 0.87, 1.61, 2.41, 3.14, 3.82, 4.48, 5.37, 6.11)
10/0	3284	10	14, 47, 87, 125, 160, 200, 238, 272, 318, (0.24, 0.82, 1.52, 2.18, 2.79, 3.49, 4.15, 4.74, 5.55, 355 6.20)
12/0	4315	12	12, 40, 75, 105, 135, 170, 202, 239, 265, (0.21, 0.70, 1.31, 1.83, 2.36, 2.97, 3.52, 4.17, 4.62, 298, 330, 360 (5.20, 5.76, 6.28)

Stresscoat patterns for the first four modes are shown in figure 63. Vibratory amplitude for these modes was sufficient to permit determination of the node line and these are shown superimposed on the stresscoat patterns.

Strain and effective stress data for the first four modes are tabulated in table 10. Only effective stresses greater than 10% of the maximum effective stress at each mode are presented in the interest of conciseness. Maximum stress always occurred at an element node along the inducer hub. The 3/0 mode had a high strain area at the location of the fatigue crack that was experienced in the test program.

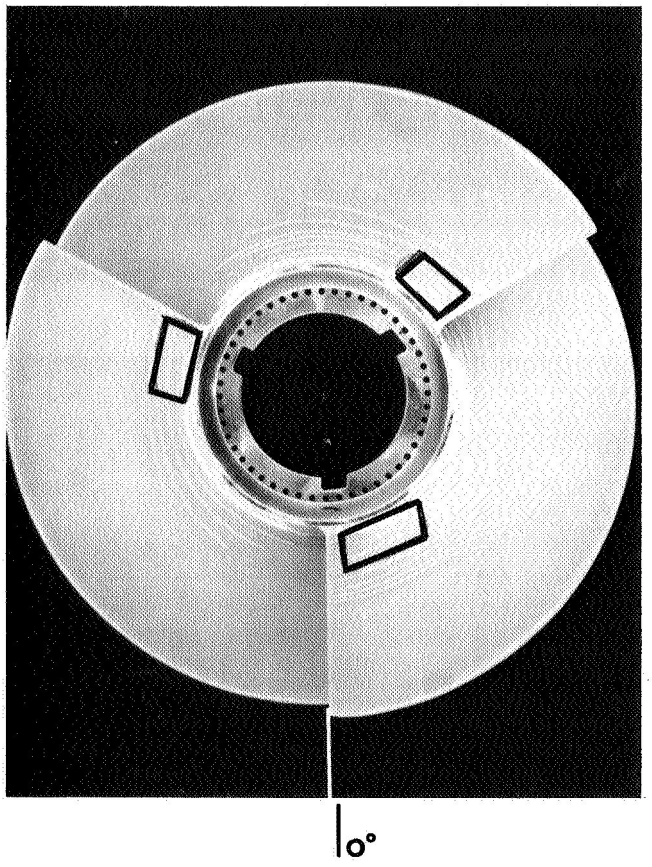

a. Umbrella Mode Stresscoat Patterns on AMS 4928 Inducer T2145887. (Enclosures Indicate Areas of High Stress.)

Figure 63. Inducer Vibratory Load Stresscoat Patterns FAL 15020

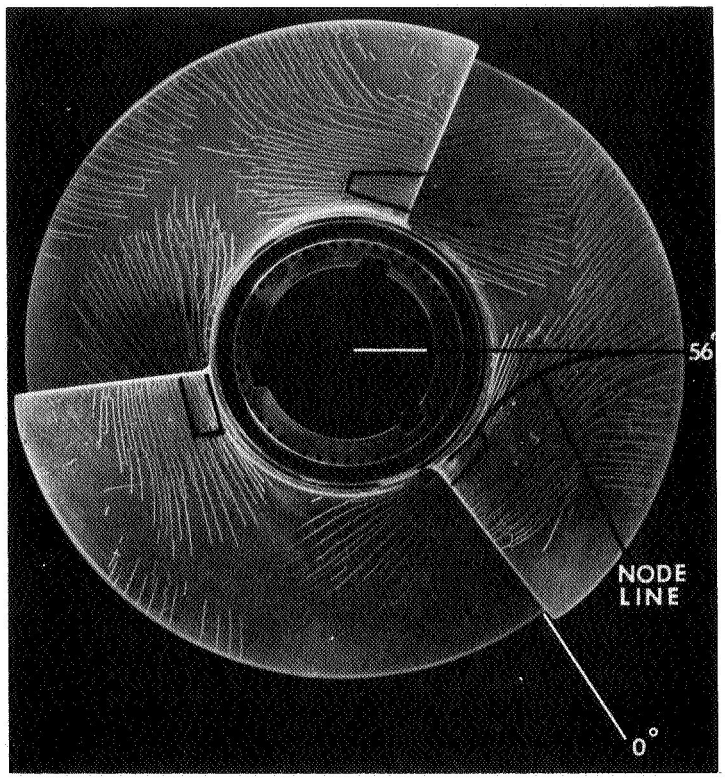

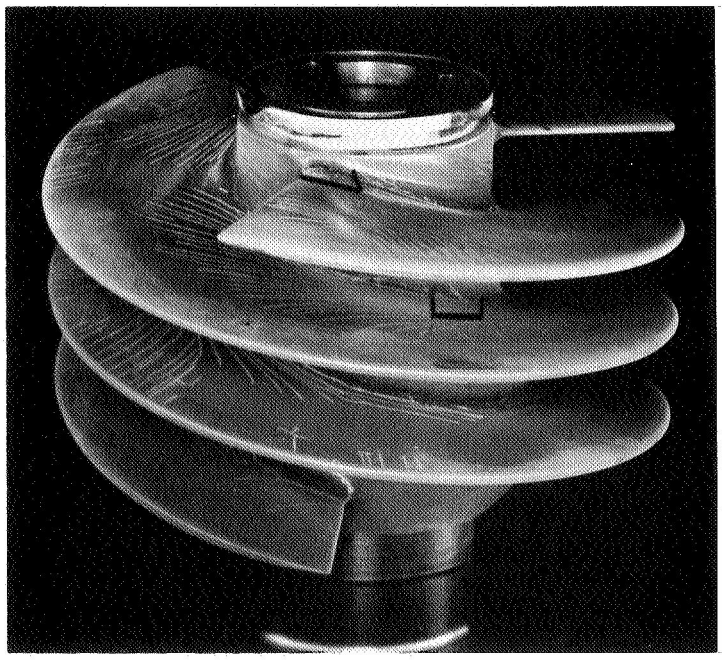

b. Second Vibration Mode Stresscoat and Nodal Patterns on AMS 4928 Inducer T2145887. Enclosures Indicate Areas of High Stress.

Figure 63. Inducer Vibratory Load Stresscoat Patterns (Continued) FAL 17432

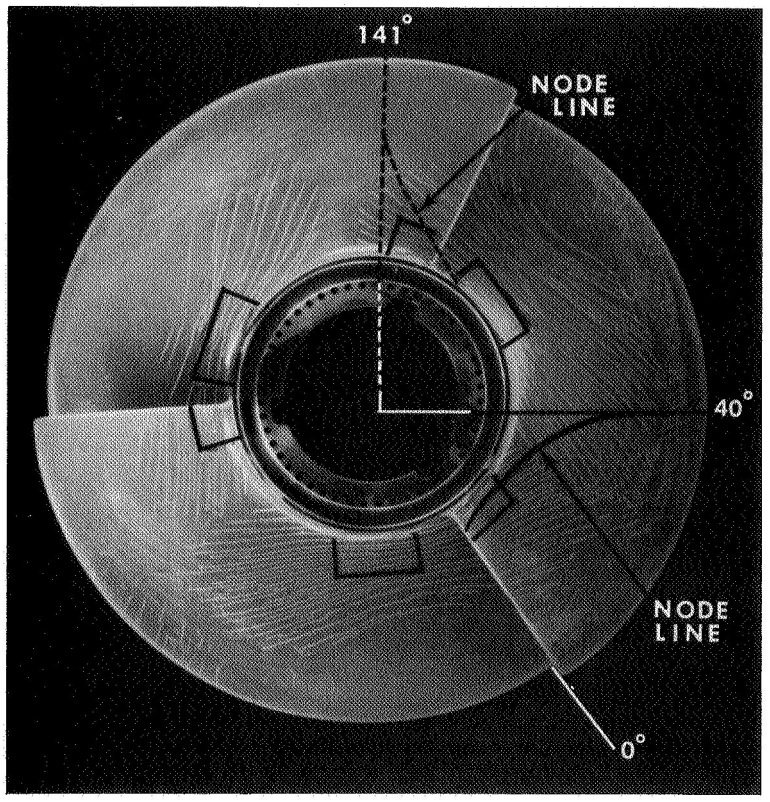

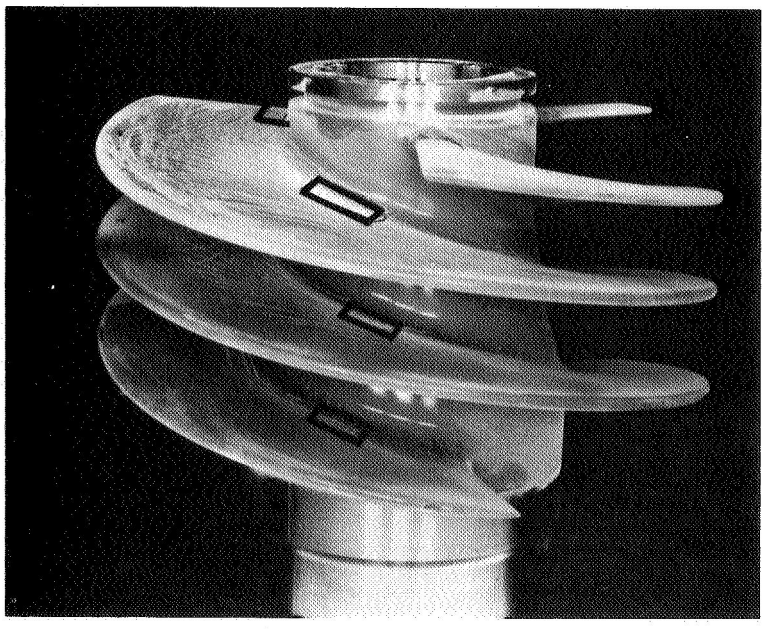

c. Third Vibration Mode Stresscoat and Nodal Patterns on AMS 4928 Inducer T2145887. Enclosures Indicate Areas of High Stress.

Figure 63. Inducer Vibratory Load Stresscoat Patterns (Continued) FAL 17433

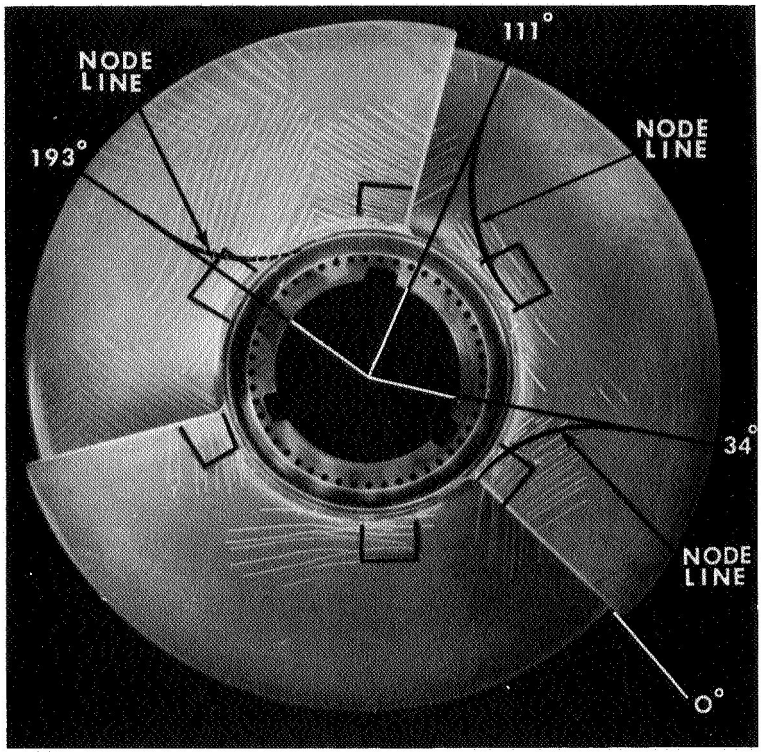

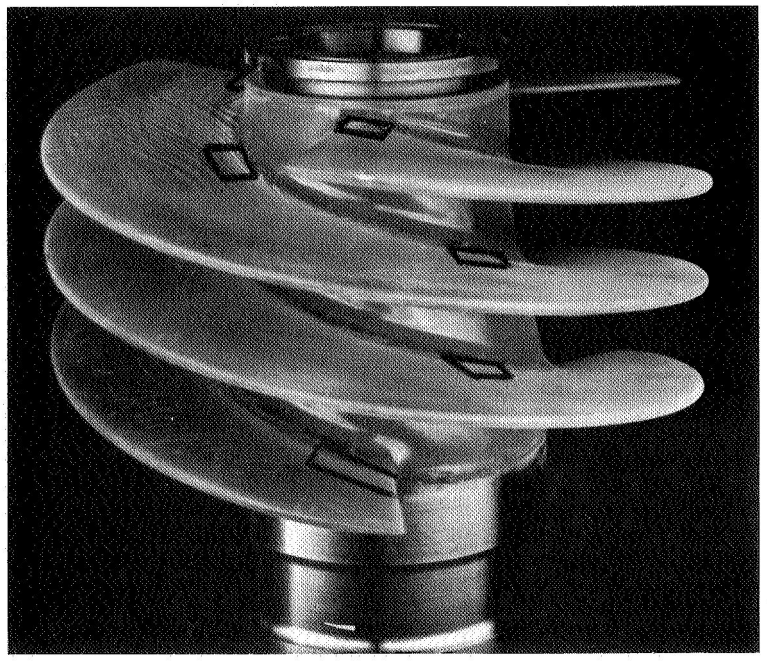

d. Fourth Vibration Mode Stresscoat and Nodal Patterns on AMS 4928 Inducer T2145887. Enclosures Indicate Areas of High Stress.

Figure 63. Inducer Vibratory Load Stresscoat Patterns (Continued) FAL 17434

Table 10. Vibratory Strain & Stress

Node	0/0 Mode Radial	Strain, $\epsilon \times 10^6$ 45 deg (0.78 rad)	Tangential	Effective lb/in^2	Stress N/cm^2	1/0 Mode Radial	Strain, $\epsilon \times 10^6$ 45 deg (0.78 rad)	Tangential	Effective lb/in^2	Stress N/cm^2
1	580	300	-50	9,200	6,340	1,000	770	-160	17,500	12,070
2	410	230	-90	6,700	4,620	640	230	-230	10,500	7,240
3	100	10	-30	1,700	1,170	170	-30	-40	3,400	2,340
4										
5	1000	520	80	16,200	11,170	770	290	40	12,700	8,760
6	530	320	150	9,100	6,270	440	140	170	8,600	5,930
7	110	90	130	3,000	2,070	140	-20	140	4,800	3,310
8	-40	0	110	1,900	1,310	-50	-50	170	3,600	2,480
9						140	-90	-90	2,900	2,000
10	310	240	180	6,000	4,140	140	-260	-50	6,700	4,620
11	50	80	210	3,700	2,550	-40	-200	150	5,900	4,070
12	-70	30	240	4,000	2,760	-120	-20	340	6,200	4,270
13						-400	-330	-160	7,300	5,030
14	220	190	150	4,500	3,100	-260	-420	-220	6,900	4,760
15	20	80	200	3,300	2,280	-160	-260	140	6,200	4,270
16	-80	50	230	3,800	2,620	-110	-20	270	4,900	3,380
17						-700	-440	160	11,800	8,140
18						-450	-470	-230	8,900	6,140
19	20	60	160	3,000	2,070	-200	-270	-40	4,600	3,170
20	-70	30	190	3,200	2,210	-30	-50	130	3,000	2,070
21						-770	-430	-80	12,500	8,620
22	210	100	90	4,000	2,760	-540	-450	-240	10,000	6,900
23	-10	30	140	2,300	1,590	-120	-220	-150	3,700	2,550
24	-60	30	160	2,700	1,860					
25	340	140	0	2,000	1,380	-820	-460	-50	13,300	9,170
26	140	60	80	1,900	1,310	-490	-320	-220	9,000	6,210

Table 10 . Vibratory Strain & Stress (Continued)

Node	0/0 Radial	0/0 Strain, $\epsilon \times 10^6$ 45 deg (0.78 rad)	0/0 Tangential	0/0 Effective Stress lb/in^2	0/0 Effective Stress N/cm^2	1/0 Mode Radial	1/0 Mode Strain, $\epsilon \times 10^6$ 45 deg (0.78 rad)	1/0 Mode Tangential	1/0 Mode Effective Stress lb/in^2	1/0 Mode Effective Stress N/cm^2
27						-60	-150	-230	3,900	2,690
28						150	-20	-230	4,200	2,900
29						-570	-300	-10	9,100	6,270
30						-420	-260	-210	8,000	5,520
31						-20	-70	-240	4,100	2,820
32						130	-40	-260	4,400	3,030
33						-470	-260	-10	7,600	5,240
34						-310	-160	-150	6,000	4,140
35						-10	-40	-230	4,100	2,830
36						140	-20	-270	4,700	3,240
37						-340	-120	0	5,500	3,790
38						-250	-80	-110	5,000	3,450
39						10	-30	-210	3,700	2,550
40						170	-20	-250	4,600	3,170
41						-270	-50	10	4,600	3,170
42						-170	-30	-70	3,600	2,480
43						10	-10	-140	2,500	1,720
44						50	-20	-210	3,600	2,480
45						-250	-50	10	4,300	2,960
46						-110	-40	-60	2,300	1,590
47										
48						40	-20	-130	2,200	1,520
49						-210	-50	10	3,500	2,410
53						-210	-50	20	3,500	2,410

Table 10. Vibratory Strain & Stress (Continued)

Node	2/0 Mode					3/0 Mode				
	Strain, $\epsilon \times 10^6$			Effective Stress		Strain, $\epsilon \times 10^6$			Effective Stress	
	Radial	45 deg (0.78 rad)	Tangential	lb/in^2	N/cm^2	Radial	45 deg (0.78 rad)	Tangential	lb/in^2	N/cm^2
1	1000	610	-220	16,600	11,450	1,000	600	-210	16,500	11,380
2	600	50	-250	10,300	7,100	590	-20	-230	10,600	7,310
3	160	-140	-50	4,900	3,380	160	-180	-50	5,600	3,860
4										
5	260	-120	-10	6,600	4,550	190	-300	10	9,000	6,210
6	150	-310	-60	7,900	5,450	-30	-510	-50	10,000	6,900
7	20	-270	40	6,400	4,410	-40	-380	30	8,000	5,520
8	-50	-210	190	6,700	4,620	-60	-260	170	7,200	4,960
9										
10	-350	-560	-190	8,800	6,070	-440	-610	-120	10,300	7,100
11	-180	-390	160	6,800	4,690	-230	-400	140	8,500	5,860
12	-120	-130	300	1,400	970	-120	-70	320	6,400	4,410
13	-900	-440	70	9,800	6,760					
14	-560	-440	-170	4,500	3,100	-350	-30	190	6,100	4,210
15	-200	-250	-40	3,300	2,280	-110	170	140	4,200	2,900
16	-50	-40	160	10,100	6,960	10	140	40	2,500	1,720
17	-360	-260	10	8,200	5,650	140	350	150	5,600	3,860
18	-400	60	30	3,400	2,340	190	660	200	10,900	7,520
19	-50	60	-100	6,000	4,140	160	500	-30	10,000	6,900
20	180	160	-240	6,000	4,140	140	220	-360	9,200	6,340
21	120	140	140	3,100	2,140					
22	-40	240	150	4,600	3,170	620	810	210	13,700	9,450
23	150	200	-210	6,200	4,270	220	420	-100	8,500	5,860
24	140	150	-370	8,300	5,720	140	140	-340	7,600	5,240
25	500	300	130	8,500	5,860	1,050	470	30	16,900	11,650

Table 10. Vibratory Strain & Stress (Continued)

Node	2/0 Strain, $\epsilon \times 10^6$ Radial	45 deg (0.78 rad)	Tangential	Effective Stress lb/in^2	N/cm^2	3/0 Strain, $\epsilon \times 10^6$ Radial	45 deg (0.78 rad)	Tangential	Effective Stress lb/in^2	N/cm^2
26	270	320	130	5,600	3,860	630	300	170	11,000	7,580
27	160	170	-140	4,700	3,240	170	140	20	2,900	2,000
28	150	20	-300	5,500	3,790	-20	-60	50	1,800	1,240
29	530	310	160	9,200	6,340	320	50	-110	5,300	3,650
30	390	340	160	7,200	4,960	240	-290	-30	9,200	6,340
31	120	160	130	3,100	2,140	-40	-300	160	8,000	5,520
32	30	20	-90	1,800	1,240	-200	-130	420	8,700	6,000
33	460	310	30	7,600	5,240	-540	-400	-190	9,500	6,550
34	370	270	140	6,600	4,550	-400	-650	-190	10,600	7,310
35	150	160	150	3,600	2,480	-230	-430	140	9,100	6,270
36	-20	40	140	2,300	1,590	-200	-120	440	8,900	6,140
37	350	190	10	5,600	3,860					
38	310	200	120	5,500	3,790					
39	50	180	140	3,100	2,140	-240	-390	20	7,100	4,900
40	-70	30	160	2,700	1,860	-70	-50	220	4,400	3,030
41	330	140	20	5,400	3,720					
42	250	140	150	5,100	3,520	-940	-360	-300	16,400	11,310
43	20	50	150	2,600	1,790	-220	-290	-230	5,600	3,860
44	-40	30	200	3,400	2,340					
45	290	130	20	4,700	3,240					
46	160	160	120	3,400	2,340	-860	-570	-320	15,300	10,550
47	20	30	150	2,700	1,860	-200	-250	-300	6,100	4,210
48	-40	30	200	3,400	2,340	160	-50	-270	4,700	3,240
49	260	120	10	4,200	2,900					
50	160	130	190	4,300	2,960					

Table 10. Vibratory Strain & Stress (Continued)

Node	2/0 Strain, $\epsilon \times 10^6$ Radial	2/0 Strain, $\epsilon \times 10^6$ 45 deg (0.78 rad)	2/0 Strain, $\epsilon \times 10^6$ Tangential	2/0 Effective Stress lb/in.^{2}	2/0 Effective Stress N/cm^2	3/0 Strain, $\epsilon \times 10^6$ Radial	3/0 Strain, $\epsilon \times 10^6$ 45 deg (0.78 rad)	3/0 Strain, $\epsilon \times 10^6$ Tangential	3/0 Effective Stress lb/in.^{2}	3/0 Effective Stress N/cm^2
51	10	50	140	2,300	1,590	-160	-280	-410	7,300	5,030
52	-50	0	110	1,900	1,310	140	70	-340	6,700	4,620
53	260	130	10	4,200	2,900					
54	160	40	40	3,000	2,070					
55	30	30	230	4,300	2,960	-220	-470	-440	8,800	6,070
56	40	30	210	4,000	2,760	160	-270	-350	6,900	4,760
57	120	120	20	2,300	1,590	-1,410	-660	30	22,500	15,510
58	130	90	20	2,200	1,520	-1,170	-460	40	18,800	12,960
59						-240	-320	-160	5,600	3,860
60						20	-190	-70	3,700	2,550
61						-200	200	140	6,100	4,210
62						-540	10	140	9,700	6,690
63	40	20	20	7,800	5,380	10	-110	10	2,600	1,790
64						40	10	10	7,500	5,170

3. Operational Testing

Operational tests on the inducer included performance evaluation, blade strain measurements and blade surface pressure measurements, all under both cavitating and noncavitating conditions. The two inducers fabricated in Task V were used alternately to conduct the three operational test series. The No. 1 inducer was used for performance evaluation while inducer No. 2 was being used for the static and vibration testing and subsequently for the operational strain gage tests. The No. 1 inducer, after performance testing, was reworked for the blade surface pressure tests.

a. Facility

The inducer test rig modified in Task III was installed in the existing water loop shown schematically in figure 64 for operational testing. The loop is identified as PWA FRDC test stand D-34. The only facility modification necessary for this program was the fabrication of a new 8 in. (20.3 cm) diameter line to fit between the facility heat exchanger and the rig inlet. A converging section just upstream of the inducer reduced the inlet line inner diameter to the 7 in. (17.8 cm) inducer housing diameter.

The test loop uses demineralized water and contains a vortex generator deaeration system for reducing air content. There are three parallel legs in the discharge section of the flow loop, each with its own flow meter, providing accurate measurement over a wide range of flow rates.

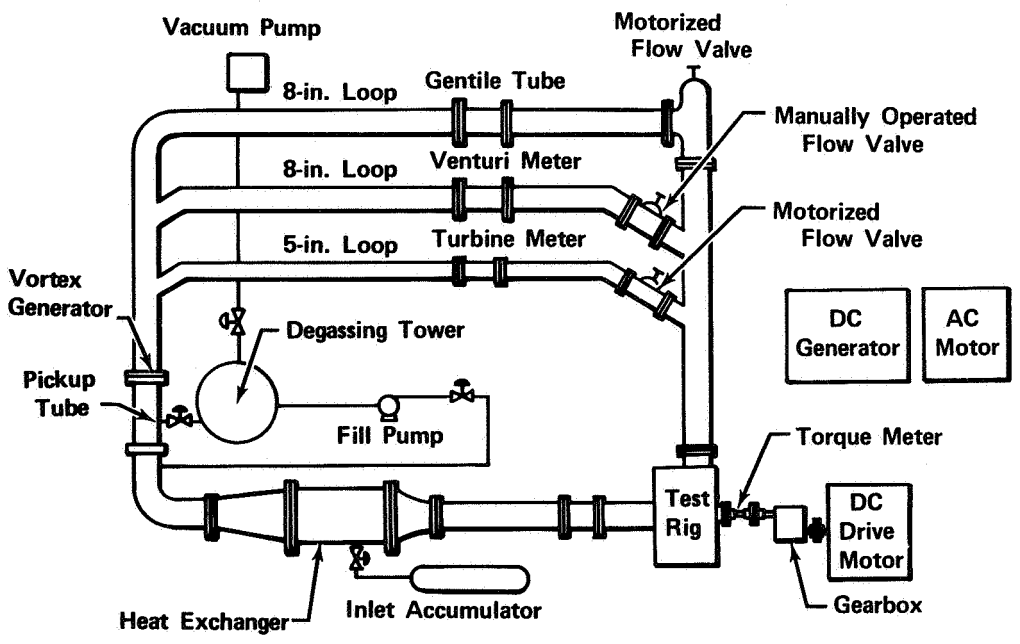

Figure 64. Schematic of Water Flow Loop FD 19703D

The loop is equipped with a heat exchanger for controlling fluid temperature and an inlet accumulator for regulation of inlet pressure. Discharge pressure is controlled with a motorized throttling valve. Drive is by means of a 250 hp (186.5 kw) DC motor through a variable ratio gearbox. Speeds to 9000 rpm (941 rad/sec) are possible and test point speed is automatically regulated within 0.03% by a servo speed control.

b. Instrumentation

(1) General

Instrumentation varied with the type of test being conducted; i.e., performance, blade pressure, or strain. Performance instrumentation was common to all three test series except that the torquemeter was replaced with a slip ring assembly for the pressure and strain tests. A summary of the performance instrumentation is given in table 11.

Pressure instrumentation was located as shown in figure 65. Wall static pressures were measured immediately upstream and downstream of the inducer and at five equally spaced locations along the length of the inducer. Inlet total pressure was measured upstream of the inducer with Kiel probes set on the pipe centerline and inlet and exit flow distributions were measured with wedge type total-static probes installed in manual traverse fixtures. The fixtures had verniers for setting traverse depth and reading flow angle. The probes were nulled during testing using a differential pressure gage. The wedge probes were air calibrated prior to installation for determination of null position and static pressure correction factor. Static pressure corrections were:

Inlet Probe Serial 847	$0.057\ (P_T - p)$
Exit Probe Serial 851	$0.048\ (P_T - p)$

All pressures were read from precision, ±0.2% F.S., pressure gages.

Test rig drive torque was measured with a strain gage type torquemeter. Shaft tare was measured by running the rig without an inducer and these torque values were subtracted from test readings to obtain inducer drive torque.

Flow was measured with a turbine type flowmeter downstream of the inducer discharge throttling valve.

Temperature was measured with a chromel-alumel thermocouple in the inlet line downstream of the loop heat exchanger.

Inducer speed was measured by electronically counting the output of a magnetic transducer which sensed the passing frequency of a 60 tooth gear on the rig drive shaft.

Estimated maximum instrumentation error is listed in table 11.

Table 11. Performance Test Instrumentation

Symbol	Parameter	Sensor	Readout	Range	Max Error
AN	Speed	Magnetic Transducer	Counter	-	1 rpm (0.1 rad/s)
Q	Flow	Turbine Flowmeter	Counter	1500 gpm (94,600 cu^3/s)	2%
T	Temperature	Thermocouple	Meter	-	2°F (1.1°K)
TORQ	Torque	S.G. Torquemeter	Meter	1000 in.-lb (113 M-N)	0.25% F.S.
PSUP	Pressure-Static, Upstream	Wall Tap	Gage	100 psia (69 N/cm^2)	0.25% F.S.
PTUP	Pressure-Total, Upstream	Kiel Probe	Gage	100 psia (69 N/cm^2)	0.25% F.S.
PSIP	Pressure-Static, Inlet	Wall Tap	Gage	100 psia (69 N/cm^2)	0.25% F.S.
PTIP	Pressure-Total, Inlet	Kiel Probe	Gage	100 psia (69 N/cm^2)	0.25% F.S.
PSGW1	Pressure-Static, Wall	Wall Tap	Gage	100 psia (69 N/cm^2)	0.25% F.S.
PSGW2	Pressure-Static, Wall	Wall Tap	Gage	100 psig (69 N/cm^2)	0.25% F.S.
PSGW11	Pressure-Static, Wall	Wall Tap	Gage	100 psig (69 N/cm^2)	0.25% F.S.
PSGW12	Pressure-Static, Wall	Wall Tap	Gage	100 psig (69 N/cm^2)	0.25% F.S.

Table 11. Performance Test Instrumentation (Continued)

Symbol	Parameter	Sensor	Readout	Range	Max Error
PSGW13	Pressure-Static, Wall	Wall Tap	Gage	100 psig (69 N/cm^2)	0.25% F.S.
PSGW14	Pressure-Static, Wall	Wall Tap	Gage	100 psig (69 N/cm^2)	0.25% F.S.
PSGW15	Pressure-Static, Wall	Wall Tap	Gage	100 psig (69 N/cm^2)	0.25% F.S.
PSG1J	Pressure-Static, Inlet Trav.	Wedge Probe	Gage	100 psia (69 N/cm^2)	0.25% F.S.
PTG1J	Pressure-Total, Inlet Trav.	Wedge Probe	Gage	100 psia (69 N/cm^2)	0.25% F.S.
PSG2J	Pressure-Static, Exit Trav.	Wedge Probe	Gage	160 psia (110 N/cm^2)	0.25% F.S.
PTG2J	Pressure-Total, Exit Trav.	Wedge Probe	Gage	160 psia (110 N/cm^2)	0.25% F.S.
*QAB1J	Pressure-Dynamic, Inlet Trav.	Wedge Probe	Transducer, VTVM	15 psid (10 N/cm^2)	0.20% F.S.
*QAB2J	Pressure-Dynamic, Exit Trav.	Wedge Probe	Transducer, VTVM	25 psid (17 N/cm^2)	0.20% F.S.
BAB1J	Flow Angle-Inlet Trav.	Wedge Probe	Vernier	360° (6.3 rad)	0.5° (0.09 rad)
BAB2J	Flow Angle-Exit Trav.	Wedge Probe	Vernier	360° (6.3 rad)	0.5° (0.09 rad)

*Used on Third Performance Tests Only

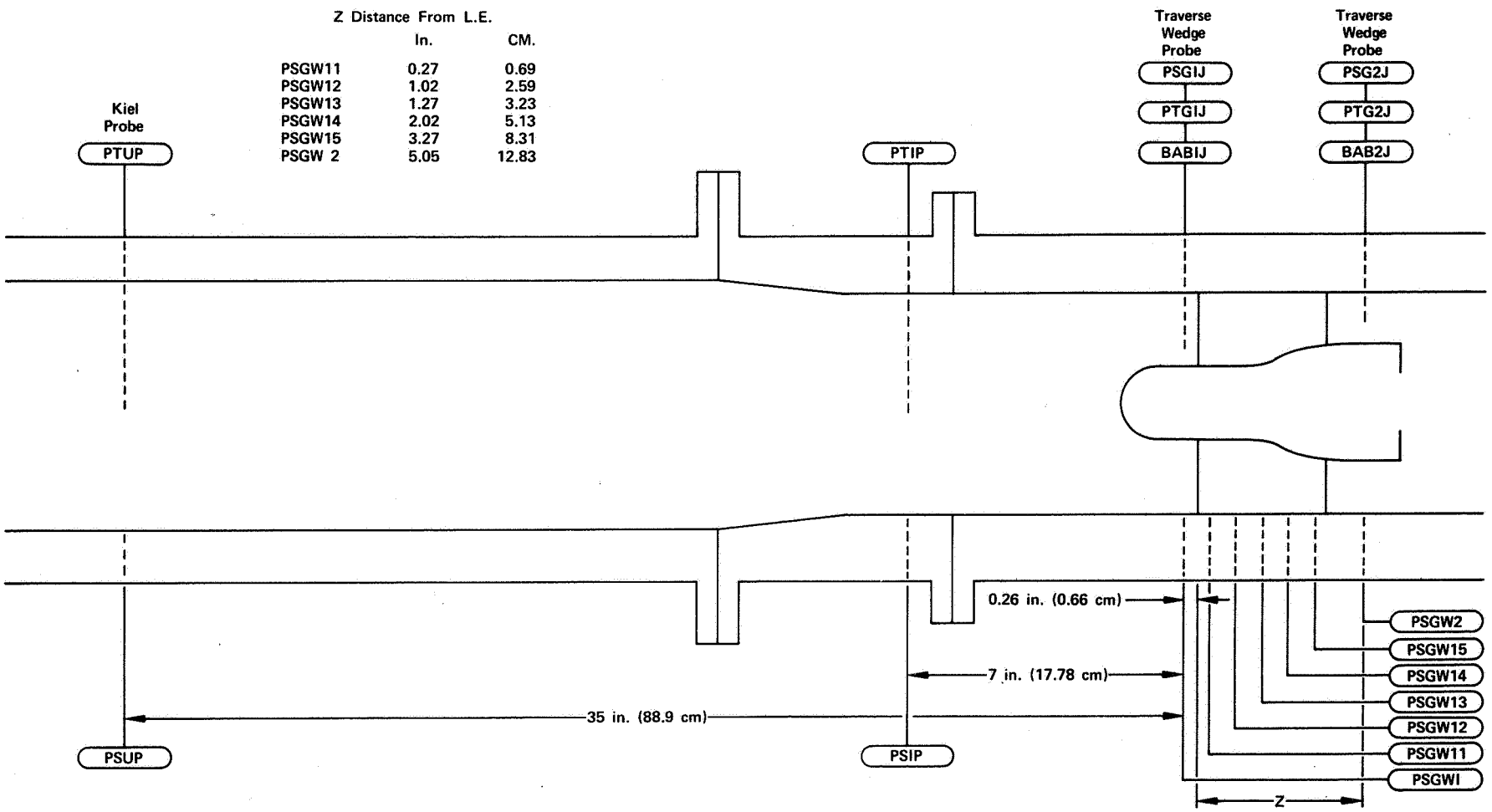

Figure 65. Performance Pressure Instrumentation Locations

FD 48166

(2) Blade and Hub Pressures

The pressure scanning valve, miniature transducers and piezoelectric transducers which were designed into the inducer rig in Task III were installed for the pressure distribution tests. In addition, inducer inlet and discharge pressure transducers were added so that data from these two parameters were suitable for tape recording and automatic data reduction. A summary of instrumentation added for these tests is given in table 12.

As shown in the table, pressure scanning valve, miniature transducer piezoelectric transducer, and inlet and discharge pressure transducers were recorded on an FM tape recorder. The pressure scanning valve data and inlet and discharge pressure data were recorded to permit automatic digital calculation of operating conditions and blade head coefficients directly from the tape recording. The miniature and piezoelectric transducer data were recorded to permit dynamic analysis of their signals.

The No. 1 inducer was reworked to install instrumentation for the pressure tests as follows: 0.049 in. (0.124 cm) deep by 0.049 in. wide radial grooves were cut in the pressure and suction surfaces of the blades at each pressure tap location by electron discharge machining (EDM), as shown in figure 66. The same size holes were drilled by EDM through the hub at the end of each groove. Stainless steel tubing, 0.040 in. (0.102 cm) in diameter, was layed in the grooves and routed through the hub and forward to the front flange of the inducer. The tubes were held in place and the blade surface faired with epoxy cement. Pressure taps were added to the tubes at the desired radial locations by EDM.

Grooves were also machined in the blade surface for installation of the miniature transducers, as shown in figure 66. The transducers were cemented in the grooves and their leads routed through holes in the inducer hub. The leads were connected to the transducer temperature compensation modules which were fastened to the inducer bore. The modules served to prevent excessive transducer drift with temperature changes. Figure 67 shows the modules mounted inside the inducer. Leads from the modules were routed down the drive shaft to the slip ring. Figure 68 shows an exploded view of the inducer, scanning valve and related hardware. Figure 69 shows the inducer installed in the test rig and the blade pressure taps connected to the scanning valve with nylon tubing. The test rig with the inducer and slip ring installed is shown in figure 70.

Table 12. Pressure Test Instrumentation

Symbol	Parameter	Sensor	Readout	Range	Max Error
PTUP	Pressure-Total, Upstream	Kiel Probe, S.G. Transducer	Gage and Tape(1)	100 psia ($69\ N/cm^2$)	3% F.S.
PTG2J	Pressure-Total, Exit	Wedge Probe, S.G. Transducer	Gage and Tape(1)	150 psia ($103\ N/cm^2$)	3% F.S.
PVW11	Pressure-Vibratory, Wall	Piezoelectric Transducer	Tape	150 psi @ 1000 Hz ($103\ N/cm^2$)	
PVW12	Pressure-Vibratory, Wall	Peizoelectric Transducer	Tape	150 psi @ 1000 Hz ($103\ N/cm^2$)	
PVB 1	Pressure-Vibratory, Blade	S.G. Transducer	Tape	150 psia @ 100 Hz ($103\ N/cm^2$)	(2)
PVB 2	Pressure-Vibratory, Blade	S.G. Transducer	Tape	150 psia @ 100 Hz ($103\ N/cm^2$)	(2)
PVB 3	Pressure-Vibratory, Blade	S.G. Transducer	Tape	150 psia @ 100 Hz ($103\ N/cm^2$)	(2)
PVB 4	Pressure-Vibratory, Blade	S.G. Transducer	Tape	150 psia @ 100 Hz ($103\ N/cm^2$)	(2)

Table 12. Pressure Test Instrumentation (Continued)

Symbol	Parameter	Sensor	Readout	Range	Max Error
PVB 5	Pressure-Vibratory, Blade	S.G. Transducer	Tape	150 psia @ 100 Hz ($103\ N/cm^2$)	(2)
PVB 6	Pressure-Vibratory, Blade	S.G. Transducer	Tape	150 psia @ 100 Hz ($103\ N/cm^2$)	(2)
PO-47	Pressure-Static, Blade	Press. Scan. Valve, S.G. Transducer	Tape	150 psia ($103\ N/cm^2$)	3% F.S.
PSBP	Position-Press. Scan Valve	Potentiometer	Tape	48	-
BDRP	Data Recording Pulse		Tape	--	-

(1) Range and error are for tape recorded data.

(2) Error estimate not available because of lack of rotating calibration information.

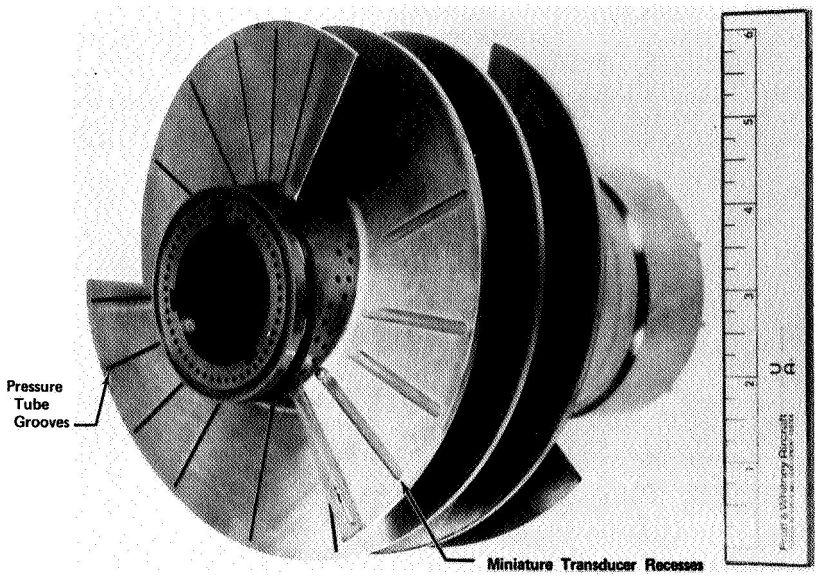

Figure 66. View of Inducer After Machining and Before Installation of Pressure Tubing FE 88107

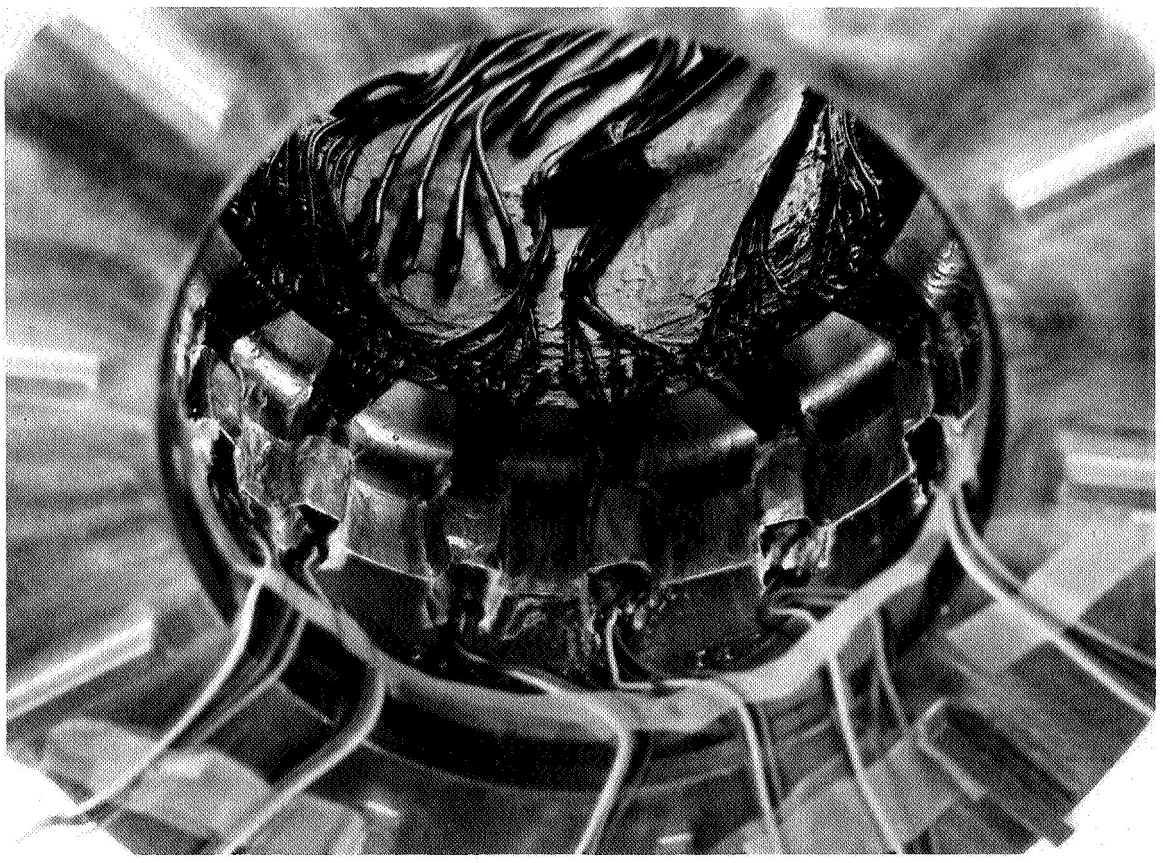

Figure 67. View of Temperature Compensation Modules in Inducer Hub FE 89905

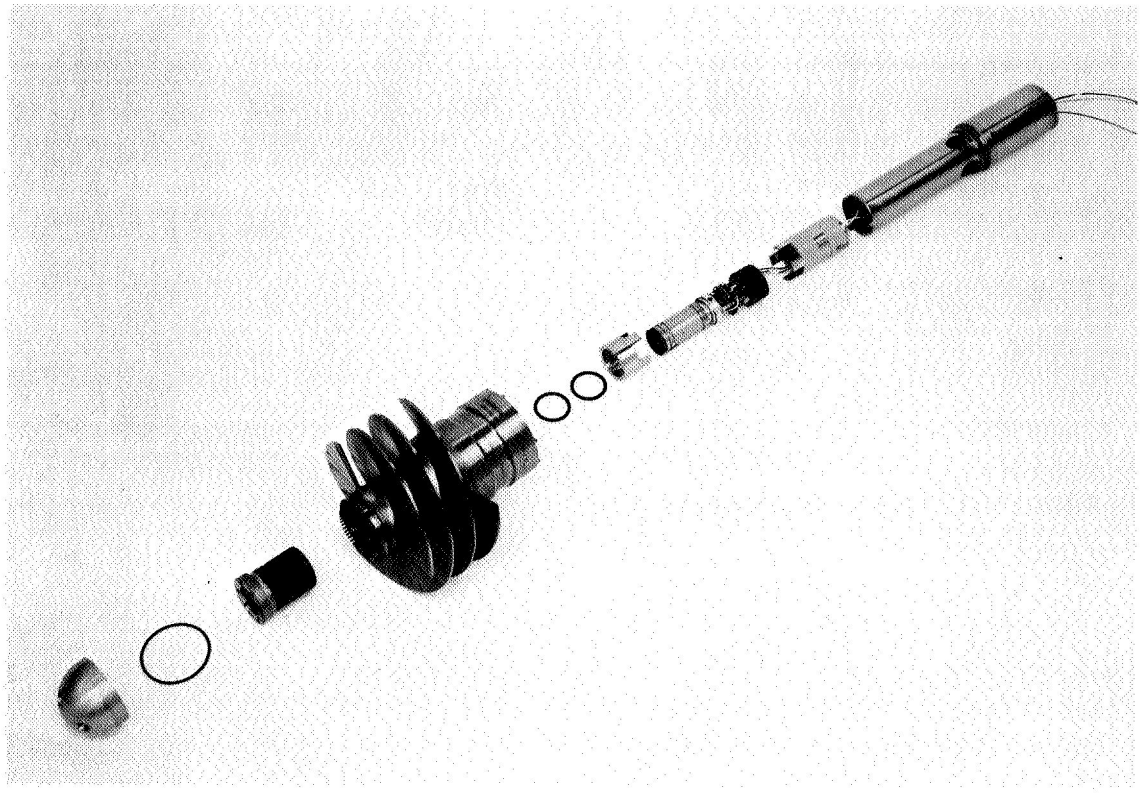

Figure 68. Exploded View of Inducer and Pressure Scanning Valve FE 94088

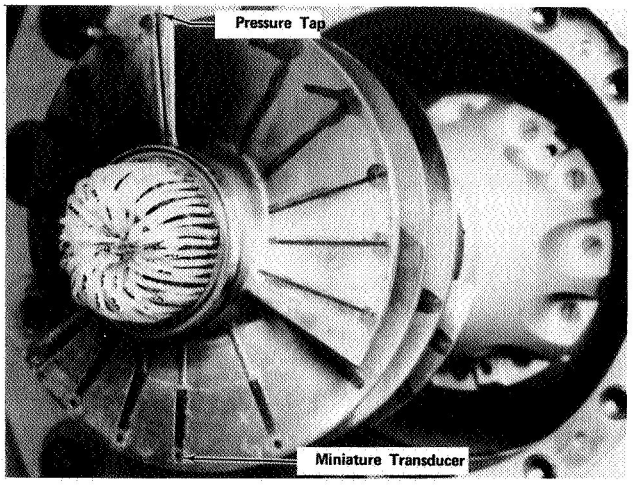

Figure 69. View of Inducer Installed in Test Rig FD 89238

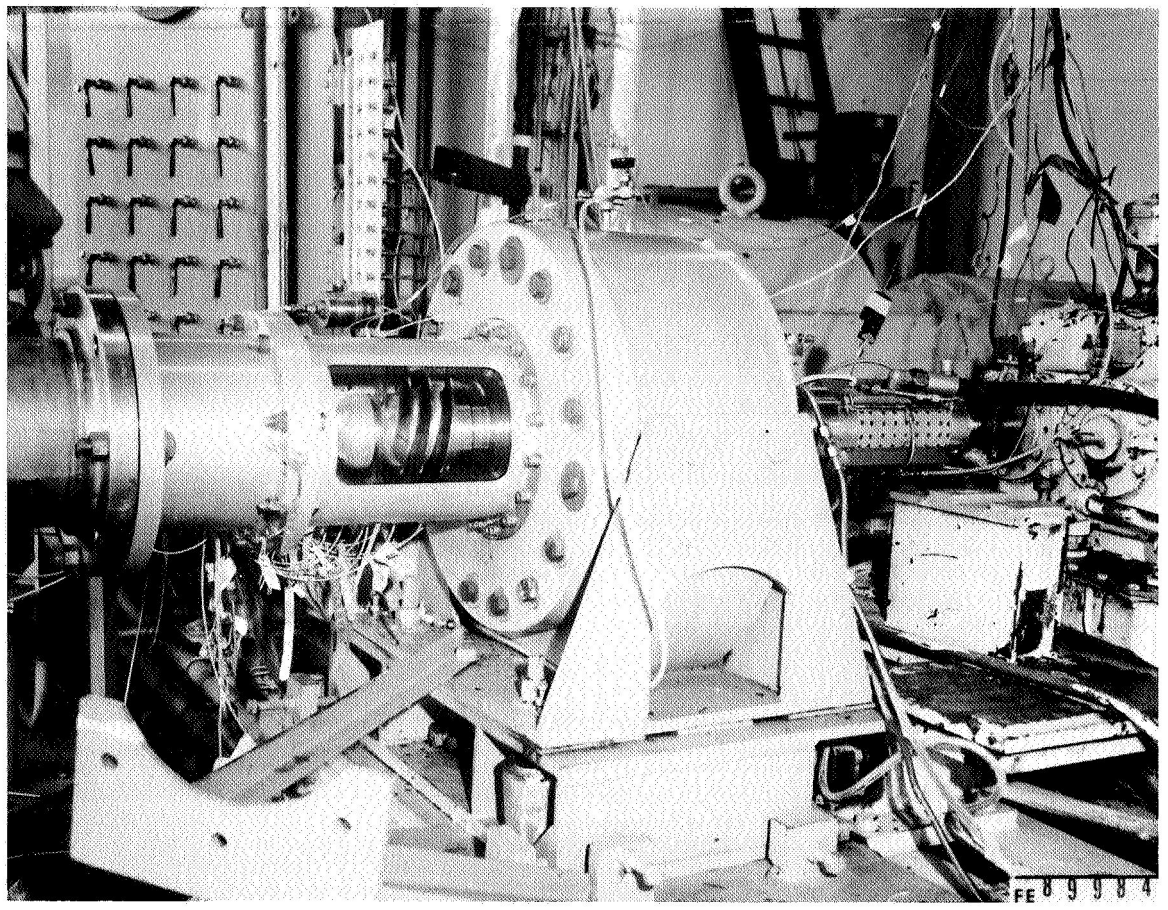

Figure 70. Overall View of Test Rig FE 89984

(3) Blade Strains

The three-element strain gage rosettes installed on inducer No. 2 for the static load and vibration tests were waterproofed and used for the operational strain tests. Gages at modes 4, 6, and 8 failed during inducer installation and checkout and were replaced by the spare gages at modes 1 and 13 before the tests were started. The strain gaged inducer after preparation for operational testing is shown in figure 71.

Static strains were read from an SR4 readout and vibratory strains were recorded on an oscillograph.

c. Test Procedure

The following procedures were followed in performing the operational tests.

Figure 71. View of Strain Gaged Inducer Prior to Test FE 88475

(1) Performance

Noncavitating performance tests were conducted by setting a speed, flow and inlet pressure and manually traversing the flow at the inducer inlet and exit. Total pressure, static pressure and flow angle were measured at each of seven radial stations (spaced at equal area increments) and all other instrumentation were recorded.

A flow restrictor screen was installed in the inducer inlet line to reduce inlet pressure for the cavitating tests. These tests were conducted by setting a speed and flow and reducing inlet pressure in approximately 10 steps until inducer pressure rise dropped by approximately ten percent. A complete set of data were manually recorded at each inlet pressure setting. Inlet total pressure was measured from the upstream Kiel probe and the inlet traverse probe was removed for the cavitating tests.

The exit traverse probe was set at the radial traverse station which was most representative of mass averaged exit total head. The station at a radius of 3.02 in. (7.66 cm) was found to meet the criteria for all flow coefficients tested. This station was just outside the root mean square radius measurement station.

(2) Strain

Noncavitating and cavitating strain tests were conducted in the same manner as performance tests except that no traverse data were taken. The inlet traverse probe was removed and the exit probe was set at the representative radius for all test points. Noncavitating data were taken at three flow coefficients (0.096, 0.090, and 0.084) and cavitating data were taken at three inlet pressures. At each test point, performance instrumentation was manually recorded, steady strains were read from an SR4 readout, and vibratory strain signals were recorded on an oscillograph at a paper speed of 40 in./sec (1.02 m/s).

(3) Pressure

Pressure test data were also taken with the inlet traverse probe removed and the exit probe set at the representative station. Two series of pressure tests were conducted; one with each of the two sets of pressure taps shown in figure 55. The first tests were conducted with the set of pressure taps near the inducer tip. After completion of these tests, the inducer was removed, the tip pressure taps were sealed with epoxy cement, and new taps were installed at the inner radius. The inducer was then reinstalled in the test loop and its taps were connected to the pressure scanning valve.

Cavitating data were taken at the same speed and flow as in the previous tests. However, it was difficult to maintain the same inlet pressure for the fully cavitating conditions because of increased pressure drop across the inlet screen caused by partial blockage with ipoxy particles from the inducer and other particles from the loop loosened by cavitation.

Pressure tests were conducted by setting the test point conditions (speed, flow, and inlet pressure), applying purge air pressure to the pressure scanning valve, starting the tape recorder (7-1/2 in./sec; 19 cm/s record speed)and then starting the pressure scanning valve. The valve automatically made one complete revolution, at approximately 1 port per second, while the recorder continuously recorded valve signals and inducer upstream and downstream pressures. The valve was stepped and controlled during tests by an off-the-shelf solenoid controller.* The standard valve had a cam operated switch on the valve to interrupt solenoid power. This switch was thought unreliable for rotating operation and a vendor designed circuit was used to bypass the cam switch and electrically interrupt solenoid power. An additional company furnished circuit was used to time and count the valve step pulses and to stop when the valve reached port #0. This circuit also generated a data signal 0.045 seconds before each valve step. Valve purge pressure was

*Scanivalve Company - San Diego, Calif. Model CLTR S2-S6

set as high as possible, within valve limits, to ensure that no blade pressure data were lost because of water entering the tap line. The valve operating limits were 100 psia (69 N/cm^2) maximum case pressure and 60 psid (41 N/cm^2) maximum case to sensing port differential. Purge pressure was therefore set at 75-80 psig (52-55 N/cm^2) for noncavitating and 45-50 psig (31-35 N/cm^2) for cavitating tests.

d. Data Reduction

(1) Performance

Performance data were calculated from manually recorded pressure, temperature, flow, rotative speed, and flow angle using the equations in table 13. Measured pressures were corrected for gage height and traverse probe static pressure measurements were corrected for probe error before fluid heads were calculated.

Table 13. Performance Data Reduction Equations

A. Blade Element Performance

Fluid Velocity: $V = \sqrt{2g(H_{i,j} - h_{i,j})}$

Fluid Axial Velocity: $V_z = V \sin \alpha$

Fluid Tangential Velocity: $V_u = V \cos \alpha$

Ideal Head Rise: $HI = \frac{U_e V_u \ell}{g}$ (Assumes $V_{uo} = 0$)

Actual Head Rise: $H = \frac{1}{\rho} P_T - H_o$

Head Rise Coefficient: $\psi = \frac{g}{\rho} \frac{\Delta P_T}{U_T^2}$

Flow Coefficient: $\phi = \frac{V_z}{U_T}$

Efficiency: $\eta = \frac{H}{HI}$

Net Positive Suction Head: $NPSH = H_o - h_v$

B. Overall Performance

Average Total Head at an Axial Station: $\left(\overline{\frac{P_T}{\rho}}\right)_j = \frac{\sum_{R_H}^{R_T} V_z R \frac{P_T}{\rho} \Delta R}{\sum_{R_H}^{R_T} V_z R \Delta R}$

Table 13. Performance Data Reduction Equations (Continued)

Average Ideal Head at an Axial Station: $\bar{HI}_j = \dfrac{\sum_{R_H}^{R_T} V_z R \frac{U V_u}{g} \Delta R}{\sum_{R_H}^{R_T} V_z R \Delta R}$

Average Inlet Velocity: $\bar{V}_{zo} = \dfrac{Q}{\pi(R_T^2 - R_H^2)}$

Average Flow Coefficient: $\bar{\phi} = \dfrac{\bar{V}_{zo}}{U_T}$

Average Head Coefficient: $\bar{\psi} = \dfrac{g\bar{H}}{U_T^2}$

Average Efficiency: $\bar{\eta} = \dfrac{\bar{H}}{\bar{HI}}$

Average Inlet Static Head: $\bar{h} = \bar{H}_o - \dfrac{\bar{V}_z^2}{2g}$

Cavitation Number: $\bar{K} = \dfrac{2g(h_o - h_v)}{\bar{V}_{zo}^2 + U_T^2}$

Static Head Coefficient: $\psi_s = \dfrac{g(h - H)}{U_T^2}$

An indication of the overall accuracy of the data is given by figure 72 where the relative error of integrated to measured flow at the exit measurement station is shown as a function of flow coefficient. The agreement is good with errors generally within 10%. The final performance data taken at clearance/blade height of 0.0052 shows agreement within 1%. Data was much less accurate at the inlet, however, with errors ranging to 35%. This level was not suitable for input to the blade loading calculations. It was found that increasing each inlet total pressure reading by 0.5 times the indicated dynamic pressure yielded integrated total flow agreement within 15% and total head agreement within 4%. This adjustment was made to the final performance data.

(3) Pressure

Inducer pressure distribution data were automatically reduced from the FM data tapes. Pressure scanning valve, inlet, and discharge pressure signals were converted from FM to digital form and reduced on a digital computer using the equations in table 13. Manually recorded values of flow, temperature, barometer, and rotative speed were input to the program for calculation of dimensionless parameters.

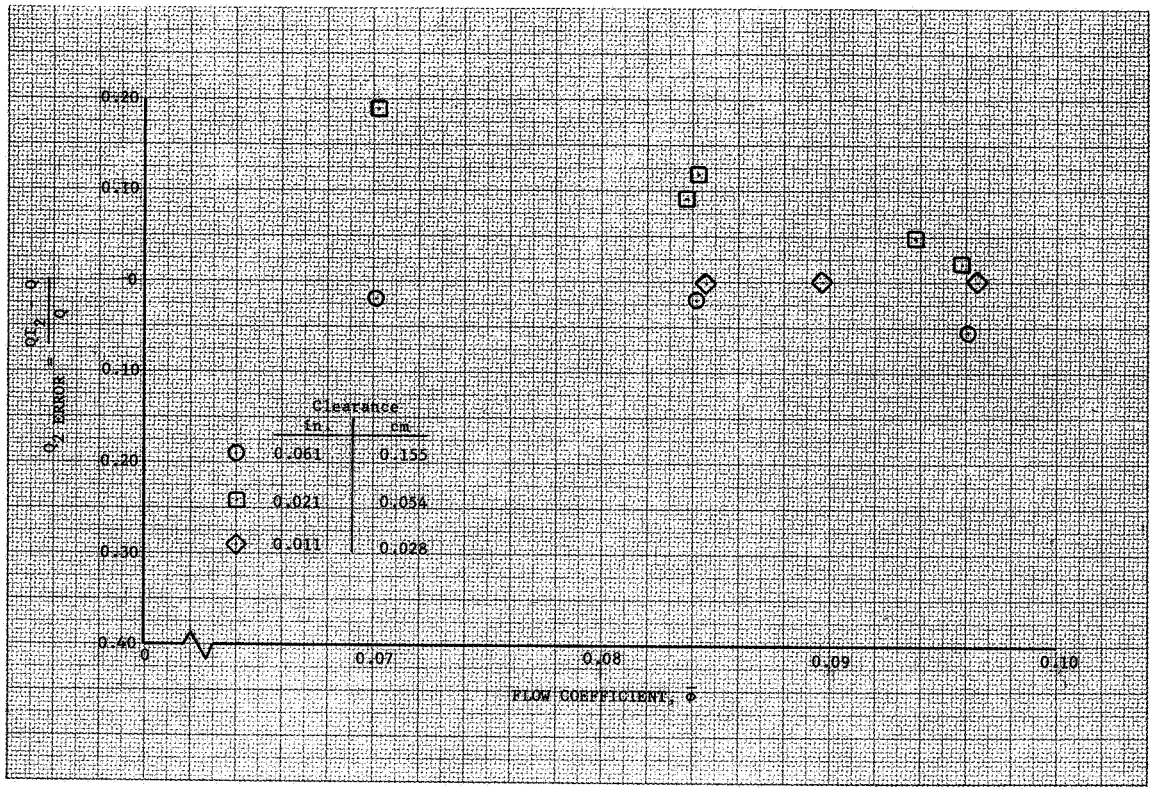

Figure 72. Comparison of Integrated and Flowmeter Measured Flow at Rotor Exit DF 85011

An indication of the accuracy of the overall data reduction process was obtained by comparing manually recorded inlet and discharge pressures (from precision gages) with the processed values from the FM tape. The data were in agreement within 2 psi (1.38 N/cm^2) at the inlet and 3 psi (2.09 N/cm^2) at the discharge, or within 3% of full scale recorded range for each parameter. The pressure scanning valve sensed ambient and approximate purge pressures once each revolution and these measurements were compared with independently measured values for an indication of accuracy. This comparison also gave agreement within 3% of transducer full scale, indicating that the accuracy of recorded parameter measurement was within ±3%.

Amplitude-frequency data from the blade mounted transducers and the housing mounted piezoelectric transducers were reduced from the FM tape with a narrow band spectrum analyzer. The analyzer automatically plotted pressure amplitude versus frequency for each test point.

(2) Strain

Steady and vibratory strain readings for the three gages in each rosette were used to calculate effective stress at each element using equations in table 7. Steady strains were read directly from an SR4 readout. Vibratory strain amplitude and frequency were measured from

oscillograph traces by measuring peak-to-peak amplitude of the oscillations and counting oscillation frequency. The strains, calculated resultant stresses, and frequencies therefore cannot be considered exact but give close approximations of the actual values.

e. Test Results

The results of the operational tests are presented in the following paragraphs.

(1) Performance Tests

(a) Noncavitating

The performance tests conducted on the inducer are summarized in table 14. It will be noted in the table that three series of performance tests were run, each with a different inducer blade-tip to housing clearance. Performance tests were conducted at tip speeds of 150 ft/sec (45.6 m/s) and 120 ft/sec (36.6 m/s) and since the data at the two speeds were in agreement, only the higher speed data are discussed. Only a limited performance evaluation had been planned in the original test program. However, data from the first test series, taken with the tip clearance of 0.061 in. (0.155 cm), showed a large amount of inlet prerotation to the point of reverse flow near the inducer tip. The inlet flow angle distribution for these tests is shown in figure 73. As shown, reverse flow was noted for the 80, 100, and 120% of design flow ($\bar{\phi}_o$ = 0.056, 0.070, 0.084) conditions and prerotation to the point of reverse flow was noted at the maximum facility flow ($\bar{\phi}_o$ = 0.096).

The reverse flow noted at the inducer inlet implies a stagnation point within the inducer. Such a stagnation point cannot be predicted by the two-dimensional, meridional streamline analysis used in the hydrodynamic computer program, and the program cannot accurately predict blade loadings when such a point exists. A three-dimensional analysis could predict stagnation and reverse flow but this type of analysis was evaluated and rejected during Task I because of excessive computing time requirements. It was decided that the two-dimensional analysis should be retained and that the test inducer or inlet configuration should be modified to eliminate the reverse flow before additional tests were conducted.

A study was therefore performed to identify the feature or features of the inducer which were causing the reverse flow. The study consisted of: (1) an empirical correlation of various inducer geometrys and inlet flow profiles, and (2) a potential flow analysis of the inlet. This study is described in the following paragraphs.

Table 14. Summary of Performance Tests

Test No.	Speed rpm	Speed rad/s	Flow gpm	Flow cm^3/s	Inlet Total Pressure psig	Inlet Total Pressure N/cm^2	Temperature °F	Temperature °K
Tip Clearance = 0.061 in. (0.155 cm)								
1.01	3920	410.5	1020	64360	30.0	20.7	80	299.7
1.02	3920	410.5	848	53510	30.0	20.7	83	301.3
1.03	3920	410.5	679	42840	30.0	20.7	85	302.4
1.04	4900	513.1	1272	80260	30.0	20.7	87	303.6
1.05	4900	513.1	1060	66890	30.0	20.7	89	304.7
1.06	4900	513.1	848	53510	30.0	20.7	90	305.2
1.07	4900	513.1	1060	66890	14.7	10.1	89	304.7
	4900	513.1	1060	66890	5.7	3.9	90	305.2
	4900	513.1	1060	66890	0.8	0.6	91	305.8
	4900	513.1	1060	66890	-2.0	-1.4	91	305.8
	4900	513.1	1060	66890	-3.4	-2.3	91	305.8
	4900	513.1	1060	66890	-5.8	-4.0	91	305.8
	4900	513.1	1060	66890	-9.0	-6.2	91	305.8
	4900	513.1	1060	66890	-9.5	-6.6	90	305.2
1.08	4900	513.1	848	53510	14.0	9.7	91	305.8
	4900	513.1	848	53510	5.8	4.0	93	306.9
	4900	513.1	848	53510	0.8	0.6	94	307.4
	4900	513.1	848	53510	-3.6	-2.5	95	308.0
	4900	513.1	848	53510	-5.0	-3.5	95	308.0
	4900	513.1	848	53510	-5.5	-4.0	94	307.4
	4900	513.1	848	53510	-6.3	-4.3	94	307.4
	4900	513.1	848	53510	-7.8	-5.4	94	307.4
	4900	513.1	848	53510	-8.0	-5.5	95	308.0
	4900	513.1	848	53510	-9,8	-6.8	95	308.0

Table 14. Summary of Performance Tests (Continued)

Test No.	Speed rpm	Speed rad/s	Flow gpm	Flow cm^3/s	Inlet Total Pressure psig	Inlet Total Pressure N/cm^2	Temperature °F	Temperature °K
1.09	4900	513.1	1272	80260	15.2	10.5	88	304.1
	4900	513.1	1272	80260	5.2	3.6	90	305.2
	4900	513.1	1272	80260	0.3	0.2	90	305.2
	4900	513.1	1272	80260	-1.3	-0.9	90	305.2
	4900	513.1	1272	80260	-2.4	-1.7	90	305.2
	4900	513.1	1272	80260	-4.0	-2.8	90	305.2
	4900	513.1	1272	80260	-5.7	-3.9	93	306.9
	4900	513.1	1272	80260	-6.1	-4.2	94	307.4
	4900	513.1	1272	80260	15.9	11.0	85	302.4
	4900	513.1	1272	80260	1.1	0.8	87	303.6
	4900	513.1	1272	80260	-3.2	-2.2	90	305.2
	4900	513.1	1272	80260	-0.5	-0.3	90	305.2
	4900	513.1	1272	80260	16.0	1.0	84	301.9
	4900	513.1	1272	80260	0.0	0.0	86	303.0
	4900	513.1	1272	80260	-4.5	-3.1	87	303.6
	4900	513.1	1272	80260	-6.0	-4.1	88	304.1
	4900	513.1	1272	80260	-7.0	-4.8	88	304.1
1.10	4900	513.1	1450	91500	30.0	20.7	79	299.1
1.11	4900	513.1	848	53510	30.0	20.7	88	304.1
Tip Clearance = 0.021 in. (0.054 cm)								
2.02	4900	513.1	1450	91500	30.1	20.8	94	307.4
2.03	4900	513.1	1272	80260	30.5	21.0	95	308.0
2.04	4900	513.1	1060	66890	30.4	21.0	97	309.1
2.05	3920	513.1	848	53510	30.3	20.9	92	306.3

Table 14. Summary of Performance Tests (Continued)

Test No.	Speed rpm	Speed rad/s	Flow gpm	Flow cm^3/s	Inlet Total Pressure psig	Inlet Total Pressure N/cm^2	Temperature °F	Temperature °K
2.06	4900	513.1	1060	66890	35.4	17.5	86.5	303.3
	4900	513.1	1060	66890	14.2	9.8	92	306.3
	4900	513.1	1060	66890	4.8	3.3	94	307.4
	4900	513.1	1060	66890	0.0	0.0	95.5	308.3
	4900	513.1	1060	66890	-1.4	-1.0	96	308.6
	4900	513.1	1060	66890	-2.9	-2.0	96.5	308.9
	4900	513.1	1060	66890	-4.2	-2.9	97	309.1
	4900	513.1	1060	66890	-5.2	-3.6	97.5	309.4
2.07	4900	513.1	1272	80260	24.8	17.1	93.5	307.2
	4900	513.1	1272	80260	15.6	10.8	94.5	307.7
	4900	513.1	1272	80260	3.5	2.4	95	308.0
	4900	513.1	1272	80260	-1.0	-0.7	95.5	308.3
	4900	513.1	1272	80260	-0.7	-0.5	95.5	308.3
2.09	4900	513.1	1272	80260	30.0	20.7	92	306.3
2.10	4900	513.1	1272	80260	30.0	20.7	92	306.3
2.11	5500	580.0	1428	90110	30.0	20.7	100	310.8
2.12	4900	513.1	1417	89410	30.1	10.8	87	303.6
2.13	5200	554.5	1500	94650	30.0	20.7	93	306.9
Tip Clearance = 0.011 in. (0.028 cm)								
4.07	4900	513.1	1458	92000	30.0	20.7	75	296.9
4.08	4900	513.1	1358	85690	30.1	20.8	79	299.1
4.09	4900	513.1	1280	80770	30.1	20.8	81.5	300.5

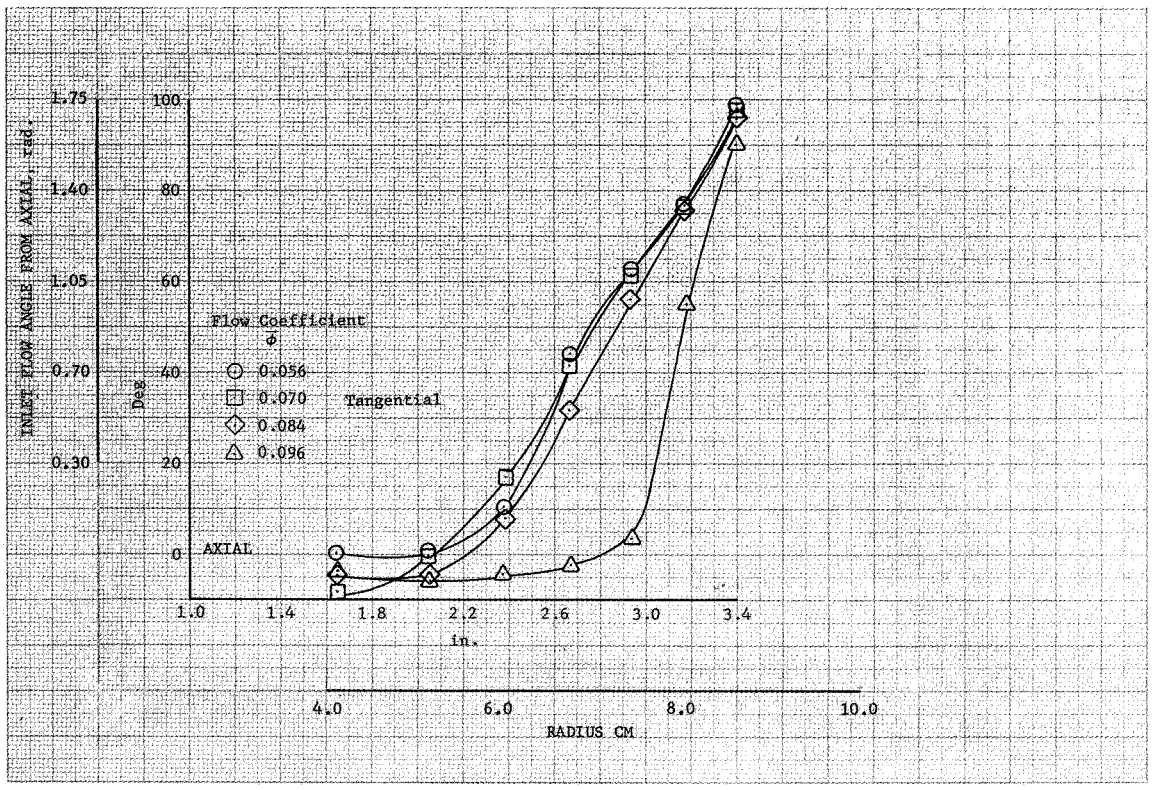

Figure 73. Radial Distribution of Inlet Flow Angle C = 0.061 in. (0.155 cm) DF 72464

1 Empirical Correlations

From the recorded results of inlet traverse measurements, the critical inlet flow coefficients, ϕ_{crit} (below which significant backflow occurred), were determined for three helical inducers with blade tip angles of 6, 9.4, and 12 deg (0.10, 0.16, and 0.21 rad) which had been tested by NASA-LeRC (References 16, 21, and 22). These values were plotted against blade tip angle and are shown in figure 74. An additional value for a 12 deg (0.21 rad) helical inducer is also available from tests performed by Acosta (Reference 23). The inlet backflow was determined visually by Acosta through the use of tufts. The value of ϕ_{crit} was bracketed by observing a range of flow coefficients in which the tufts reversed axial orientation. The value of ϕ_{crit} for the P&WA test inducer is also plotted in figure 74.

Examination of the plotted data shows that P&WA test results indicated a more severe backflow problem (i.e., backflow occurs at a higher $\bar{\phi}$) than that which occurred in the tests conducted by NASA-LeRC or Acosta. A comparison of significant variables for the inducers is given in table 15. The only parameter that showed a variation consistent with the trend in reduced ϕ_{crit} was tip clearance leakage. This is indicated by the level of leakage area ratio, which was smallest for the Acosta inducer and largest for the P&WA inducer. A reduction in tip clearance was therefore indicated by the empirical correlation as a method of reducing reverse flow.

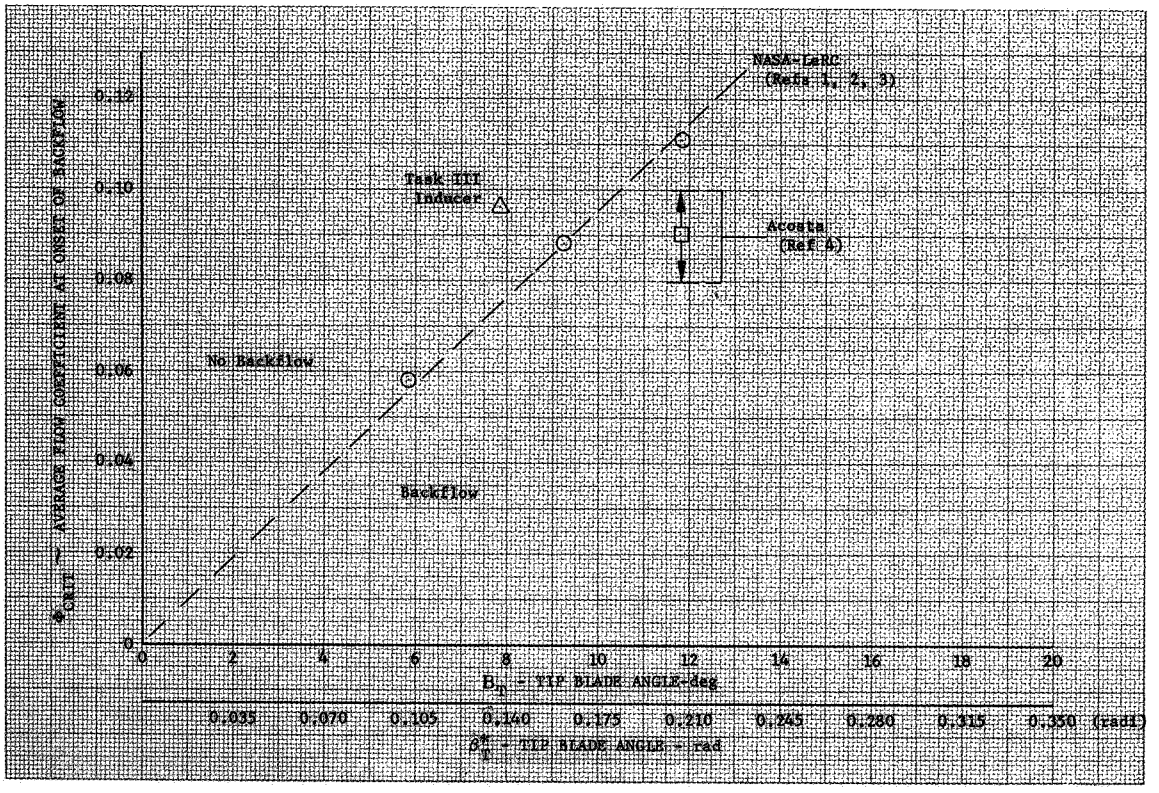

Figure 74. Critical Flow Coefficient vs Tip Blade Angle DF 85010

2 Potential Flow Analysis

A two-dimensional analysis of the potential flow at the inducer inlet was also made to further define the reverse flow problem. The analysis involved solving for the average inlet flow coefficient at which the axial velocity at the tip was equal to zero. For flow coefficients below this value (ϕ_{crit}), backflow would be predicted simply from potential flow considerations. Additional real effects, such as viscous forces, tip clearance leakage, boundary layer separation, and three-dimensional effects could cause the actual critical flow coefficient to be higher or lower than the value predicted by simplified analysis. However, this analysis did allow the determination of the effects of hub/tip ratio on the potential flow. It also gave some indication of the effect of possible boundary layer separation from the blade leading edge due to a relatively blunt leading edge shape.

The analysis was based on the following assumptions:

1. The flow conditions far upstream are uniform
2. No preswirl upstream of the inducer leading edge
3. Inviscid flow
4. No loss in relative total pressure

Table 15. Comparison of Task III, Acosta, and NASA Series Inducers

Inducer(s)	Tip Radius in.	Tip Radius cm	Hub/Tip Ratio	Tip Blade Angle deg	Tip Blade Angle rad	Upstream Geometry	*Leading Edge Profile	Tip Leakage Clearance, C in.	Tip Leakage Clearance, C cm	Tip Leakage Clearance Ratio**	Tip Leakage Area*** Ratio
NASA Series	2.50	6.35	0.50	6.0	0.10	Stationary Hub	0.600	0.025	0.063	0.020	0.0267
				9.4	0.16		0.554	0.030	0.076	0.024	0.0320
				12.0	0.21		0.433	0.030	0.076	0.024	0.0320
Acosta	1.00	2.54	0.50	12.0	0.21	Stationary Hub	0.833	0.002	0.005	0.004	0.0053
PWA	3.50	8.89	0.40	8.0	0.14	Rotating Nose Cone	1.000	0.061	0.155	0.0286	0.0410

*Ratio of Tip Leading Edge Wedge Angle to Blade Inlet Metal Angle
**Tip Clearance to Blade Height Ratio
***Leakage Area to Inlet Area Ratio

5. The relative fluid angle is discontinuous in the axial direction at the inducer leading edge and equals the blade angle just downstream of the leading edge

6. The static pressure and axial velocity are continuous everywhere.

The results of the analysis indicated that the value of ϕ_{crit} for the test inducer varies with blade tip angle and hub/tip ratio, as shown in figure 75. It can be seen that the predicted level and variation of ϕ_{crit} with blade angle are consistent with the test data.

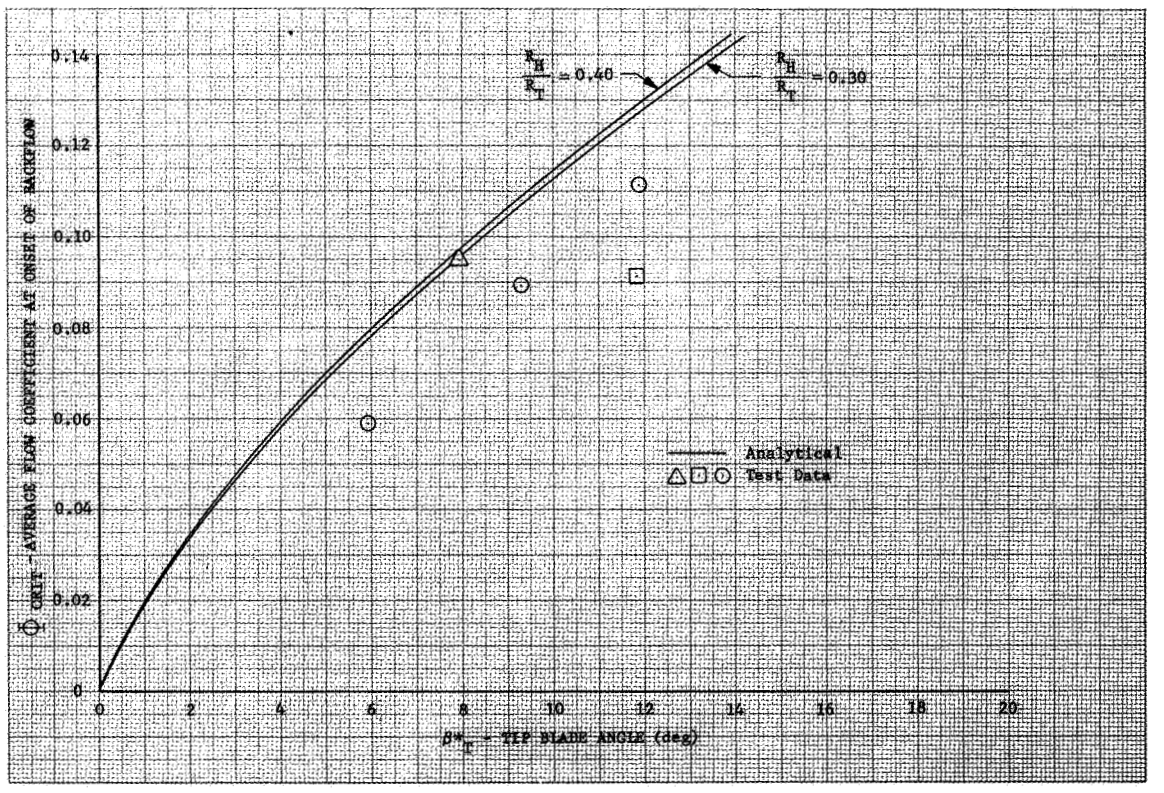

Figure 75. Predicted Critical Flow Coefficient Based on Potential Flow Theory DF 72466

The analysis was used to evaluate the effects of hub/tip ratio (Λ), leading edge fairing, upstream inlet configuration, and tip clearance on reverse flow. Hub/tip ratio was shown to have very little effect on the value of ϕ_{crit} (figure 75). If the flow at the PWA inducer leading edge had separated from the blade suction surface because of the relatively blunt leading edge configuration, the pressure gradient should be reduced due to increased fluid angle and higher axial velocity. This would allow the inducer to operate to a lower value of ϕ_{crit} rather than higher, indicating that leading edge fairing was not a factor.

The NASA and Acosta inducer test rigs both had a continuous stationary hub located in the inlet section, whereas the PWA inducer has a short rotating nose cone. It was possible that this contributed to the higher value of ϕ_{crit} obtained in our testing. However, the potential flow analysis indicated that the short hub section on the nose cone is long enough to diminish any leading edge effects before they reach upstream to a point where the flow area is increased by the absence of a hub. Also, since both the NASA and Acosta inducers had the stationary hub upstream, this effect could not be responsible for the difference between the backflow characteristic of these inducers.

The single difference in the configurations that was consistent with the test results was the difference in the tip leakage area ratio. The area (A_ℓ) available for the backflow of tip leakage is given by

$$A_\ell = 2\pi R_T C$$

where

R_T = tip radius

C = tip clearance

The area (A) available for the delivered flow is

$$A = \pi R_T^2 (1 - \Lambda^2)$$

where

$$\Lambda = R_H/R_T$$

Therefore, the area ratio is

$$\frac{A_\ell}{A} = \frac{2\pi R_T C}{\pi R_T^2 (1 - \Lambda^2)} = \frac{2\left(C/R_T\right)}{1 - \Lambda^2}$$

The average velocity ($\overline{V}_z$) of the delivered flow is

$$\overline{V}_z = \overline{\phi}\, U_T$$

where

$\overline{\phi}$ = average flow coefficient

U_T = tip speed

If it is assumed that the axial velocity (V_ℓ) of the tip leakage backflow is due to a static head differential, (Δh_s)

$$V_\ell = \sqrt{2\ g\ \Delta h_s}$$

and that this head differential is given by

$$\Delta h_s = \psi_s \frac{U_T^2}{g}$$

where

ψ_s = local static head coefficient

then the leakage velocity is given by

$$V_\ell = U_T \sqrt{2\ \psi_s}$$

It is probable that the ratio of leakage backflow volumetric flowrate to delivered flowrate (Q_ℓ/Q) is a significant leakage parameter in its effect on the onset of the mainstream backflow. Since the leakage backflow has obtained a tangential velocity, it increases the pressure gradient at the tip causing the axial velocity of the inlet flow at the tip to equal zero at a higher value of $\bar{\phi}$.

$$Q_\ell/Q = \left(\frac{V_\ell}{V_z}\right)\left(\frac{A_\ell}{A}\right)$$

or

$$Q_\ell/Q = \left(\frac{U_T\sqrt{2\psi_s}}{\bar{V}_z}\right) \frac{2\left(\frac{C}{R_T}\right)}{1 - \Lambda^2}$$

and, since $\bar{\phi} \equiv \bar{V}_z/U_T$

$$Q_\ell/Q = \frac{2\sqrt{2\psi_s}\left(\frac{C}{R_T}\right)}{\bar{\phi}\ (1 - \Lambda^2)}$$

For a given blade angle ψ_s is assumed to be a constant. In that case, for the same critical value of Q_ℓ/Q,

$$\bar{\phi}_{crit} \sim \frac{2\left(\frac{C}{R_T}\right)}{1 - \Lambda^2} = \frac{A_\ell}{A}.$$

This indicates that the volumetric leakage ratio will be the same at a flow coefficient that is proportional to the leakage area ratio. However, this analysis does not define the actual effect of leakage backflow on the potential flow. Therefore, the relative values of the A_ℓ/A should be used only for trends rather than for absolute levels. Thus, the values indicate that the Acosta inducer should have a value of $\overline{\phi}_{crit}$ lower than that obtained in the NASA inducer tests. Similarly, it indicates that the P&WA inducer would have a higher value of $\overline{\phi}_{crit}$ than that obtained for the NASA series of inducers. These predictions of trends, based on A_ℓ/A, were consistent with the test results and indicated that the P&WA inducer tip clearance should be reduced to reduce prerotation and reverse flow.

Based on these study results, the inducer tip clearance was reduced to 0.021 in. (0.054 cm) to eliminate reverse flow. The value of 0.021 was selected as a safe minimum consistent with test rig mechanical considerations. The reduction was accomplished by applying epoxy cement to the bore of the acrylic inducer housing and remachining to a smaller diameter. The radial distribution of inlet flow angle for this clearance is shown in figure 76. Reverse flow was essentially eliminated above a flow coefficient of 0.070 and prerotation was eliminated at the 0.096 flow coefficient. Prerotation was still significant at the 0.070 and 0.084 flow coefficients. These data were considered suitable for analysis by the hydrodynamic computer program but it was decided to conduct the remainder of the test program at flow coefficients of 0.084, 0.090, and 0.096 to provide data at three reasonably incremented flow coefficients in the area of least prerotation.

During these performance tests the bore of the inducer housing was damaged by cavitation and a new housing was fabricated for subsequent testing. The lack of mechanical problems with the 0.021 in. clearance housing encouraged a further reduction in tip clearance to further reduce prerotation. A new acrylic housing which provided a tip clearance of 0.011 in. (0.028 cm) was fabricated and used in all subsequent tests. The measured inlet flow angle, axial velocity, and total head profiles for this tip clearance are also shown in figure 76. As expected, the smaller tip clearance did result in a reduction in prerotation.

Overall noncavitating performance for the 0.011 in. tip clearance tests is shown in figure 77. These results were obtained from a series of three traverse tests at the flow coefficients to be used for blade pressure and strain distribution tests. The measured radial distribution of discharge flow parameters is shown in figure 78. The performance data were calculated between the discharge station and an upstream inlet measure vent station where there was no tangential velocity component because of the difficulty experienced in obtaining accurate inlet traverse measurement. (An interesting side benefit of the three tip clearance tests was the determination of the effects of clearance on performance. These effects are shown in figure 79 as plots of head coefficient and efficiency vs clearance ratio. The maximum efficiency and head rise are shown to occur, not for the minimum tip clearance of 0.011 in., but for the 0.021 in. clearance. However, the minimum tip clearance test was conducted with pressure instrumentation on the inducer blades that may have affected the results reducing both efficiency and head rise.)

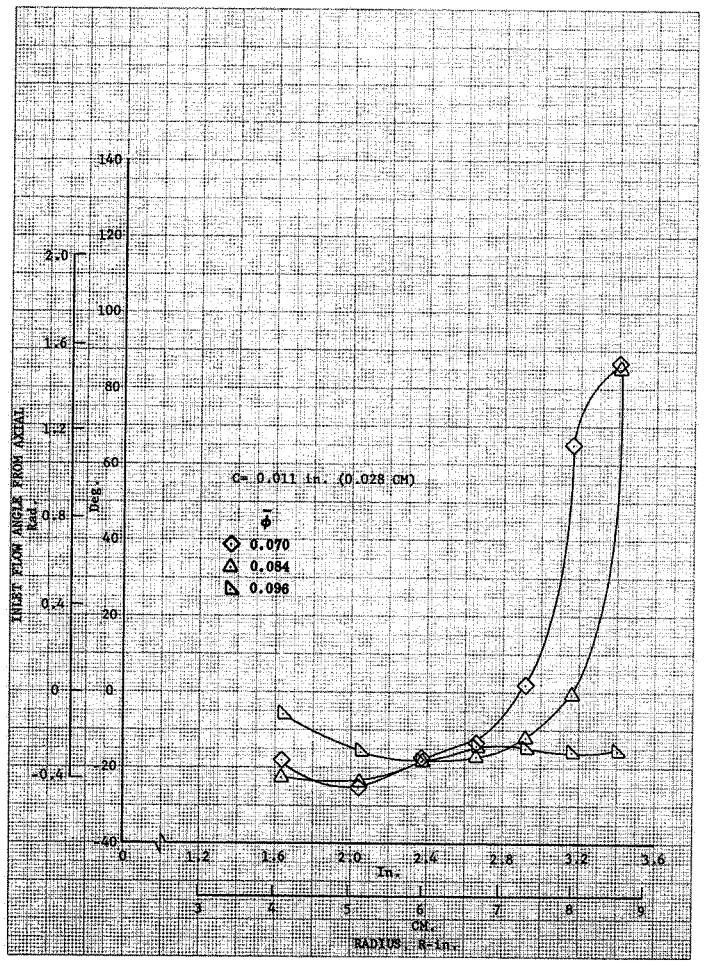

DF 85002

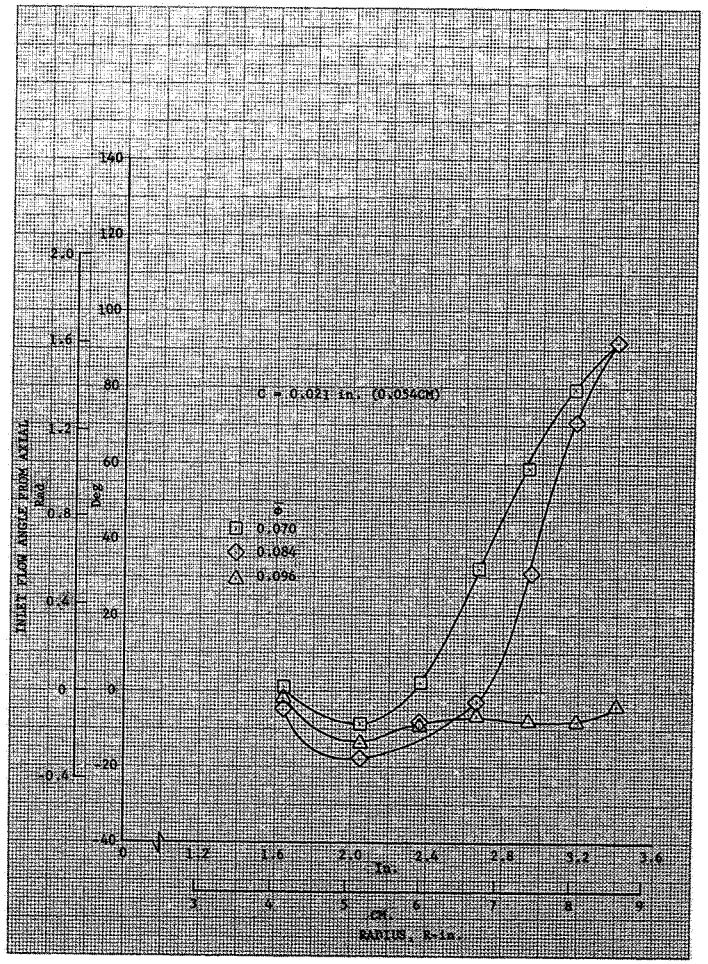

DF 85005

Figure 76. Radial Distribution of Inlet Flow Parameters
U_T = 150 ft/sec (45.6 m/sec), NPSH = 106 ft (32.3 m)

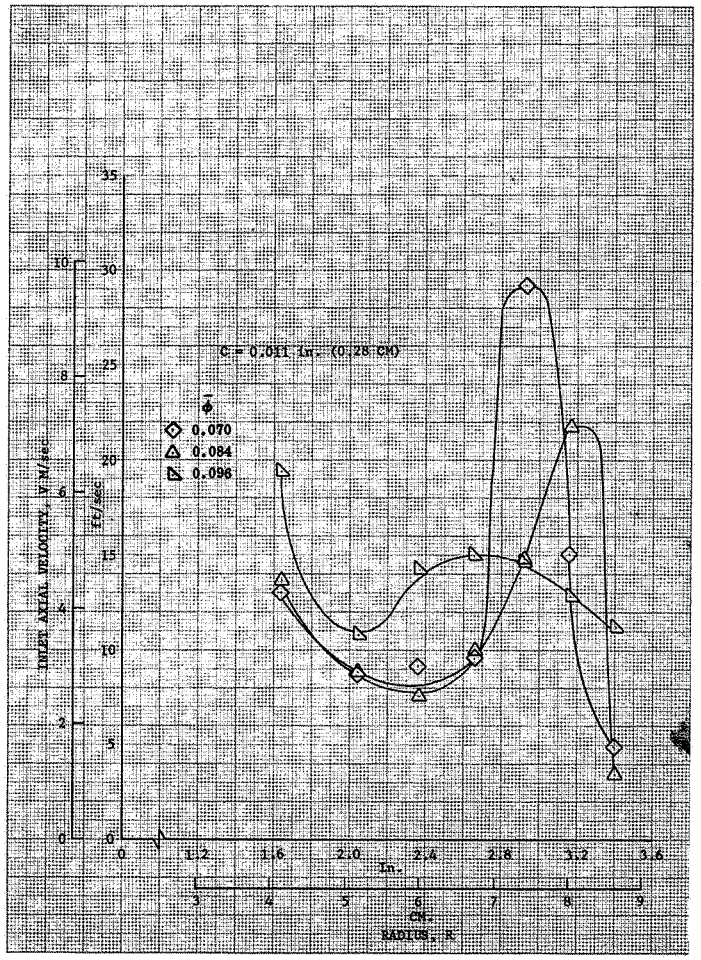

DF 85004

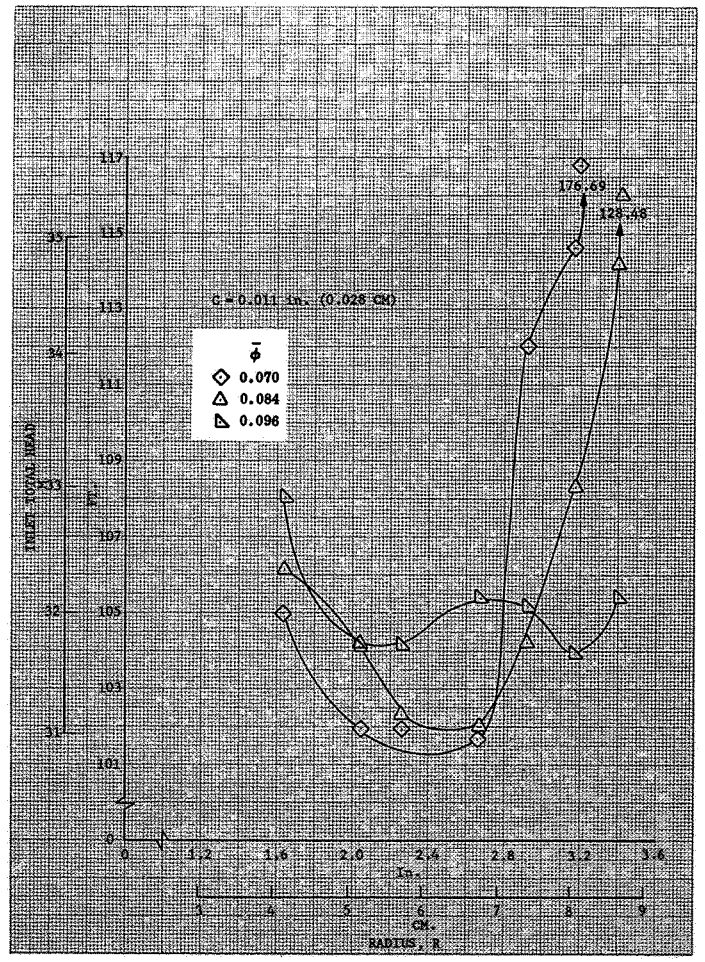

DF 85003

Figure 76. Radial Distribution of Inlet Flow Parameters (Continued)
U_T = 150 ft/sec (45.6 m/sec), NPSH = 106 ft (32.3 m)

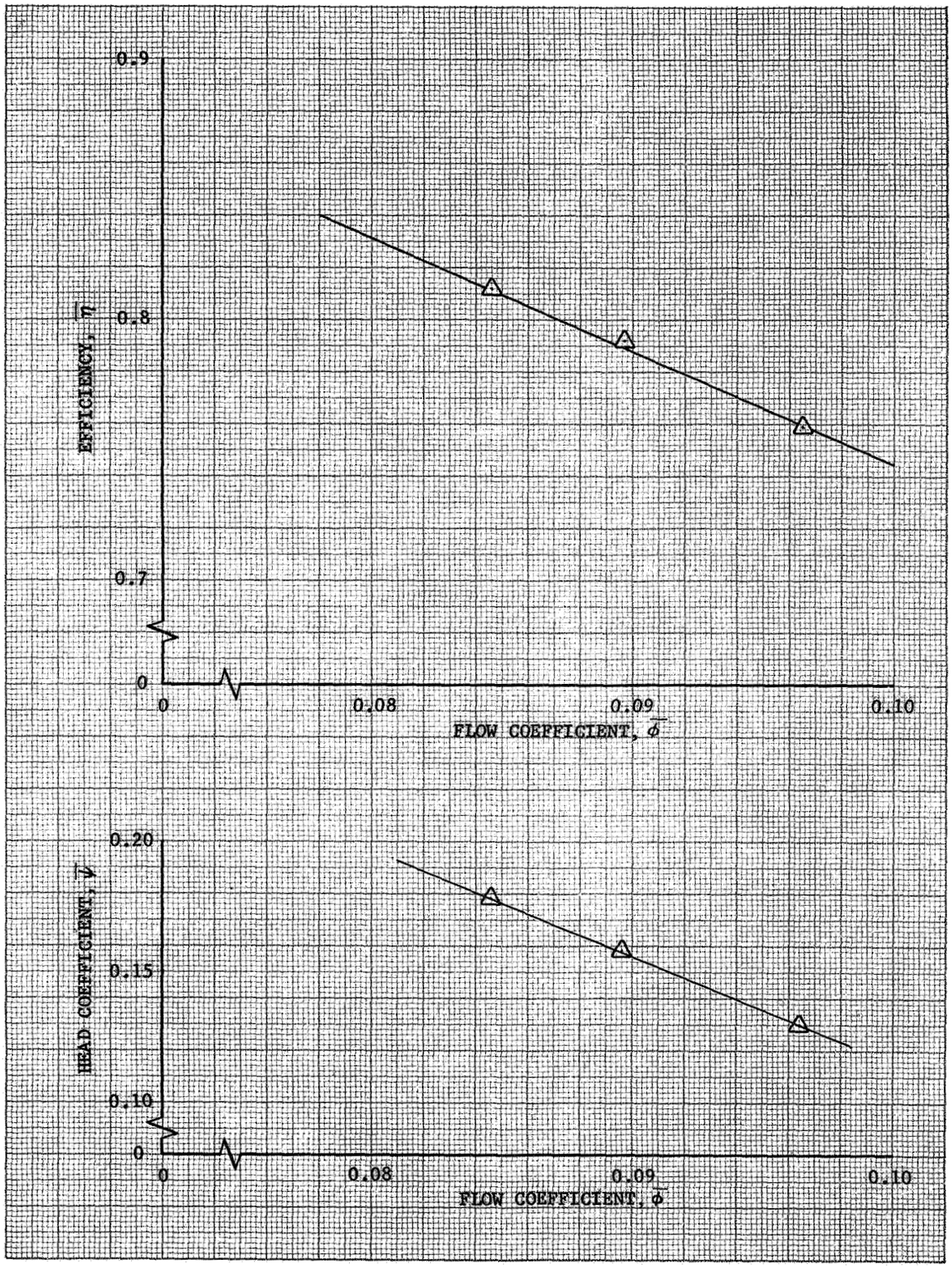

Figure 77. Noncavitating Performance - C = 0.011 in. (0.028 cm) DF 85020

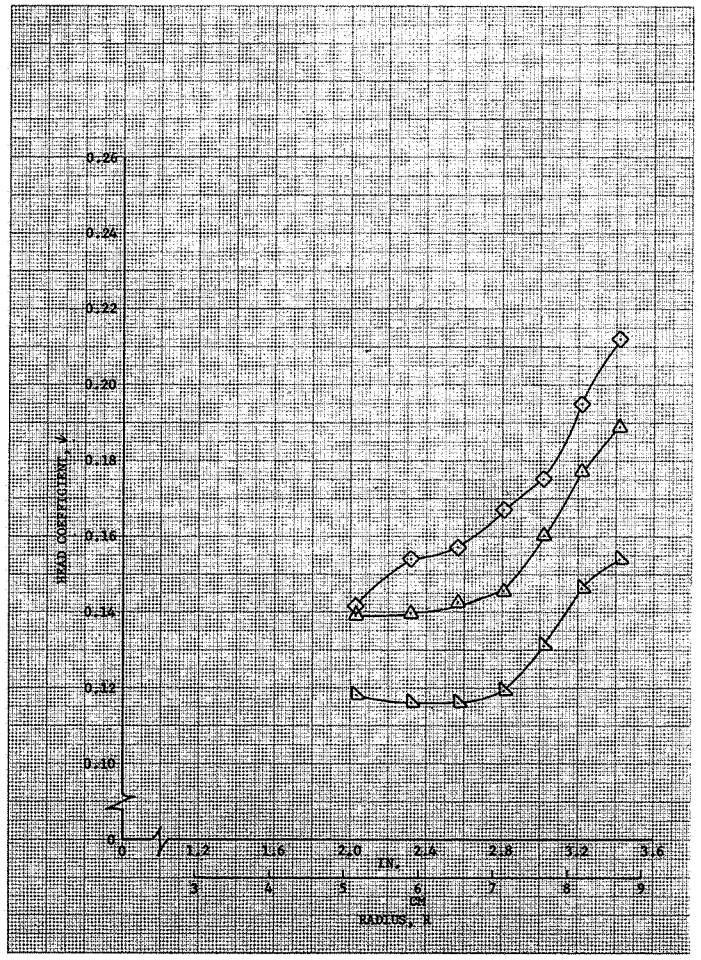

DF 85009

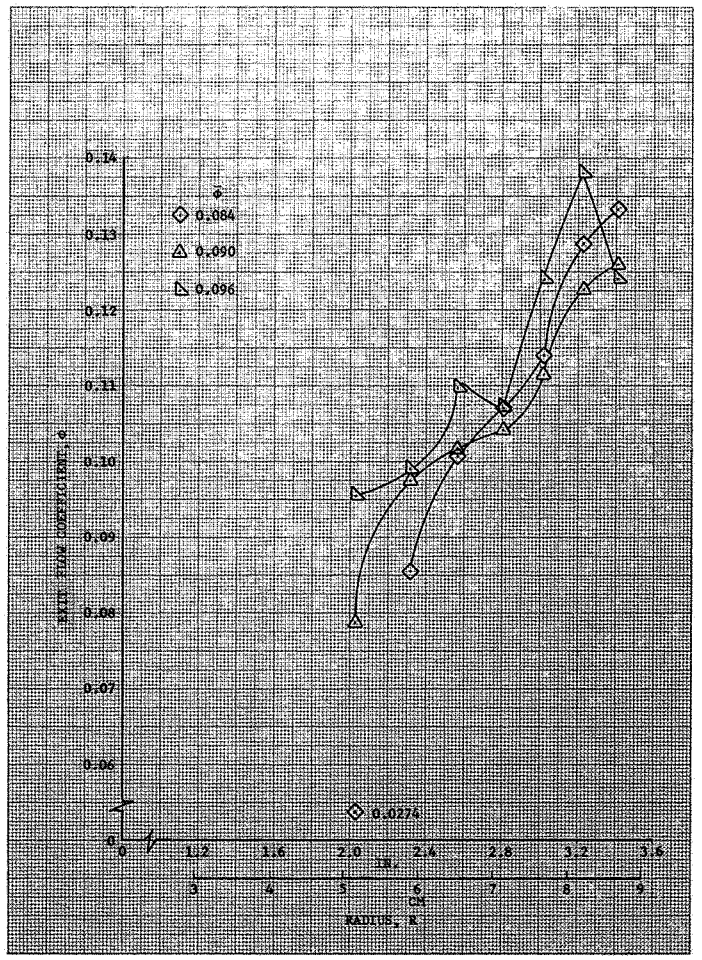

DF 85008

Figure 78. Radial Distribution of Discharge Flow Parameters
C = 0.011 in. (0.028 cm), U_T = 150 ft/sec (45.6 m/sec), NPSH = 106 ft (32.3 m)

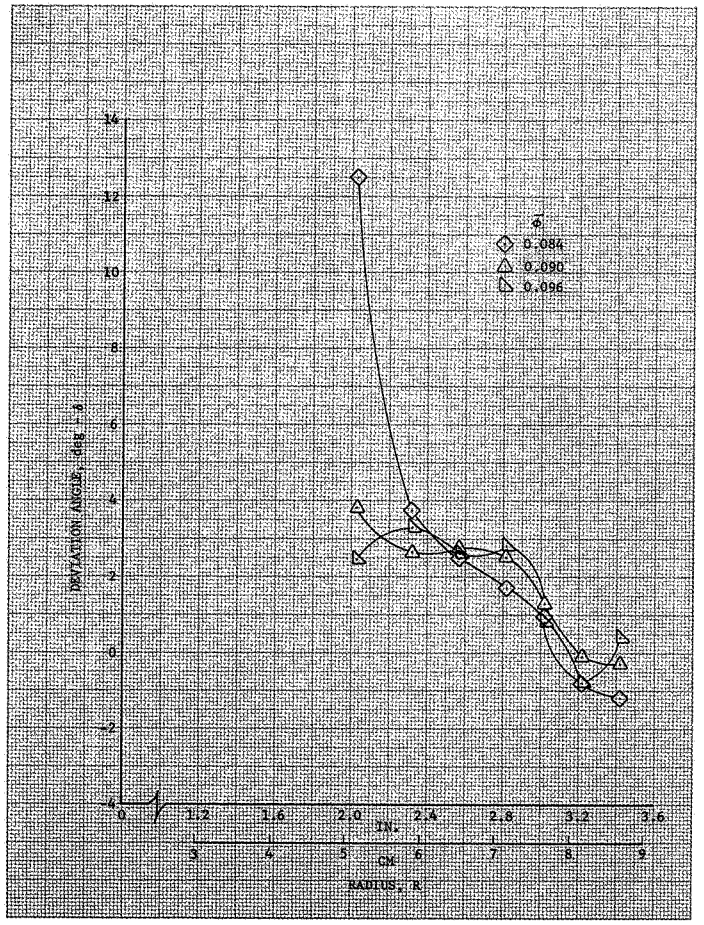

DF 85007

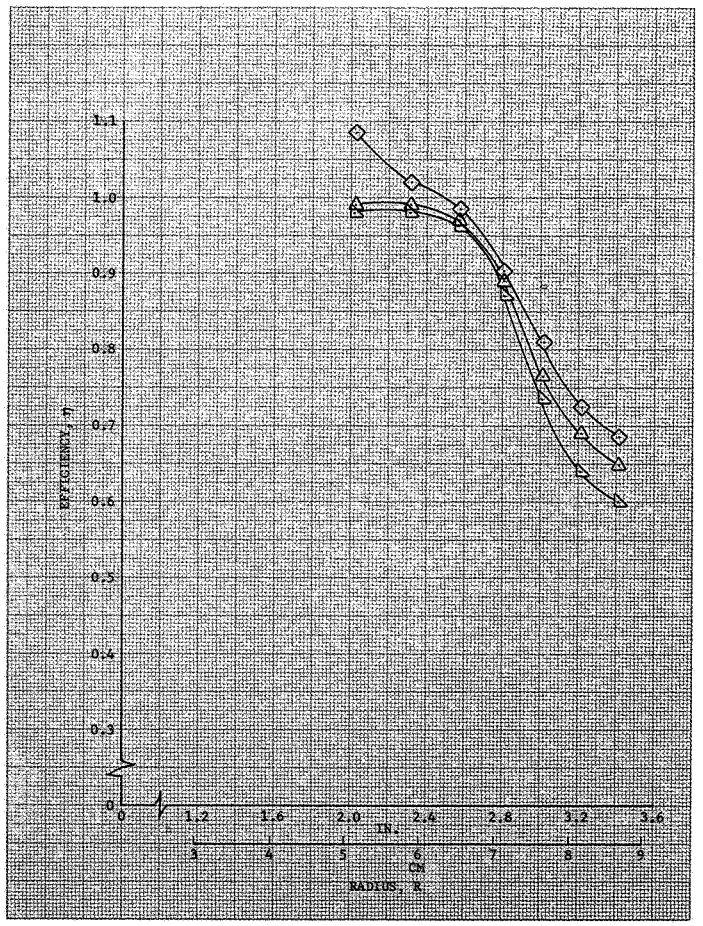

DF 85006

Figure 78. Radial Distribution of Discharge Flow Parameters (Continued)
C = 0.011 in. (0.028 cm), U_T = 150 ft/sec (45.6 m/sec), NPSH = 106 ft (32.3 m)

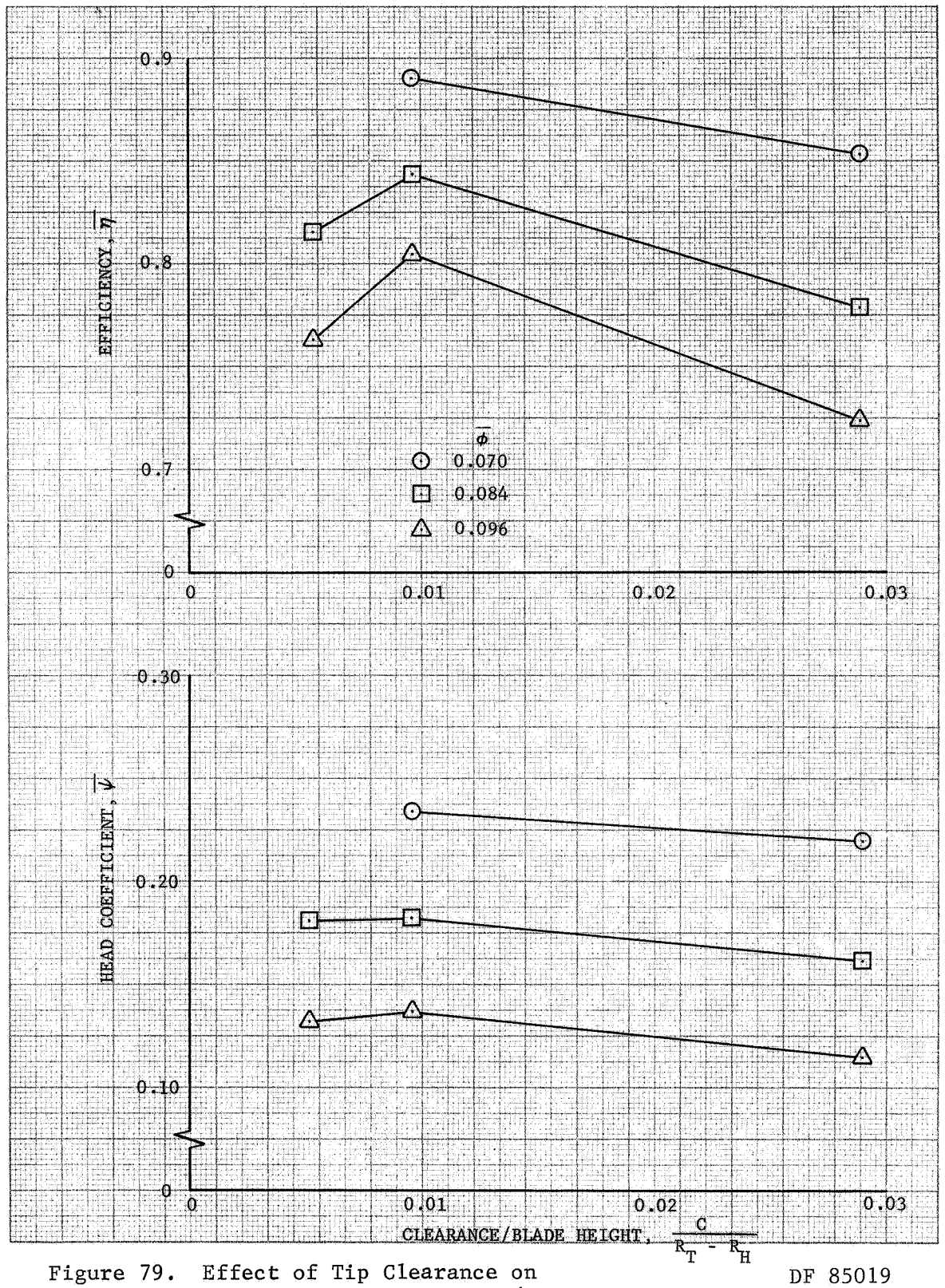

Figure 79. Effect of Tip Clearance on Performance [U_T = 150 ft/sec (45.6 m/s), NPSH = 106 ft (32.3 m)]

DF 85019

(b) Cavitating

A complete investigation of cavitating performance was made only for the 0.061 in. tip clearance configuration. These data are shown in figure 80 as a fraction of noncavitating head vs cavitation number, $\bar{K}$. A minimum K of 0.035 was achieved. This corresponds to a suction specific speed of 22,100 at the original design flow coefficient of 0.070.

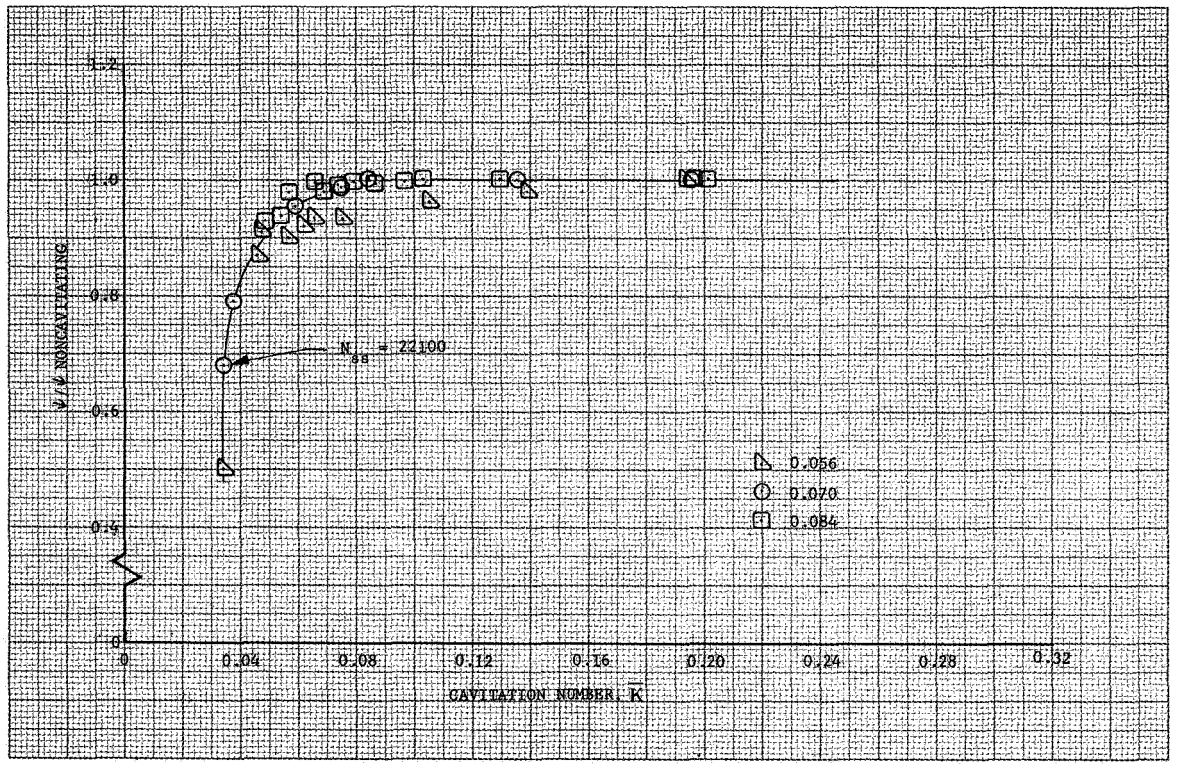

Figure 80. Cavitating Performance [C = 0.061 in. (0.155 cm), U_T = 150 ft/sec (45.6 m/sec)] F33537-7 DF 85018

(2) Strain Tests

Operating conditions (speed, flow and inlet pressure) for each of the strain tests are summarized in table 16. The static strain gage data recorded in each test are listed in tables 17 and 18. Also included in these tables are the corresponding calculated effective stresses for each gage location. As the tables show, the maximum static strain of 2330μ in./in. occurred at gage location 14 during test 3.03-2. This gage was located at node 1 of figure 61. A number of gages failed during the strain gage testing. The rate of failure increased during the cavitating tests, eventually resulting in an early termination of the strain gage testing.

Table 16. Summary of Strain Tests

Test No.	Speed		Flow		Pressure		Temperature	
	rpm	rad/s	gpm	cm^3/s	psig	N/cm^2	°F	°K
3.02	3920	410.5	1087	68,650	29.8	20.5	81	300.2
3.03-1	4900	513.1	1445	91,500	30.0	20.7	81	300.2
3.03-2			1363	85,820			83.5	301.6
3.03-3			1269	80,260			85.5	302.6
3.05-1	4900	513.1	1344	84,810	5.6	3.9	85	302.4
3.05-2			1328	83,800	2.6	1.8	88	304.1
3.05-3			1196	75,470	-8.0	5.5	89	304.7

Table 17. Noncavitating Static Strain and Stress NPSH = 106 ft, 32.3 m

Node	Strain, $\epsilon \times 10^6$ Radial	45 deg (0.78 rad)	Tangential	Effective Stress lb/in^2	N/cm^2	Strain, $\epsilon \times 10^6$ Radial	45 deg (0.78 rad)	Tangential	Effective Stress lb/in^2	N/cm^2
U_T = 120 ft/sec, (36.6 m/s) $\overline{\phi}_1$ = 0.90 Test 3.02						U_T = 150 ft/sec, (45.6 m/s) $\overline{\phi}_1$ = 0.096 Test 3.03-1				
1	-1060	-350	410	17,400	12,000	-1170	-510	570	20,300	13,400
1	-1050	-1210	250	24,000	16,550	-1410	-1930	390	37,600	25,930
1	-840	-450	180	13,600	9,380	-890	-520	310	15,300	10,550
2	-550	-110	160	9,000	6,210	-700	-110	300	11,800	8,140
3	10	150	100	2,600	1,790	40	220	180	3,800	2,620
5	-890	-380	0	14,300	9,860	-1240	-440	60	20,000	13,790
9	-440	-180	90	7,000	4,830	-540	-180	140	8,700	6,000
10	-260	-200	-100	4,700	3,240	-230	-100	-40	3,900	2,690
11	30	0	-180	3,300	2,280	160	150	-160	4,600	3,170
12	130	0	-280	5,000	3,450	250	100	-330	6,900	4,760
13	-360	-130	10	5,800	4,000	-330	-70	160	5,600	3,860
U_T = 150 ft/sec, (45.6 m/s) $\overline{\phi}$ = 0.090 Test 3.03-2						U_T = 150 ft/sec, (45.6 m/s) $\overline{\phi}$ = 0.084 Test 3.03-3				
1	-1340	-930	760	27,000	18,620	-1410	-710	830	26,300	18,130
1	-1640	-2090	450	41,200	28,410	-1920	-2330	470	45,800	31,580
1	-1080	-630	390	18,600	12,820	-1450	220	430	28,000	19,310
2	-	-140	390			-	-180	440		
3	110	310	240	5,300	3,650	100	340	250	5,700	3,930
5	-1480	-530	210	23,600	16,270	-	-	-		
9	-660	340	180	16,200	11,170	-810	-250	180	13,000	8,960
10	-250	-100	-40	4,200	2,900	-360	-100	90	6,700	4,620
11	210	280	-150	6,600	4,550	230	400	-170	8,900	6,140
12	320	140	-340	7,700	5,310	350	230	-380	9,300	6,410
13	-410	-80	190	6,900	4,760	-530	-160	140	8,500	5,860

Table 18. Cavitating Static Strain and Stress U_T = 150 ft/sec, 46.7 m/s

Node	Strain, $\epsilon \times 10^6$ Radial	45 deg (0.78 rad)	Tangential	Effective Stress lb/in.^{2}	N/cm^2	Strain, $\epsilon \times 10^6$ Radial	45 deg (0.78 rad)	Tangential	Effective Stress lb/in.^{2}	N/cm^2
$\overline{\phi}_1$ = 0.088, NPSH = 50 ft, (15.2 m) Test 3.05-1						$\overline{\phi}_1$ = 0.087, NPSH = 43 ft, 13.1 m Test 3.05-2				
1	-	-	270			-	-	320		
1	-1280	200	340	25,000	17,240	-40	310	330	6,300	4,340
1	-1040	-730	-			-840	-630	-		
2	-	-190	410			-	-180	430		
3	-	-	-			-	-	-		
5	-	-	-			-	-	-		
9	-1120	-440	90	17,900	12,340	-1160	-490	90	18,500	12,760
10	-500	-90	-120	9,700	6,690	-480	-210	-130	8,400	5,790
11	1380	-	-			-	-	-		
12	-	-	-			-	-	-		
13	-370	-140	310	7,600	5,240	180	-220	360	12,400	8,550
$\overline{\phi}_1$ = 0.079, NPSH = 17 ft, (5.2 m) Test 3.05-3										
1	-	-	440							
1	230	570	100	9,500	6,550					
1	120	220	-							
2	-	320	410							
3	-	-	-							
5	-	-	-							
9	30	140	170	2,900	2,000					
10	160	160	110	3,300	2,280					
11	-	-	-							
12	-	-	-							
13	-60	100	350	5,600	3,860					

The vibratory stress data from the tests are presented in tables 19 and 20. The vibratory data are shown as plus and minus deviations from the existing static stress values and are computed with the assumption of a uniaxial stress condition within the proportional limit of the material (modulus of elasticity equal to 16.2 x 10^6 psi (11.03 x 10^6 N/cm^2). Also shown in the tables are the frequencies at which the listed stresses occurred.

Table 19. Noncavitating Vibratory Strain and Stress
NPSH = 106 ft, 32.3 m

Node	Strain, ϵ x 10^6 Radial	45 deg (0.78 rad)	Tangential	Frequency Hz	Effective Stress lb/in^2	N/cm^2
U_T = 120 ft/sec, (36.6 m/s) $\bar{\phi}_1$ = 0.090 Test 3.02						
1	69	33	0	1000	1110	7650
1	0	0	25	-	0	
1	64	55	33	1000	1220	8411
2	31	25	0	1000	540	370
3	33	0	0	-	0	
5	0	0	0	-	0	
7	58	33	Out	700	930	640
9	0	0	0	-	0	
10	43	41	0	1000	810	560
11	31	33	32	1000	760	520
12	0	0	0	-	0	
13	0	0	0	-	0	
U_T = 150 ft/sec, (45.6 m/s) $\bar{\phi}$ = 0.096 Test 3.03-1						
1	0	0	0	-	0	
1	0	0	0	-	0	
1	80	37	0	1150	1290	890
2	0	0	0	-	0	
3	0	0	0	-	0	
5	Out	Out	Out	-	-	
7	Out	Out	Out	-	-	
9	0	0	0	-	0	
10	35	49	0	1800	880	610
11	31	41	0	-	740	510
12	0	0	0	-	0	
13	0	0	0	-	0	

Table 19. Noncavitating Vibratory Strain and Stress
NPSH = 106 ft, 32.3 m (Continued)

Node	Strain, $\epsilon \times 10^6$ Radial	45 deg (0.78 rad)	Tangential	Frequency Hz	Effective Stress, lb/in.^{2}	N/cm^2
U_T = 150 ft/sec, (45.6 m/s) $\overline{\Phi}_1$ = 0.090 Test 3.03-2						
1	139	82	0	1050	2240	1540
1	82	49	0	1000	1330	920
1	0	0	0	-	0	
2	Out	49	32	1100	-	
3	32	0	0	1000	610	420
5	Out	Out	Out	-	-	
7	Out	Out	Out	-	-	
9	0	0	0	-	0	
10	121	66	0	1000	1940	1340
11	0	49	40	1000	890	610
12	40	0	0	1000	770	530
13	0	0	0	-	0	
U_T = 150 ft/sec, (45.6 m/s) $\overline{\Phi}_1$ = 0.084 Test 3.03-3						
1	70	82	0	1000	1500	1030
1	0	0	0	-	0	
1	128	74	41	1100	2240	1540
2	Out	82	80	1500	-	
3	0	0	0	-	0	
5	Out	Out	Out	-	-	
7	Out	Out	Out	-	-	
9	128	83	49	1100	2290	1580
10	52	66	0	-	1185	820
11	78	82	80	2200	1900	1310
12	0	0	0	-	0	
13	0	0	0	-	0	

(3) Pressure Tests

Table 21 presents a summary of the operating points at which the inducer blade surface pressures were recorded. Attempts were made to set exactly the same test conditions for both series of pressure tests, i.e. for tests with the tip streamline pressure tap location (radius No. 1) and the mean streamline tap location (radius No. 2). As table 21 shows, the noncavitating test conditions were repeated very closely; this was not the case, however, in the cavitating tests. It became difficult to maintain a constant inlet pressure due to the partial blockage of the fine screens, installed ahead of the inducer to provide the low pressures required, by gasket material and scale loosened by the cavitation. As a result the NPSH values for the cavitating tests varied from -9 psig (-6.2 N/cm^2) for the radius 1 tests to 2.4 psig (1.7 N/cm^2) for the radius 2 tests. This deviation required some interpolation and extrapolation of the data for correlation with predicted values.

Table 20. Cavitating Vibratory Strain and Stress
U_T = 150 ft/sec, 45.6 M/s

Node	Strain, $\epsilon \times 10^6$ Radial	45 deg (0.78 rad)	Tangential	Frequency Hz	Effective Stress lb/in.^{2}	N/cm^2
NPSH = 50 ft, (15.2 m) $\bar{\Phi}_1$ = 0.088 Test 3.05-1						
1	1560	990	0	950	2540	1750
1	0	0	0	-	0	
1	0	0	Out	-	-	
2	Out	66	40	1000	-	
3	Out	Out	Out	-	-	
5	Out	Out	Out	-	-	
7	Out	Out	Out	-	-	
9	0	0	0	-	0	
10	0	0	0	-	0	
11	47	Out	Out	1000	1360	940
12	Out	Out	Out	-	-	
13	0	0	0	-	0	
NPSH = 43 ft, (13.1 m) $\bar{\Phi}_1$ = 0.087 Test 3.05-2						
1	Out	Out	0	-	-	
1	164	82	42	1000	2830	1950
1	0	0	Out	-	-	
2	Out	49	48	1000	-	
3	Out	Out	Out	-	-	
5	Out	Out	Out	-	-	
7	Out	Out	Out	-	-	
9	0	0	0	-	0	
10	0	0	0	-	0	
11	Out	Out	Out	-	-	
12	Out	Out	Out	-	-	
13	39	41	41	1000	960	660
NPSH = 17 ft, (5.2 m) $\bar{\Phi}_1$ = 0.079 Test 3.05-3						
1	Out	Out	0	-	-	
1	0	0	0	-	0	
1	0	0	Out	-	-	
2	Out	99	64	900	-	
3	Out	Out	Out	-	-	
5	Out	Out	Out	-	-	
7	Out	Out	Out	-	-	
9	0	0	0	-	0	
10	0	0	0	-	0	
11	Out	Out	Out	-	-	
12	Out	Out	Out	-	-	
13	0	0	0	-	0	

Table 21. Summary of Pressure Tests

Test No.	Speed rpm	Speed rad/s	Flow gpm	Flow cm^3/s	Inlet Total Pressure psig	Inlet Total Pressure N/cm^2	Temperature °F	Temperature °K
Pressure Taps at Outer Radius								
4.01-1	3920	410.5	1165	73,200	29.0	20.0	68	293
4.01-2	3920		1091	68,650	30.0	20.7	70	294.1
4.01-3	3920		1020	64,240	30.0	20.7	71	294.7
4.02-1	4900	513.1	1450	91,500	30.0	20.7	73	295.8
4.02-2	4900		1350	85,820	30.0	20.7	75	296.9
4.02-3	4900		1282	80,260	30.0	20.7	76	297.4
4.02-4	4900		1286	80,260	53.2	36.7	77	298
4.03-1	4900	513.1	1361	85,820	6.2	4.3	76	297.4
4.03-2	4900		1181	74,520	-9.0	6.2	78	298.6
Pressure Taps at Inner Radius								
5.01-1	3920	410.5	1168	73,200	30.1	20.8	56	286.3
5.01-2	3920		1089	68,650	30.2	20.8	56.5	286.6
5.01-3	3920		1013	64,240	30.3	20.9	57.5	287.2
5.02-1	4900	513.1	1457	91,500	29.9	20.6	59	288
5.02-2	4900		1353	85,820	29.4	20.3	61	289.1
5.02-3	4900		1281	80,260	29.5	20.3	62	289.7
5.03-1	4900	513.1	1355	85,820	5.0	3.5	64	290.8
5.03-2	4900		1336	84,240	2.4	1.7	66	291.9

The blade pressure data recorded at the major test points are presented in tables 22 and 23. The values shown are absolute levels at each location and it should be noted that the inlet pressure was not exactly the same for each test. The differences in inlet pressure must be considered in any test-to-test comparison, in particular with the cavitating test data.

The data are presented by axial station for the suction and pressure surfaces for each test. The very low pressures on the suction surface of the blade indicate the presence of a vapor cavity even though the pressures are not at the vapor pressure of water [0.5 lb/in^2 (0.34 N/cm^2)]. The reason for this deviation in pressure is primarily the normal inaccuracy associated with measuring such low pressure with the 100 psi (69 N/cm^2) transducer required to measure pressures in the rear portion of the inducer.

A few of the data points in tables 22 and 23 have been left blank where the readings were obviously in error. The validity of the pressure data was judged by playing back the FM tapes and obtaining an oscillograph trace of the transducer output, like that shown in figure 81. Obviously erroneous points, such as those indicated by a gradual decrease or increase in pressure as opposed to a step change, were readily apparent. A varying pressure signifies a leaking or partially plugged pressure tap tube. A pressure tap reading of the same level as purge pressure indicates a plugged tube or a surface pressure higher than purge pressure. Static pressures along the inducer hub (Ref figure 55) were recorded during each test using the pressure scanning valve. These data from the first test series are presented in table 24.

Most of the data accumulated from the scanning valve appears to be valid and repeatable. This application of the scanning valve and the techniques employed to obtain accurate surface pressures were highly successful.

At each test point listed in table 21 data was recorded from the blade-mounted miniature transducers and the housing-mounted piezoelectric transducers. Data from two of the blade-mounted transducers for a typical noncavitating test, are presented in figure 82 as pressure amplitude vs frequency. These two transducers were in locations 2 (PVB-2) and 3 (PVB-3) as shown in figure 57. The transducers were installed primarily to obtain information on vibratory pressures during cavitation. However, before the first fully cavitating point could be set, all of the surface mounted transducers had failed. The noncavitating data show relatively high vibratory pressures in the low frequency range (0-200 Hz) but very little amplitude in the range of the resonant frequencies of the blade (900-1200 Hz).

Table 22. Noncavitating Pressure Distribution
U_T = 150 ft/sec, (45.6 m/s) NPSH = 106 ft (32.3 m)

Pressure Tap Location	$\bar{\phi}$ = 0.096 Test 4.02-1				$\bar{\phi}$ = 0.090 Test 4.02-2				$\bar{\phi}$ = 0.084 Test 4.02-3			
	Suction Surface		Pressure Surface		Suction Surface		Pressure Surface		Suction Surface		Pressure Surface	
	lb/in.^{2}	N/cm^2	lb/in.^{2}	N/cm^2	lb/in.^{2}	N/cm^2	lb/in.^{2}	N/cm^2	lb/in.^{2}	N/cm^2	lb/in.^{2}	N/cm^2
TIP STREAMLINE												
1	0.5	0.3	69.7	48.1	0.5	0.3	74.5	51.4	0.3	0.2	77.8	53.6
2	2.1	1.5	66.5	45.9	2.2	1.5	69.5	47.9	3.3	2.3	71.9	49.6
3	11.0	7.6	65.0	44.8	9.9	6.8	70.0	48.3	9.7	6.7	70.4	48.5
4	43.1	29.7	65.9	45.4	22.1	15.2	68.9	47.5			69.7	48.1
5	46.1	31.8			42.1	29.0			41.9	28.9		
6	44.9	31.0	66.6	45.9	44.5	30.7	71.8	49.5	46.3	31.9	70.9	48.9
7	50.5	34.8	64.4	44.4	48.5	33.4	67.6	46.6	47.8	33.0	70.1	48.3
8	51.0	35.2	69.5	47.9	51.8	35.7	75.3	51.9	50.3	34.5	76.5	52.7
9	52.3	36.1	64.4	44.4	51.2	35.3	67.1	46.3	51.0	35.2	72.1	49.7
10	58.0	40.0	65.0	44.8	55.7	38.4	70.3	48.5	55.8	38.5	74.0	51.0
11	60.7	41.9	67.6	46.6	62.1	42.8	71.2	49.1	59.8	41.2	73.6	50.7
12			73.1	50.4			79.5	54.8			80.2	55.3
13			72.3	49.9			75.8	52.3			78.6	54.2
14			73.2	50.5			77.8	53.6			79.8	55.0
15	71.0	49.0	75.3	51.9	77.1	53.2	81.6	56.3	79.4	54.7	83.4	57.5
16	73.4	50.6	76.4	52.7	76.5	52.7	82.4	56.8	78.0	53.9	84.0	57.9
17	77.6	53.5	71.6	49.4	82.2	56.7	77.4	53.4	85.0	58.6	82.3	56.7
18	81.4	56.1	68.7	47.4	83.7	57.7	76.8	53.0	86.7	59.8	80.7	55.6
19	75.0	51.7	75.5	52.1	80.9	55.8	82.7	57.0	83.4	57.5	84.9	58.5
	Test 5.02-1				Test 5.02-2				Test 5.02-3			
MIDSPAN STREAMLINE												
1	1.1	0.8	59.6	41.1	0		64.1	44.2	1.3	0.9	67.6	46.6
2	2.5	1.7	60.1	41.4	1.9	1.3	65.0	44.8	4.6	3.2	63.3	43.6
3	37.0	25.5	61.0	42.1	39.2	27.0	61.3	42.3	39.6	27.3	63.3	43.6
4	42.0	29.0	58.0	40.0	40.7	28.0	62.0	42.7	45.5	31.4	63.1	43.5
5	38.2	26.3			38.1	26.3			37.9	26.1		
6	18.3	12.6	57.7	39.8	17.3	11.9	61.6	42.5	15.8	10.9	64.1	44.2
7	42.8	30.0	55.7	38.4	44.1	30.4	62.3	43.0	41.1	28.3	62.6	43.2
8	43.8	30.2	64.7	44.6	46.3	31.9	69.4	47.9	43.6	30.1	69.2	47.7
9	48.1	33.2	58.2	40.1	48.0	33.1	62.8	43.3	50.7	35.0	64.7	44.6
10	50.9	35.1	60.4	41.6	50.8	35.1	64.1	44.2	51.8	35.7	66.6	45.9
11	55.8	38.5	61.7	42.5	58.6	40.4	65.2	45.0	57.1	39.4	66.6	45.9
12			64.4	44.4			68.3	47.1			70.5	48.6
13	63.1	43.5	62.9	43.4	67.4	46.5	66.8	46.1	68.6	47.3	72.3	49.9
14			63.5	43.8			69.5	47.9			71.2	49.1
15	63.0	43.4			69.1	47.6			71.1	49.0		
16	63.7	43.9	67.3	46.4	69.2	47.7	69.8	48.1	73.5	50.7	72.1	49.7
17	69.7	48.0	64.4	44.4	74.0	51.0	68.0	46.9	74.3	51.3	71.7	49.4
18	66.8	46.0	64.8	44.7	70.4	48.5	70.0	48.3	72.7	50.1	69.6	48.0
19	65.4	45.1	72.3	49.9	73.0	50.3	74.6	51.4	74.9	51.6	75.3	51.9

Table 22. Noncavitating Pressure Distribution
U_T = 150 ft/sec, (45.6 m/s) NPSH = 106 ft (32.3 m) (Continued)

Pressure Tap Location	ϕ = 0.095 Test 4.01-1 Suction Surface lb/in.^{2}	N/cm^2	Pressure Surface lb/in.^{2}	N/cm^2	ϕ = 0.090 Test 4.01-2 Suction Surface lb/in.^{2}	N/cm^2	Pressure Surface lb/in.^{2}	N/cm^2	ϕ = 0.084 Test 4.01-3 Suction Surface lb/in.^{2}	N/cm^2	Pressure Surface lb/in.^{2}	N/cm^2
TIP STREAMLINE												
1	8.6	5.9	63.0	43.5	7.6	5.2	66.5	45.8	4.8	3.3	68.8	47.4
2	37.7	26.0	61.9	42.7	36.4	25.1	64.2	44.3	24.0	16.6	64.7	44.7
3	41.0	28.3	60.4	41.7	39.0	26.9	63.4	43.8	39.5	27.2	67.0	46.2
4	44.0	30.4	60.5	41.7	44.2	30.5	65.1	44.9	44.6	30.7	64.9	44.8
5	45.7	31.5			45.7	31.5			44.2	30.5	62.7	43.3
6	46.5	32.1	60.5	41.7	45.9	31.7	63.6	43.9	46.2	31.9	66.0	45.5
7	50.0	34.5	60.1	41.4	49.7	34.3	63.0	43.5	50.3	34.7	65.0	44.8
8	49.9	34.4	64.4	44.4	52.3	36.1	67.4	46.5	49.7	34.3	70.6	48.7
9	50.1	34.6	61.3	42.2	51.7	35.7	63.3	43.7	51.1	35.2	66.1	45.6
10	53.9	37.2	61.9	42.7	54.5	37.6	64.4	44.4	54.3	37.4	68.1	47.0
11	56.0	38.6	62.4	43.1	58.4	40.3	65.5	45.2	58.0	40.0	67.5	46.6
12			65.2	44.9			69.0	47.6			70.9	48.9
13			63.7	43.9			68.1	47.0			69.6	48.0
14			65.8	45.3			69.4	47.9			72.7	50.2
15	63.6	43.8	67.0	46.2	68.3	47.1	70.2	48.4	70.6	48.7	74.0	51.0
16	65.0	44.8	70.0	48.2	68.3	47.1	71.6	49.4	70.7	48.7	74.2	51.2
17	65.0	44.8	65.0	44.8	70.7	48.8	70.0	48.3	72.5	50.0	72.9	50.3
18	71.5	49.3	63.0	43.5	73.0	50.4	68.3	47.1	76.8	52.9	71.8	49.5
19	68.3	47.2	66.0	45.5	70.6	48.7	71.4	49.3	73.8	50.8	73.3	50.6
	Test 5.01-1				Test 5.01-2				Test 5.01-3			
MIDSPAN STREAMLINE												
1	18.7	12.9	54.2	37.4	18.8	13.0	60.3	41.6	10.8	7.5	60.4	41.7
2	33.3	23.0	57.1	39.4	32.5	22.4	58.1	40.1	32.0	22.1	56.2	38.8
3	41.3	28.5	55.9	38.6	40.6	28.0	56.3	38.8	37.7	26.0	60.6	41.8
4	43.9	30.3	52.9	36.5	43.1	29.7	56.4	38.9	42.6	29.4	58.3	40.2
5	39.9	27.5	56.0	38.6	39.6	27.3	51.9	35.8	41.4	28.6	55.6	38.3
6			56.5	39.0			58.0	40.0			58.8	40.6
7	44.8	30.9	51.9	35.8	45.2	31.2	54.7	37.7	42.3	29.2	57.5	39.7
8	45.0	31.1	56.2	38.8	45.3	31.3	58.7	40.5	42.4	29.3	62.7	43.3
9	48.8	33.7	55.3	38.1	46.8	32.3	58.2	40.2	49.4	34.1	57.2	39.5
10	49.9	34.4	58.9	40.6	50.0	34.5	60.8	41.9	49.4	34.1	60.7	41.9
11	50.4	34.8	55.5	38.3	53.9	37.2	58.5	40.3	54.8	37.8	62.5	43.1
12	52.8	36.4	60.1	41.4	56.2	38.8	63.8	44.0	60.2	41.5	62.6	43.2
13	55.6	38.3	56.2	38.8	60.4	41.7	59.9	41.3	61.0	42.1	64.0	44.2
14	57.7	39.8	57.9	39.9	61.1	42.1	60.2	41.5	61.1	42.1	64.8	44.7
15	58.8	40.6	57.4	39.6	60.8	41.9	60.2	41.5	63.1	43.5	65.6	45.2
16	61.1	42.1	58.4	40.3	61.8	42.6	62.7	43.2	65.0	44.8	65.7	45.3
17	61.1	42.1	57.8	39.9	61.6	42.5	63.7	43.9	67.4	46.5	64.6	44.5
18	57.5	39.6	58.5	40.3	62.6	43.2	60.9	42.1	66.2	45.7	65.1	44.9
19	61.4	42.3	61.6	42.5	63.6	43.8	62.9	43.4	65.7	45.3	68.7	47.4

Table 23. Cavitating Pressure Distribution
U_T = 150 ft/sec (45.6 m/s)

Pressure Tap Location	Suction Surface lb/in.^{2}	Suction Surface N/cm^2	Pressure Surface lb/in.^{2}	Pressure Surface N/cm^2	Suction Surface lb/in.^{2}	Suction Surface N/cm^2	Pressure Surface lb/in.^{2}	Pressure Surface N/cm^2
				TIP STREAMLINE				
	NPSH = 51 ft (15.5m) ϕ = 0.090 Test 4.03-1				NPSH = 16 ft (4.9m) ϕ = 0.078 Test 4.03-2			
1	2.8	1.9	49.7	34.3	3.2	2.2	5.4	3.7
2	4.3	3.0	46.6	32.1	2.7	1.9	2.9	2.0
3	4.7	3.2	44.9	31.0	5.2	3.6	5.0	3.4
4	4.6	3.2	45.8	31.6	3.2	2.2	5.2	3.6
5	4.1	2.8	41.7	28.8	2.2	1.5		
6	3.3	2.3	46.3	31.9	2.0	1.4	5.2	3.6
7	5.4	3.7	43.5	30.0	5.6	3.9	4.6	3.2
8	5.1	3.5	52.4	36.1	4.5	3.1	3.9	2.7
9	34.1	23.5	45.7	31.5	5.3	3.7	2.4	1.7
10	36.0	24.8	46.0	31.7	2.5	1.7	2.3	1.6
11	41.6	28.7	47.7	32.9	5.8	4.0	4.9	3.4
12	43.4	29.9	54.7	37.7			7.0	4.8
13	21.0	14.5	52.3	36.1			6.5	4.5
14	25.7	17.7	53.8	37.1	4.8	3.9	38.2	26.3
15	53.0	36.5	56.2	38.8	4.2	2.9	43.8	30.2
16	51.0	35.2	58.0	40.0	41.4	28.5	47.5	32.8
17	57.6	39.7	53.9	37.2	41.9	28.9	44.1	30.4
18	58.2	40.1	52.8	36.4	45.0	31.0	40.1	27.7
19	59.1	40.8	56.9	39.2	48.7	33.6	45.6	31.4

Table 23. Cavitating Pressure Distribution
U_T = 150 ft/sec (45.6 m/s) (Continued)

Pressure Tap Location	Suction Surface lb/in.^{2}	Suction Surface N/cm^2	Pressure Surface lb/in.^{2}	Pressure Surface N/cm^2	Suction Surface lb/in.^{2}	Suction Surface N/cm^2	Pressure Surface lb/in.^{2}	Pressure Surface N/cm^2
				MIDSPAN STREAMLINE				
	NPSH = 49 ft (14.9m) $\bar{\phi}_1$ = 0.090 Test 5.03-1				NPSH = 43 ft (13.1m) $\bar{\phi}_1$ = 0.088 Test 5.03-2			
1	2.0	1.4	43.4	30.0	2.9	2.0	37.1	25.6
2	4.5	3.1	43.2	29.8	3.9	2.7	42.5	29.3
3	3.2	2.2	44.0	30.3	1.8	1.2	40.3	27.8
4	4.1	2.8	42.7	29.4	3.9	2.7	37.6	25.9
5	3.5	2.4	44.2	30.5	0.5	0.3	39.7	27.4
6	6.0	4.1	41.5	28.6	9.7	6.7	39.4	27.2
7	21.5	14.8	41.1	28.3	1.1	0.8	35.7	24.6
8	28.4	19.6	46.5	32.1	18.6	12.8	45.8	31.6
9	33.4	23.0	39.9	27.5	32.9	22.7	34.8	24.0
10	30.4	20.9	47.2	32.5	26.7	18.4	43.3	29.9
11	36.3	25.0	42.4	29.2	34.4	23.7	41.4	28.5
12	42.1	29.0	51.0	35.2	38.2	26.3	48.6	33.5
13	48.7	33.6	49.6	34.2	43.9	30.3	46.2	31.9
14	47.1	32.5	47.3	32.6	44.4	30.6	45.4	31.3
15	47.5	32.8	48.1	33.2	45.3	31.2	44.1	30.4
16	48.5	33.4	48.9	33.7	45.2	31.2	48.6	33.5
17	52.8	36.4	49.1	33.9	49.6	32.4	47.1	32.5
18	48.8	33.6	46.6	32.1	47.6	32.8	44.3	30.5
19	51.4	35.4	53.9	37.2	47.8	32.9	54.1	37.3

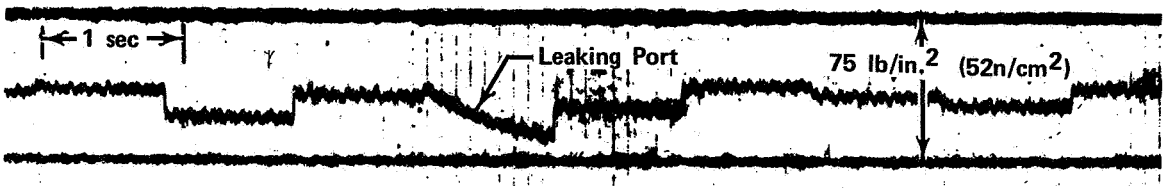

Figure 81. Oscillograph Trace of Pressure Scanning Valve Transducer Output

Data from the housing-mounted transducers are shown as pressure amplitude vs frequency in figure 83. One transducer, PVW-11, was located 0.250 in. (0.62 cm) behind the plane of the inducer leading edge and the other, PVW-12, 1.00 in. (2.54 cm) behind the leading edge. The amplitude-frequency data show pressure peaks at integrals of rotor speed, (1E, 2E etc.) and at integrals of blade passing frequency (3E, 6E, 9E). The housing-mounted transducers were installed to provide a comparison of blade-to-blade pressure variations with the blade surface pressure measurements. To make this comparison, the tape recorded transducer output was transferred to an oscillograph trace such as that shown in figure 84. This trace represents the pressure variation, in the tangential direction, within the blade passage and the differential between the peaks and the valleys should correspond to the difference between the measured pressures on the blade pressure and suction surfaces.

The pressure traces in figure 84 do not agree with the calculated blade pressure differential using the scanning valve data. The reason for the disagreement is the leakage flow across the blade tip that prevents the housing mounted transducer from "seeing" the low pressure on the suction surface of the blade. This effect is indicated in the pressure trace by the gradual drop in pressure on the suction side of the blade, instead of the sharp drop that should occur.

The actual distribution of pressure across the passage can be approximated by indicating, on the plane of the suction surface, in figure 84, the blade pressure differential taken from the scanivalve readings at station 2. The pressure trace between blades can be extrapolated to the pressure level thus indicated on the suction surface as shown by the dashed line in figure 84.

The pressure differential across the blade at the location of the second transducer was too low to make an accurate comparison.

During Task VI the static load testing, vibration testing and operational testing data were used to validate and/or develop the computer programs. The comparisons of predicted and measured parameters obtained during Task VI are discussed in the following paragraphs. The modifications made in the hydrodynamic loading program are included in this discussion. The original programs for blade stress and vibration characteristics have been validated, and the agreement between predictions and test data are illustrated.

Table 24. Noncavitating Hub Static Pressures
NPSH = 106 ft (32.3 m)

Pressure Tap Location	U_T = 120 ft/sec (36.6 m/s)						U_T = 150 ft/sec (45.6 m/s)					
	ϕ = 0.096 Test 4.01-1		ϕ = 0.090 Test 4.01-2		ϕ = 0.084 Test 4.01-3		ϕ = 0.096 Test 4.02-1		ϕ = 0.090 Test 4.02-2		ϕ = 0.084 Test 4.02-3	
	lb/in.^{2}	N/cm^2	lb/in.^{2}	N/cm^2	lb/in.^{2}	N/cm^2	lb/in.^{2}	N/cm^2	lb/in.^{2}	N/cm^2	lb/in.^{2}	N/cm^2
PH1	50.5	34.8	51.1	35.2	51.5	35.5	49.7	34.3	51.0	35.2	47.5	32.8
PH2	56.2	38.8	58.6	40.4	57.2	39.5	58.2	40.2	57.6	39.7	59.4	41.0
PH3	59.5	42.1	60.8	41.9	60.9	42.1	62.2	42.9	64.6	44.6	63.6	43.8
PH4	60.7	41.9	63.2	43.6	63.8	44.0	64.3	44.4	67.0	46.2	68.2	47.1
PH5	63.4	43.8	66.2	45.7	67.8	46.8	69.6	48.0	70.3	48.5	73.6	50.8

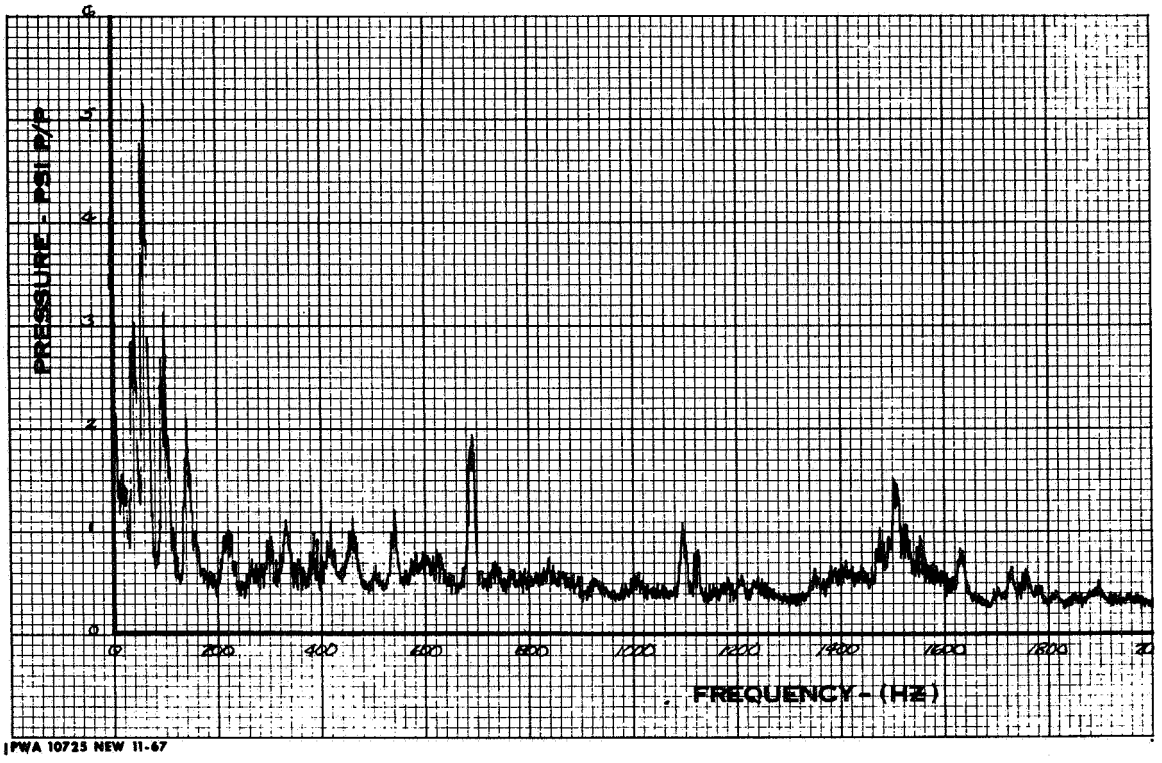

Figure 82a. Blade Transducer Spectrum Analysis - Gage Location No. 2

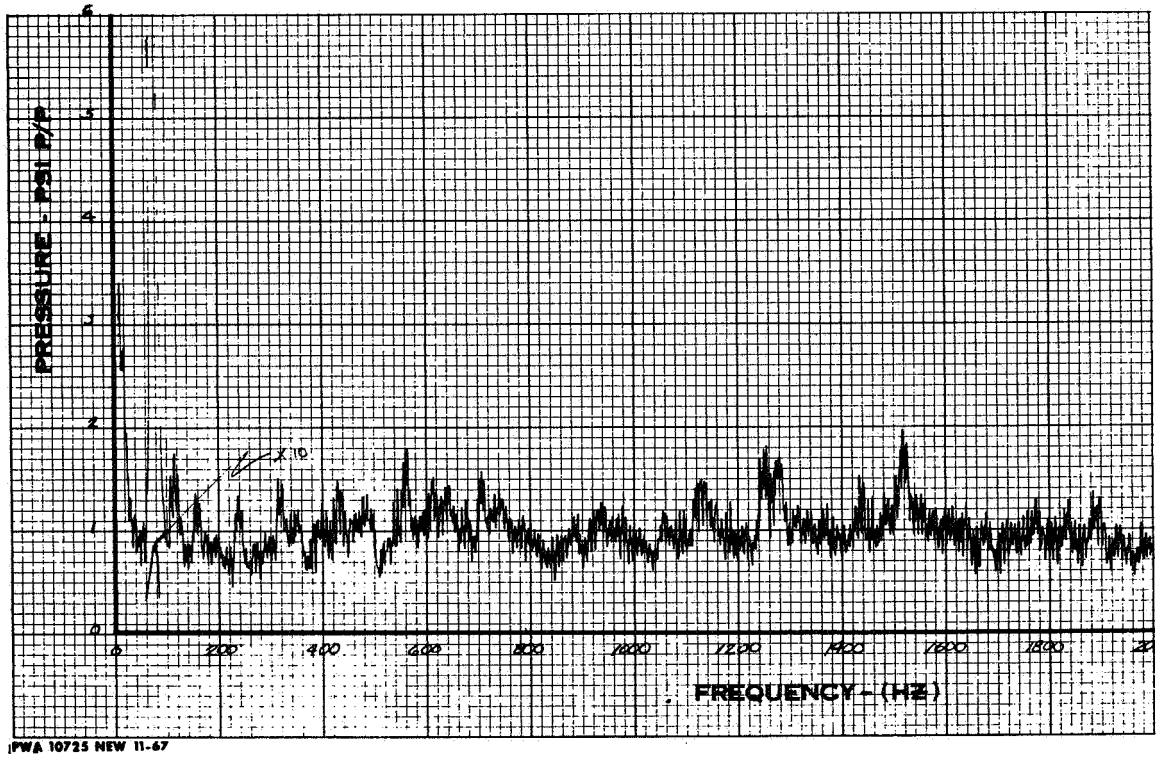

Figure 82b. Blade Transducer Spectrum Analysis - Gage Location No. 3

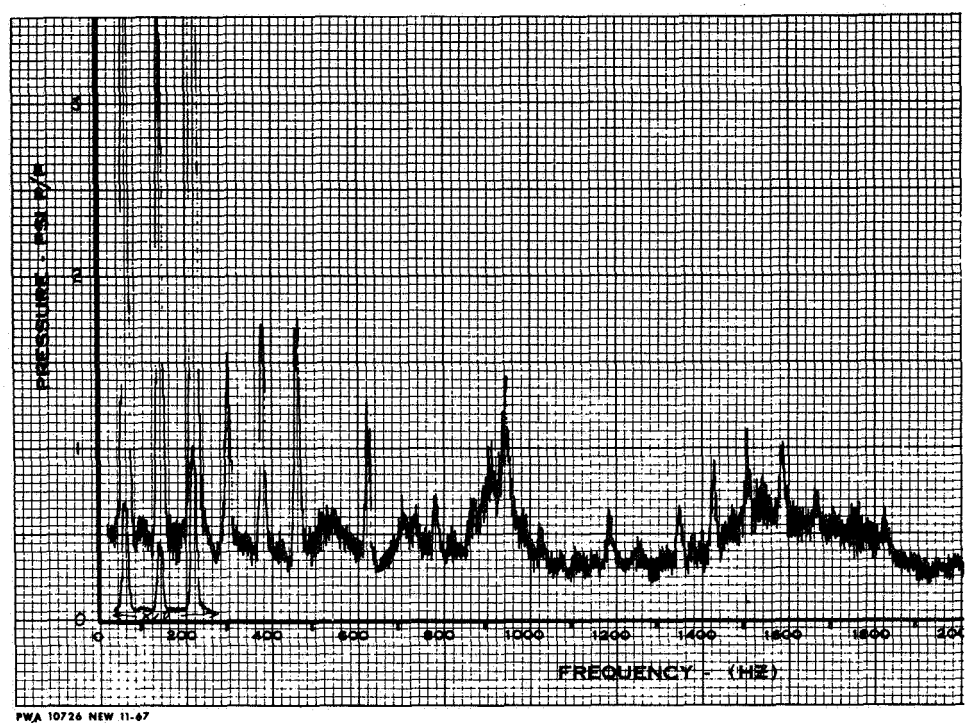

Figure 83a. Housing Transducer Spectrum Analysis - Location PVW-12

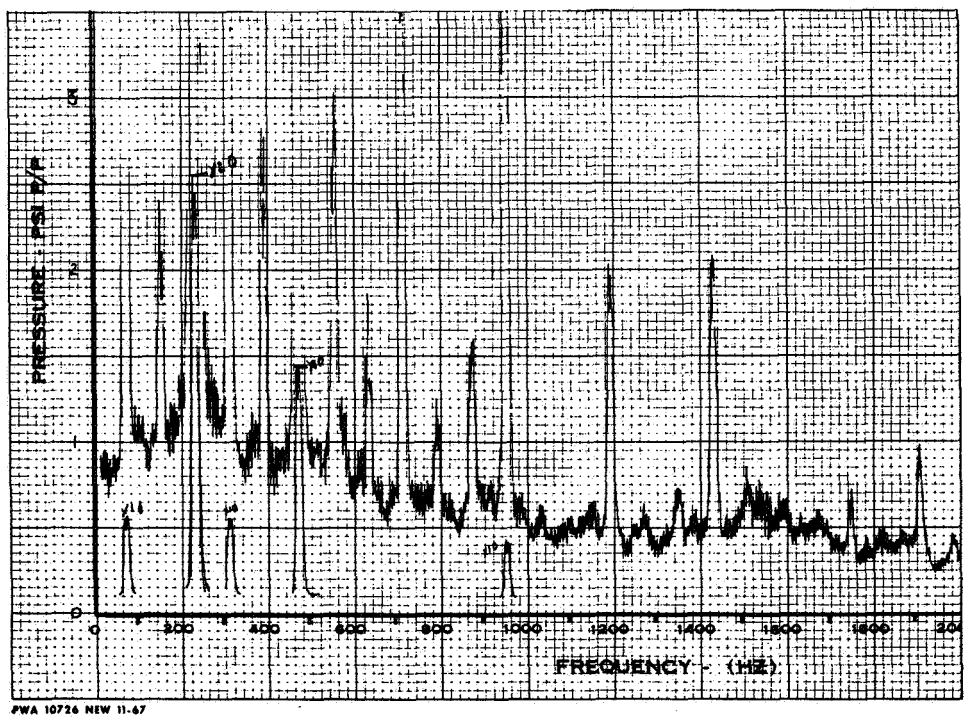

Figure 83b. Housing Transducer Spectrum Analysis - Location PVW-11

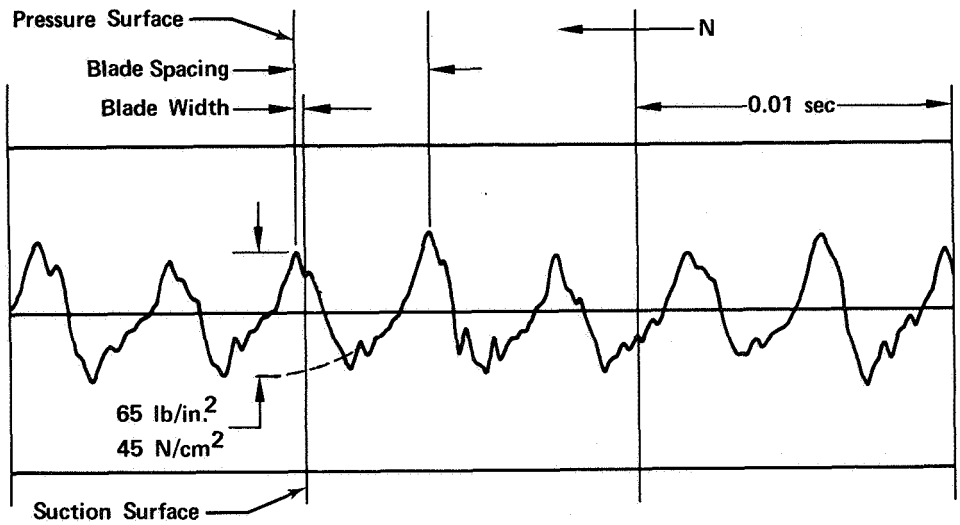

Figure 84. Oscillograph Trace of Housing Transducer Output, PVW-11 Test 4.02-1

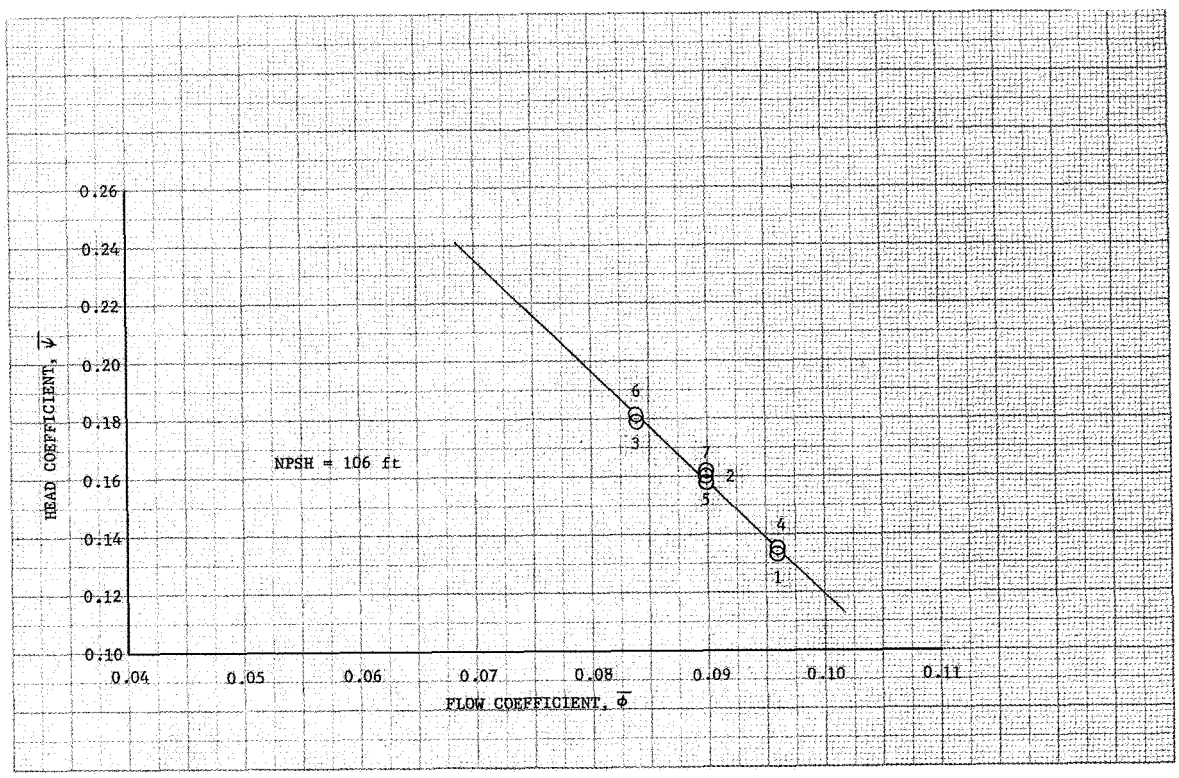

Figure 85. Summary of Performance Data for Operational Tests (Noncavitating)

DF 85017

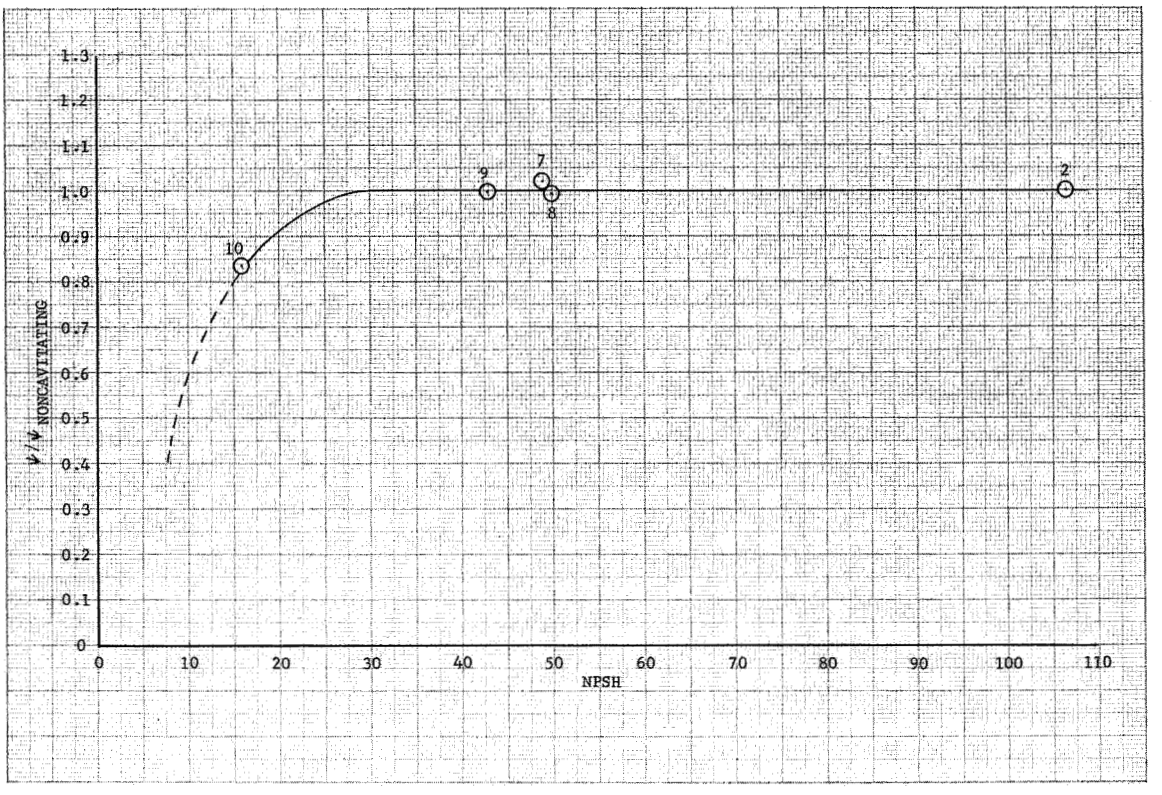

Figure 86. Summary of Performance Data for Operational Tests (Cavitating)

DF 85016

Table 25 summarizes the pressure and strain data taken during water loop testing for which predicted and experimental data comparisons have been made. Data points obtained were discussed in the preceding section and include pressure and strain data at numerous locations (radial and axial) within the inducer for two rotor speeds, three flow coefficients, and several inlet total pressures. The operating points used in the validation or development of the computer programs have been assigned numbers as indicated in table 25. The relationship of these operating points to the noncavitating and cavitating performance of the inducer is indicated on the curves in figures 85 and 86.

Table 25. Operating Points used in Computer Program Development

Run Conditions						Loading		
Point	Speed (%)	ϕ	ψ_S	NPSH (ft)	NPSH (m)	Run No.	Radius	Strain Run No.
1	100	0.096	0.132	106	32.3	4.02-1	1	
						5.02-1	2	3.03-1
2	100	0.090	0.162	106	32.3	4.02-2	1	
						5.02-2	2	3.03-2

Table 25. Operating Points used in Computer Program Development (Continued)

Point	Run Conditions Speed (%)	ϕ	ψ_s	NPSH (ft)	NPSH (m)	Loading Run No.	Loading Radius	Strain Run No.
3	100	0.084	0.176	106	32.3	4.02-3	1	
						5.02-3	2	3.03-3
4	80	0.096	0.134	106	32.3	4.01-1	1	
						5.01-1	2	---
5	80	0.090	0.160	106	32.3	4.01-2	1	
						5.01-2	2	3.02
6	80	0.084	0.180	106	32.6	4.01-3	1	
						5.01-3	2	---
7	100	0.090	0.166	49	14.9	5.03-1	2	---
8	100	0.089	0.160	51	15.2	4.03-1	1	3.05-1
9	100	0.088	0.162	43	13.1	5.03-2	2	3.05-2
10	100	0.078	0.139	16	4.9	4.03-2	1	3.05-3

a. Hydrodynamic Program

(1) Comparison of Predicted and Measured Blade Hydrodynamic Loadings

Predicted blade pressures were generated from the computer program for comparison with the test data. All blade pressure data were reduced to a nondimensional static head coefficient (ψ_s) to facilitate comparisons at different tip speeds and inlet pressures. The static head coefficient is defined as:

$$\psi_s = \frac{g}{\rho} \frac{(P - P_{T_o})}{U_T^2}$$

where

P is local static pressure

P_{T_o} is inlet total pressure

ρ is fluid density

U_T is rotor tip speed.

The variation of predicted and measured blade static head coefficient with radius, rotor speed, and flow coefficient for noncavitating and cavitating operation were examined and are discussed in the following paragraphs.

(a) Noncavitating

Noncavitating operation is defined as operation in an area where inlet pressure has no effect on performance. In actuality, the test measurements do show a cavity on the blade suction surface for all test points including those points for which no degradation of performance was noted. Blade pressure measurements for the 100% and 80% speed points are compared with predictions in figures 87 and 88, respectively. Each figure shows data at both test radii for a single tip speed. The exact location of the streamline radii along which the pressures were measured is defined in figure 55.

The predicted and measured pressure surface pressures for all cases (noncavitating) are shown to agree quite well over the region for which experimental data were available. The predicted blade pressure surface head coefficient at the blade leading edge is based on the local inlet total relative pressure. Although the available test data does not show this, there will be a stagnation point close to the leading edge at which the static pressure will be equal to the relative total pressure. Predicted suction surface pressure at the blade leading edge is shown to be at fluid vaporization pressure, the same as observed for the experimental data. The region over which vapor pressure is predicted to exist is somewhat larger than the region indicated by the experimental data. The predicted recovery from vapor pressure along the suction surface also occurs slightly more rapidly than experimentally observed.

Except for a small region on the suction surface near the blade leading edge, the test data and predictions both show a slightly higher static pressure along both the suction and pressure surfaces for the tip radius as compared to the midspan radius. The generally higher blade surface pressures at the outer radius indicate a higher mean or mid-channel pressure. This is consistent with what would be expected since rotation of the flow would cause an increase in static pressure with radius because of centrifugal effects.

A comparison of the 100% and 80% rotor speed data illustrates a variation of blade pressures with speed. It should be noted that fluid vapor pressure corresponds to a static head coefficient of approximately -0.150 for the 100% speed and -0.230 for the 80% speed points since both sets of data were run at the same inlet pressure. Pressure data that is in the area of a vapor cavity is therefore not properly normalized by the static head coefficient.

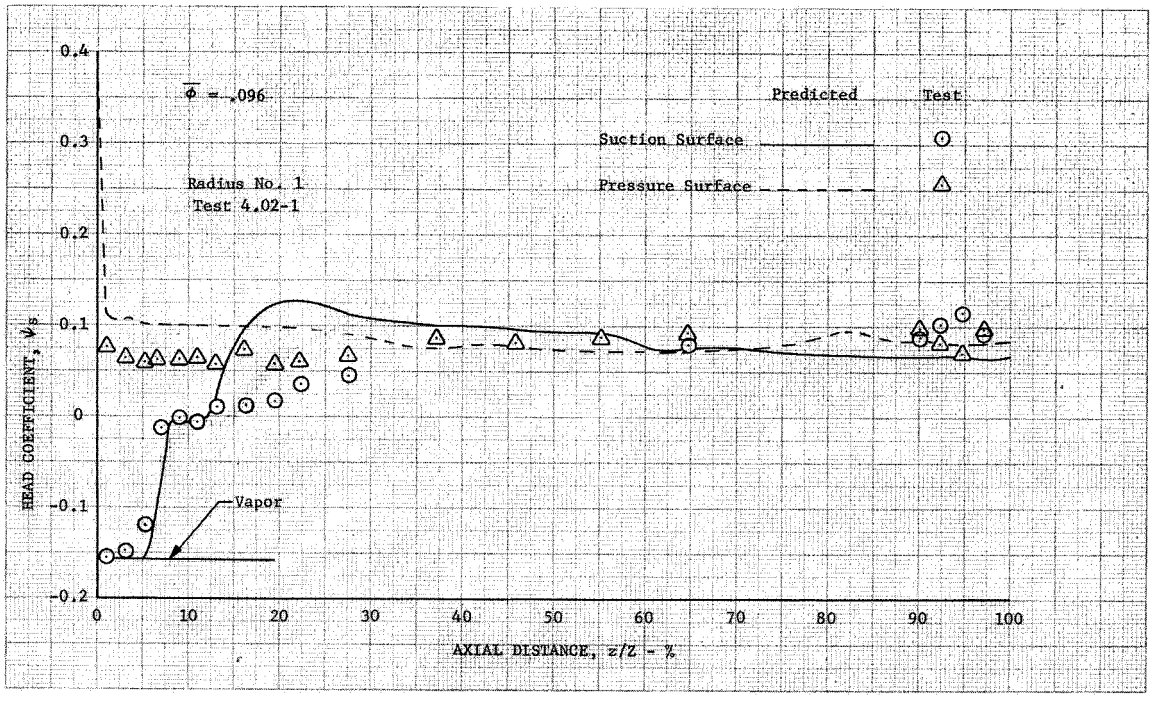

DF 85046

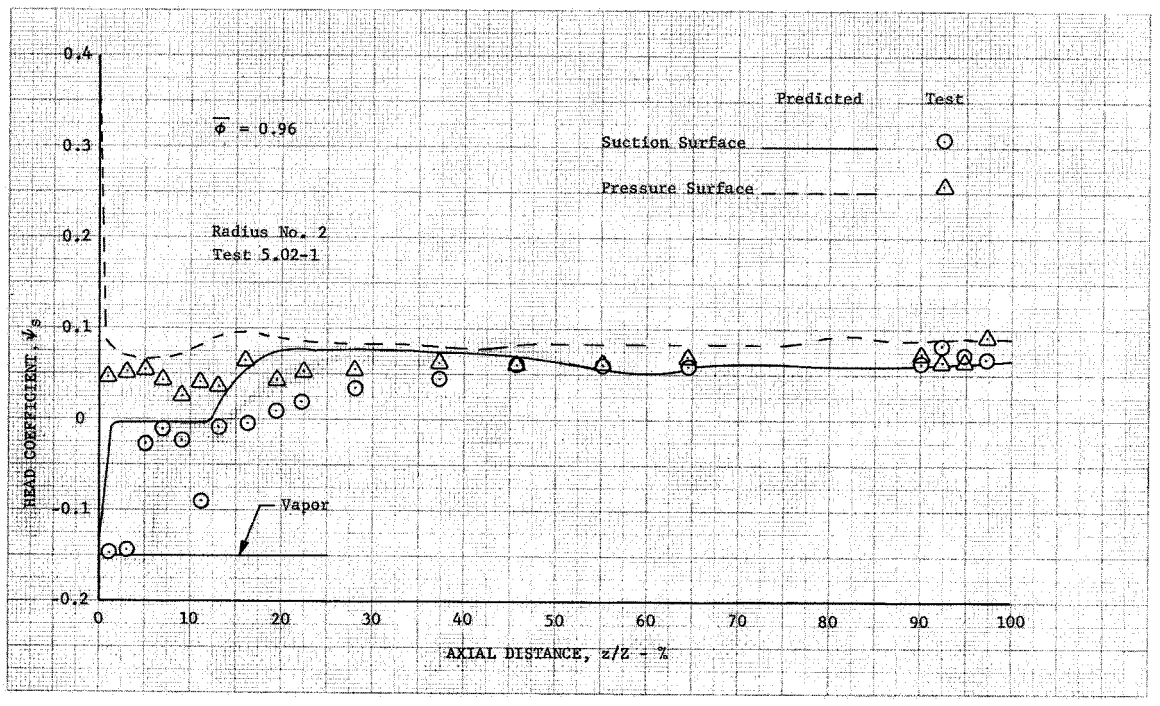

DF 85047

Figure 87. Noncavitating Blade Pressure Distribution
(U_T = 150 ft/sec (45.6 m/sec), NPSH = 106 ft (32.3 m))

Foldout #1

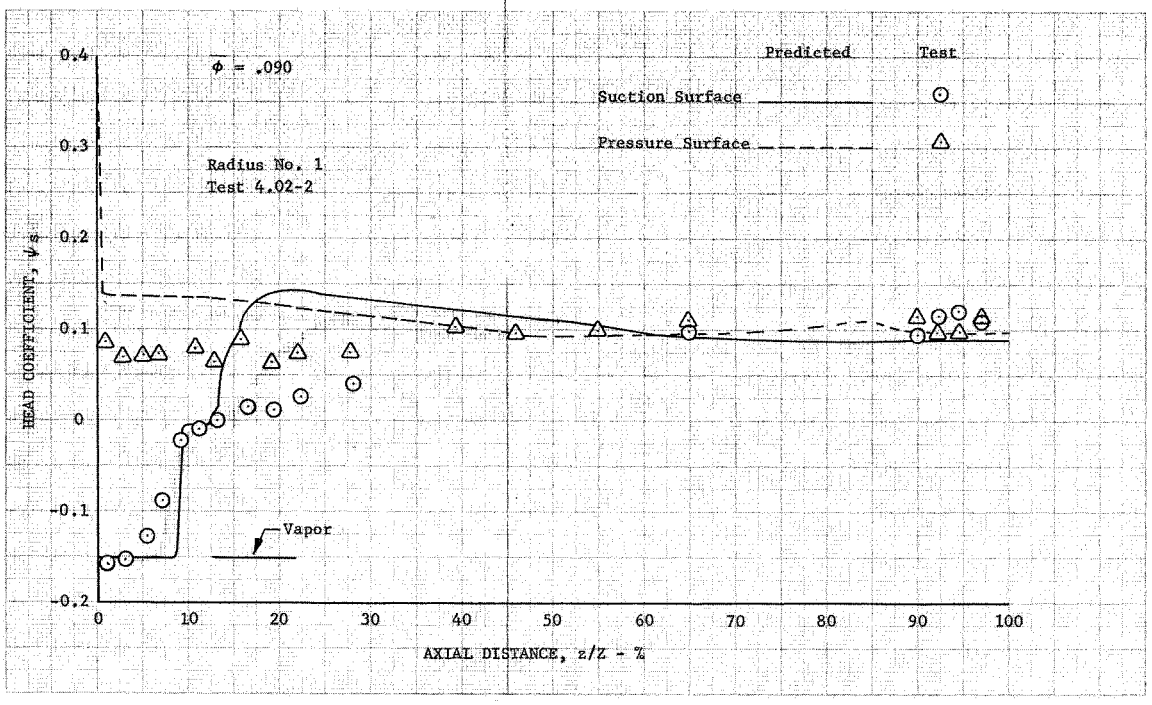

DF 85048

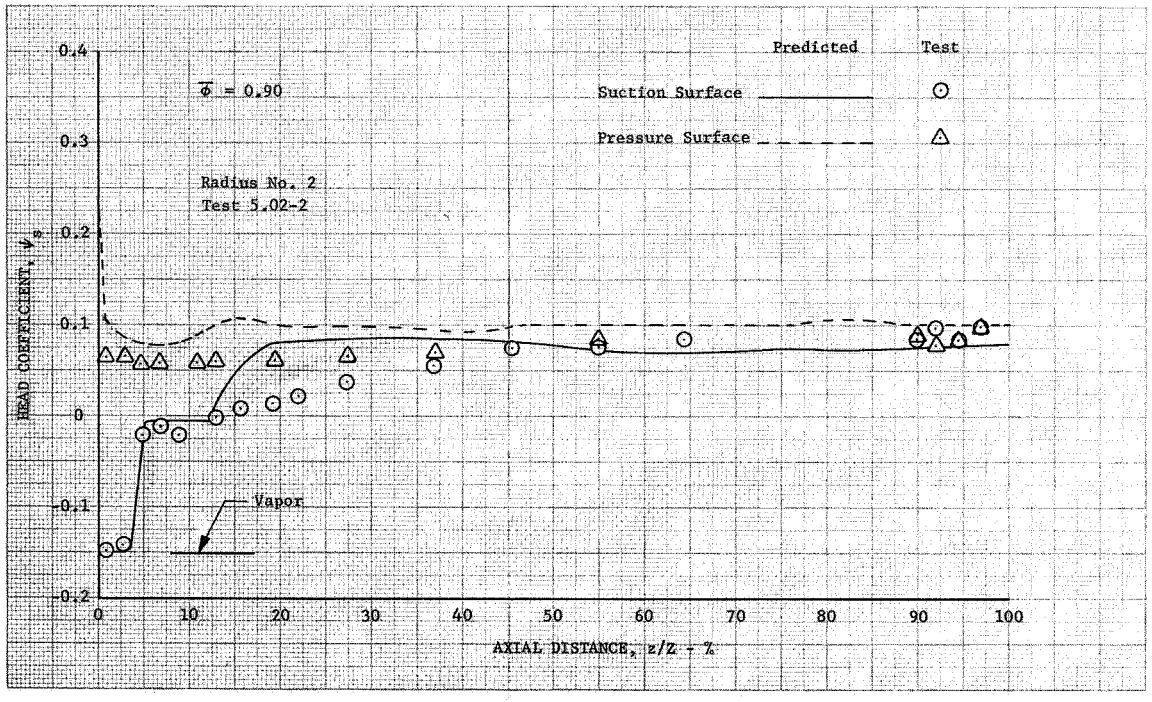

DF 85049

Fold out #2

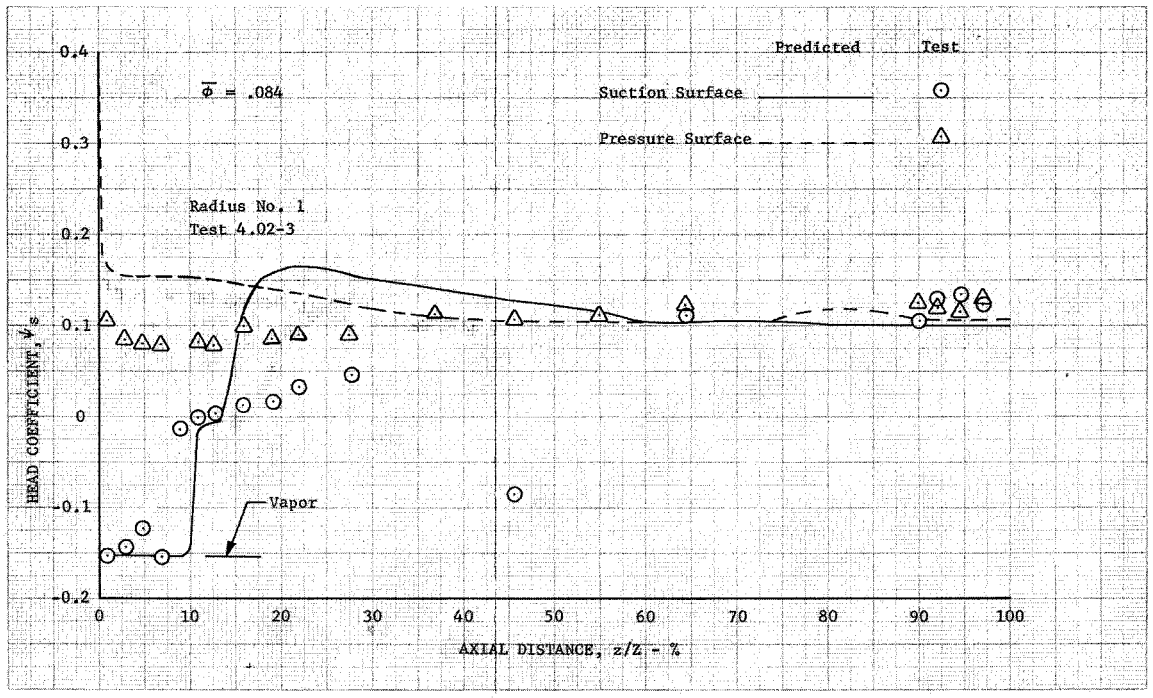

DF 85050

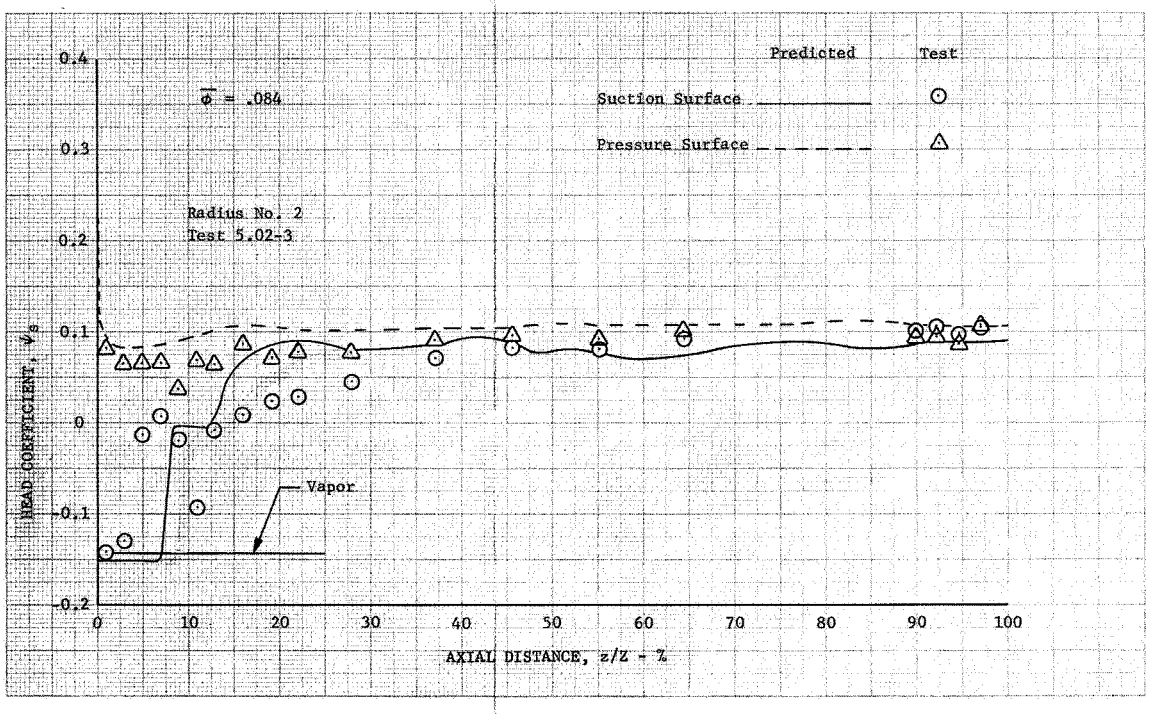

DF 85051

Foldout #3

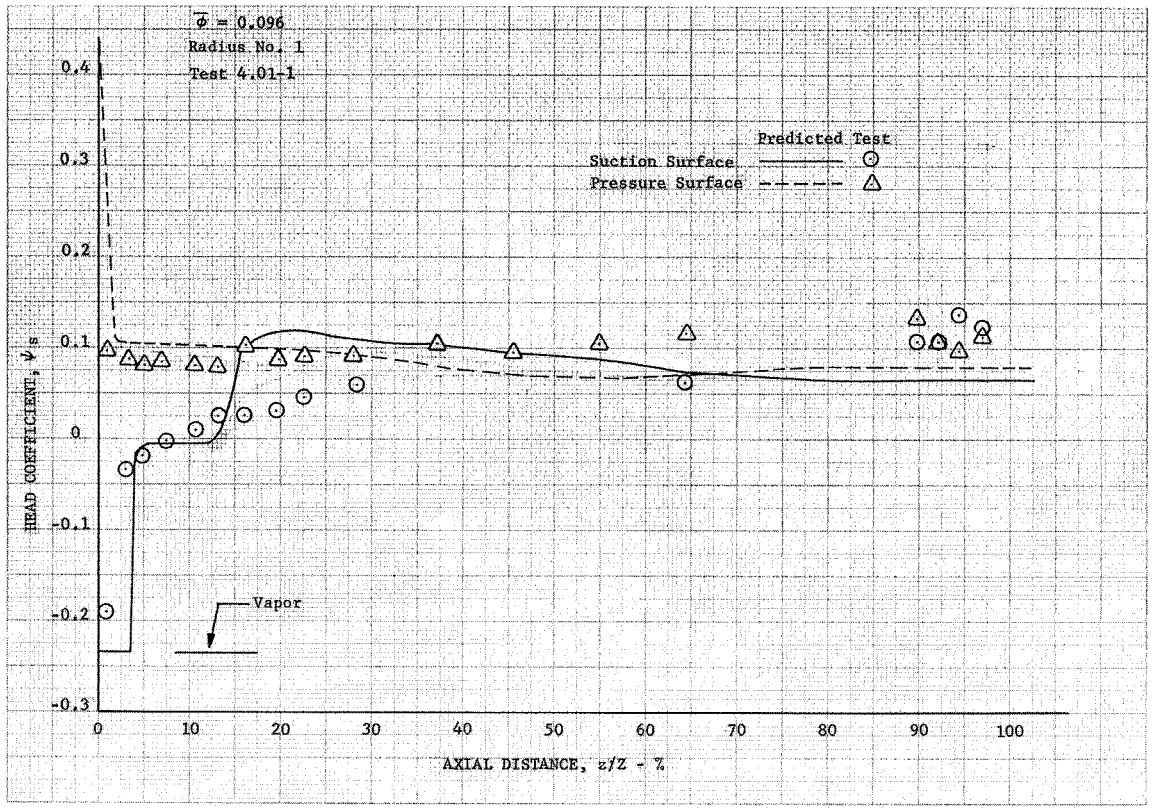

DF 85053

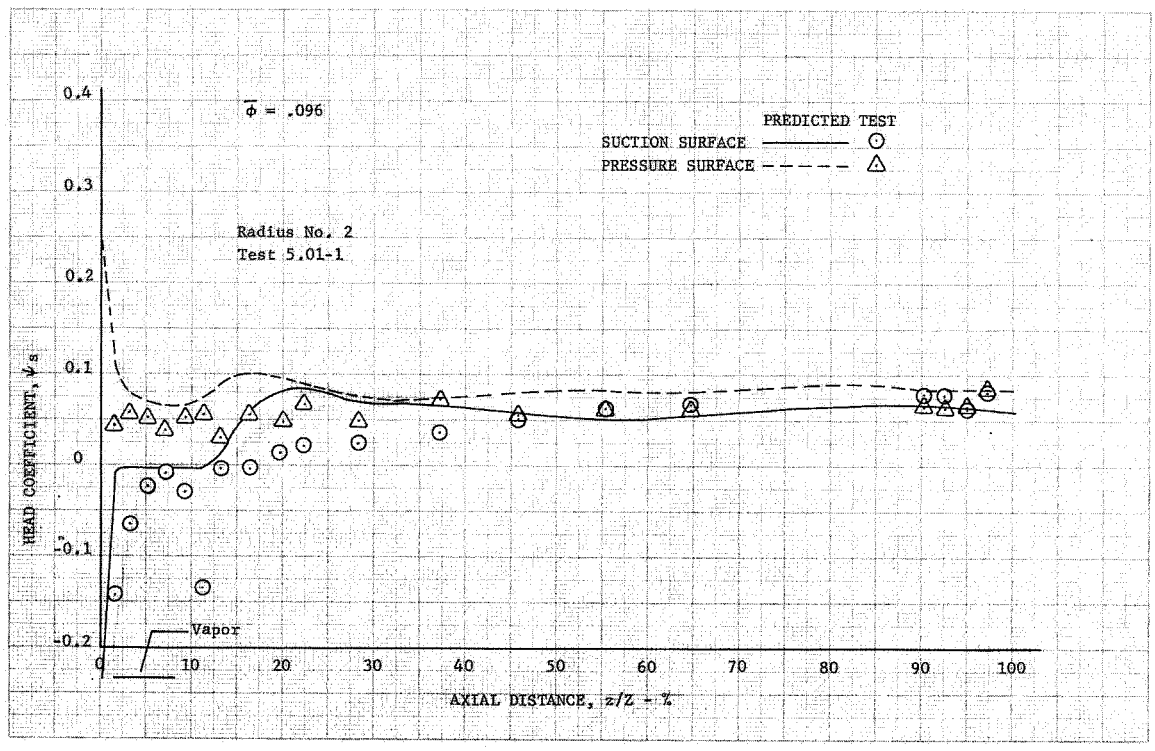

DF 85052

Figure 88. Noncavitating Blade Pressure Distribution
(U_T = 120 ft/sec (37.5 m/sec), NPSH = 106 ft (32.3 m))

Foldout #1

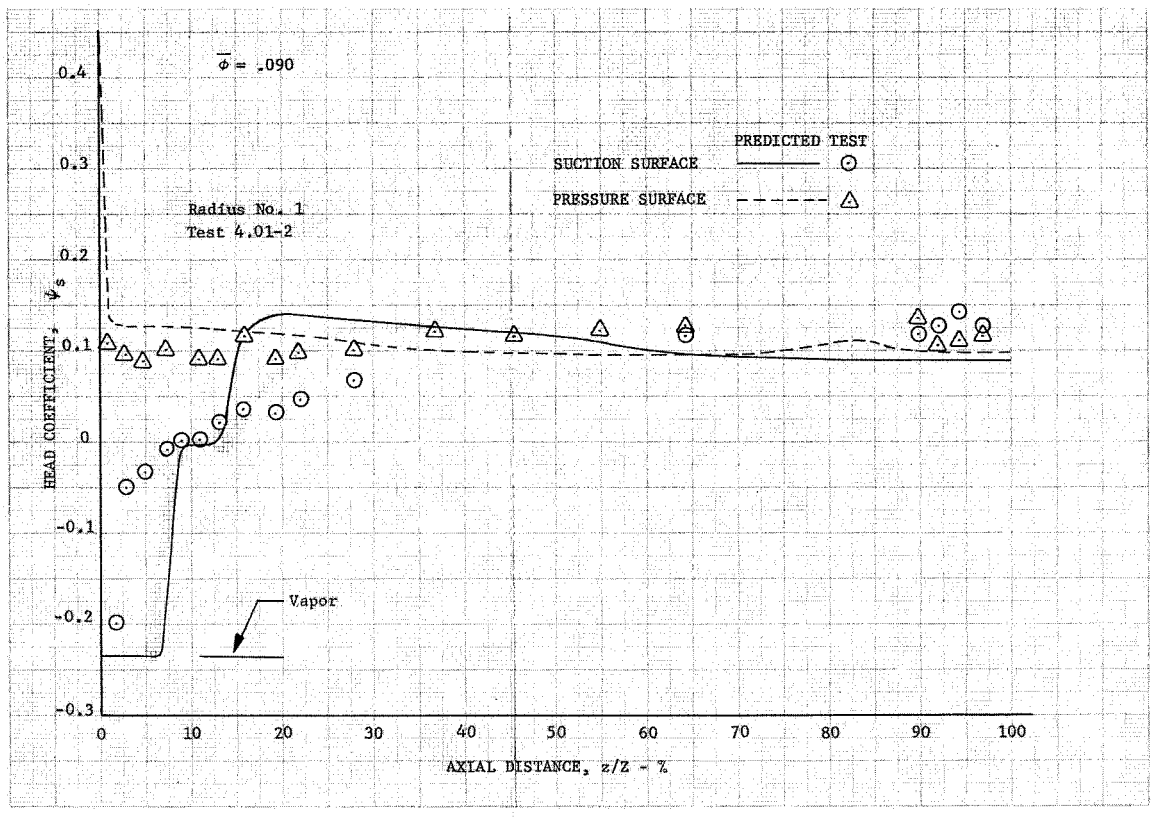

DF 85054

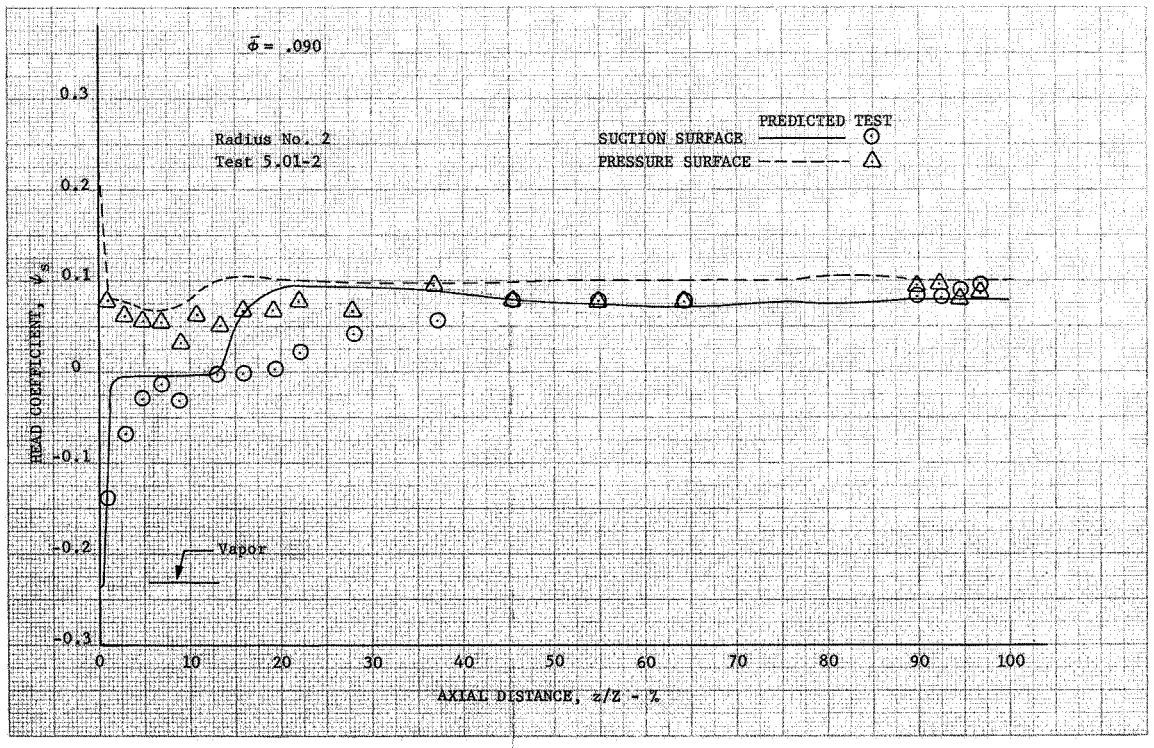

DF 85056

Foldout #2

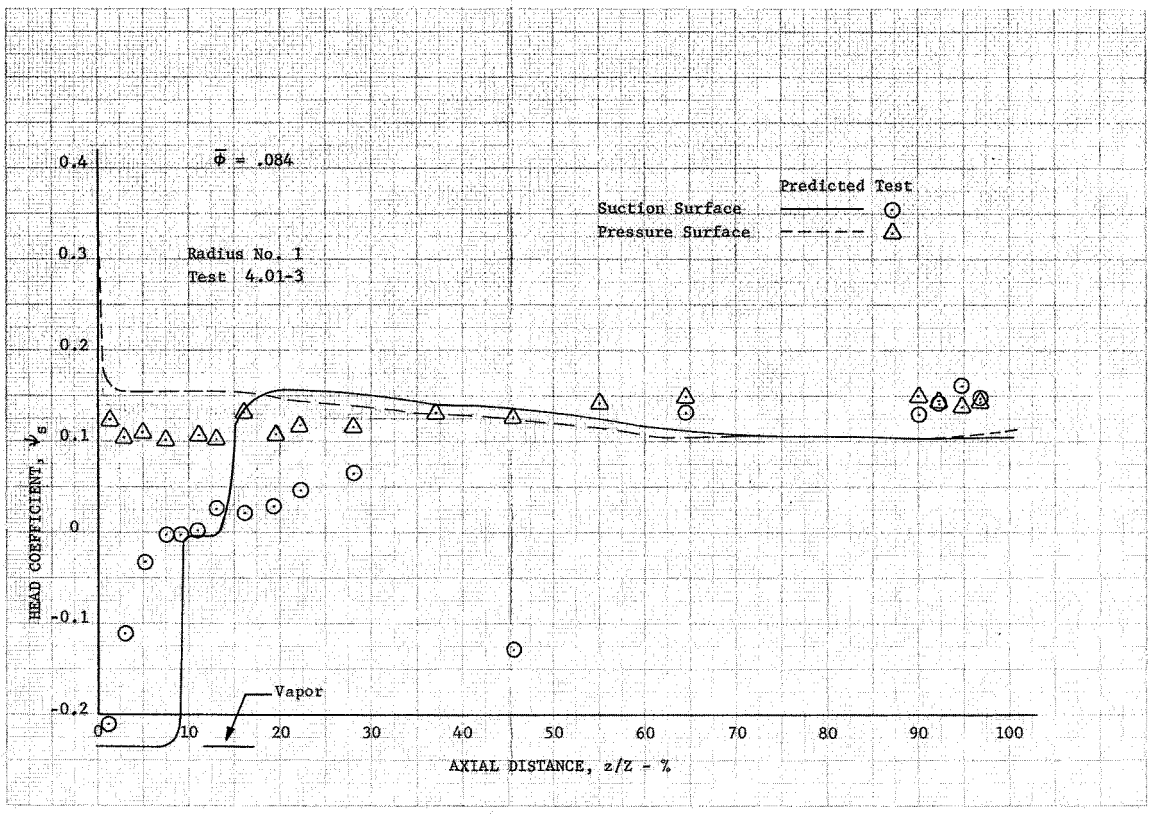

DF 85057

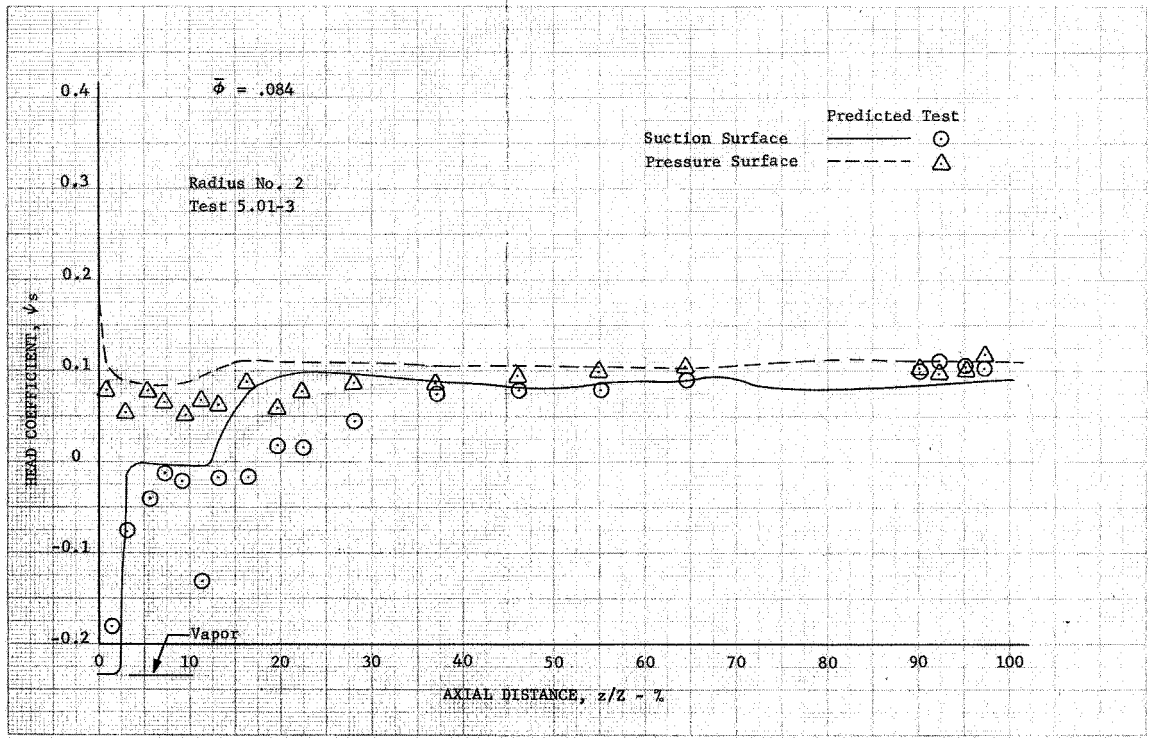

DF 85055

Fold out #3

This small effect of rotor speed is observed to be small. Head coefficients, away from the cavity region, are higher for the low speed tests than for the high speed. In the cavity region, the high speed points show a longer vapor cavity than the low. Again, it is noted that since both speeds were run with the same inlet pressure the higher speed points would be the more severe from a cavitation viewpoint, and the vapor cavities would be expected to be larger. Predicted blade pressures away from the vapor cavity do not show the effect of speed indicated by the test data. In the area of the vapor cavity, however, predicted and test data both show the same trend of increasing cavity size with speed.

The effect of flow coefficient on blade pressure distribution can be seen by comparing horizontally in figures 87 and 88. Both test and predicted data show a gradual increase in cavity length and blade loading as flow coefficient is reduced from 0.96 to 0.084. Blade head coefficients also increase gradually as flow coefficients are lowered in regions away from the vapor cavity. These trends are reasonable since flow incidence increases as flow coefficient decreases and additional blade force is required to turn the flow.

(b) Cavitating

Data at reduced inlet pressures are shown in figure 89. As discussed under "Test Results", it was impossible to set exactly the same NPSH for cavitating tests at the two test radii. Therefore, data at each radius must be compared selectively.

The effect of reduced NPSH on blade pressure distribution at a given radius can be seen by comparing data for the same flow coefficient but at different NPSH. Thus, for the tip radius, the $\phi = 0.090$, NPSH = 51 ft (15.2 m) plot in figure 89 can be compared with data at the same flow coefficient but at an NPSH of 106 ft (32.3 m) in figure 87. For the midspan radius, the $\phi = 0.088$ and 0.090 at NPSH of 43 ft (13.1 m) and 49 ft (14.9 m) plots of figure 89 can be compared with the $\phi = 0.090$ plot in figure 87. The expected trend of increasing cavity length with decreasing NPSH is evident for both comparisons.

Cavity length increases as NPSH is lowered because the lower inlet pressure results in a lower mean pressure within the inducer. All pressures tend to be reduced in direct proportion to the inlet pressure with fluid vaporization pressure as a lower limit. The result of decreasing NPSH is therefore a longer cavity and a relatively constant blade pressure loading over the region covered by the cavity. The blade loading is redistributed so that leading edge load is reduced but relatively high loadings extend further into the inducer.

Predicted and measured pressures along the blade surface agree well, but inaccuracies in the prediction of cavity length are evident. Some increase in predicted cavity length with decreasing NPSH can be seen, but the predicted length increase is smaller than experimentally observed. This inaccuracy in the prediction of cavity length is responsible for the discrepancy between predicted and measured suction surface pressures in the region of the blade leading edge.

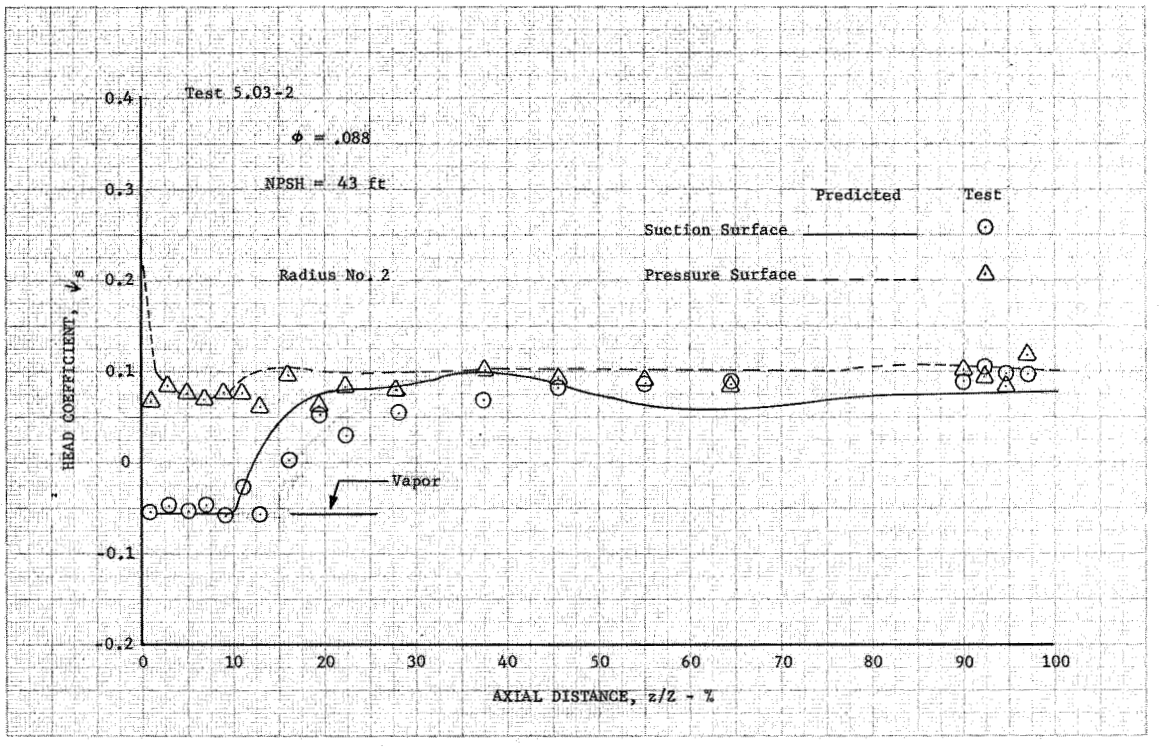

DF 85058

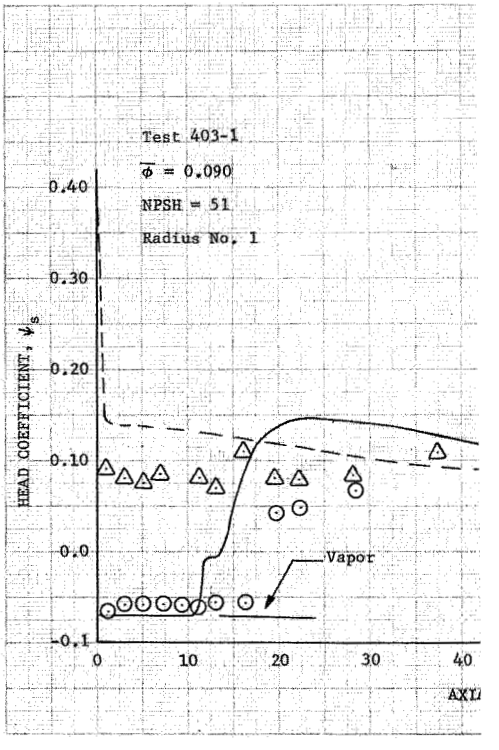

Figure 89. Cavitating Blade Pressure Distribution (U_T = 150 ft/sec(45.6 m/sec))

Foldout #1

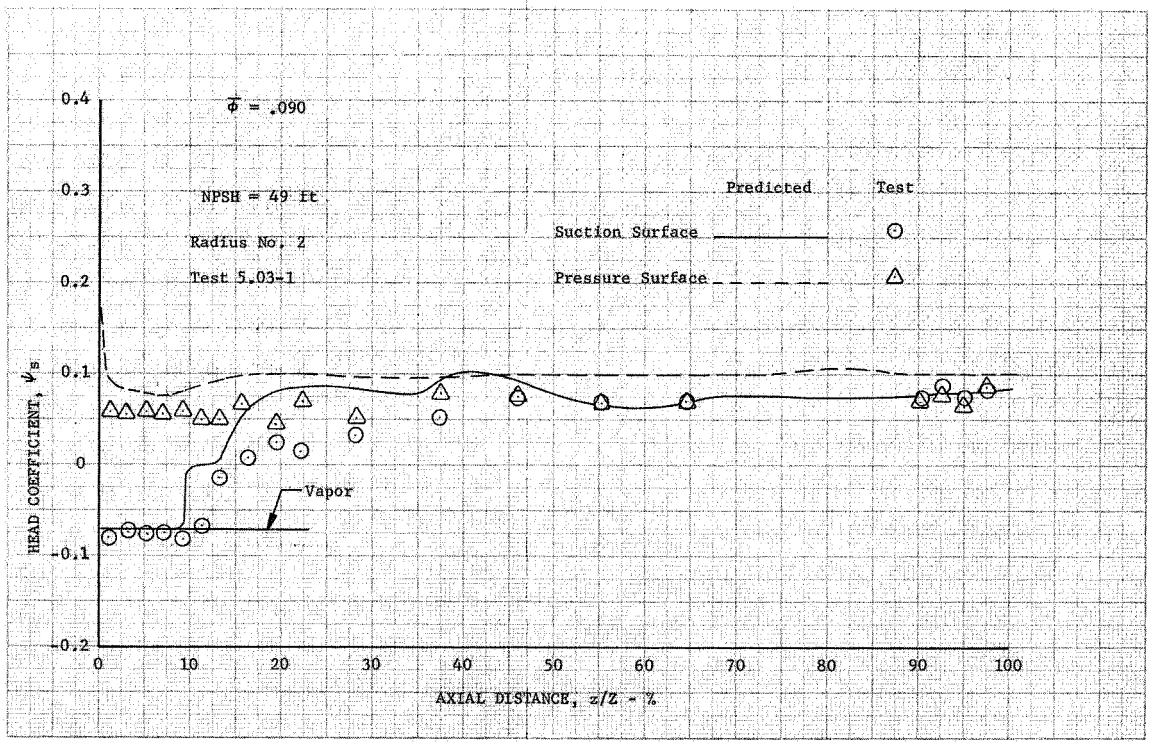

DF 85059

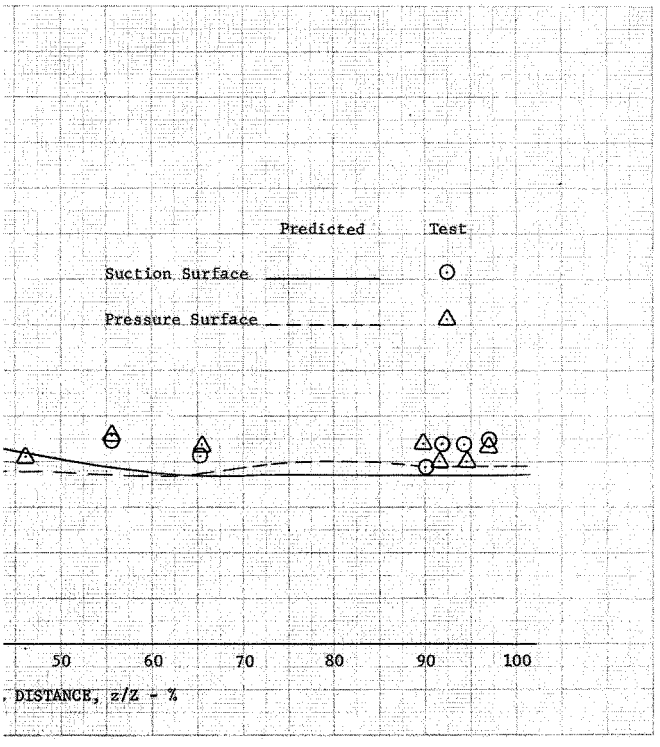

DF 85060

Foldout #2

(c) Summary

In all cases, the maximum blade pressure loadings are seen to occur at the blade leading edge. In this region, saturation pressure was shown to occur over some small region, indicating the existence of a finite vapor cavity even at relatively high values of inlet total pressure. The loading in the region where the vapor cavity collapsed was shown to decrease as a pressure recovery from saturation pressure was made along the blade suction surface. Although blade loadings occurred at the exit of the inducer resulting from blade camber and exit flow deviation, the magnitudes of these were insignificant compared to the loadings which occur on and in the region of the blade leading edge as a result of inlet flow incidence.

Overall comparison between predicted and experimental blade pressure data (both suction and pressure surfaces) indicates good agreement for all regions within the inducer with the exception of the region immediately downstream of the inducer leading edge. In this region, differences between predicted and experimental data along the suction surface result from inaccuracies in prediction of the correct vapor cavity length. Leading edge loadings are accurately predicted, showing vapor pressure to exist on the blade suction surface and total relative pressure existing on the blade pressure surface. The predicted pressure surface pressure was shown to damp out rapidly, as can be surmised from the experimental data. The trends of increased loading with decreased flow coefficient and the redistribution of loading under cavitating conditions, as observed in the experimental data, was also evident in the predicted data.

(2) Modifications to Hydrodynamic Computer Program

During Task VI it was necessary to modify the computer program for the prediction of blade hydrodynamic loading. The modifications were made to the boundary layer and loss system models, the vapor cavity model, the blade pressure loading model, the deviation model and inlet and exit station calculations. These changes were required to improve the accuracy of the computer program predictions for various possible inducer configurations and to improve the agreement between predictions and test data. The present models have been discussed in Section B. The following paragraphs include comments on the reasons for replacing the old models (discussed in Reference 15) and the approach used in the new models.

(a) Boundary Layer and Loss System Models

The boundary layer and loss system models discussed in Section B were added to the computer program during Task VI. The original version of the program (Reference 15) did not directly relate the two models. Instead, a flat plate boundary layer equation was used to calculate displacement thickness, and the loss system was based on pipe flow friction and empirical diffuser loss data. The boundary layer model was in error because it ignored the effect of pressure gradients on displacement thickness. The loss system model was incorrect because: (1) the wall friction loss should vary with the amount and distribution of pressure gradient, (2) the empirical diffuser data is based on constant diffuser

angle, whereas the inducer flow has varying equivalent diffuser angle, and (3) the loss in flow momentum should be related to the boundary layer displacement thickness.

The present boundary layer model is analyzed by a finite difference solution of the Von Karman momentum integral equation, which includes the effect of pressure gradient. The boundary layer shape factor, which relates displacement thickness to momentum defect thickness, is based on Garner's method, which includes the effect of pressure gradients. Thus, the effects of both wall friction and pressure gradient can be accounted for without resorting to inadequate empirical diffuser data. The momentum defect thickness can then be used to calculate the mass average total pressure and pressure loss resulting in improved accuracy and simplification of the calculations.

(b) Vapor Cavity Model

The cavity model originally used in the hydrodynamic loading program assumed that the cavity formed a circular arc. The maximum cavity height and the location along the blade suction surface at which it occurred were solved for, using the results of Stripling and Acosta (Reference 2). A circular arc was fit from the blade leading edge tangent to the point of maximum cavity height. The assumption of symmetric cavity shape was made, thus collapsing the cavity in the same circular arc shape in which it was formed.

A basic weakness in the use of the solutions in Reference 2 is that the two-dimensional model does not include real fluid viscous and three-dimensional flow effects, such as boundary layer blockage, streamline divergence and centrifugal forces for non-axial flow conditions. Therefore, during Task VI, this cavity model was replaced with the model discussed in Section B1. The basic approach of the new model is to satisfy conservation of momentum parallel to the blade at all points in the flowpath. Solution by finite differences allows viscous and three-dimensional effects to be included.

The new model gives essentially the same cavity shape to the point of maximum cavity height as the idealized model of Stripling and Acosta for the special case of two-dimensional, inviscid flow in flat plate cascades (see Section B1). The circular arc cavity collapse assumed in Reference 15 has been replaced by a model which assumes a free jet mixing process when the cavity has reached its maximum height. A comparison of predicted and measured blade suction surface pressures (taken during Task VI testing) shows that the agreement based on this cavity model, although displaying the proper trends with inlet conditions, can be improved.

(c) Blade Hydrodynamic Loading Model

The hydrodynamic computer program employs a two-dimensional hub-to-shroud meridional flow analysis. Blade surface pressures are calculated based on blade-to-blade mid-channel normal pressure gradients, with pressure linearly extrapolated to the blade surfaces.

The original loading model (Reference 15) was based on a tangential pressure gradient. The mid-channel pressure gradient calculated included the flow forces resulting from Coriolis effects, streamline curvature, and through-flow diffusion. Comparison of magnitudes of these effects indicated that the diffusion dominated the calculated blade loading. The sensitivity of the loading to this term, plus the requirement that the through-flow pressure gradient be linearly extrapolated over the tangential blade spacing, which is large for low blade angle rotors, led to inaccurate predicted blade surface pressures.

The calculation of cross-channel pressure gradients normal to the flow direction (discussed in Section B1) includes the same effects as the tangential loading calculation, with the exception of the diffusion effect. The resulting normal cross-channel loadings are small compared to the tangential cross-channel loading. The normal distance between blades for typical inducers is small, thus resulting in much less error in linear extrapolation of the normal blade to blade mid-channel pressure gradient.

Use of normal channel loadings requires that blade loadings be calculated after all the mid-channel static pressures and pressure gradients are calculated so that it is not necessary to extrapolate mid-channel pressures. The success of this model is illustrated in the predicted vs experimental data blade surface pressure comparisons previously discussed.

(d) Deviation Model

As in the original model (Reference 15), deviation is divided into three parts; deviation due to fluid inertia, the cavity shape, and the dumping of the flow downstream of the inducer blades. The description of deviation resulting from the vapor cavity shape is unchanged, and is not discussed here.

The present fluid inertia model discussed in section B1 employs a simplified exponential damping function. The previous model discussed in Reference 15 utilized a model derived from unstaggered flat plate cascade theory. The new model differs from the previous one in that the distribution function is a maximum at the inducer inlet plane, and the effect of staggered blades is taken into account. Comparisons between predicted and measured data indicate that the present model provides more accurate predicted blade pressure loadings.

The exit deviation model as it appeared in the interim report was a function of passage meridional velocity. In improving the method of boundary layer calculation sufficient changes in predicted flow blockage occurred to cause appreciable errors in prediction of exit deviation. The errors in deviation in turn resulted in significant errors in predicted inducer performance. Review of blade pressure loading data taken during Task VI indicated that the major blade loading does indeed occur near the blade leading edge in a region over which a vapor cavity exists.

This fact minimizes the importance of accurate prediction of inducer exit deviation relative to accurate prediction of inducer blade loading in the exit region of the inducer. The previous exit deviation model as it appeared in Reference 15 was replaced by a model similar to that of Carter (Reference 17). That is, deviation is determined by knowing the exit blade angle, the inlet fluid angle, and the rotor solidity. If it is desired to refine the blade pressure loadings in the exit region of the inducer, an improved deviation model is required.

The present method utilized for anticipation of the deviation occurring at the inducer exit is of the same form as that used for the inlet fluid inertia effect. Again, this distributing function is unimportant in this region as the blade pressure loadings are small compared to those which occur near the blade leading edge.

(e) Inlet Station Calculations

Inducer inlet traverse data indicates radial distribution of inlet flow parameters for most operating conditions. The previous inlet model discussed in Reference 15 did not make provisions for varying these parameters. Modifications were made to the program to remove these restrictions and make it possible to input radial distributions of inlet total pressure, axial velocity and absolute flow angle.

(f) Exit Station Calculations

The pressure losses and diffusion that occur due to mixing of the blade wake downstream of the inducer cause streamline locations to change from the positions they assumed at the blade trailing edge. The exit station calculations as discussed in Reference 15 included the dump loss effects but made no provisions for streamline relocation. The exit station calculations have been modified such that radial momentum is preserved by relocation of the streamlines. The method of relocation is based on satisfying simple radial equilibrium.

b. Stress Program

The computer program for prediction of inducer blade stresses, which was formulated during Task II, was validated during Task VI. Both static loading tests and operational tests were conducted with strain gages mounted on the inducer blades. The loading conditions were input to the computer program, and predicted stresses were compared with the test data. In general, the agreement between predicted and measured values was good. The maximum stress was predicted very accurately for all conditions where comparisons were made with the exception of the cavitating case, as shown in table 26.

Table 26. Comparison of Values of Maximum Stress

Type Test	Maximum Stress (Thousands) Predicted lb/in.^{2}	Predicted N/cm^2	Test lb/in.^{2}	Test N/cm^2
Static Load - Leading Edge	70	48	68	47
Static Load - Midchord	30	21	29	20
Static Load - Trailing Edge	80	55	83.5	58
Operational (Noncavitating) - Test 3.02	22.5	15.5	24	17
Operational (Noncavitating) - Test 3.03-1	36.5	25.2	38	26
Operational (Noncavitating) - Test 3.03-2	39	26.9	41	28
Operational (Noncavitating) - Test 3.03-3	45.5	31.3	46	32
Operational (Cavitating) - Test 3.05-1	34	23.4	25	17

(1) Static Loading Tests

The original 90-element breakup of the inducer blade which was used for the design analysis of the inducer is shown in figure 61. This breakup was used to select the load points for concentrated loads on the blade tip near the leading edge (LE), near the midchord region, and near the trailing edge (TE). Elements 6, 48, and 90, respectively, were selected for the static load areas. As discussed in Section F1, a known load was applied to each of these areas so that a value of loading pressure could be input to the computer program.

(a) Leading Edge Loading

To achieve a high degree of accuracy the prediction of blade stress resulting from a load applied to element 6 of the breakup shown in figure 61, a finer element breakup was selected for input to the computer program as shown in figure 90. The total number of elements was held to 102 by using a coarser breakup in the blade trailing edge region, since the stresses were expected to be low in this region. However, the new breakup required that the pressure load be applied over several of the new elements to duplicate the load condition on the previous element 6. This was accomplished by applying the load to elements 11-14, 25-27, and 36, as shown in figure 90.

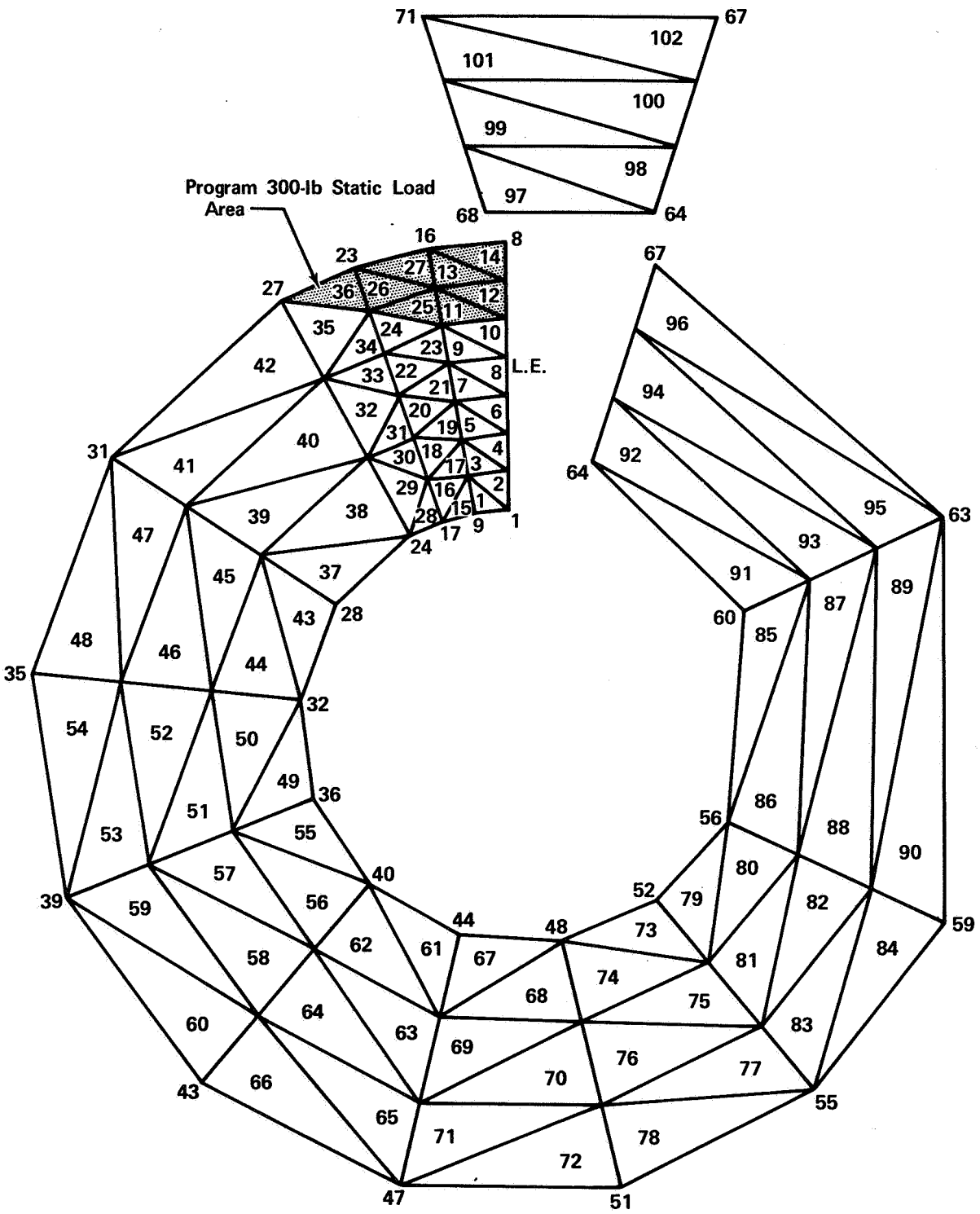

Figure 90. 102 Element Break-Up of Inducer Blade for Stress Analysis FD 39066B

Both the predicted and test values of blade stresses resulting from the LE load are shown in figure 91. The test data can be compared with predictions by interpolating between the constant stress contours plotted in the figure. With a few exceptions, the test data agrees with the predicted distribution of stress. Note that the maximum measured stress (near the LE at the hub) of 67,880 psi (46,700 N/cm^2) falls between the predicted 60,000 psi (41,400 N/cm^2) and 70,000 psi (48,300 N/cm^2) locii. In spite of the relatively high gradients of stress in the LE region the test data generally fell very close to the locations where the predicted distribution would place the measured values.

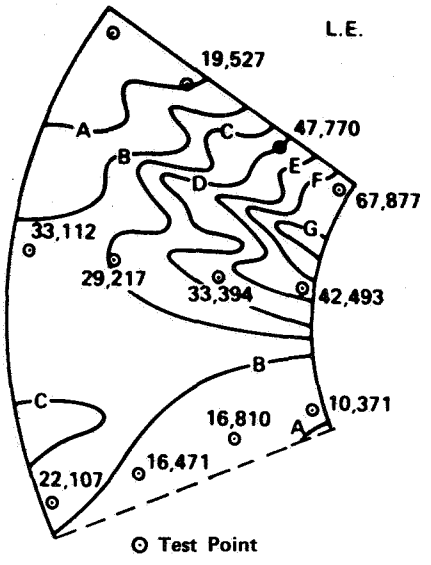

INDEX	PREDICTED EFF STRESS CONTOURS
A	10,000
B	20,000
C	30,000
D	40,000
E	50,000
F	60,000
G	70,000

Figure 91. Measured and Predicted Effective Stresses for Leading Edge Static Loading FD 39066B

(b) Midchord Loading

The 90-element breakup was used for prediction of the blade stresses resulting from a load applied at the tip in the midchord region. A uniform pressure loading on element 48 was input to the computer program. Predicted and measured values of the blade stress are shown in figure 92. Again, the agreement is good for maximum stresses and reasonably good for values away from the maximum stress area. The maximum measured stress occurred on the hub and was 29,050 psi (20,000 N/cm^2). The maximum value predicted was approximately 30,000 psi (20,700 N/cm^2), in the same location as the test point.

(c) Trailing Edge Loading

A new 116 element breakup was used for the case of a trailing edge load (figure 93). The breakup in the trailing edge region was made finer than the leading edge to improve the accuracy in the area where stresses would be higher and changing rapidly. The load element 90, from figure 61, was replaced by the new elements 100-102 and 116 (figure 94).

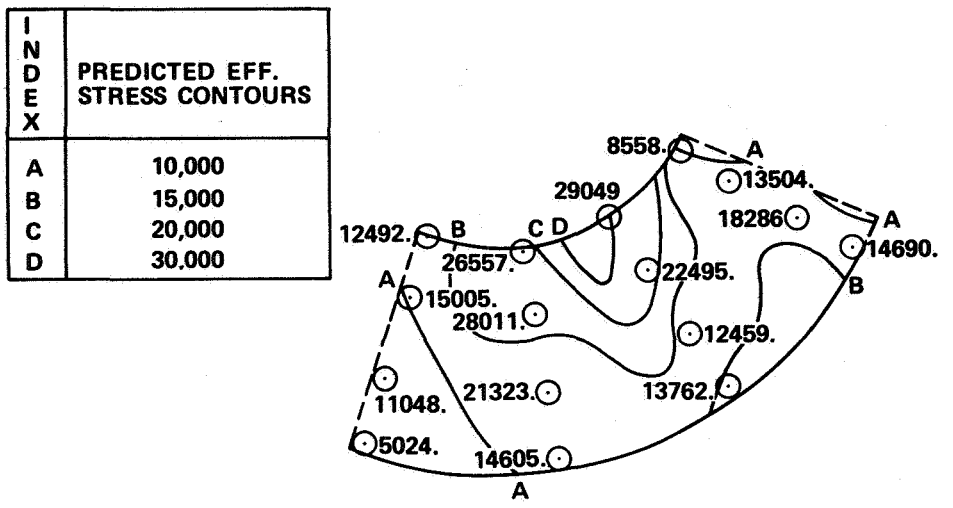

Figure 92. Measured and Predicted Effective Stresses for Midchord Static Loading FD 48212

Figure 94 shows once again that the computer program predictions agree with test data. The maximum measured stress of 83,521 psi (57,500 N/cm^2) falls on top of the predicted 80,000 psi (55,100 N/cm^2) line. The gradients in the trailing edge region were very high for this loading condition. Even better agreement at points away from the maximum stress point could possibly be obtained using a finer breakup for the computer program.

(d) Blade Deflections

As a final check on the computer program results, a 200-lb (890 N) load was applied separately at each of the three load elements and deflections of the blade along the LE and tip normal to the surface were measured and predicted as shown in figure 95. The first predictions were made without accounting for the effect of the fillet between the blade and the hub. To improve the agreement, a second prediction was made by increasing the effective hub diameter to the point of tangency between the fillet and the blade. The curves show good agreement between predicted and measured deflections for all three load configurations.

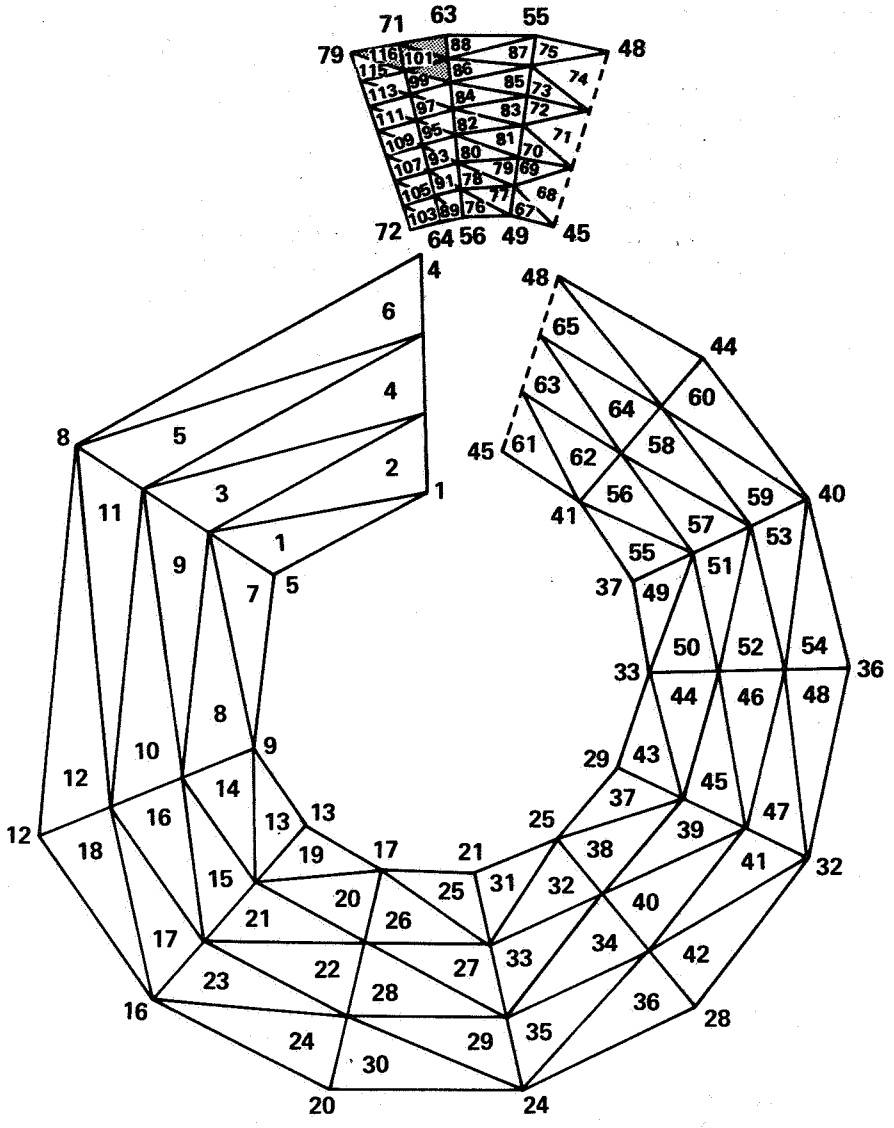

Figure 93. 116-Element Break-up of Inducer Blade for Stress Analysis FD 48213

Index	Predicted Effective Stress Contours
A	20,000
B	30,000
C	40,000
D	50,000
E	60,000
F	80,000

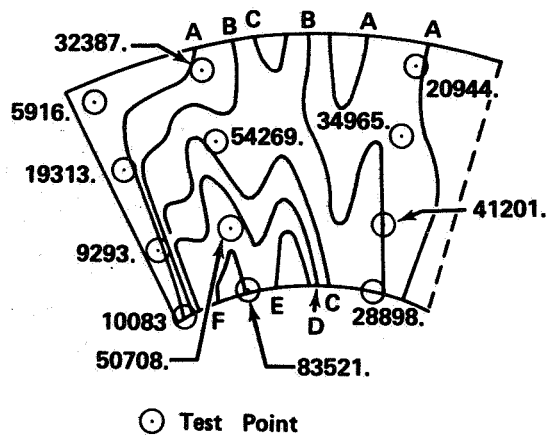

Figure 94. Measured and Predicted Effective Stresses for Trailing Edge Static Loading FD 48211

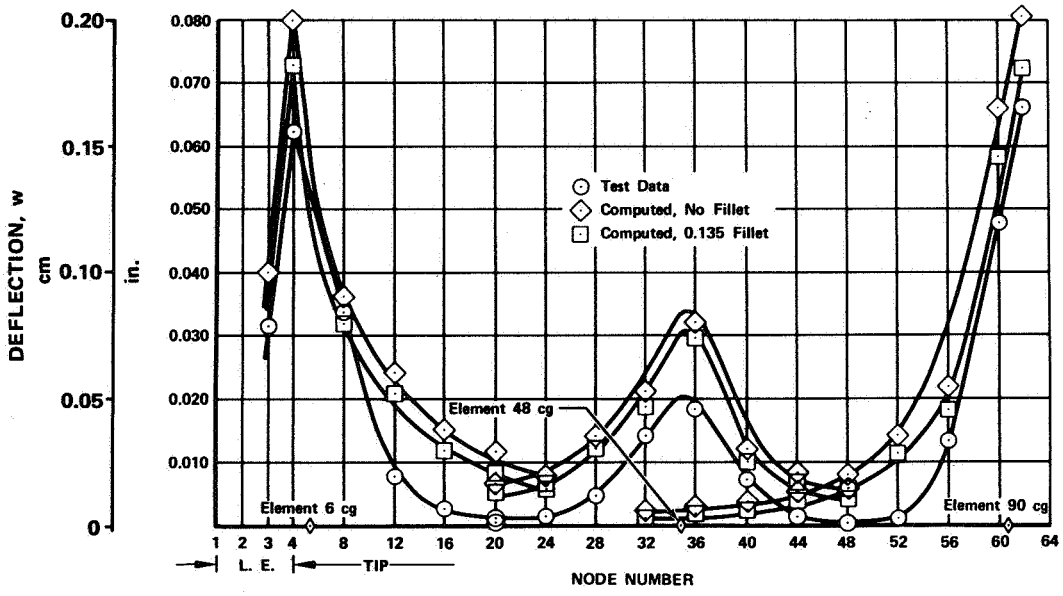

Figure 95. Deflection of Inducer Blade Under Static Load FD 38866A

(2) Operational Tests

(a) Finite Element Breakup

A new breakup consisting of 127 elements (figure 96) and a tapered leading edge was used for the prediction of blade stress under cavitating and noncavitating operating conditions. Results from the hydrodynamic loading computer program had indicated the extent of the blade pressure load under extreme conditions. For noncavitating operation, the blade loading should decrease rapidly from the LE. Under cavitating conditions, the high loading would extend further back. The flow deviation and unloading at the blade trailing edge was expected to cause a slight rise in stress in that area. Accordingly, the breakup shown in figure 96 was selected for analyzing blade stresses under above expected operating conditions.

(b) Blade Hydrodynamic Loading

Measured blade hydrodynamic pressure loads were available for only two radii. Therefore, some interpolation and extrapolation, based on the theoretical radial distribution of blade loading, was required to provide sufficient information for input to the computer program for prediction of blade stresses. Measured pressure data were linearly extrapolated and interpolated to obtain the blade loading distribution away from the leading edge area. Pressure taps were necessarily slightly removed from the leading edge so that the use of predicted loadings was necessary in this area. An example of a loading distribution derived in this manner is shown in figure 97. The difficulty experienced in setting repeatable NPSH points for cavitating tests resulted, in some cases, in obtaining pressure data along only one radius. For these points, a radially constant loading was assumed at locations away from the leading edge, and predicted loading was again used for the leading edge. A loading distribution calculated in this manner is shown in figure 98.

(c) Noncavitating Operation

Figure 99 shows the predicted and measured stresses for noncavitating operation (NPSH = 106 ft, 32.3 m) at 100% speed and at inlet flow coefficients of 0.096, 0.090, and 0.084 (points 1, 2, and 3). Note the agreement between maximum measured stress and predicted stress distribution. The value of predicted stress at the hub was found by extrapolating from the predicted distribution along the dashed line shown in figure 99a. One such curve is shown in figure 100. A maximum stress on the hub equal to 36,500 psi (25,200 N/cm^2), compared to the test value of 37,600 psi (25,800 N/cm^2) is shown. Note also in figure 99a that the other two test values on the dashed line also are close to the predicted values.

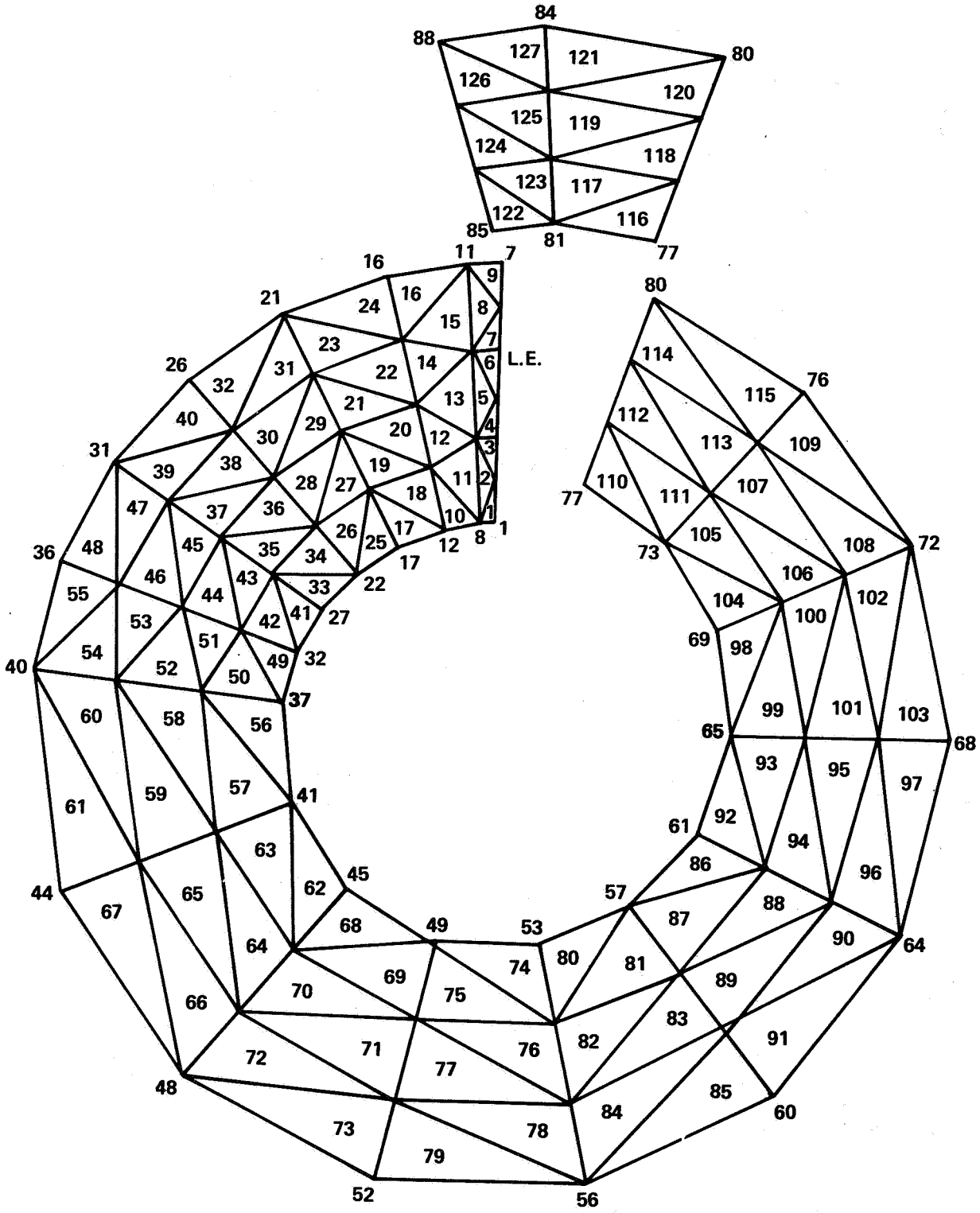

Figure 96. 127 Element Break-up of Inducer Blade for Stress Analysis FD 38863

Index	Pressure Load Contour psi	N/cm^2
A	25	17.25
B	50	34.5
C	75	51.6
D	100	68.9
E	125	86.1
F	150	103.4
G	175	120.6

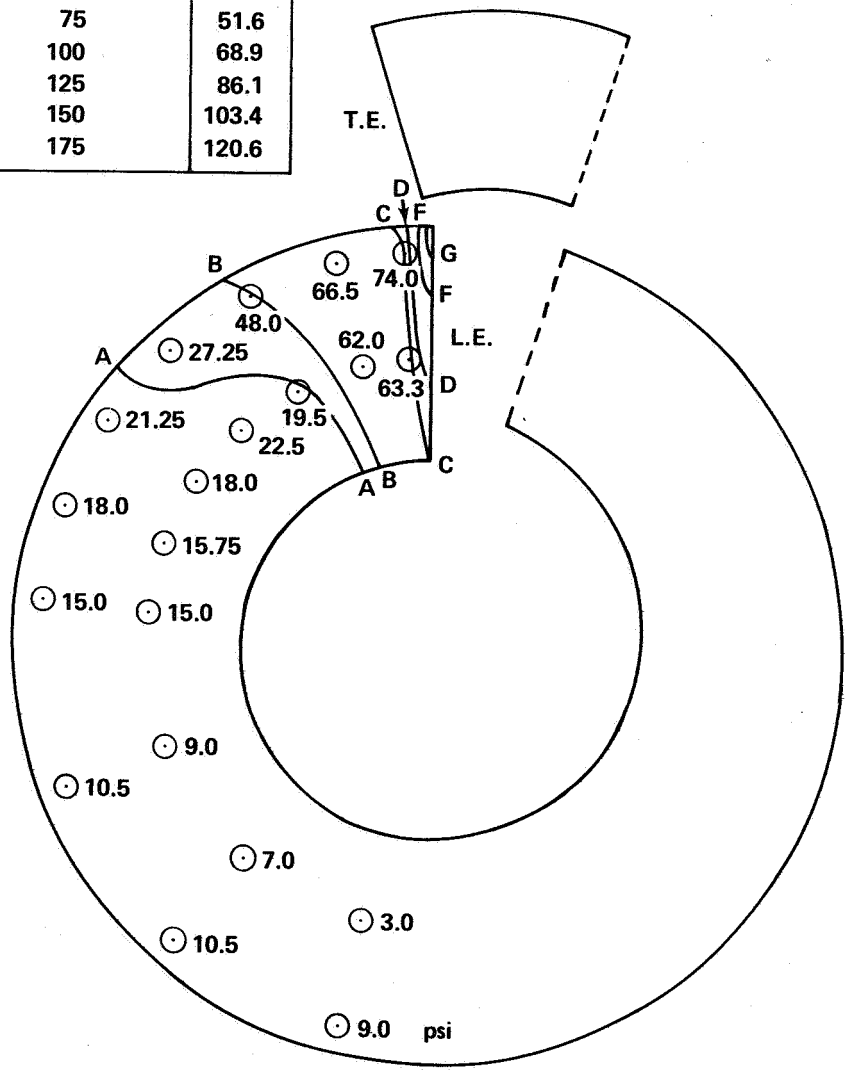

Figure 97. Pressure Load Distribution Used for Input to Inducer Stress Program - Point 2

FD 48214

Index	Pressure Load Contours	N/cm^2
A	psi 25	17.25
B	50	34.5
C	75	51.6
D	100	68.9
E	125	86.1
F	150	103.4
G	175	120.6

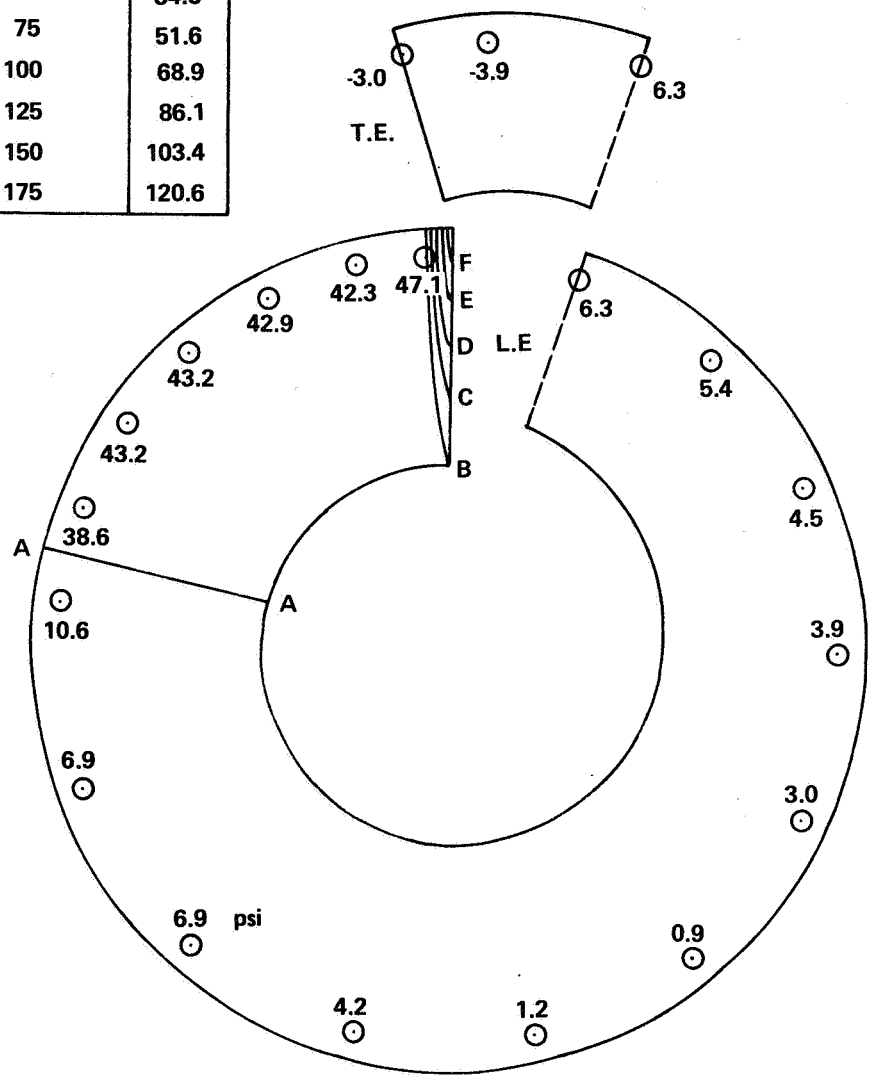

Figure 98. Pressure Load Distribution Used for Input to Inducer Stress Program - Point 8 FD 48215

Index	Predicted Eff Stress Contours	
	Psi	N/CM
A	2,500	1725
B	5,000	3450
C	10,000	6890
D	15,000	10,540
E	20,000	13,780
F	25,000	17,250
G	30,000	20,670
H	35,000	24,100

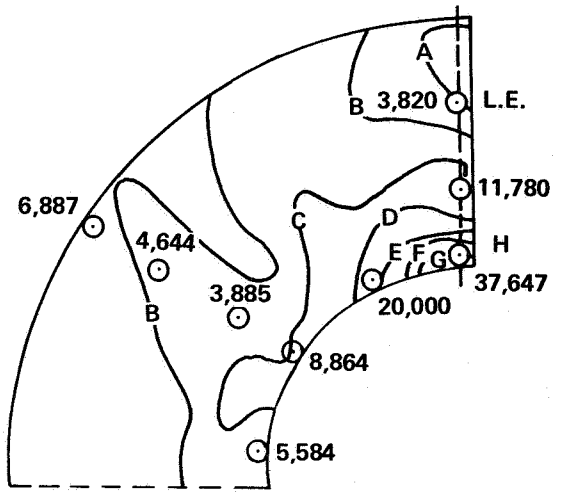

Figure 99a. Measured and Predicted Effective Stresses - Operational Test Point 1 FD 38863A

Index	Predicted Effective Stress Contours, psi	N/cm^2
A	2,500	1,725
B	5,000	3,450
C	10,000	6,890
D	15,000	10,340
E	20,000	13,780
F	25,000	17,250
G	30,000	20,670
H	35,000	24,100

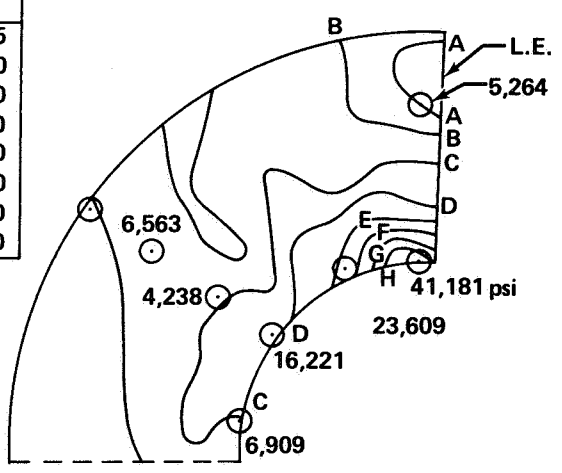

Figure 99b. Measured and Predicted Effective Stresses - Operational Test Point 2 FD 48216

Index	Predicted Effective Stress Contours psi	N/cm^2
A	2,500	1,725
B	5,000	3,450
C	10,000	6,890
D	15,000	10,340
E	20,000	13,780
F	25,000	17,250
G	30,000	20,670
H	35,000	24,100

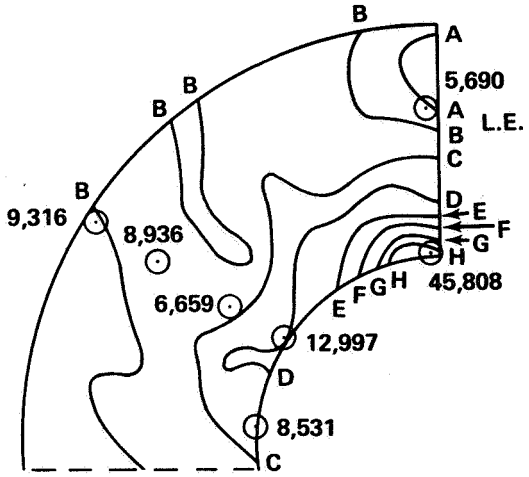

Figure 99c. Measured and Predicted Effective Stresses - Operational Test Point 3 FD 48217

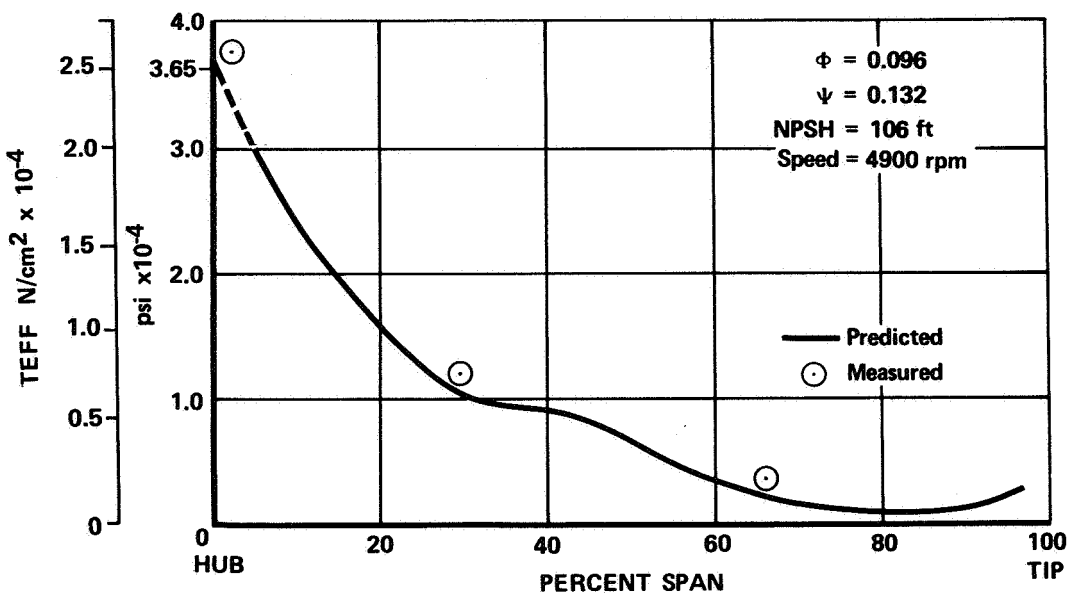

Figure 100. Distribution of Stress With Radius at Leading Edge- Point 1 FD 38864A

Figure 99 shows that the maximum stress decreases as the flow coefficient increases. This is caused by the reduction of hydrodynamic loading resulting from the decrease in incidence as flow rate is increased. Zero incidence would occur at a value of flow coefficient approximately equal to the tangent of the tip blade angle, i.e., a flow coefficient of approximately 0.14. The rate of change in measured maximum stress with flow coefficient (a decrease of 8160 psi (5630 N/cm^2) for an increase of 0.012 in flow coefficient) indicates that the stress would approach zero at approximately 0.15 flow coefficient.

For a given flow coefficient and noncavitating operation, the hydrodynamic loading and resulting stresses and centrifugal stress at all given points theoretically are proportional to the square of the rotor speed. Table 27 is a tabulation of the measured stresses for $\bar{\phi} = 0.09$, at 80% and 100% speed as shown in figures 99b and 101, and the stress obtained by scaling the 100% speed stress to 80% speed. Although close agreement is not obtained everywhere, the general trends are reasonable. Some of the differences at the lower stress levels may be due to inability to set the exact same flow coefficient in the two tests and the sensitivity of stresses to changes in flow coefficient, as discussed above. Therefore, the scaling of stresses by the square of speed (at constant flow coefficient), under noncavitating conditions, is acceptable. However, under cavitating conditions, the cavitation parameter, which varies inversely with speed squared, must also be held constant to allow speed scaling.

Table 27. Effect of Speed on Blade Stress Distribution ($\bar{\phi} = 0.09$)

Measured 100% (4900 rpm)		Measured 80% (3920 rpm)		100% Values Scaled to 80% (3920 rpm)	
lb/in.^{2}	N/cm^2	lb/in.^{2}	N/cm^2	lb/in.^{2}	N/cm^2
5,200	3,590	2,590	1,780	3,330	2,320
---	---	9,040	6,210	---	---
41,180	28,400	24,000	16,500	26,360	18,200
23,610	16,300	14,310	9,880	15,110	10,400
7,680	5,290	4,960	3,420	4,920	3,380
6,560	4,530	3,270	2,250	4,200	2,880
4,240	2,910	4,660	3,220	2,710	1,870
16,220	11,100	7,010	4,830	10,380	7,160
6,910	4,760	5,820	4,010	4,420	3,060

Index	Predicted Effective Stress Contours psi	
A	2,500	1,725
B	5,000	3,450
C	10,000	6,890
D	15,000	10,380
E	20,000	13,780
F	25,000	17,250
G	30,000	20,670
H	35,000	24,100

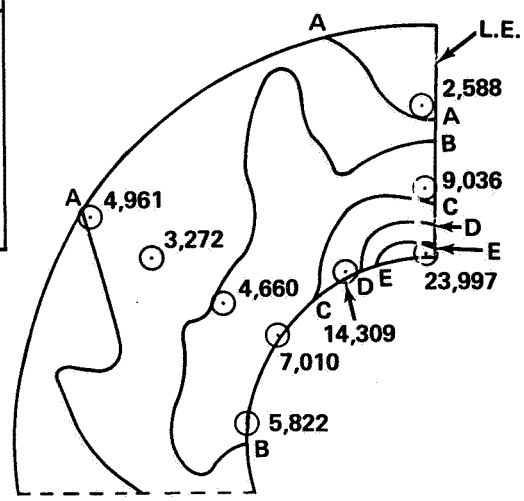

Figure 101. Measured and Predicted Effective Stresses - Operational Test Point 5 FD 48218

(d) Cavitating Operation

Predicted and measured stresses for cavitating operation at point 8 are shown in figure 102. Test conditions were 100% speed, ϕ = 0.089, and NPSH = 50 ft (15.2 m). Most of the twelve strain gages installed for the operational tests were lost during the cavitating runs. Hence, only a limited amount of data was available for correlation with predictions. The agreement between predicted and measured stress was good with the exception of two points on the hub. The maximum predicted value of 34,000 psi (24,100 N/cm^2) at the hub, compared to the measured value of 25,000 psi (17,200 N/cm^2) was obtained by extrapolation along the desired straight line in figure 102.

The pressure distribution input into the stress program is shown in figure 98. Note that the pressure loading at the LE is lower than that of the noncavitating run at the same condition, as shown in figure 97, but the load extends further back. Since the total blade loading for cavitating conditions is the same as for noncavitating conditions, (i.e., no loss in head rise) the lower LE loading and the distribution of the load over a larger area will result in lower stresses as demonstrated.

c. Vibration Program

The computer program formulated in Task II for the prediction of inducer blade natural frequencies, mode shapes, and relative stress distribution was validated in Task VI using laboratory test data. The test data and the methods by which it was obtained are discussed in Sections F1 and F2.

	Predicted Effective Stress Contours psi	N/cm^2
A	2,500	1,725
B	5,000	3,450
C	10,000	6,890
D	15,000	10,340
E	20,000	13,780
F	25,000	17,250
G	30,000	20,670
H	35,000	24,100

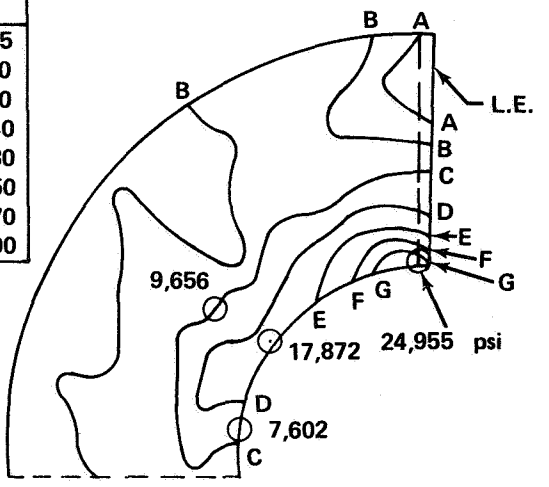

Figure 102. Measured and Predicted Effective Stresses - Operational Test Point 8 FD 48219

Predicted data were obtained using the 90-element analytic breakup of the inducer blade shown in figure 61. Natural frequencies and node shapes for the first thirteen vibration modes and relative effective stress distribution for the first four modes were computed and compared with the test data. The test data were converted to relative stress by comparing the relationship of all stress data to the highest stress data. Predicted relative stress distributions were obtained by extrapolating finite element stresses to locate the highest stress and normalizing all other values to this highest stress.

A comparison of predicted with measured natural frequency and tip nodal position is shown in table 28. Generally, the agreement between predicted and measured frequency was good. For the first four modes predicted frequencies agreed with measured values within 4%; however, the error in frequency prediction was as much as 27% for the other modes. Node shapes could not be measured accurately because of the small displacements away from the tip, but the node-tip intersection for the first four modes is shown in the table. A consistent error in the predicted location of the nodes is apparent but the predicted node locations are spaced approximately the same as the measured nodes.

Errors in predicting tip nodal positions and high mode resonant frequencies are probably due to the choice of the displacement function (Section B2) and the use of a relatively coarse finite element breakup in the analysis. A finer breakup would more accurately account for the increased bending which occurs at the higher modes.

Table 28. Predicted and Experimental Natural Frequencies

Mode	Predicted Frequency, (Hz)	Predicted Tip Node Position	Experimental Frequency, (Hz)	Error	Experimental Tip Node Position
0/0*	1105	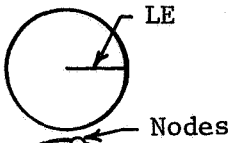	1067	3.5%	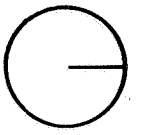
1/0	1262	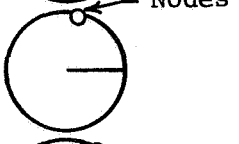	1245	1.3%	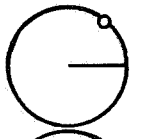
2/0	1438	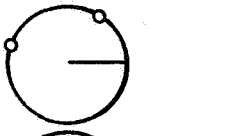	1408	2.1%	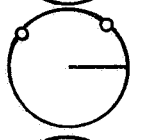
3/0	1583	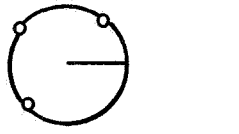	1522	4.0%	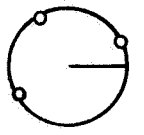
4/0	1782		1640	7.4%	
5/0	2019		1740	16%	
6/0	2294		1947	18%	
7/0	2709		2158	26%	
8/0	3127				
9/0	3633		2858	27%	
10/0	4167		3284	27%	
11/0	4751				
12/0	5345		4315	24%	

*First number is number of radial nodes and second number is number of circumferential nodes.

Predicted and measured relative stress distribution for the first four modes are compared and discussed separately in the following paragraphs. Generally, it is shown that the computer program accurately predicts the finite element at which maximum stress occurs at each of the first four modes.

(1) First Mode (0/0, Umbrella)

The measured first natural frequency was 1067 Hz compared with a predicted frequency of 1105 Hz. Predicted and measured stress contours are shown in figure 103. In general, the predicted and measured contours are consistent. More important from a design point of view, the highest predicted and measured stresses are shown to occur at the same point (node 5).

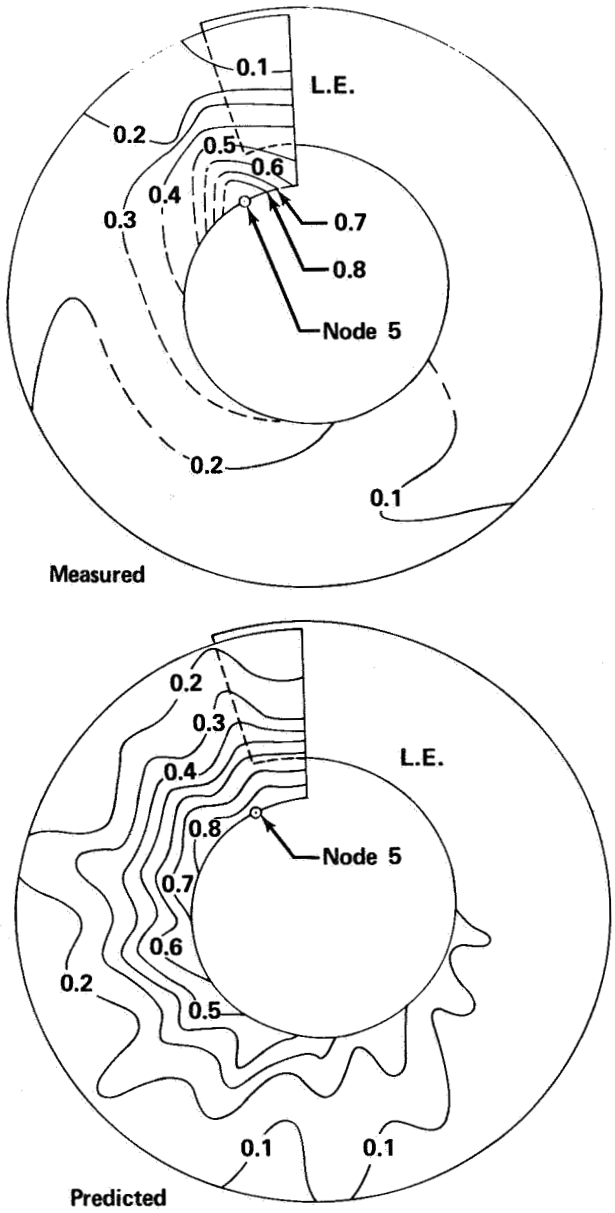

Figure 103. Measured and Predicted Relative Vibratory Stress Contours - First Mode

FD 38862C

(2) Second Mode (1/0)

The measured second natural frequency was 1245 Hz as compared to a predicted frequency of 1262 Hz. Again, stress contours as shown in figure 104, show that test data are consistent with predicted data. The highest stresses were predicted to occur at node 1 which was again verified by tests.

(3) Third Mode (2/0)

The measured value of the third natural frequency was 1408 Hz as compared to a predicted frequency of 1438 Hz. Stress contours, as shown in figure 105, do not agree as closely as they did for the first and second modes. The highest stress was predicted to occur at the centroid of element 56 with slightly lower stresses occurring at the LE root and at root positions around the rest of the hub. The test data, however, indicates that the maximum stress occurs at the LE root and decays to much lower values at root positions around the hub. As discussed in Section F2, there were indications of rear strain gages slipping during the higher mode tests. When this happens the recorded stress will be too low and relative stresses would be based on a reading at some other point, distorting the contour plots. Because of the suspected gage slippage, the measured relative stresses near the LE hub were adjusted to agree with predicted values as shown in figure 106. Note that the predicted and measured relative stress contours are consistent over the front half of the blade. Also, the measured relative stresses in the rear half tend to much lower values than predicted, which is consistent with the conclusion that the rear strain gages were indicating low strains due to strain gage slipping.

When the predicted data is compared with the adjusted measured data a good correlation of the predicted and measured maximum stress point and stress contours is shown for this mode.

(4) Fourth Mode (3/0)

The measured fourth natural frequency was 1522 Hz as compared to a predicted frequency of 1583 Hz. The predicted and measured relative stress contours are consistent, as shown in figure 107. The maximum stress was predicted to occur at the centroid of element 80, whereas tests indicated that it occurred at node 57. As in the case of the third mode, it was suspected that gages had slipped in the region of element 80 and that the stress was actually higher than that measured. The measured relative stress at the LE hub was therefore again adjusted to agree with the predicted value at this point as shown in figure 108. The resulting measured relative stress contour again shows close agreement between predicted and measured maximum stress locations.

In general, the agreement of predicted vibratory characteristics of the inducer with test data obtained in Task VI indicates that the inducer vibration program is a useful tool for design purposes and no changes are required. This accuracy is further substantiated by the agreement between predicted data and theoretical plus experimental data for geometric shapes as discussed in Section B2.

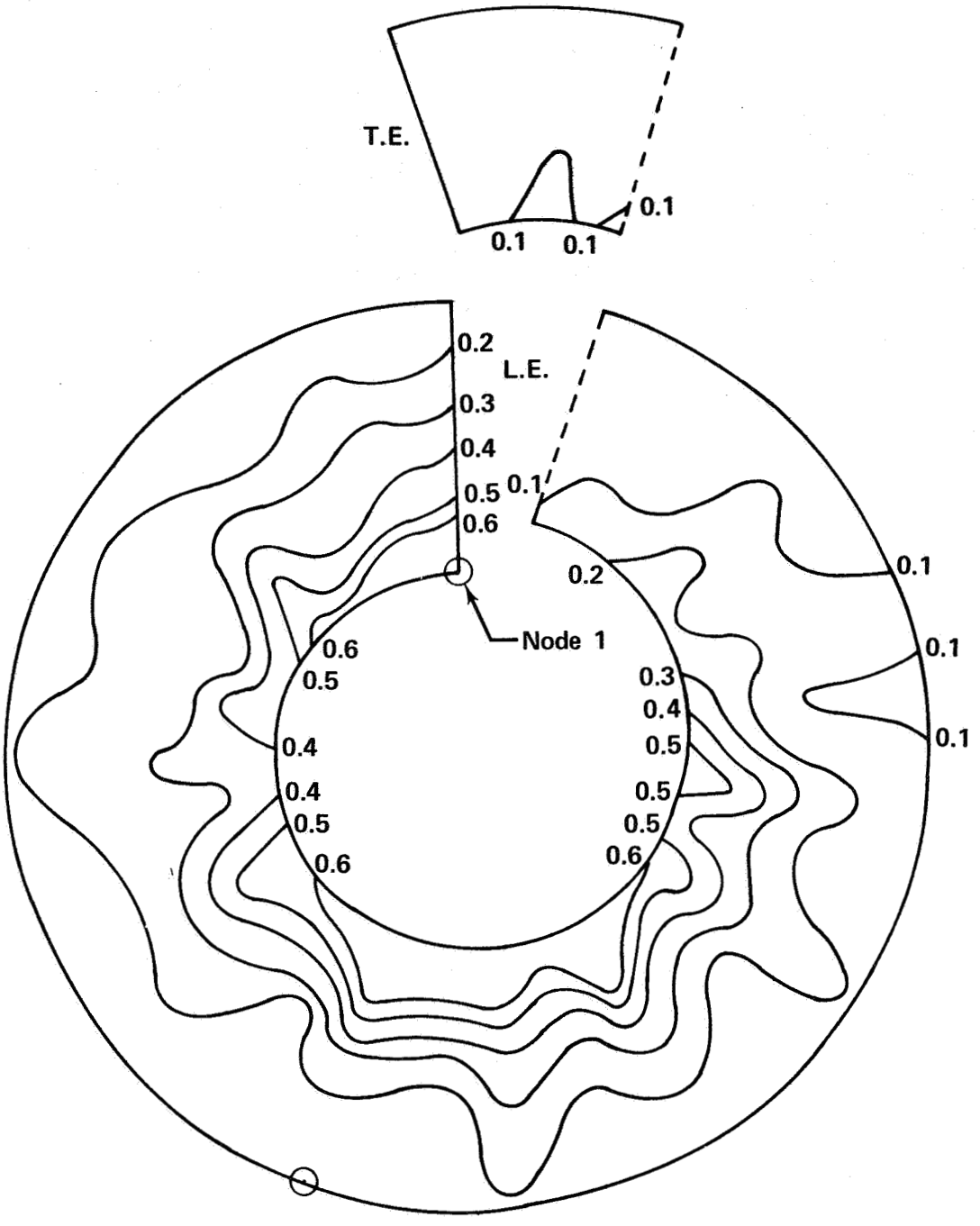

Figure 104a. Measured and Predicted Relative Vibratory Stress Contours - Second Mode, Predicted

FD 48220

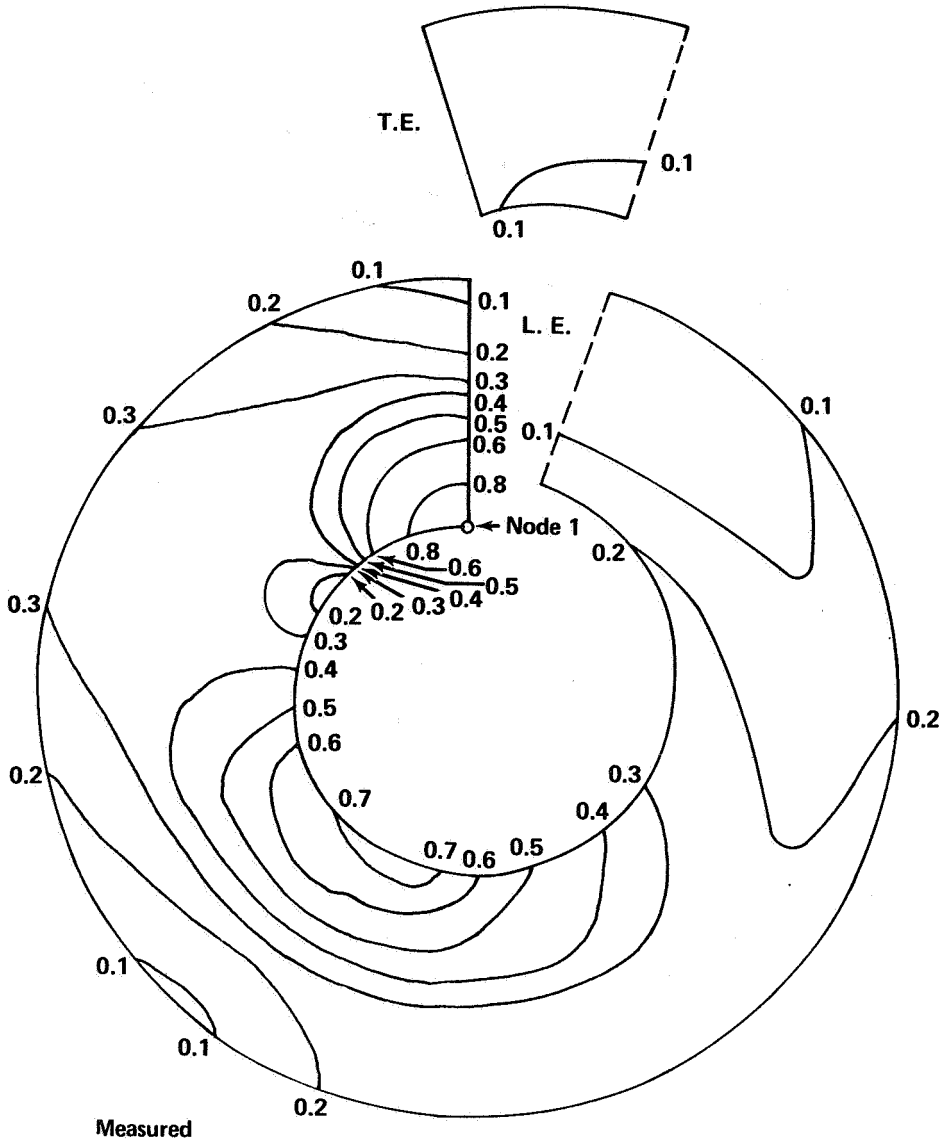

Figure 104b. Measured and Predicted Relative Vibratory Stress Contours - Second Mode, Measured

FD 48221

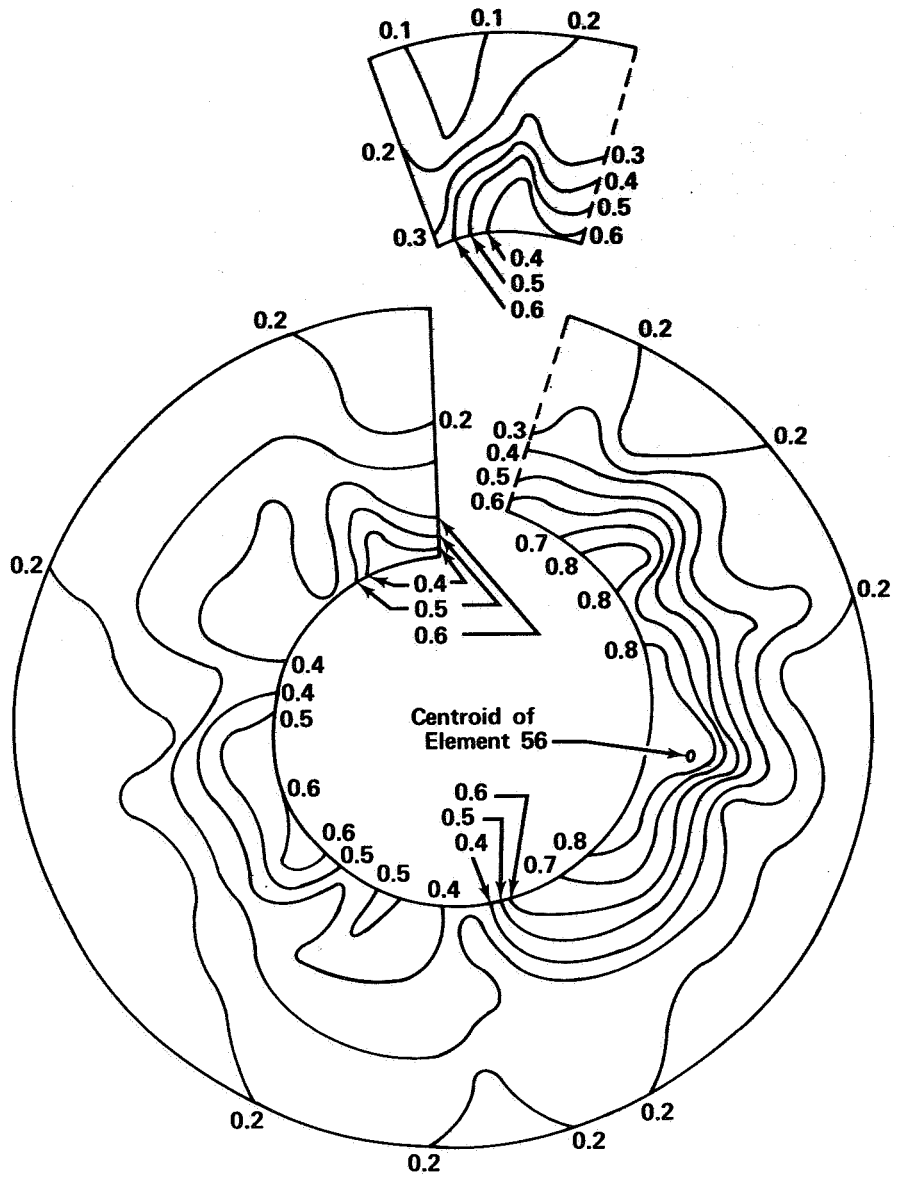

Figure 105a. Measured and Predicted Relative Vibratory Stress Contours - Third Mode, Predicted FD 48222

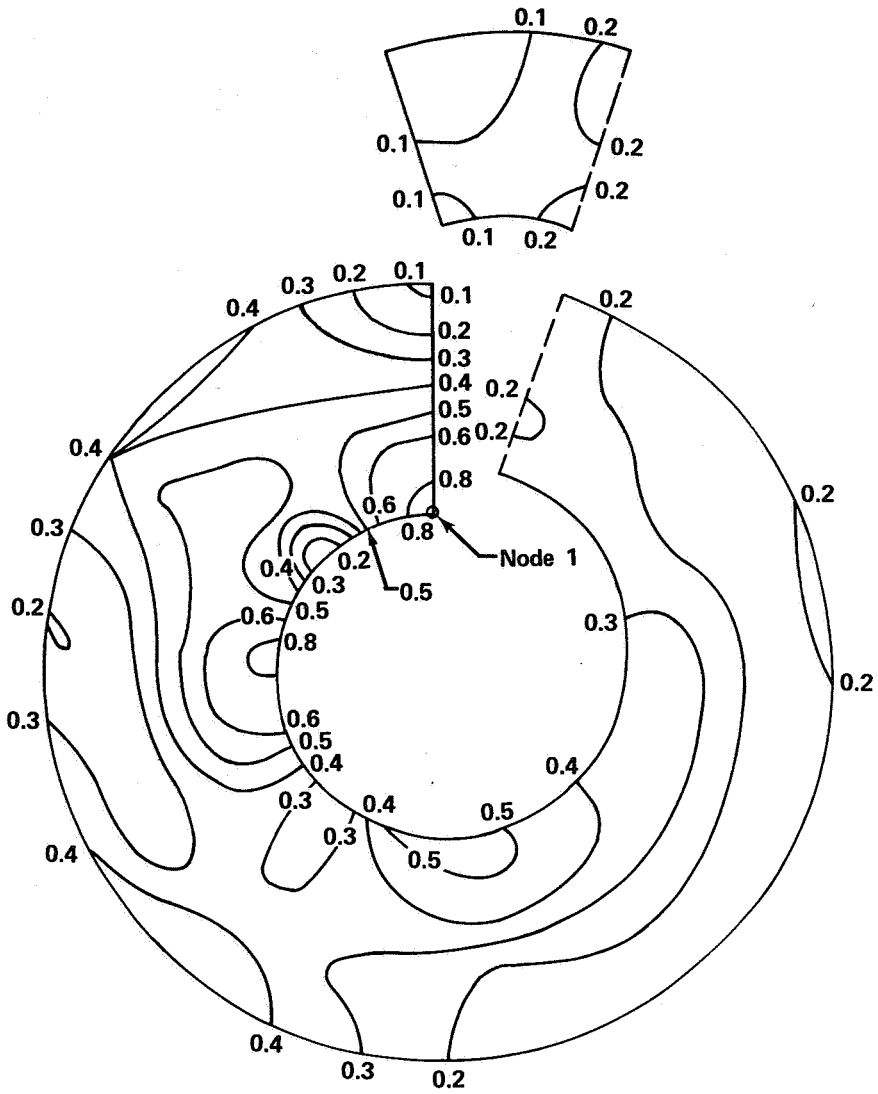

Figure 105b. Measured and Predicted Relative Vibratory Stress Contours - Third Mode, Measured

FD 48223

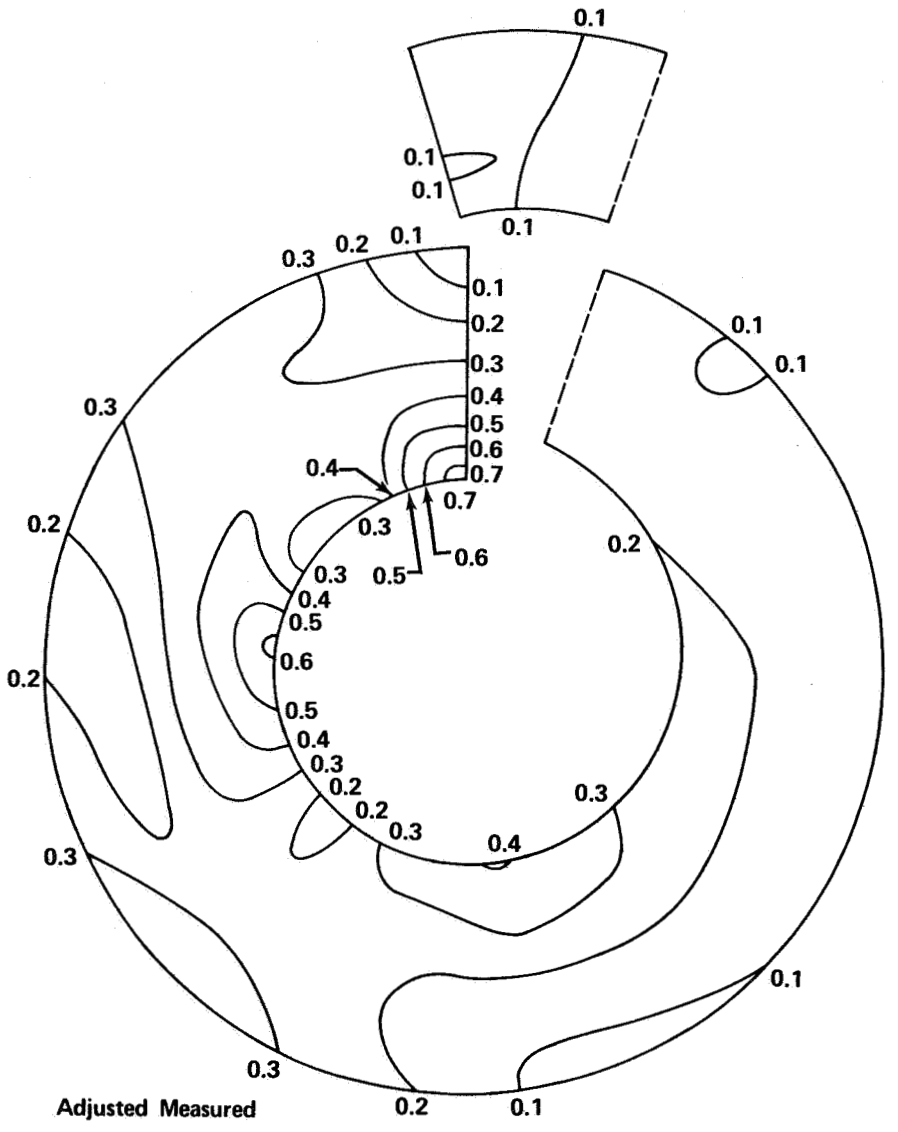

Figure 106. Adjusted Measured Relative Vibratory Stress Contours - Third Mode FD 48224

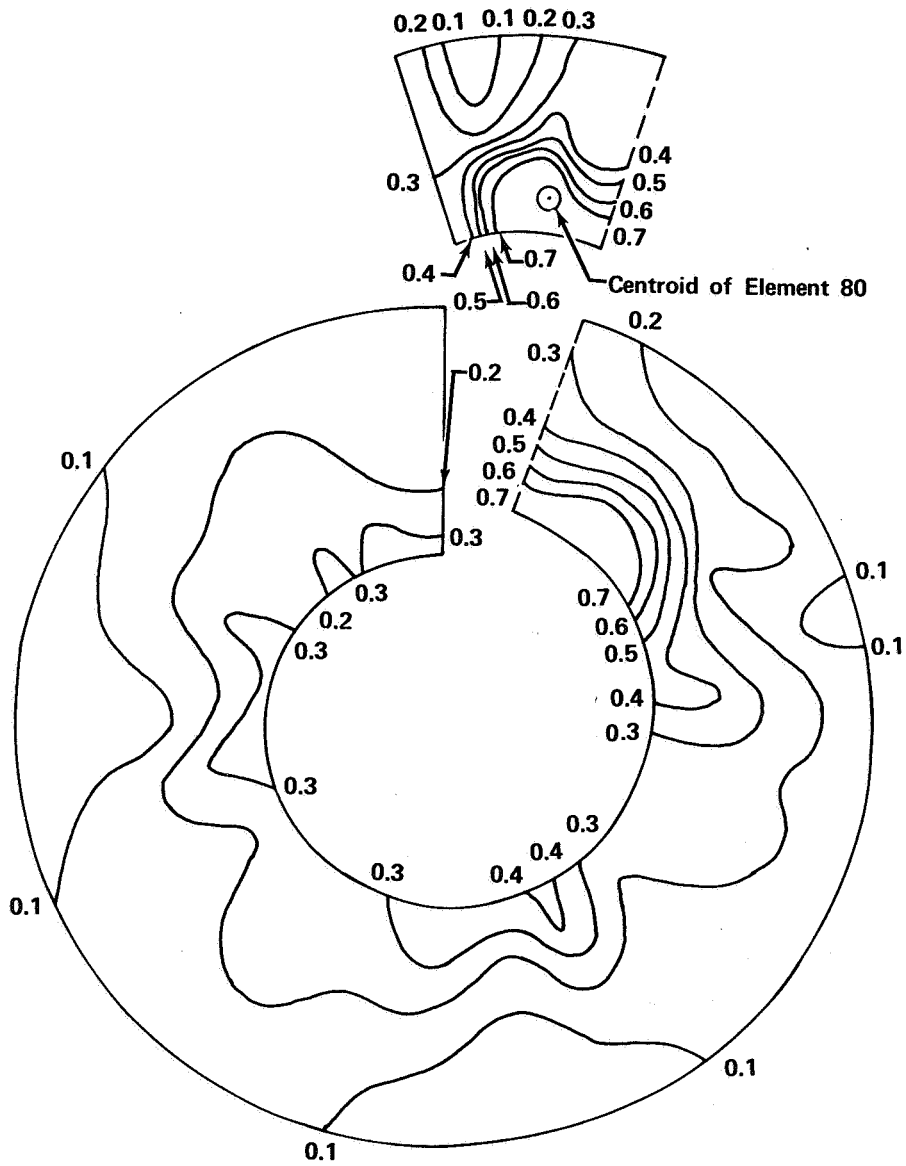

Figure 107a. Measured and Predicted Vibratory Stress Contours - Fourth Mode, Predicted FD 48225

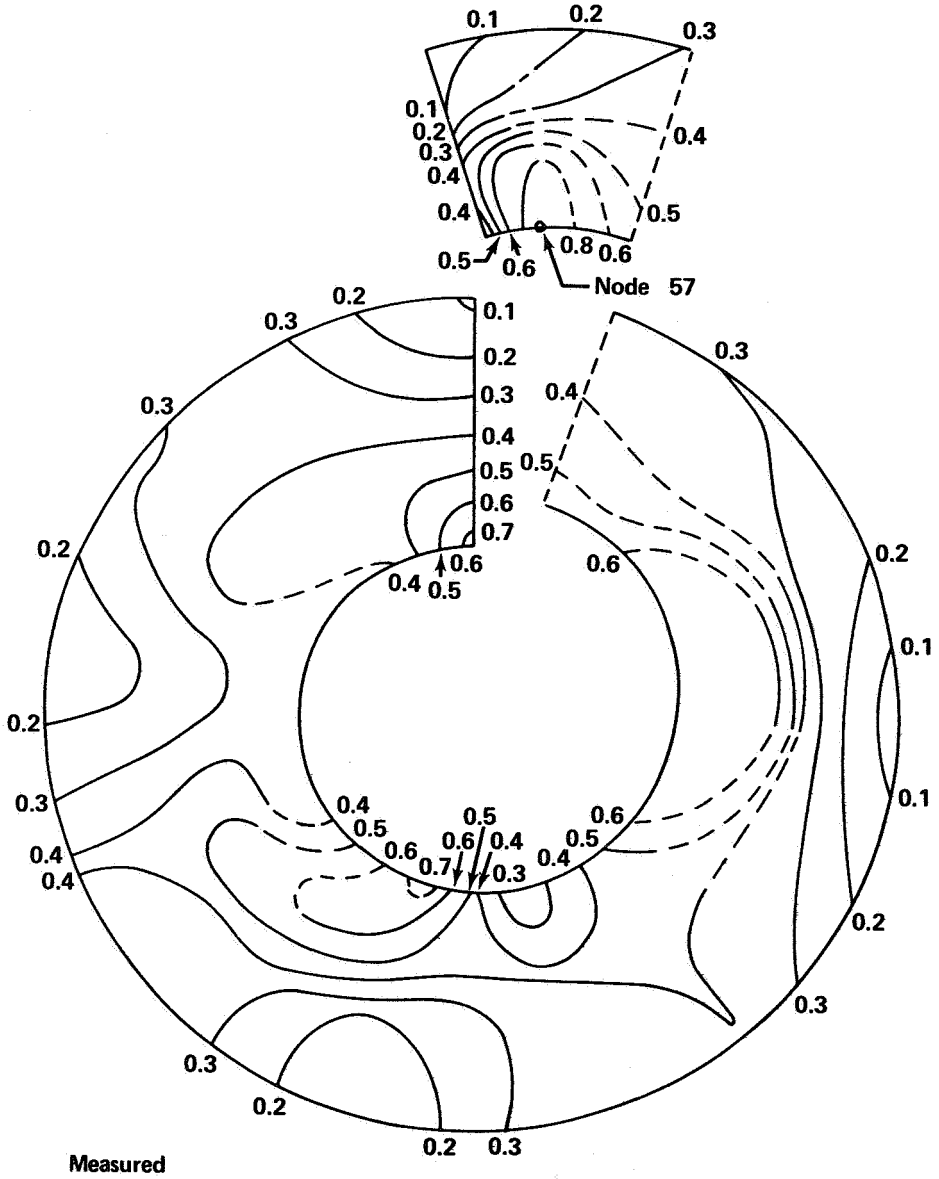

Figure 107b. Measured and Predicted Vibratory Stress Contours - Fourth Mode, Measured FD 48226

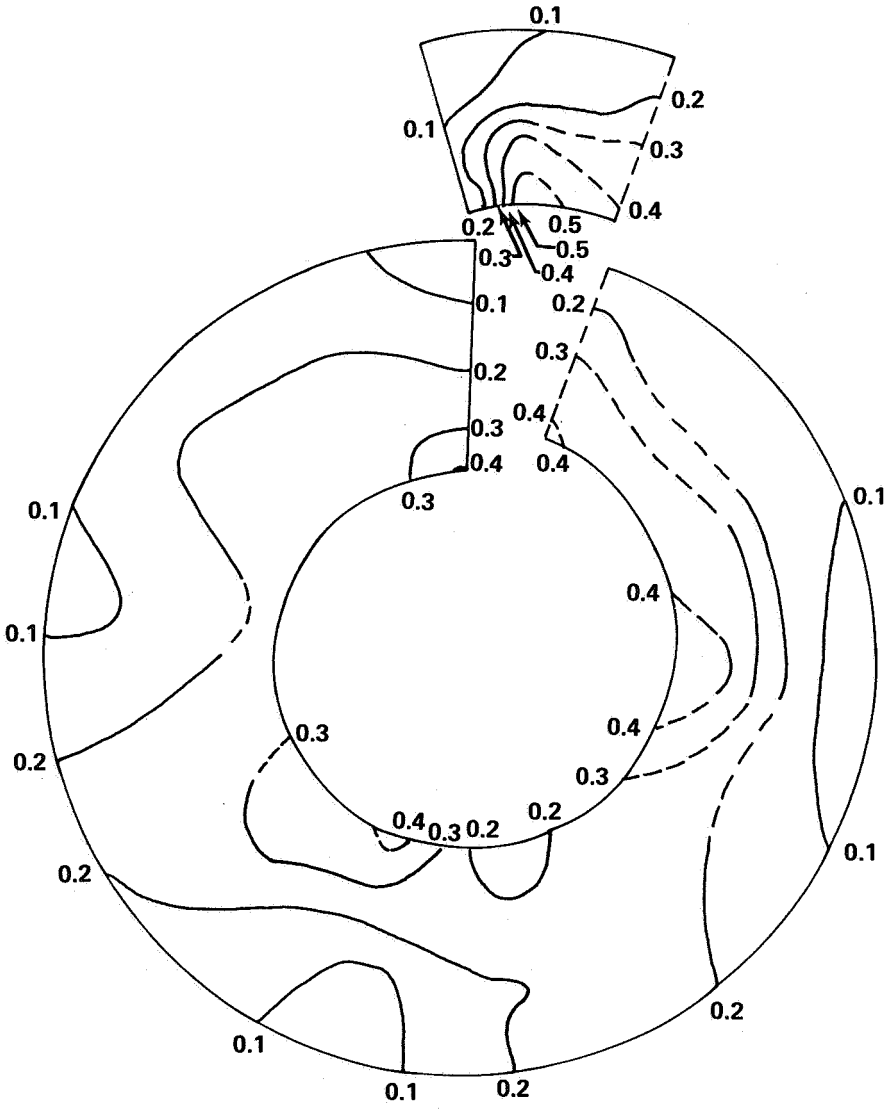

Figure 108. Adjusted Measured Relative Vibratory Stress Contours - Fourth Mode FD 48227

G. REFERENCES

1. Durand, W. F., "Flow Through a Lattice Composed of Air Foils," Aerodynamic Theory, Volume II (General Aerodynamical Theory - Perfect Fluids by T. von Karman and J. M. Burgers. First Edition, 1963), p 91-96.

2. Stripling, L. B., and A. J. Acosta, "Cavitation in Turbopumps," ASME - Papers 61-WA-112 13 p. 61-WA-98 11 p for meeting Nov 26-Dec 1 1961. Paper WA-112 (Pt. 1).

3. Fanti, R., "Elementary Incompressible Solution for the Performance of Airfoils of Arbitrary Shape in an Arbitrary Cascade," United Aircraft Corporation Research Department, Report R-23010-12, Feb 23, 1953.

4. Jakobsen, J. K., "Supercavitating Cascade Flow Analysis," Trans ASME, Jl of Basic Engineering, Dec, 1964, p. 805-814.

5. Stanitz, J. D., "Some Theoretical Aerodynamic Investigations of Impellers in Radial - and Mixed-Flow Centrifugal Compressors," ASME Gas Turb Power Fall Meeting, Minneapolis, September 1951. Paper 51-F-13, 25 pp. -- Trans. ASME 74, 4, 473-497, May 1952.

6. Stockman, N. O., and J. L. Kramer, "Method for Design of Pump Impellers Using a High Speed Digital Computer," NASA TN D-1562, 1963.

7. Cooper, P. and H. B. Bosch, "Three-Dimensional Analysis of Inducer Fluid Flow," NASA CR-54836, February 11, 1966.

8. Wan, F. Y. M., "A Class of Unsymmetrical Stress Distributions in Helicoidal Shells," Quarterly of Applied Mathematics, Volume 24, November 4, 1967.

9. Reissner, E., "On Finite Twisting and Bending of Circular Ring Sector Plates and Shallow Helicoidal Shells," Quarterly of Applied Mathematics, Volume 11, 1963, p 473-483.

10. Knowles, J. K., and E. Reissner, "Torsion and Extension of Helicoidal Shell," Quarterly of Applied Mathematics, Volume 17, 1959, p 409-422.

11. Argyris, J. H., "Recent Advances in Matrix Methods of Structural Analysis," Progress in Aeronautical Sciences, Volume 4, The Macmillan Company, 1964.

12. McGrattan, R. J., and E. L. North, "Vibration Analysis of Shells Using Discrete Mass Techniques," Transactions of ASME, November 1967, p 766-772.

13. Turner, M.J., R.W. Clough, H.C. Martin and L.J. Topp, "Stiffness and Deflection Analysis of Complex Structures," Journal of the Aeronautics Sciences, Volume 25, No. 9, September 1956, p 805-823.

14. Utka, S., "Stiffness Matrices for Thin Triangular Elements of Nonzero Gaussian Curvature," AIAA Journal, Volume 5, No. 9, September 1967, p 1659-1667.

15. Barten, H.J., L.L. Coons, and R.E. Davis, "Study of Inducer Load and Stress," Interim Report under Contract NAS3-11216, NASA CR-72514, April 1969.

16. Soltis, R.F., D.A. Anderson, and D.M. Sandercock, "Investigation of the Performance of a 78 Degree Flat-Plate Helical Inducer," NASA TN D-1170, March 1962.

17. Carter, A.D.S. and H.P. Hughes, "A Theoretical Investigation Into the Effect of Profile Shape on the Performance of Aerofoils in Cascade," R&M No. 2384, British ARC, March, 1946.

18. Tieblein, S., "Incidence and Deviation-Angle Correlations for Compressor Cascades," Journal of Basic Engineering, September, 1960.

19. Schlecting, H., "Boundary Layer Theory," McGraw-Hill, Inc., 1960.

20. Barton, M.V., "Vibration of Rectangular and Skew Cantilever Plates," J. Appl. Mech., 18, pp 129-34, June, 1951.

21. Anderson, D.A., R.F. Soltis, D.M. Sandercock, "Performance of 84 Degree Flat-Plate Helical Inducer and Comparison with Performance of Similar 78 Degree and 80.6 Degree Inducers," NASA TND-2553, December 1964.

22. Anderson D.A., R.F. Soltis, D.M. Sandercock, "Cavitation and Noncavitation Performance of an 80.6 Degree Flat-Plate Helical Inducer at Three Performance Speeds," NASA TND-1439, November 1962.

23. Acosta, A.J., "An Experimental Study of Cavitating Inducers," Second Symposium on Naval Hydrodynamics.

SECTION III
CONCLUDING REMARKS

Based on the results of the analytical and experimental program described herein, the following conclusions can be drawn in regard to the computer programs developed to predict inducer blade pressures, stresses, and vibration characteristics.

1. Hydrodynamic Program

The hydrodynamic computer program is capable of accurately predicting blade surface pressures under noncavitating conditions. However, the present cavitation model, while satisfactory at some NPSH levels, does not accurately predict cavity length over the complete NPSH range from cavitation inception to head fall-off. The predicted cavity length is too long at high NPSH levels and too short at low NPSH values.

The approach taken in the cavitation model appears to be sound and the discrepancy in cavity length is attributed to the influence of some variable not considered in the model. Additional refinements may be required to improve the accuracy of the prediction system.

The hydrodynamic program can analyze various blade leading edge configurations, including radial edges and varying degrees of sweepback. However, all of the testing was performed on an inducer with a radial leading edge, and the accuracy of the model with sweepback has not been validated.

As fall-out from the development of a blade loading prediction system, the hydrodynamic program also provides a unique performance prediction tool. With only minor modifications the program can predict the effect on performance of geometric changes including blade tip clearance.

2. Stress and Vibration Programs

The capability of the computer programs, developed for the prediction of stress and vibration characteristics of inducers, has been demonstrated by comparing predicted results with the results of theoretical analysis and measured results. This correlation has proven that a complex shape such as an inducer can be analyzed by the finite element technique. In general, predicted values using both programs show good agreement with theoretical and measured results. The level and location of the maximum blade stress under both static and operational loads can be predicted very accurately. The predicted natural frequencies of the blades fall within 4% of measured values in the first four modes. The location of nodal points at all modes and natural frequencies at the higher modes (modes fourth) cannot be predicted as accurately.

This discrepancy seems to point to the necessity of using so-called "compatible" triangles which are not used in these programs. Stiffness matrices for such triangles are derived so that the normal slopes between common edges of triangles are equal. This technique guarantees that the solution will approach an asymptotic value monotonically and will not oscillate as the element is made smaller.

The vibration program can also be improved by not only using "compatible" triangles, but by also using a finer breakup. Since the eigenvalue program limits the breakup to only 50 free nodes, a finer breakup can be achieved only by increasing the allowable number of nodes to more than 50. This can be accomplished either by using an iteration technique, by using an eigenvalue subroutine which requires more computer storage, or by using subsystem analysis in a manner similar to that used in the stress program.

It would also be advantageous to combine the two (stress and vibration) programs by solving the eigenvalue problem in the common system, so that no approximations to the direction of blade motion would have to be made.

Potentialities of these programs can be increased by providing other options as follows:

1. Variable thickness blade in place of tapered blade

2. Prescribed displacements of all boundaries. This could be used for flexible hubs

3. Variable offset radius. This would allow more flexibility in describing surfaces

4. Thermal stresses

5. Shear deformation

6. Forced vibrations

7. Equate leading and trailing edge deflections for analysis of complete shells.

3. General

In the course of providing experimental data for correlation with computer program predictions, a highly refined and accurate technique has been developed for measuring blade surface pressures on a rotating inducer. Although variations of the scanning valve have been used previously, they had not been operated at such high rotative speeds or in water. The pressure tap purge system employed, overcame the inherent problem of accounting for centrifugal effects of water in the pressure tap tubing. This purge procedure makes practical the measurement of pressures within almost any type of pump impeller.

APPENDIX A
LITERATURE SURVEY

1. VANE HYDRODYNAMIC LOADING UNDER CAVITATING AND NONCAVITATING CONDITIONS

a. Velocity and Pressure Distribution

1. Acosta, A. J., "An Experimental and Theoretical Investigation of Two-Dimensional Centrifugal-Pump Impellers," Trans. ASME 76, 5, 749-763, July 1954. An experimental and theoretical investigation on a series of two-dimensional centrifugal-pump impellers has been made in an effort to determine the usefulness of potential theory for the description of the flow. Computed values of the developed head and pressure distribution on the vane surfaces are compared with measurements on two-, four-, and six-vaned logarithmic spiral impellers. The agreement between the observed and predicted quantities is reasonably good for operating points where the influence of the inlet turn on the internal flow is least. The discrepancies which occur at other flow rates are attributed to real fluid effects which are observed in the impeller passages.

2. Betz, A., "On the Calculation of Cascade Flow at Fairly Great Distances Between the Blades," (in German), ZAMM 33, 4, 113-116, April 1953. The singularity method for calculating the flow around airfoils in cascade was developed by the author in 1931. The fundamental idea of this method consists in replacing the airfoils in cascade either by single vortexes or by continuous distributions of vortexes. The flow around each airfoil will then be found by the superposition of three flows: (1) The flow which is not being disturbed by the airfoil in cascade ("mean flow"); (2) the flow which is induced by the airfoil in question; (3) the flow which is induced by the remaining airfoils. By application of sources and sinks one can also take into consideration the shape (thickness) of the airfoils.

   The calculations following this method can generally be executed only by a graphical integration. In this case both principal tasks - (a) calculation of the shape of the airfoils, and (b) study of the effect of any existing airfoils in cascade - can be solved with any sufficient exactness. (See, e.g., APM 462, 1952.)

   In this paper, the author considers infinitely thin airfoils in cascade. The third of the above-mentioned flows is represented by a series development. Only the first term need be used when there are sufficiently great distances between the airfoils in cascade. The consideration of a certain distribution of vorticity $\gamma(\ell)$ along the airfoil's length ℓ is reduced to turning moments and moments of inertia of the distribution of vorticity. This means a considerable abridgment of the calculational work, and sufficient exactness will be obtained for large distances between the airfoils in cascade.

3. Brown, R. L., and R. G. Trout, "Axially-Symmetric Flow Between Prescribed Surfaces and Pump Inlet Design," ASME-Paper 63-AHGT-32 for Meeting 3 to 7 March 1963, 5 p. Study to determine actual velocity distributions between surfaces of revolution from experimental data, and design of impeller on this basis to see to what extent performance could be improved; test data were run on water at 530,000 Re, and on air at 180,000 Re: results compared with potential pattern predicted on basis of nonviscous fluid flow.

4. Carter, A. D. S., "Blade Profiles for Axial-Flow Fans, Pumps, Compressors, etc.," Proc. Instn. Mech. Engrs. (Appl. Mech.) 175, 15, 775-806, 1961. In this paper the basic factors controlling blade-section performance are first examined. It is shown that substantial differences in performance may be expected from profiles having different fluid surface velocity distributions. Thus some distributions favor a wide working range while another may be more suitable for very high-speed operation, and so on. A desired velocity distribution may be achieved by appropriately selecting the various physical parameters, such as maximum thickness, position of maximum thickness, position of maximum camber, etc. which define the blade profile. Thus if a particular performance in terms of inlet angle, deflection, Mach number, and incidence and Mach number range is specified, there will be a particular blade profile to do the job. These conditions will have been determined by the overall design considerations, and the various features which the profile designer can then choose to meet them are fully discussed in the second part of the paper.

   In the final section the requirements of some illustrative applications are discussed. It is shown that, on the basis of the earlier parts of this paper, certain applications demand significantly different blade profiles. Evidence is given that substantial gains have been achieved by using the appropriate blade profile for some duties, from which it is concluded that proper attention to the selection of profiles for all duties must lead to an all-round improvement in the performance of these machines.

5. Costello, G. R., R. L. Cummings, and J. T. Sinnette, Jr., "Detailed Computational Procedure for Design of Cascade Blades with Prescribed Velocity Distributions in Compressible Potential Flows," NACA - Report 1060, 1952, 14 p. diagrs. charts, tables. Supersedes NACA - Tech Note 2281 indexed in Engineering Index 1951 p 486.

   A detailed step-by-step computational outline is presented for the design of two-dimensional cascade blades having a prescribed velocity distribution on the blade in a potential flow of the usual compressible fluid. This outline is based on the assumption that the magnitude of the velocity in the flow of the usual compressible nonviscous fluid is proportional to the magnitude of the velocity in the flow of a compressible nonviscous fluid with linear pressure-volume relation. The computational procedure includes several ways of adjusting the prescribed velocity to satisfy restrictions imposed by the method. Tables of coefficients are given for evaluating the necessary integrals, including the determination of the harmonic conjugate function. Numerical examples are included.

6. Durand, W.F., "Flow Through a Lattice Composed of Air Foils," p 91-96. Aerodynamic Theory, Volume II (General Aerodynamical Theory - Perfect Fluids by T. von Karman and J. M. Burgers. First Edition, 1963.) An exact solution is presented for the two-dimensional flow field through a lattice of flat, straight airfoils using conformal mapping techniques with use of a generalization of the Joukowski transformation. Treatment for both staggered and nonstaggered flat (uncambered) airfoils is given. Extension of the theory to include airfoils of various camber and thickness can be made. (See United Aircraft Research Department Report R-23010-12, Feb 23, 1953.)

7. Eichenberger, H.P., "Secondary Flow Within a Bend," J. Math. Phys. 32, 1, 34-42, Apr 1953. The paper presents a theoretical solution and comparison with experiment for the secondary flow within a bend of a tube with rectangular cross section. The theory neglects viscosity and compressibility and utilizes linearized equations of motion for the secondary flow. The equations are solved for the initial conditions of constant stagnation pressure in the radial direction and linear decrease from the center to the upper and lower walls. The theoretical results agree well with experiments at the 30° station of an 8-in. x 8-in. square tube with a 90° bend of mean radius 28 in. The agreement is, however, only slightly better than it is for the simplified theory of Squire and Winter, which assumes two-dimensional flow and neglects changes in the direction of increasing bend angle. It is concluded that, for cases the same as or less severe than that investigated, the simplified theory is adequate for corrections to the flow in the blade passages of a compressor.

8. Ellis, G.O., and J.D. Stanitz, "Two-Dimensional Compressible Flow in Centrifugal Compressor With Logarithmic-Spiral Blades," NACA TN 2255, 46 pp., Jan. 1951. Authors apply methods previously developed by the second author to investigate flow in a compressor where the center line of the flow passages lies in a right circular cone, the axis of which is coincident with the axis of the compressor.

   The quantitative results, obtained by relaxation-method techniques, indicate that a reduction in eddy flow may be attained with backward or forward curved blades as compared to radial blades. The suggestion of improved adiabatic efficiency follows immediately. Indicated constancy of static pressure ratio between straight and curved blades suggest that the diffuser problem is less critical with backward curved blades.

   Not intended for establishing design criteria, the computed results clearly indicate the desirability of experimental investigations upon which design criteria may be based.

9. Fanti, R., "Elementary Incompressible Solution for the Performance of Airfoils of Arbitrary Shape in an Arbitrary Cascade," United Aircraft Corporation Research Department, Report R-23010-12, Feb 23, 1953. A solution for the incompressible, two-dimensional pressure distribution on an arbitrary airfoil in cascade is derived using a combination of the conformal transformation and singularity methods. The conformal mapping technique is used to transform the flow about a circle in one plane into a lattice of staggered flat-plate airfoils in another plane. Source and sink potentials are then distributed along the surfaces of the flat-plate airfoils to produce the contribution of velocity potential resulting from airfoil thickness and shape. The solution is presented in the form of an integral equation, which is easily solved by iterative procedure, and is rapidly convergent.

10. Gruber, J., "Design of Blade Profiles for Axial-Flow Turbomachines," (in German), Maschinenbau-Technik 2, 5, 209-217, May 1953. A simplification of Theodorsen's "Theory of Wing Sections of Arbitrary Shape" (NACA TR 411) has been presented by Thwaites (Aero. Res. Counc. Rep. Mem. nos. 2166, 2167). Present paper simplifies Thwaites' method, particularly as to calculation of effect of blade curvature. Simplified method can be used for calculation of velocity and pressure distribution around relatively thin, slightly curved blades of arbitrary section, and for converse problem. Paper includes useful review of fundamental theory.

11. Hargest, T.J., "The Theoretical Pressure Distribution Around Some Conventional Turbine Blades in Cascade," Aero. Res. Counc. Lond. Rep. Mem. 2765, 10 pp., Mar. 1950, published 1953. This report presents comparative results between theoretical pressure distributions around a specific series of turbine blades in cascade arrangement and the observed aerodynamic performance of blades of the same shape as tested in the No. 3 high-speed cascade tunnel of the National Gas Turbine Establishment.

   The theoretical pressure distributions around the blades were determined over the range of incidence covered in the aerodynamic tests by means of Relf's analogy between aerodynamic streamline flow and electric potential flow. It is shown that these theoretical pressure distributions and their variation with incidence can explain the corresponding cascade test results and can form a basis of general comparison of the turbine cascades.

12. Johnsen, I.A., and A. Ginsburg, "Some NACA Research on Centrifugal Compressors," Trans. ASME 75, 5, 805-814, July 1953. Paper represents effort to replace some of the "art" of centrifugal compressor design with a better understanding of the flow processes taking place. It summarizes some of the results obtained in the NACA theoretical and experimental research program on centrifugal compressors. First section deals with impeller research, discussing the inducer function and the impeller function. These were investigated and analyzed separately as much as possible, and the effect of configuration on performance noted. Second section deals with vaneless diffuser research. Purpose of paper is to establish general trends of good design practice rather than to establish specific rules.

13. Kramer, J.J., N.O. Stockman, and R.J. Bean, "Incompressible Nonviscous Blade-to-Blade Flow Through a Pump Rotor With Splitter Vanes," NASA TN D-1186, 31 pp., Apr. 1962. Report describes an application of an established method of analysis (Kramer, Trans. ASME 80, 1, 236-275, Jan. 1958) to the study of the inviscid flow in a mixed flow pump impeller in which splitter vanes are placed between the main vanes. Differential equation for the "blade-to-blade" stream function is solved numerically.

Calculations indicate:

(i) flow upstream of leading edge of splitter vanes is little affected by their presence,

(ii) slip factor and head rise are increased by inserting splitter vanes.

Authors report that calculations are very sensitive to assumed position for rear stagnation point, and suggest that this might be determined from experiment. Reviewer suggests trailing edges of blades might have been made much thinner, both for purposes of calculation and in practice.

14. Lakshminarayana, B. and J.H. Horlock, "Review: Secondary Flows and Losses in Cascades and Axial-Flow Turbomachines," Internat. J. Mech. Sci. 5, 3, 287-307, July 1963. Very useful review of secondary flow and losses, with extensive bibliography (126 items). Comparisons are given of various theoretical relationships and of experimental data where possible, together with recommended expressions in light of existing knowledge. Nearly all approaches are valid only for incompressible, inviscid flow; authors recommend attention to compressibility, rotational effects, radial flow and interaction of leakage with cascade secondary flow.

15. Leist, K., "Experimental Arrangement for Measurement of Pressure Distribution on High-Speed Rotating Blade Rows," Am Soc Mech Engrs - Trans v 79 n 3 Apr 1957 p 617-26. How research staff of Institute for Turbomachines of Aachen Technical University, Germany, carried out measurements on rotating turbine blading: program is part of comprehensive effort directed toward investigation of 3-dimensional flow through axial flow turbomachines. Paper 56-GTP-13.

16. Linhardt, H.D. and A.J. Acosta, "Note on Application of Cascade Theory to Design of Axial-Flow Pumps," ASME-Paper 62-WA-222 for meeting Nov 25-30 1962 4 p. Theoretical and experimental results are presented which reassure usefulness of 2-dimensional cascade theories to design of axial flow pumps; it is necessary to include effect of blade thickness upon impeller flow, found to be responsible for reported discrepancies between predictions of thin airfoil theories and performance of axial flow pumps characterized by high stagger angle and low aspect ratio.

17. MacGregor, C.A., "Two Dimensional Losses in Turbine Blades," J Aeronautical Sciences, v 19 n 6 June 1952 p 404-8. Tests on three typical blades in 2-dimensional cascade tunnel were run at varying angles of attack, stagger angle, solidity, and downstream survey stations at Mach Number of about 0.4 and Reynolds Number of 6.5×10^5; static pressure distribution about blade was measured by 27 static pressure taps; wake behind blade row was surveyed and loss determined.

18. Marble, F.E. and I. Michelson, "Analytical Investigation of Some Three-Dimensional Flow Problems in Turbomachines," NACA TN 2614, 109 pp., Mar. 1952. Paper collects further useful contributions to linear theory of axially symmetrical flow of incompressible, inviscid fluid in axial-flow turbomachines (see also, Marble, AMR 1, Rev. 1400). Linearization means that radial velocity and deviation of axial velocity from mean through-flow velocity are considered small, and are calculated to first-order approximation. Axially symmetrical solution (infinite number of blades) provides corrections accounting for most of three-dimensional effects neglected by cascade theory, especially for low pitch-chord ratios.

Theory distinguishes three (additive) components of flow, viz., (1) uniform through-flow, (2) radial equilibrium solution, correct for upstream and downstream of the blade row, (3) fine-structure accounting for radial acceleration. Tables of an influence function, for hub ratio 0.6, permit rapid evaluation of fine structure by punch-card method; two numerical examples are given.

A simple, actuator-disk approximation to fine-structure solution is applied, with a numerical example in each case, to the discussion of (1) transients in the first few stages of a multistage machine, (2) fluctuations of the axial velocity distribution within the deeply embedded stages (see also Wu and Wolfenstein, AMR 4, Rev. 1316), (3) performance, in its dependence on the radius and on the aspect ratio, of a single-blade row with prescribed distribution of flow angle at trailing edge; (4) off-design performance of a blade row. In addition to their immediate interest, the examples provide a useful introduction to how theoretical knowledge of the fine-structure solution can be employed to obtain simple, approximate answers to practical questions.

A modified linear theory is proposed for the case of a through-flow velocity varying with the radius. The linearized solution is also given for a machine such that hub and casing are coaxial cones with common vertex.

19. Morelli, D.A. and R.D. Bowerman, "Pressure Distributions on the Blade of Axial-Flow Propeller Pump," Trans. ASME-75, 6, 1007-1012, Aug. 1953. In the design of screw propellers, the demand for uniform energy input at all radii is satisfied by a blade circulation constant over the radius. With the authors' additional assumption of linear increase of circulation strength in axial direction, an approximative formula is given for the disturbance velocities in the blade space dependent on radius and distance from the blade's leading edge; they effect a curvature of the free streamlines which require a curvature of the blade profile computed according to airfoil theory.

Using this formula a propeller pump has been designed; its pressure distribution has been investigated by means of a rotating manometer under various working conditions. The measurements approximately agree with potential-theoretical pressure distributions. In design condition, the energy supply proves to be really uniform over the radius; hereby, the practical use of this design method is shown.

20. Oba, R.,"Linearized Theory of Supercavitating Flow Through an Arbitrary Form Hydrofoil," (in English), ZAMM 41, 9, 354-363, Sept. 1961. Faster and more powerful hydraulic machines result in cavitation problems such as drop in efficiency, damage due to erosion and vibration and noise. Author suggests that supercavitating hydrofoil such as Tulin hydrofoil be used. Problem is treated in two dimensions. A linearized theory is presented including (a) method to estimate hydrofoil form for given pressure distribution and (b) method to estimate characteristics of hydrofoil form. Numerical examples of hydrofoil computation are also presented.

21. Seidel, B.S., "Asymmetric Inlet Flow in Axial Turbomachines," Trans. ASME 86 A (J. Engng. Power) 1, 18-28, Jan. 1964. Paper improves on the prediction of the attenuation of a distorted flow approaching blade rows in axial turbomachinery. The previous analysis of Rannie and Marble (AMR 12 (1959), Rev. 5708) and Ehrich (J. Aero. Sci. 24, 6, 413-417, June 1957) utilized the actuator-disk approach together with a blade force-flow angle relationship which was assumed to be the same as the uniform flow case. The essential, new feature of Seidel's paper is an improved blade force determination which accounts for the direct effect of the flow distortion.

This paper also includes a rather nice comparison of theory and data.

22. Smith, L.H., Jr., S.C. Traugott, and G.F. Wislicenus, "A Practical Solution of a Three-Dimensional Flow Problem of Axial-Flow Turbomachinery," Trans. ASME 75, 5, 789-799, July 1953. Paper presents methods of determining the meridional flow pattern through turbomachines when there are strong departures from free vortex flow, arising from endeavor to design compressors and turbines for maximum head and flow, subject to Mach number limitations.

Frictionless flow, an infinite number of vanes, and axial symmetry are assumed, though authors themselves admit "that there is no known physical reason why this assumption should be considered as sufficiently accurate to describe the flow through actual vane systems of finite vane spacing."

Methods of computation are described and results given of two worked examples, reference being made to M.S. theses by two of the authors for full details.

23. Stanitz, J.D., "Some Theoretical Aerodynamic Investigations of Impellers in Radial- and Mixed-Flow Centrifugal Compressors," ASME Gas Turb. Power Fall Meeting, Minneapolis, Sept. 1951. Paper 51-F-13, 25 pp. -- Trans. ASME 74, 4, 473-497, May 1952. Paper presents numerical results of relaxation solutions of flow of ideal fluid through a centrifugal impeller. Theory and results are given in dimensionless form. Two types of problems are treated: (1) Axial symmetry solutions in which blade forces are replaced by distributed body forces; (2) blade-to-blade solutions giving circumferential variation of pressure and velocity between blades.

Equations for flow with axial symmetry are given for compressible fluids, but the two solutions presented are for incompressible flow through an arbitrary impeller profile with radial vanes, with and without inducer vanes. Results show that the form of streamlines in meridian section is little affected by presence of inducer vanes.

Blade-to-blade solutions are given for radial-flow impellers with constant flow area and with radial or log spiral blades, for compressible fluids in seven cases, and for incompressible fluids in one case, so that influence of change of impeller-tip Mach number, flow coefficient, angular blade spacing, blade angle and compressibility may be studied. Plots of streamlines, relative Mach numbers, and static pressure ratios allow easy qualitative comparison of different cases.

Author also presents simplified approximate methods of estimating velocity distributions along driving and trailing faces of blades and compares their accuracy with the relaxation solutions. He discusses qualitatively the influence of viscosity and boundary-layer development as affected by the frictionless flow pattern, and concludes that future centrifugal compressor development may lead to mixed-flow impellers with backward curved blades. He does not suggest, however, how the mechanical difficulties involved in producing a high-speed impeller of this type may be overcome.

The paper must be regarded as a valuable contribution to the literature on this difficult subject.

24. Stockman, N.O., and J.L. Kramer, "Method for Design of Pump Impellers Using a High Speed Digital Computer," NASA TN D-1562, 1963. Centrifugal pumps are being considered for space applications in chemical and nuclear-rocket engines using cryogenic fluids and in power-conversion systems using liquid metals. For these applications, the pumps should be of minimum size and weight, should have high efficiency, and should operate cavitation-free or with controlled cavitation at high rotative speeds. A knowledge and control of the internal flow are necessary to meet these requirements.

The hub-shroud design method presented herein (with optional blade-surface computations) is a rapid and easy-to-use method. It enables the designer to proceed from a known streamline and its velocity distribution to an adjacent streamline and its velocity distribution. Thus, given the conditions along the hub, the entire hub-shroud profile is built up by proceeding from the hub streamline to the next streamline, and so on, until the shroud is reached.

25. Woods, L.C., D. Phil, and A. Thom, "A New Relaxational Treatment of the Compressible Two-Dimensional Flow About an Aerofoil With Circulation," Aero. Res. Counc. Lond. Rep. Mem. 2727, 17 pp., Mar. 1950, published 1953. The two-dimensional incompressible and compressible flow over a profile is computed by relaxation in a grid with potential and stream functions as independent variables. Thus the profile appears as a straight line. Circulation is chosen in advance; angle of attack is found at the end of the computations. Boundary conditions at the profile are taken into account by successive approximations. Known circulation is used to formulate an approximate boundary condition at the outer edge of the relaxation field. Treatment of stagnation region is discussed in AMR 6, Rev. 1310. Comparison of theoretical and experimental results is carried out for profile NACA 16.

26. Wu, C.H., C.A. Brown, and V.D. Prian, "An Approximate Method of Determining the Subsonic Flow in an Arbitrary Stream Filament of Revolution Cut by Arbitrary Turbomachine Blades," NACA TN 2702, 46 pp., June 1952. A method is presented to obtain a relatively quick approximate determination of the detailed subsonic flow of a nonviscous fluid past arbitrary turbomachine blades. The method is illustrated with examples of compressible flow in a turbine cascade and in a centrifugal compressor. For these high-solidity blades, three terms of the Taylor series are found to give sufficient accuracy. Sufficient convergence is obtained in the turbine cascade after two cycles of computation and in the centrifugal compressor after four cycles of computation. The detailed flow variation obtained compares very well with an available numerical solution and experimental data for the turbine cascade, and with detailed experimental measurements for the centrifugal compressor.

b. Cavitation (Two-Phase Flow) - Theoretical

1. Cooper, P., "Application of Pressure and Velocity Criteria to Design of Centrifugal-Pump Impeller and Inlet," ASME - Paper 63-AHGT-58 for meeting Mar 3-7 1963 12 p. Centrifugal pump impeller and inlet designed by use of criteria for distributions of pressure and velocity that lead to satisfactory performance at low net positive suction heads; calculations made for nonviscous, single-phase (liquid) flow with view toward minimizing bubble formation; tests run under cavitating and single-phase flow conditions; results show that design method leads to good suction performance.

2. Cooper, P. and H. B. Bosch, "Three-Dimensional Analysis of Inducer Fluid Flow," NASA CR-54836, Feb 11, 1966. Analytical studies were conducted to provide means for improving the design of inducers for high-speed, high-flow rocket engine pumps. Exact and approximate methods are presented for obtaining three-dimensional solutions to turbomachine flows with losses and vaporization, and results are presented for two sample inducers. The exact method solves four nonlinear differential equations of motion simultaneously by finite-difference and relaxation techniques that employ a "total residual" concept. The approximate method employs a finite difference solution of the basic flow equations in two dimensions and then superimposes an assumed solution in the third dimension, resulting in an approximate three-dimensional solution. Conclusions on inducer performance and design are made on the basis of several approximate solutions of both incompressible and two-phase flows, together with analysis of fluid thermal and scale effects. Fortran IV listings of the analysis computer programs are presented.

3. Goldman, K., R. Hankel, and R. P. Stein, "Equation for Critical Mass Velocity of Homogeneous Vapor Liquid Mixtures at Low Pressures," ASME - Paper 64-APM-12 for meeting June 9-11 1964 3 p; see also ASME - Trans J Applied Mechanics v 31 n 3 Sept 1964 p 380-2. Equations have been developed expressing critical mass velocity and isentropic expansion coefficient of single-component, homogeneous vapor-liquid mixtures at low pressures in terms of tabulated thermodynamic properties; two-phase flow relations are analogous to relations governing flow of single-phase compressible fluids, most readily formulated in terms of Mach numbers.

4. Jacobs, R. B., "Prediction of Symptoms of Cavitation," US Bur Standards - J Research - Eng & Instrumentation v 65C n 3 July-Sept 1961 p 147-56. Analysis of some basic problems in cavitation and which may permit prediction of cavitation characteristics of hydraulic equipment; application to pumps; practical results compared with theory; it is concluded that analysis may be applicable to prediction of symptoms of cavitation but that more information related to metastability, nucleation, and vapor phase dynamics is required.

5. Jakobsen, J. K., "On Mechanism of Head Breakdown in Cavitating Inducers," ASME - Paper 63-AHGT-29 for meeting Mar 3-7 1963 15 p. Mechanism, as affected by thermodynamic properties of turbopump fluid and scale effects, is discussed; approach taken by other investigators and limitations to cavitation scaling in relation to experimental data; hypothesis introduced relates head breakdown process to acoustic shock phenomenon at point of leading-edge blade cavity collapse; integrated model for cavitating cascade blade is developed to correlate potential flow cavity cascade model with influence of thermodynamic properties, thermostatic approach, and application of bubble dynamic studies to understand how suction performance is limited by inlet pressure; pertinence to propellant pumps.

6. Jakobsen, J. K., "Supercavitating Cascade Flow Analysis," Trans ASME, J1 of Basic Engineering, Dec, 1964, p. 805-814. An exact mathematical theory of supercavitating flow in cascades with arbitrary blade shapes is developed. Applying conformal mapping methods to the potential flow problem involved, a general mapping procedure is established. The geometric interpretation of the obtained mappings is discussed in general and completed in the case of the flat-plate cascade. All results assume infinitely long cavities. The application of the established mapping procedure to the case of a cascade with arbitrary blade shape requires the solution of a nonlinear integral equation for one of the mapping functions, or the approximation of this mapping function by a Fourier series whose coefficients must be determined from implicit conditions imposed by the blade shape.

7. Lewis, W. P., "Design of Centrifugal Pump Impellers for Optimum Cavitation Performance," Instn Engrs. Australia - Elec & Mech Eng Trans v EM6 n 2 Nov 1964 p 67-74. Examination of influence of velocity distributions in flow entering impeller to establish design procedure for flows with and without prerotation. 29 refs.

8. Sack, L. E., and H. B. Nottage, "System Oscillations Associated With Cavitating Inducers," ASME-Paper 65-FE-14 for meeting June 7-9 1965 8 p. Nature and inception of pressure and flow-rate oscillations associated with high-speed cavitating inducer employed to extend suction performance capabilities of high-speed, high-flow pumps were investigated by nonlinear analog computer simulation; favorable accord between simulation findings and typical actual dynamic oscillation characteristics validates general technique for extension into inducer design analyses; it was found that nature and behavior of cavitation vapor volume and dynamic response characteristics of complete fluid circuit play key roles in incidence and suppression of oscillations.

9. Spraker, W. A., "Effects of Fluid Properties on Cavitation in Centrifugal Pumps," ASME - Paper 64-WA/FE-14 for meeting Nov 29- Dec 3 1964 10 p. see also ASME - Trans - J Eng for Power v 87 n 3 July 1965 p 309-18. Analytical model of cavitation process in pump is developed assuming that flow is adiabatic, frictionless, steady, and irrotational; relationship is developed relating volume percentage of fluid vaporized during cavitation process to thermal cavitation parameter; experimental and analytical methods for determining cavitation characteristics of pumps handling petroleum-based hydrocarbon mixtures are described; cavitation data for two pipe-line pumps handling gasoline, fuel oil, and crude oil are presented.

10. Starkman, E. S., V. E. Shrock, K. F. Neusen, and D. J. Maneely, "Expansion of Very Low Quality Two-Phase Fluid Through Convergent-Divergent Nozzle," ASME - Paper 63-AHGT-4 for meeting Mar 3-7 1963 8 p. Flow in de Laval nozzles of h-p steam water mixtures was investigated to determine mass flow rates and design criteria; qualities ranged from 0 to 20% and pressures up to 1000 psia; comparisons of data to isentropic expansion, frozen composition, and slip flow showed satisfactory correspondence except for qualities very close to saturated liquid; condition similar to shock resulted when nozzles were overexpanded; pertinence to very high heat flux heat power devices, e.g., nuclear reactors, with applications in nucleate boiling region.

11. Stepanoff, A. J., "Cavitation Properties of Liquids," ASME - Paper 63-AHGT-22 for meeting Mar 3-7 1963 5 p. Method of representing thermal properties of liquids is offered such that cavitation behavior of centrifugal pumps handling any liquid molten metal, hydrocarbons, cryogenics can be accurately evaluated; there are sufficient test data to illustrate use of method.

12. Stepanoff, A. J., and H. A. Stahl, "Cavitation Criterion for Dissimilar Centrifugal Pumps," ASME - Paper 61-WA-139 for meeting Nov 26-Dec 1.1961 5 p. Method of expressing net positive suction head for centrifugal pumps in terms of impeller design elements as they appear in inlet velocity triangle; procedure is applicable to pumps of different specific speeds, of different suction specific speeds, and to pumps having impellers of either overhung type or with shaft through eye.

13. Stripling, L. B., and A. J. Acosta, "Cavitation in Turbopumps," ASME - Papers 61-WA-112 13 p. 61-WA-98 11 p for meeting Nov 26-Dec 1 1961. Paper WA-112 (Pt. 1). Several simplified free streamline models suitable for flow through inducer discussed. Paper WA-98 (Pt. 2). Results are compared with tests on actual inducers; relevance to development of light weight turbomachine components for liquid rocket propulsion systems.

14. Wang, Y. L., and P. A. Longwell, "Laminar Flow-In Inlet Section of Parallel Plates," A.I.Ch.E. J v 10 n 3 May 1964 p 323-9. Numerical solutions of exact momentum equations for steady isothermal laminar flow of incompressible Newtonian fluid in inlet section of parallel plates; velocity distributions, pressure gradients, and overall pressure drop for two cases at Re 300; it was verified that usual boundary-layer assumptions are not valid near leading edge.

15. Warner, C. F., and D. W. Netzer, "Investigation of Flow Characteristics in Converging-Diverging Nozzles," ASME - Paper 63-WA-192 for meeting Nov 17-22 1963 9 p. Analytical method based on 1-dimensional model is presented for determining flow characteristics of 2-phase flow of liquid drops in gas stream expanding through converging-diverging nozzle; analysis can be utilized to predict liquid velocity, gas velocity, static pressure, and droplet diameter as function of axial distance along nozzle axis for flows containing approximately 10 times as much liquid as gas by weight.

16. Wu, T. Y. and D. P. Wang, "An Approximate Numerical Scheme for the Theory of Cavity Flows Past Obstacles of Arbitrary Profile," Trans. ASME, Jl of Basic Engineering, Sept-1964, p 556-560. Previously one of the authors has developed an exact theory for the cavity flow past an obstacle of arbitrary profile at an arbitrary cavitation number by adopting a free-streamline wake model. In the present paper the authors introduce an approximate numerical method for the computation of the dual functional equations which result from the theory. The new method is shown to provide a drastic simplification to the computations while maintaining a high degree of accuracy of the numerical result.

c. Cavitation (Two-Phase Flow) - Experimental

1. "Facilities and Techniques Employed at Lewis Research Center in Experimental Investigations of Cavitation in Pumps," ASME - Symposium on Cavitation Research Facilities and Techniques, May 18-20 1964, p 60-76. Study of cavitation as it occurs in pumping of high-energy propellants (cryogenic liquids) used in chemical and nuclear rocket engines and alkali metals used in space-electric-power generation systems; paper lists and describes facilities and techniques utilized to supply experimental input to program studies; test fluids include water, cryogenic liquids, and alkali metals.

2. Grindell, A.G., "Correlation of Cavitation Inception Data for Centrifugal Pump Operating in Water and in Sodium-Potassium Alloy (NaK)," ASME-Trans-J Basic Eng v 82 Ser D n 4 Dec 1960 p 821-8. Static head at pump suction at time of cavitation inception was correlated for water and for 1500 F NaK on basis of differences of vapor pressures of two liquids; difference between vapor pressures, for same conditions of pump speed and liquid flow, was added to water test cavitation inception value; this proved to be good approximation to experimental value found for cavitation inception with NaK. Paper 59-A-156.

3. Hartmann, M.J. and R.F. Soltis, "Observation of Cavitation in Low Hub-Tip Ratio Axial-Flow Pump," ASME-Paper 60-HYD-14 for meeting Mar 6-9 1960, 12p. Cavitation formations in pump rotor are examined in attempt to determine important characteristics of flow model which may be used to indicate effects of cavitation; data were obtained at Lewis Water Tunnel at NASA Lewis Research Center; besides instrument surveys, high speed photographs were taken, for which latter purpose upper half of pump casing is of plastic.

4. Horie, C. and M. Oshima, "Experimental Study on Cavitation in Mixed Flow Pump Impellers," Japan Soc Mech Engrs - Bul v 7, n 25, Feb 1964, p. 62-70. Series of experimental studies of cavitation characteristics of mixed flow pump impellers was performed; report clarifies mainly how cavitation inception and performance decrease are influenced by number of vanes and shape of vane inlet edge; it was also found that certain amount of flow deviation must be taken into account in determination of vane inlet angles.

5. Jekat, W.K., "Reynolds Number and Incidence-Angle Effects on Inducer Cavitation," ASME-Paper WA/FE-31 for meeting Nov 27-Dec 1 1966, 9 p. Tests of various hubless inducers in water show that suction specific speed increases with Reynolds number and incidence angle; analysis is presented which reduces this observation to Reynolds number-dependency and approximate incidence-independency of newly defined "vane coefficient;" relationships are general and apply to other inducer types and normal pump impellers. 22 refs.

6. Langteau, R.R. and E.R. Dodge, "Cavitation in Impeller-Looking from Inside Out," ASME-Paper 63-AHGT-30 for meeting Mar 3-7 1963 12 p. Low specific speed, double suction centrifugal pump was modified by splitting casing and impeller in half and incorporating transparent inserts and housings to permit visual observations of flow; "half pump" was operated in water test facility at prototype design heads with both Francis and radial-vaned inlet impeller design; photographic records of cavitating and noncavitating conditions at various points along pump characteristic are correlated with various performance parameters.

7. Miller, M.J., J.E. Crouse, and D.E. Sandercock, "Summary of Experimental Investigation of Three Axial-Flow Pump Rotors Tested in Water," ASME-Paper 66-WA/FE-24 for meeting Nov 27-Dec 1 1966, 11 p. Three rotors located immediately downstream of pump inducer were tested to study flow and performance across loaded axial-flow blade rows; principal design parameters varied were flow coefficient, blade loading parameter at tip, and hub-tip radius ratio; overall and blade element performances under noncavitating flow conditions are discussed; comparisons between measured, three-dimensional design parameters and those computed from two-dimensional cascade correlations; performance obtained during operation of rotors in unstable flow and cavitating flow conditions.

8. Salemann, V., "What Engineers Should Know About Cavitation and NPSH," Pipe Line Industry v 15 n 1 July 1961 p 55-61. Relationship between pump suction characteristics and fluid properties has been obtained; satisfactory performance of pumps on hydrocarbons with less net positive suction head available than required by cold water was studied; data collected and theory developed aim at accurate prediction of pump suction requirements for all liquids, on basis of cold water requirements; causes of cavitation; test stand, instrumentation, results, and benefits of investigation.

9. Soltis, R. F., D. A. Anderson, and D. M. Sandercock, "Investigation of the Performance of a 78° Flat-Plate Helical Inducer," NASA TND-1170, 1962. The coupling of a cavitating inducer with a pump, in order to realize the advantages of higher mechanical speeds, has found wide use in missile applications. An effective and quite easily fabricated blade shape employed in the inducer has been the flat-plate helix. This report presents the measured performance of an inducer of this type. The rotor, 5 inches in diameter, consisted of three blades with a hub-tip ratio of 0.5 and a helix angle of 78 degrees at the tip. All tests were made in water.

Performance results over a range of flows are presented at both cavitating and noncavitating conditions. This includes both the overall performance and radial distributions of flow conditions and selected blade-element performance parameters. In addition, photographs that visually describe flow conditions at various modes of operation are presented. A comparison of the measured axial velocity distributions with those computed assuming simple radial equilibrium provides a check on the validity of the radial equilibrium assumption.

10. Wood, G.M., "Visual Cavitation Studies of Mixed Flow Pump Impellers," Trans. ASME 85 D (J. Basic Engng.) 1, 17-28, Mar. 1963. Three mixed impellers (design parameters; 3800, 4920, 8500 rpm, 1760, 1545, 1245 gpm; 287, 235, 245 ft) have been tested in a closed water loop. Author compares cavitation curves at three test points at rpm 1900, 2460, 4250 with the high-speed photographic records. He concludes that cavitation occurs for all impellers at higher values of NPSH than those associated with a drop in the head rise. Cavitation in vane channels is cyclic, whereas cavitation near the vane leading edges was more stable.

In author's opinion, the mean static pressure gradient is a prime variable in the determination of cavitation performance characteristics. Some data on vane channel cavitation frequency are presented.

11. Wood, G.M., J.S. Murphy, and J. Farquhar, "Experimental Study of Cavitation in Mixed Flow Pump Impeller," ASME-Trans-J Basic Eng v 82 Ser D n 4 Dec 1960 P 929-40. Hydraulic performance of impeller design tested with 6, 5, and 4 vanes in closed water loop; 2 idealized flow models for incipient cavitation were derived to illustrate limits of cavitation design; both vane blockage and solidity effects are important. Paper 60-Hyd-7.

12. Wright, M.K., "Design Comments and Experimental Results for Cavitation-Resistant Inducers up to 40,000 Suction Specific Speed," ASME-Paper 63-AHGT-59 for meeting Mar 3-7 1963 8 p. Paper considers general geometric considerations of inducer design, correlation of dimensionless design parameters, experimental data obtained from 2 models developed by Bell Aerosystems Co. and suggests several auxiliary means of augmenting cavitation resistance of inducer; inducer is axial flow pump capable of digesting large scale fluid vapor formations at its inlet without seriously affecting head generation.

13. Yokoyama, S., "Effect of Profile of Entrance of Centrifugal Pump Impeller on Cavitation," Japan Soc Mech Engrs-Bul v 5 n 19 Aug 1962 p 485-91. Velocity distribution just before vane entrance edge differs according to difference of impeller entrance profile; irrespective of velocity distribution, static pressure distribution at point just before vanes was almost same for all profiles; in comparison of cavitation occurrence of profiles designated A and C, no distinctive difference was observed except that head drop due to cavitation in large flow rate range was smaller for second profile.

14. Yokoyama, S., "Effect of Tip Shape at Entrance of Impeller Vane of Centrifugal Pump on Cavitation," Japan Soc Mech Engrs-Bul v 3 n 11 Aug 1960 p 326-32. Experiments were carried out on three different types of tip shape; in each case, head capacity curve, static pressure distribution on surfaces of vanes near entrance tips and modes of cavitation occurrence were measured; results indicate that at shockless entry there are more changes of cavitation for round tip vane than for other type vanes; for sharp tip vane no cavitation occurs in experiments.

2. VANE STRESSES (STRESSES IN CURVED PLATES)

a. Exact Solutions

1. Candela, F., "Structural Applications of Hyperbolic Paraboloidal Shells," J. Amer. Concr. Inst. 26, 5, 397-415, Jan. 1955. After a short exposition of the properties of the hyperbolic paraboloid, author gives in simple form Pucher's general equations of the stress system analysis. More especially, the warped parallelogram is studied, arising from consideration of a portion of a hyperbolic paraboloid limited by four straight generatrix. In general, the stress system is given for the following cases: (1) snow load; (2) dead load; (3) fill load. The f,(x),F,(y) functions relative to the boundary conditions are to be determined in all aforesaid cases. The finite-differences method is recommended for the more complex solution of case (2).

   Some existing examples are shown of constructions in Mexico City built up as associations of the warped parallelogram.

   The possibilities of the use of these shells in reinforced-concrete construction makes this work particularly interesting.

2. Deverall, L. I. and C. J. Thorne, "Bending of Thin Ring-Sector Plates," J. appl. Mech. 18, 4, 359-363, Dec. 1951. Authors attack the problem by a method they used for rectangular plates in a previous paper (AMR 4, Rev. 3837). General expressions for the deflection of plates whose planform is a sector of a circular ring are given for cases in which the straight edges have arbitrary but given deflection and bending moment. The solutions are given for all combinations of physically important edge conditions on the two circular edges. Sectors of circular plates are included as special cases. Solutions are given for a general load which is a continuous function of r and a sectionally continuous function of θ, where r and θ are the usual polar coordinates with the pole at the center of the ring. Several specific examples for angles of the sector 30° and 90° are given.

3. Griffin, D. S., "Stresses and Deflections of Thick, Curved Plates," ASME - Paper 64-WA/MD-8 for meeting Nov. 29-Dec. 4 1964 6 p.: See also ASME - Trans - J Eng for Industry v 87 n 3 Aug 1965 p 303-8. Solution is obtained using linear theory of elasticity for stresses in long, thick, uniformly curved plate due to pressure on curved surfaces and forces or deflections specified on straight edges; maximum stresses are compared with those obtained by elementary thin beam theory, showing range of applicability of simpler theory: in general, accuracy of elementary theory depends on total plate angle, as well as mean-radius-to-thickness ratio.

4. Haas, A. M., "Design of Thin Concrete Shells: Vol. 1, Positive Curvature Index," New York, John Wiley & Sons, Inc., 1962, viii + 128 p. This book represents the first of a set of several volumes concerning various aspects of shell analysis, design, and construction that the author intends to publish. This first volume deals with the design and analysis of doubly curved shells of positive curvature and in particular axisymmetric shells.

   The book begins with a brief outline of the membrane theory of shells and a concise summary of the necessary relationships of differential geometry for the analysis of thin shells. Next, the membrane analysis of axisymmetric deformation of axisymmetric shells is formulated and a number of special cases pertaining to membranes stresses existing in symmetrically deformed shells of revolution are treated. These include the spherical dome, the elliptical dome, and conical shells subjected to various types of symmetric loads. Analytical as well as graphical solutions are discussed. The next chapter presents the case of unsymmetrically loaded shells of revolution and linear elastic theory is completely developed for this situation. Solutions involving expansions in terms of harmonic series are treated in detail for spherical shells and shells on discrete supports, and, lastly, various aspects of design consideration for such shells are discussed.

5. Knowles, J. K., and E. Reissner, "Torsion and Extension of Helicoidal Shell," Quarterly of Applied Mathematics, Vol 17, p 409-422, 1959. The authors determine the elastic behavior of a pretwisted strip in the form of a helicoidal shell when acted upon by axial forces and a twisting moment. In this instance the rotationally symmetric states of strain depend upon the states of displacement that are not rotationally symmetric. Torsional rigidity and axial stiffness are obtained as a function of pretwist by perturbation solutions.

6. Langhaar, H. L., "An Invariant Membrane Stress Function for Shells," J. appl. Mech. 20, 2, 178-182, June 1953. The equations of equilibrium of membrane stresses in a shell are shown to be satisfied with certain restrictions by a generalized Airy stress function. For shells of constant Gaussian curvature the stress function is shown to be unrestricted. For other shells, it is expressed as a function of the Gaussian curvature. Comparisons are made with Pucher's stress function. Shells of revolution with constant and variable curvature are discussed.

7. Langhaar, H. L. and D. R. Carver, "On The Strain Energy of Shells," J. appl. Mech. 21, 1, 81-82, Mar. 1954. In a previous paper (AMR 3, Rev. 1641) of the first author, the strain energy was derived with the assumption that only the linearized terms in the thickness coordinate z need be retained in the geometrical equations between the strains and the displacements of the middle surface. The present paper shows that, in general, the strain-energy density is only a rational function of z , and the evaluation of the strain energy in terms of the displacements is not difficult. In the simple example of the cantilever curved beam the authors point out that the linearizing of the geometrical equations in connection with the use of strain energy and calculus of variations leads to questionable approximations. The conditions of equilibrium are not satisfied; the net tension disagrees grossly. But if the shell is thin, the linearizing causes only a small error in the stresses.

8. Lew, H. G., J. A. Fox, and T. T. Loo, "Large Deflection Of Curved Plates," NACA TN 3684, 38 pp.; Oct. 1956. The specific problems treated are the deflections of doubly curved plates with normal edge loads, doubly curved plates under edge shear loads, and nearly cylindrical curved plates under longitudinal compression. The difference between the first two plates and the third one lies in the fact that the initial deflection is axially symmetric in the first two cases whereas the third plate is very close to a portion of a straight circular cylinder but has, in addition, a slight bulge along the length of it.

   The principle of minimum potential energy, or equivalently the Ritz method, is used to determine the coefficients in the assumed expression for the stress function, and it is found that, for the initial deflections considered, only a few coefficients were necessary to represent the complete solution. This is, of course, merely another way of saying that if the initial deflection can be represented well by a few terms in a double sine series and if the loads such that the total deflections under load are similar in form to the initial deflection, then only a few terms in a double sine series will suffice equally well to describe the deformed state.

   In addition to the determination of the stresses and deflections, the effective widths of the curved plates were calculated for several cases and compared to flat sheets and circular cylindrical curved panels.

9. Libai, A., "Invariant Stress and Deformation Functions for Doubly Curved Shells," Transactions of ASME, Vol 89, Series E, No. 1, Journal of Applied Mechanics, March 1967, p 43-54. Exact invariant stress and deformation functions for doubly curved (nondevelopable) shells are derived. The invariant stress function reduces the six shell equilibrium equations into a single equation in the stress function and moment resultants. The deformation function reduces the three surface strain-displacement relations into a single compatibility equation in the strains and deformation function, in terms of which the changes of curvature are also expressed. Application of these functions in the formulation of an approximate bending theory for shells is presented.

10. Reissner, E., "On Finite Twisting and Bending of Circular Ring Sector Plates and Shallow Helicoidal Shells," Quarterly of Applied Mathematics, Vol 11, 1963, p 473-483. The author considers the behavior of a thin circular ring sector plate subjected to two equal and opposite forces perpendicular to the plane of the plate and later analyzes an initially deflected helicoidal shell. Stress resultants and couples are assumed independent of the polar angle, θ , and transverse displacement is assumed proportional to θ . The solutions are obtained in terms of an Airy stress function.

11. Reissner, E., "Rotationally Symmetric Problems in the Theory of Thin Elastic Shells," Proc. Third U.S. Nat. Congr. Appl. Mech., June 1958; Amer. Soc. Mech. Engrs., 1958, 51-69. Paper presents an exhaustive and concise survey of linear and nonlinear theory of rotationally symmetric problems of thin elastic shells. Numerous important contributions to the subject by author and others are summarized with aim of constructing a unified and generalized theory.

   Theory of shallow shells of revolution is treated for linear and small nonlinear deflections. Method for closed nonlinear solution of shallow spherical shell is given. In view of examination of applicability of membrane solutions, boundary-layer theory is summarized. Condition for existence of boundary-layer solution is developed for general case, thus generalizing known condition for spherical shell.

   Second-order correction theory for influence coefficients of shell loaded on edges only is developed. General condition for negligibility of this correction is given, thus generalizing earlier result of author for cylindrical shell.

Other subjects treated are: Linear theory of pure bending of incomplete shells of revolution, shells of revolution with small variation of radial dimensions, asymptotic solutions for toroidal shells, and bending correction to membrane solution of closed ellipsoidal shell.

Lastly, differential equation of finite bending of thin-walled pressurized tubes of initial circular cross section is set up. Explicit solution is given by series expansion for case of initially straight center line.

Reviewer believes that paper is of major importance in thin-shell theory.

12. Vol'mir, A. S., "Survey of Investigations on the Theory of Flexible Plates and Shells (Covering the Period from 1941 to 1957)," NASA Tech. Transl. F-180, 45 pp., Oct. 1963. (From Raschet Prostranstvennykh Konstruktsiy 4, 451-475, 1958.) The literature on the theory of flexible plates and shells is reviewed, and information is abstracted on pertinent areas such as fundamental and approximate methods of solution, large deflections of plates and shells, and postbuckling deformations of plates and shells.

13. Wan, F. Y. M., "A Class of Unsymmetrical Stress Distributions in Helicoidal Shells," Quarterly of Applied Mathematics, Vol 24, No. 4, 1967. The author develops a theory for the elastic behavior of a helicoidal shell in which the displacements are multivalued in the polar angle, θ, while the strain distribution, although single valved in θ, is dependent upon θ. Ten strain displacement relations are used to set up the differential equations which govern the elastostatic behavior of the shell. The bending of a helicoidal shell by end moments is solved as an example.

b. Approximate Methods

1. Archer, J. S., "Consistent Matrix Formulations for Structural Analysis Using Finite-Element Techniques," AIAA Journal, Vol 3, No. 10, Oct 1965, p 1910-1918. The discrete-element stiffness matrix technique for formulation of linear structural problems in engineering mechanics is examined to develop techniques that give exact or closely approximate solutions for static load-displacement, elastic stability, and dynamic response problems. An exact relationship is derived for determining the coordinate load matrix equivalent to a general distributed load function. Use of the load matrix in static load-displacement problems results in an exact solution for the coordinate displacements consistent with the theoretical basis used for constructing the stiffness matrix. Explicit expressions are derived for a finite-displacement matrix for beam and plate elements for use in formulating the general elastic-stability problem. The approach discussed provides closely approximate buckling loads that are upper bounds to the precise solution. The dynamic problem, including elastic-stability considerations, is formulated using a consistent mass matrix approach. This approach provides closely approximate natural frequencies that are upper bounds to the exact solution. The data required for stiffness, load, finite-displacement, and mass matrices for a system composed of Timoshenko beam elements with linearly varying properties are provided. An example cantilever stepped beam problem is solved to illustrate the techniques involved and the exact or closely approximate nature of the solutions obtained.

2. Argyris, J.H., "Recent Advances in Matrix Methods of Structural Analysis," Progress in Aeronautical Sciences, Vol 4, The Macmillan Company, 1964. This book discusses methods of using matrices to solve aircraft structural problems by computer techniques. Methods of solving linear and nonlinear problems by matrix force-methods and matrix displacement methods are presented. These are many examples in which the results are compared with experimental test data with good agreement. Of particular interest is the general discussion on a method of approaching the problem of the curved cover by replacing the cover surface with triangular elements, as discussed in Appendix I.

3. Dawe, D.J., "A Finite Element Approach To Plate Vibration Problems," Journal of Mechanical Engineering Science, Vol 7, No. 1, p 28-32. A method of computing the natural frequencies of vibration of flat plates of arbitrary shape is outlined in which the plate is considered as an assemblage of elements.

Both stiffness and inertia matrices are derived for a rectangular isotropic plate element of uniform thickness, and these matrices are used to find the natural frequencies of square plates subject to various boundary conditions. Comparison of finite element frequencies with known exact, experimental, and energy solutions shows the method to give good results even for relatively few elements.

4. Dawe, D.J., "Vibration of Rectangular Plates of Variable Thickness," Journal of Mechanical Engineering Science, Vol 1, No. 1, p 42-51, 1966. In a previous paper the application of the finite element method to plate vibration problems was discussed. It was shown that the method gave good results when applied to the vibration of plates of uniform thickness.

The present paper extends the method to include plates of variable thickness. In particular, stiffness and inertia matrices are derived for an isotropic rectangular plate element of linearly variable thickness in one co-ordinate direction. These matrices are used to find the natural frequencies and mode shapes of a number of rectangular planform cantilever plates of non-uniform thickness. Experimental results provide a basis for comparison with the finite element results.

5. Flügge, W., and S. C. Chou, "Large-Deformation Theory of Shells of Revolution," Transactions of ASME, Vol 89, Series E, No. 1, Journal of Applied Mechanics, March 1967, p 56-58. In this paper, nonlinear membrane equations are derived for a shell of revolution under the assumption that not only are the displacements and rotations large, but that, also, large strains are admitted. The equations, therefore, are aimed at shells which are not only very thin, but which are also made of a material which permits large elastic strains. The special difficulties resulting from this extension of the theory are discussed. As an example for the application of the equations, a circular toroid subjected to internal pressure is studied. Numerical results are given for a level of loading which lies clearly outside the domain of a large-deflection, small-strain theory.

6. Gallagher, R. H., R. A. Gellatly, J. Padlcg, and R. H. Mallett, "A Discrete Element Procedure for Thin-Shell Instability Analysis," AIAA Journal, Vol 3, No. 1, Jan 1967, p 138-145. The concepts of the matrix displacement approach to discrete element structural analysis are extended to predict general instability. Instability phenomena are accounted for by considering the influence of element membrane forces on element effective flexure stiffnesses. Particular attention is given to the problem of determining membrane force distributions that account for interelement membrane-flexure coupling. Representations of instability effects are formulated for several levels of approximation for an arbitrary quadrilateral plate element. Critical applied load intensities are predicted for plate, arch, and spherical cap structures to demonstrate convergence characteristics and to provide comparisons with test data and classical solutions.

7. Gerstenkoru, G. F. and A. S. Kobayashi, "Application of the Direct Stiffness Method to Plane Problems Involving Large, Time-Dependent Deformations," Journal of Basic Eng., Dec 1966, p 771-776. The direct stiffness method is used to formulate a numerical procedure for solving plane structural problems involving large, time-dependent deformations and nonhomogeneous, time-dependent material properties. The stiffness matrix in polar coordinates is derived for the state of plane strain. The nonlinear structural response is incrementally linearized by considering the deformation process to be linear within small time increments. The developed procedure is compared numerically with a known solution of creep deformations in a thick-walled cylinder subjected to internal pressure loading and elevated temperature.

8. Hermann, L. R., "A Bending Analysis for Plates," March 1965, Aerojet-General Corp., Technical Paper No. 7 SRO. In this paper, a general, approximate solution method applicable to the bending analysis of structural plates is presented and illustrated. The analysis includes the effects of shearing deformations and, as a consequence, is applicable to both thin and moderately thick plates.

The plate bending equations (including shear deformations), written as functions of the transverse deflection, and the bending moments are expressed by means of a variational theorem. The plate to be analyzed is represented by a series of finite elements (triangles). Forms of the primary dependent variables (transverse deflection and moments) are assumed within each element and are related to their values at the element nodes (i.e., at the triangle vertices). The approximate solution is obtained by taking the variational of the function with respect to the node values of the unknowns, thus generating a set of linear algebraic equations that define these nodal values. The rotations and shears are calculated from the values of deflection and moments.

The consideration of transverse shear deformations permits the specification of three boundary conditions at each boundary point, instead of two, as in the case of the classical thin plate theory. Thus, for example, along a free edge of a plate, the actual boundary conditions may be applied (vanishing of the normal moment, normal shear, and twisting moment) instead of the rather artificial boundary conditions demanded by thin plate theory (vanishing of the normal moment and the "effective" transverse force).

The solution technique is utilized to analyze two significant problems, for which exact solutions are available, with excellent accuracy.

9. Holston, A., Jr., "Approximate Analytical Solutions of the Finite-Deflection Equations for a Shallow Spherical Shell," Transactions of ASME, Vol 89, Series E, No. 1, Journal of Applied Mechanics, March 1967, p 65-86. Approximate solutions are obtained, by Newton's method, for shells subjected to uniform and/or point loads in the prebuckled or postbuckled configurations. Comparison of results with numerical solutions shows maximum deviations of 5 percent for clamped shells subjected to uniform loads in the prebuckled configuration. Similar comparisons for other cases show larger deviations. A characteristic load is developed which compares favorably with numerical buckling loads.

10. Hrennikoff, A., "Solution of Problems of Elasticity by the Framework Method," Journal of Applied Mechanics, Trans. ASME 63, Dec 1941, p A169-A175. Because of mathematical difficulties which make the solution of differential equations of the theory of elasticity impossible in many cases, the author has been impelled to seek some other method of approach than one of pure mathematical analysis. The method outlined in this paper is of this character and may with some qualifications be applied to problems of two-dimensional stress, bending of plates, bending of cylindrical shells, the general case of three-dimensional stress, and a great variety of others. Essentially, the method consists in replacing the continuous material of the elastic body

being studied by a framework of bars arranged according to a definite pattern, the elements of which are endowed with elastic properties suitable to the type of problem. This framework is then analyzed, according to the procedure outlined in the paper for various types of elastic problems. Examples of the application of the principles involved are also given.

11. Kalnius, A. and J. F. Lestingi, "On Nonlinear Analysis of Elastic Shells of Revolution," Transactions of ASME, Vol 89, Series E No. 1, Journal of Applied Mechanics, March 1967, p 59-64. A multisegment method is developed for the solution of two-point boundary-value problems governed by a system of first-order ordinary nonlinear differential equations. By means of this method, rotationally symmetric shells of arbitrary shape under axisymmetric loads can be analyzed with any available nonlinear bending theory of shells. The basic equations required by the method are given for one particular theory of shells, and numerical examples of a shallow spherical cap and a complete torus subjected to external pressure are presented in detail. The main advantage of this method over the finite-difference approach is that the solution is obtained everywhere with uniform accuracy, and the iteration process with respect to the mesh size, which is required with the finite-difference method, is eliminated.

12. Kaufman, S. and D. B. Hall, "Bending Elements for Plate and Shell Networks," AIAA Journal, Vol 3, No. 3, March 1967, p 402-405. Triangular bending elements that can be applied to irregular plate or shell networks are presented. Equilibrium as well as elastic properties of these elements are derived. Also presented are parallelogram plate bending elements whose elastic properties include core shear deformations for sandwich or thick plates. The elements presented are peculiar to the matrix force method with virtual work concepts forming the basis for computation of the elastic properties of the elements. A method of providing transition elements between triangular and parallelogram networks is also given.

13. Khanna, J. and R. F. Hooley, "Comparison and Evaluation of Stiffness Matrices," AIAA Journal, Vol 4, No. 12, Dec 1966, p 2105-2111. Previous developments in the comparison and evaluation of stiffness matrices are reviewed. A simplification to the method of making comparisons on the basis of strain energy is presented, and it is shown that the results of element stiffness matrix comparisons apply to the structure. The theoretical basis for obtaining approximate qualitative comparisons from stiffness matrix eigenvalues is described, and the existing hypothesis on their use evaluated. Some plane stress stiffness matrices for square, isotropic elements are compared, and it is shown that it is reasonable to expect bounding of the strain energy by varying a stiffness matrix parameter. A method of comparing stiffness matrices of different orders is proposed. It also is shown that square elements generally will provide a better approximation to the strain energy than constant-stress triangular elements.

14. Klein, B., "A Simple Method of Matric Structural Analysis," Journal of Aero/Space Sciences, Jan 1957, p 39-41. A simple method of matric structural analysis is presented which is believed to have certain distinct advantages over existing methods as explained in the text. The possible disadvantages of the method eventually may be minimized as the size and scope of automatic computing equipment are made larger. Certain two- and three-dimensional problems are worked to illustrate the ease and simplicity of the method.

15. Klein, B., "A Simple Method of Matric Structural Analysis: Part II - Effects of Taper and Consideration of Curvature," Journal of Aero/Space Sciences, Nov 1957, p 813-820. The matric method of structural analysis presented previously in Part I is extended to include the effects of panel geometry and gage taper, stringer taper, and a consideration of curved elements. The resulting matrices are of the same form as the previous matrix and of comparable simplicity. Several problems are presented to illustrate the mechanics and simplicity of the extended method.

16. Klein, B., "A Simple Method of Matric Structural Analysis: Part III - Analysis of Flexible Frames and Stiffened Cylindrical Shells," Journal of Aero/Space Sciences, June 1958, p 385-394. The method presented in Part II (reference 2) is extended to cover the case of stiffened cylinders. Treatable loadings include those producing peak shear, such as in flexible frame problems, and those involving thermal stresses. Various structural irregularities may be accounted for, such as variable frame moment of inertia, tapered longerons, variable skin gage, cutouts, noncircular cylindrical shells, etc. A flexible frame problem is solved for illustration purposes.

17. Klein, B., "A Simple Method of Matric Structural Analysis: Part V - Structures Containing Plate Elements of Arbitrary Shape and Thickness," Journal of Aero/Space Sciences, Nov 1960, p 859-865. Simple equations are used to treat plate elements. The equations are basic equilibrium and force-displacement equations. The plate elements may be of any shape and have any thickness variation. The stresses in the elements may vary in a complex pattern. There need not be any edge members attached to the plates. All equations are simple to derive and simple in principle. Most equations contain definite integrals. Since in general the shapes and thicknesses of the plate elements are arbitrary, a simple numerical integration scheme is used to evaluate the integrals. Numerous numerical examples are worked out to illustrate the mechanics of the method and the accuracy attained.

18. Klein, B., "A Simple Method of Matric Structural Analysis, Part VI - Bending of Plates of Arbitrary Shape and Thickness Under Arbitrary Normal Loading," Journal of Aero/Space Sciences, March 1962, p 306-322. Method for analysis of general kinds of complex plates under complex normal loading: work is extension of previously given matric method for solution of in-plane plate problems; method is of comparable simplicity; all boundary conditions are satisfied easily and directly; numerical examples illustrate mechanics of method. Part V indexed in Engineering Index 1961 p 1285.

19. Lo, C. C., F. W. Niedenfuhr, and A. W. Leissa, "Further Studies in the Application of the Point Matching Technique to Plate Bending and other Harmonic and Biharmonic Boundary-Value Problems," Air Force Flight Dynamics Laboratory Technical Report AFFDL-TR-65-114, 175 pp. (Jan. 1966). Contract No. AF 33(657)-8772. This work is the second report summarizing work in applying the point matching technique to plate bending and other harmonic and biharmonic boundary value problems. Ideas to improve the numerical convergence are investigated. One idea involves using multiple poles of expansion; this is demonstrated by a torsion problem. Sources of round-off error are identified and means of minimizing it are described, along with examples. The concept of multiple poles is extended further to the use of a large number of origins located along the boundary itself. Singularity functions referred to these origins are used to represent concentrated forces and moments. Used in conjunction with point matching, a method results which is an approximation to the solution of singular integral equations, and yields excellent results for intricate shapes. Suitable equations are formulated for representing the boundary conditions by step function or polygonal function approximation for several classes of problems, including: conductive heat transfer, torsion, plate bending, and plane elasticity with mixed boundary conditions. Numerous numerical examples are presented which demonstrate the technique and convergence for these classes of problems.

20. Lu, Z. A., J. Penzien, and E. P. Popov, "Finite Element Solution for Thin Shells of Revolution," NASA CR-37, 76 pp., July 1964. (Prepared under Grant no. NsG-274-63 by Univ. of Calif., Berkeley, Calif.) Thin shells of revolution are widely used in flight structures and their analysis is of great importance to the design engineer. In such shells for symmetrical loadings and small displacements, the membrane stresses and the corresponding elastic displacements can be readily computed. However, due to the variations in thickness, ring-like reinforcements at openings and junctures with the adjoining shells and/or structures, very important bending stresses develop. The analysis of such stresses may be very complex. In fact, solutions are available only for the few simplest possible shapes of the meridian. Also very few solutions exist for the cases of variable thickness and, in some of the solutions which are available, the thickness variation is prescribed for reasons of mathematical expediency. On the other hand, functional and manufacturing requirements often demand arbitrary shape and thickness variation of the shell of revolution. To achieve a practical solution for such a general problem is the primary purpose of this investigation.

21. "Matrix Methods in Structural Mechanics," (proceedings of the conference held at Wright-Patterson Air Force Base, Ohio, 26 to 28 October 1965), AFFDL-TR-66-80. The Conference on Matrix Methods in Structural Mechanics held at Wright-Patterson Air Force Base on 26 to 28 October 1965 was sponsored jointly by the Air Force Flight Dynamics Laboratory, Research and Technology Division, Air Force Systems Command, and the Air Force Institute of Technology, Air University. The purpose of the conference was to discuss the recent developments in the field of matrix methods of structural analysis and design of aerospace vehicles.

The 36 papers presented were arranged into 6 sessions under 5 different themes; General Matrix Methods, Finite Element Properties, Nonlinear Effects, Dynamics, and Applications. The papers cover practically all major aspects of recent research and development work in the field of matrix methods of structural analysis and design.

22. Melosh, R. J., "Basis for Derivation of Matrices for the Direct Stiffness Method," AIAA Journal, Vol 1, No. 7, July 1963, p 1631-1637. Previous developments in the direct stiffness method are reviewed. The advantages of extending the definitions to make the method a variational approach are cited. The finite element formulation of the method of minimum potential energy is given. Explicit requirements of potential energy displacements are presented, and a criterion insuring monotonic convergence is developed. Illustrative displacements yielding matrices resulting in monotonic convergence are included. Available matrices are reviewed with respect to the extended developments.

23. Melosh, R. J. and R. G. Merritt, "Evaluation of Spar Matrices for Stiffness Analyses," Journal of the Aero/Space Sciences, Vol 25, No. 9, Sept 1958, p 537-543. Convergence difficulties have been encountered in the deflection analysis of certain structures with most of the bending material in the skin using the stiffness method. The difficulties are attributed to the use of the elementary beam spar matrix. Two new spar matrices are developed and compared with the matrix based on elementary beam concepts. The error, as a function of the nodal breakdown and the structural parameters, is determined for a beam analyzed using the spar matrix for the web and stringer matrices for the flanges.

Convergence to the final stiffness coefficients is shown to be much more rapid using either of the new matrices for structures with most of the bending material in the skin.

An unswept box beam is analyzed to demonstrate convergence of the stiffness solutions and the superiority of the new moment-shear spar matrix in an actual problem characteristic of a wing. The stiffness method results are shown to converge to analytical results obtained with elementary bending theory including transverse shear deformation and shear lag corrections.

24. Percy, J. H., T. H. H. Pian, S. Klein, and D. R. Navaratna, "Application of Matrix Displacement Method to Linear Elastic Analysis of Shells of Revolution," AIAA Journal, Vol 3, No. 11, Nov 1965, p 2138-2145. The paper describes the application of the matrix displacement method to the linear elastic analysis of shells of revolution. The shell is idealized as a series of conical frusta, joined at nodal circles. In the present paper the use of the idealization to handle asymmetric deformations is demonstrated. Also shown is how approximations to the mass and stiffness matrices may be consistently derived; these may then be used to solve both static and dynamic problems. The effect on the results of static analyses of improving the approximation to the stiffness matrix, using the procedure suggested by Pian, is demonstrated and discussed. Results are presented of static analyses of several shell configurations, and these are compared with solutions by other methods. It is found that the method provides accurate solutions for shells of revolution under both axisymmetric and asymmetric loadings by using a reasonable number of elements.

25. Tuma, J. J., K. S. Havner, and S. E. French Jr., "Analysis of Flat Plates by Algebraic Carry-Over Method," Oklahoma State Univ Eng Experiment Station, Publication 118, Dec 1960, 230 p. Lagrange's 4th order partial differential equation of thin plate is replaced by 2nd order equations in terms of loads, moments and deflections: these equations together with boundary conditions are expressed by 2 sets of finite difference equations in algebraic form: numerical evaluation of these algebraic results is made by means of electronic computer; tables; references.

26. Turner, M. J., R. W. Clough, H. C. Martin, and L. J. Topp, "Stiffness and Deflection Analysis of Complex Structures," Journal of the Aeronautical Sciences, Vol 25, No. 9, Sept 1956, p 805-823. A method is developed for calculating stiffness influence coefficients of complex shell-type structures. The object is to provide a method that will yield structural data of sufficient accuracy to be adequate for subsequent dynamic and aeroelastic analyses.

Stiffness of the complete structure is obtained by summing stiffnesses of individual units. Stiffnesses of typical structural components are derived in the paper. Basic conditions of continuity and equilibrium are established at selected points (nodes) in the structure. Increasing the number of nodes increases the accuracy of results. Any physically possible support conditions can be taken into account. Details in setting up the analysis can be performed by nonengineering trained personnel; calculations are conveniently carried out on automatic digital computing equipment.

Method is illustrated by application to a simple truss, a flat plate, and a box beam. Due to shear lag and spar web deflection, the box beam has a 25 percent greater deflection than predicted from beam theory. It is shown that the proposed method correctly accounts for these effects.

Considerable extension of the material presented in the paper is possible.

27. Turner, M. J., E. H. Dill, H. C. Martin, and R. J. Melosh, "Large Deflections of Structures Subjected to Heating and External Loads," Journal of Aero/Space Sciences, Feb 1960, p 97-106. The method of direct formulation of the stiffness matrix is extended to include the effects of nonuniform heating and large deflections. The purpose is to develop an analytical tool for the treatment of actual structures.

In the solution of aeroelastic problems the relations between forces and deflections must be determined. The usual stiffness matrix formulation of this relationship is limited to small temperature changes and small deflections. For large temperature changes additional terms are required. Also the problem becomes geometrically nonlinear when large deflections are involved. To overcome the inherent difficulties of the nonlinear problem for practical structures either an iterative or a step-by-step procedure must be used. The force-deformation relations necessary for this step-by-step or iterative approach are derived for an axially loaded member and for a plate element including the effects of thermal strains.

28. Utku, S., "Stiffness Matrices for Thin Triangular Elements of Nonzero Gaussian Curvature," AIAA Journal, Vol 5, No. 9, Sept 1967, p 1659-1667. Flat triangular elements, when used to approximate shells, may cause geometrical idealization errors in addition to the errors associated with assumptions on deflection distributions. Taking into account average curvatures of the middle surface, these idealization errors may be reduced without additional grid refinement. The curved triangular elements are defined by joining the selected nodes with the geodesic lines of the middle surface. In computer applications, the average values of normal curvatures of a curved triangular element may be either input or computed from the cartesian coordinates of elemental nodes. A piecewise linear deflection field is assumed. The nodal values of this field are the undetermined parameters of the problem which yield a minimizing sequence with grid refinement. Using the shallow shell theory, strains may be expressed in the natural coordinate system of the base triangle. Expressing the strain energy of the curved triangle in terms of its nodal deflections, the elemental stiffness matrix is obtained by the usual minimization process coupled with the condition that no nodal forces result from rigid body modes. By setting the average curvatures equal to zero, the stiffness matrix of a flat triangular element is obtained.

29. Utku, S., and R. J. Melosh, "Behavior of Triangular Shell Element Stiffness Matrices Associated with Polyhedral Deflection Distributions," NASA Technical Report 32-1217, 13 February 1968. Invariants of the triangular shell element stiffness matrices are examined. The stiffness matrix is considered as the sum of membrane, bending, and transverse shear stiffness matrices representing respective strain energies. For various geometries and curvatures, eigenvalues of these matrices are obtained numerically. By studying the eigenvalues, it is shown that stiffness matrices produced with the help of equilibrium requirements may display nonpositive behavior depending upon element geometry. The grave consequences of nonpositive behavior are demonstrated. Since equilibrium algorithms can be used to accelerate the convergence, two schemes are developed to correct the nonpositive behavior. These schemes are based on the observation that nonpositive behavior originates from the base matrix to which equilibrium algorithm is applied. The effect of thickness/area ratio on the overall behavior is studied. The behavior associated with true potential energy approach is demonstrated on several test cases. The effect of geometry is also discussed in the assembled matrix. Guidelines have been presented for the use of the triangular shell element in structural analysis.

30. Zienkiewicz, O. C. and Y. K. Cheung, "The Finite Element Method in Structural and Continuum Mechanics," McGraw-Hill, 1967. The powerful method of "finite elements" permits almost all problems of structural stress analysis, or the analysis of such field problems as heat transfer and fluid flow, to be presented in a mathematical form suitable for solution on a digital computer. This is indispensible if complex structures are to be economically designed, not only to serve the advanced needs of aeronautics, space flight, turbine design, and nuclear technology, but also for use in such general engineering fields as dam and bridge building.

"The Finite Element Method in Structural and Continuum Mechanics" is the first comprehensive textbook on a subject that until now has been presented mainly in specialist papers. Although it begins with first principles and is a relatively simple treatment of a wide subject, the book takes the reader up to the frontiers of present-day research. It also includes many examples of solutions to practical problems, such as those relating to the design of dams, nuclear reactors, and turbines, as well as those concerned with rock mechanics and seepage in civil engineering projects. A final chapter gives details of typical computer programs written in FORTRAN language with comments on data preparation and digital solutions.

c. Experimental Methods

1. Isler, H., "Experimental Shell Design," Proceedings of the Symposium on Shell Research, New York, John Wiley & Sons, Inc., 1962, p 356-358. Experimental methods are described, helping to solve shell problems at different levels: to find new shapes; to visualize design; to elaborate accurate shape; to determine stresses and deflections; to analyse stability; to check built shells.

Applications in prestressed concrete and reinforced plastics are shown.

2. Rowe, R. E., "Tests on Four Types of Hyperbolic Shell," Proceedings of the Symposium on Shell Research, New York, John Wiley & Sons, Inc., 1962, p 16-35. Tests are described and principal results are reported. One test was performed on a 1/10 scale model of one quarter of a square shell roof, with edge beams, made of reinforced cement mortar. Another test was on a similar model without edge beams. The third model was a square mushroom roof on a central column made of reinforced mortar to 1/6 scale. The fourth model was a grillage of Perspex plastic beams welded with chloroform, simulating to 1/32 scale the construction of part of a composite hypar roof from precast concrete units. In these tests bending stresses were shown to have the same order of magnitude as membrane stresses.

3. VANE VIBRATIONS (VIBRATIONS OF CURVED PLATES)

a. Exact Solutions

1. Cummings, B. E., "Large Amplitude Vibration and Response of Curved Panels," AIAA Journal, Vol 2, 4, p. 709-716, Apr 1964. The dynamic nonlinear shallow-shell equations are examined in the special case of a cylindrical shell segment. Different developments are given for two systems: in system A, the stress boundary conditions are satisfied exactly, and compatibility is satisfied on the average; in system B, compatibility is satisfied exactly, and the stress boundary conditions are satisfied on the average. Perturbation and exact integral expressions are found for the frequencies of vibration. The response to delta-function, step-function, and harmonic-function loading is examined. Dynamic buckling is predicted by shock response method.

2. Galletly, G. D., "On The In-Vacuo Vibrations of Simply Supported, Ring-Stiffened Cylindrical Shells," Proceedings of the Second U. S. National Congress of Applied Mechanics (1954), p 225-231. An analytical solution is presented for the problem of determining the in-vacuo frequencies of vibration of a simply supported thin cylindrical shell

which is reinforced by equally spaced, equal strength circular ring stiffeners. The displacement configuration assumed permits inter-ring deformation of the shell. Numerical calculations were made for a cylindrical shell with various sizes of stiffening rings, and curves were plotted which show the effect of the rings upon the frequency of vibration. The numerical values obtained were also compared with those calculated by approximate methods and were found to agree within ±10 percent.

3. Guyan, R. J., "Reduction of Stiffness and Mass Matrices," AIAAJ, Volume 3, No. 2, p 380, February 1965. This paper discusses a matrix condensation technique by which the order of stiffness and mass matrices can be reduced. Reduction is accomplished by eliminating coordinates at which a zero force is applied. The reduced matrices retain the structural and mass properties of the original matrices in a complex form. This will be useful in the inducer vibration program by reducing the number of degrees of freedom per free node to one. In this manner, an existing FRDC eigenvalue or latent root program that is limited to 50 degrees of freedom will allow an inducer with a maximum of 50 free nodes to be analyzed.

4. Kalnins, A., "Free Vibration of Rotationally Symmetric Shells," Journal of the Acoustical Society of America, Vol 36, No. 7, July 1964. This paper is concerned with a theoretical investigation of the free vibration of arbitrary shells of revolution by means of the classical bending theory of shells. A method is developed that is applicable to rotationally symmetric shells with meridional variations (including discontinuities) in Young's modulus, Poisson's ratio, radii of curvature, and thickness. By means of the method of this paper, the natural frequencies and the corresponding mode shapes of axisymmetric or nonsymmetric free vibration of rotationally symmetric shells can be obtained without a limitation on the length of the meridian of the shell. To illustrate the application of the method given in this paper to particular shells, some results of free vibration of spherical and conical shells obtained earlier by means of the bending theory are reproduced by the general method of this paper, and a detailed comparison is made. In addition, paraboloidal shells and a sphere-cone shell combination are considered, which have been previously analyzed by means of the inextensional theory of shells, and natural frequencies and mode shapes predicted by the bending theory are given.

5. Kalnins, A., "Free Nonsymmetric Vibrations of Shallow Spherical Shells," Proceedings of the Fourth U.S. Congress of Applied Mechanics, Vol I, p 225-233, 1962. This paper is concerned with the investigation of the natural frequencies and mode shapes of free vibrations of shallow spherical shells with the use of the classical theory of shallow shells. Explicit solutions for the three displacement components of the middle surface are derived in terms of Bessel functions, and the frequency equation for a shallow spherical cap with a clamped edge is deduced. All natural frequencies within a certain frequency band are determined for various values of the circumferential wave number, curvature, and thickness of the shell. The mode shapes of the first six modes are calculated and their character is examined. It is found that the modes are such that either the longitudinal or the transverse displacement is predominant. The corresponding frequency equation given by the theory of transverse vibration is deduced and by comparing its frequencies to those of the classical theory the modes not predicted by the theory of transverse vibrations are determined.

6. Palmer, P. J., "Natural Frequency of Vibration of Curved Rectangular Plates," Aeronautical Quarterly v 5 pt 2 July 1954 p 101-10. Vibration evaluated for fundamental extensional mode, thought to be applicable when plates are excited by uniformly distributed pressure as may occur with dynamic pressure wave; natural frequencies corresponding to this mode increase fairly rapidly with curvature of plate.

b. Approximate Methods

1. Dawe, D. J., "A Finite Element Approach to Plate Vibration Problems," J. Mech. Engng. Sci. 7, 1, 28-32, Mar. 1965. Energy considerations are used to derive stiffness and inertia matrices for a rectangular isotropic plate element of uniform thickness. The deflected form of each element is assumed to contain terms proportional to 1, x, y, x^2, xy, y^2, x^3, x^2y, xy^2, y^3, x^3y, xy^3, and the twelve associated unknowns are determined from continuity of w, $\partial w/\partial x$, $\partial w/\partial y$ at the corner points. (See also Zienkiewicz and Cheung, AMR 18 (1965), Rev. 131). The matrices are used to find the natural frequencies of certain square plates, and comparisons with other solutions show that the method gives good results even for relatively few elements.

2. Deak, A.L. and T.H.H. Pian, "Application of Smooth-Surface Interpolation to the Finite Element Analysis," AIAA Journal, Vol 5, No. 1, p 187-189, Jan 1967. Compatibility of the slopes along the normal of the inter-element boundaries of finite retangular elements in bending is achieved by the use of special polynomial functions. Stiffness and mass matrices based upon these functions have been used to make static and dynamic analyses of retangular plates. This method yields a considerable improvement in numerical solutions of displacements in numerical solutions of displacements and frequencies as obtained without the use of the interpolation functions.

3. Laursen, H. I., R. P. Shubinski, and R. W. Clough, "Dynamic Matrix Analysis of Framed Structures," Proceedings of the Fourth U.S. Congress of Applied Mechanics, Vol I, 1962, p 99-105. The matrix methods developed in recent years for static analysis of structures can be used effectively to determine the natural frequencies of these structures. This can be accomplished by developing a dynamic stiffness matrix for the individual members and subsequently obtaining a dynamic stiffness matrix for the entire structure. Substitution of this matrix into the appropriate equilibrium expression results in an expression for the natural frequencies of the structure. Application of this technique is demonstrated here with several different examples. The results may be considered exact in the sense that the mass of all members is assumed to be distributed and the stiffness of all members is assumed to be finite.

4. Leckie, F. A., "Application of Transfer Matrices to Plate Vibrations," Ingenieur-Archiv v 32 n 2 1963 p 100-11. Successful application of transfer matrices to computation of natural frequencies and normal modes of elastic systems described by single space variable suggested extension to include systems described by 2 space variables such as plates; when, instead of plate, model suggested by A. Hrennikoff was used, problem could be reduced to one with finite degrees of freedom.

5. "Matrix Methods in Structural Mechanics," (proceedings of the conference held at Wright-Patterson Air Force Base, Ohio, 26 to 28 October 1965), AFFDL-TR-66-80. The Conference on Matrix Methods in Structural Mechanics held at Wright-Patterson Air Force Base on 26 to 28 October 1965 was sponsored jointly by the Air Force Flight Dynamics Laboratory, Research and Technology Division, Air Force Systems Command, and the Air Force Institute of Technology, Air University. The purpose of the conference was to discuss the recent developments in the field of matrix methods of structural analysis and design of aerospace vehicles.

The 36 papers presented were arranged into 6 sessions under 5 different themes; General Matrix Methods, Finite Element Properties, Nonlinear Effects, Dynamics, and Applications. The papers cover practically all major aspects of recent research and development work in the field of matrix methods of structural analysis and design.

6. McGrattan, R. J., and E. L. North, "Vibration Analysis of Shells Using Discrete Mass Techniques," Transactions of ASME, November 1967, p 766-772. A method for analyzing thin shells by a discrete mass technique is presented. The shells and stiffeners are idealized as a system of lumped masses and an elastic framework having the equivalent mass and stiffness of the actual shell. This method is most useful for shells without rotational symmetry, since classical solutions are not available for these cases. Four examples are presented and a comparison with experimental results and classical theory is made for a case of a symmetrically stiffened cylinder.

7. Navaratna, D. R., "Natural Vibrations of Deep Spherical Shells," AIAA Journal, Vol 4, No 11, p 2056-2058, Nov 1966. The author represents a shell of revolution by a series of discrete frustra of shells which satisfy the displacement and slope continuity at the common nodal circles. Stiffness and mass matrices are determined and the matrix frequency equation is solved for the natural frequencies and the generalized displacements. Calculations for spherical shells with free, hinged, and clamped edges agree satifactorily with those obtained by other methods.

8. Nowinski, J. L., "Large-Amplitude Oscillations of Oblique Panels with an Initial Curvature," AIAA J. 2, 6, 1025-1031, June 1964. Von Kármán field equations for flexible oblique plates with an initial curvature are extended to a dynamical case. Using series representation of initial and additional deflections and Galerkin's procedure, the governing equation for an admissible mode time function is established. Using this single assumed modal deflection, and assuming built-in edge free to move in the inplane directions, the following particular cases are discussed: buckling of an oblique plate under uniaxial compressive load, free linear vibrations of a square plate, large deflections of a uniformly loaded square plate, snap-through phenomena of a curved oblique plate under uniform transverse load, and free nonlinear vibrations. A numerical example concerning a rhombic plate is discussed in more detail. The well-known fact of a decrease of the period of nonlinear vibrations with an increasing amplitude is corroborated, this relation being less pronounced for larger sweep angles.

9. Petyt, Maurice, "Finite Element Vibration Analysis of Cracked Plates in Tension," Technical Report AFML-TR-67-396, January 1968. A finite element method of analysis is developed to determine the vibration characteristics of an aircraft fuselage panel containing a fatigue crack. Experimental observations show that as the length of the crack increases, the frequency of vibration reaches a minimum when the free edge of the crack buckles. The variation in this phenomena with increasing plate width is studied both experimentally and theoretically.

The analysis is developed in a systematic manner and calculations are performed at each stage on problems with known solutions to determine the accuracy of the method. The problems considered include the vibrations of flat plates of varying planform, the vibrations of a cylindrical shell, the buckling of a rectangular plate, and the vibrations of a rectangular plate in compression.

The method is finally applied to the problem of a cracked plate in tension and the results compared with experimental

measurements. The post buckling behavior is calculated using a step-by-step analysis to permit linearization of the governing equations. By considering the calculated stress distributions, the variation in buckling stress with crack length and plate width is explained.

10. Plass, H. J. Jr., J. H. Gaines, and C. D. Newsom, "Application of Reissner's Variational Principle to Cantilever Plate Deflection and Vibration Problems," Journal of Applied Mechanics, March 1962, p 127-135. A variational principle due to E. Reissner has been rewritten in a form which is applicable to small deflection problems for thin plates. The modified principle is used to obtain approximations to static deflection and vibration problems of square and skew cantilever plates of uniform thickness.

11. Ross, E. W., Jr. and W. T. Matthews, "Frequencies and Mode Shapes for Axisymmetric Vibration of Shells," Transactions of ASME, Vol 89, Series E, No. 1, Journal of Applied Mechanics, March 1967, p 73-86. This paper treats the axisymmetric vibration of thin elastic shells. Estimates of natural frequencies and modes are obtained for a general class of domes by applying the approximations obtained in a previous paper by one of the authors. Numerical results are obtained for ellipsoidal shells, and one new theoretical result is found.

12. Witmer, E. A., H. A. Balmer, J. W. Leech, and T. H. H. Pian, "Large Dynamic Deformations of Beams, Rings, Plates, and Shells," AIAA J. 1, 8, 1848-1857, Aug. 1963. Authors develop a finite difference lumped-stringer type of formulation for the dynamic response of simple two-dimensional and axisymmetric structures subjected to impulse loadings which deform the structures into the plastic region. The method considers elastic strain-hardening behavior, strain rate and large deflections.

    The resulting numerical solutions for particular cases are compared with limited experimental data - particularly some recent beam tests at Picatinny Arsenal. A comparison between authors' theory and experiment shows generally good agreement although there are some unexplained differences between predicted and observed time histories.

    A major difficulty in applying their method is, as the authors note, the large number of difference equations which requires considerable computer time. Simpler, less time-consuming methods are desirable.

13. Zienkiewicz, O. C., and Y. K. Cheung, "The Finite Element Method in Structural and Continuum Mechanics," McGraw-Hill, 1967. The powerful method of "finite elements" permits almost all problems of structural stress analysis, or the analysis of such field problems as heat transfer and fluid flow, to be presented in a mathematical form suitable for solution on a digital computer. This is indispensible if complex structures are to be economically designed, not only to serve the advanced needs of aeronautics, space flight, turbine design, and nuclear technology, but also for use in such general engineering fields as dam and bridge building.

    "The Finite Element Method in Structural and Continuum Mechanics" is the first comprehensive textbook on a subject that until now has been presented mainly in specialist papers. Although it begins with first principles and is a relatively simple treatment of a wide subject, the book takes the reader up to the frontiers of present-day research. It also includes many examples of solutions to practical problems, such as those relating to the design of dams, nuclear reactors, and turbines, as well as those concerned with rock mechanics and seepage in civil engineering projects. A final chapter gives details of typical computer programs written in FORTRAN language with comments on data preparation and digital solutions.

c. Experimental Methods

1. Hoppmann, W. H., II, and C. N. Baronet, "A Study of the Vibrations of Shallow Spherical Shells," Trans. ASME 30 E (J. Appl. Mech.) 3, 329-334, Sept. 1963. Paper is sequel to papers by senior author alone or with collaborators (see, for example, AMR 15 (1962), Revs. 1370, 2026) on vibration of spherical caps. Additional experimental results are presented and compared with results of theory previously presented for symmetrical vibration. New data are given for shells which have 12-inch chord; 0.5 and 1.6-inch rise; thicknesses of 1/16, 1/8, and 1/4 inch; and both clamped and hinged edges. Agreement is moderately good. Experimental results are also presented for asymmetrical vibration. As authors point out, it is interesting to note that frequencies for clamped and for momentless cases do not differ greatly. Appendix presents formulas for symmetrical vibration but no basic theory; the reader is referred to previous paper for the complete analytical treatment.

APPENDIX B
RESUMES OF SOURCE MATERIAL

1. HYDRODYNAMIC LOADING OF INDUCER BLADES

The following are resumes of those articles included in the Literature Survey (Appendix A) from which prediction methods were selected for use in formulating analytical models.

a. Exact Methods: Noncavitating

1. Durand, W. F., Aerodynamic Theory, Vol II (General Aerodynamic Theory - Perfect Fluids by Th. von Karman and J. M. Burgers), First Edition, 1963; "Flow Through a Lattice Composed of Airfoils," p 91-96.

   An exact two-dimensional solution to the basic potential flow operations is presented for both staggered and unstaggered flat plate cascades. The solution to these potential flow equations employs the techniques of conformal mapping. A general form of the Joukowski transformation is used to map from the potential flow about a circle in one plane into the flow around a cascade of airfoils (staggered or unstaggered) in the real plane. This method considers ideal or no-loss flow only, while giving a solution to the flow field in two dimensions. Cavitation is not considered. This method of analysis, however, does allow determination of incidence effects on loading around the blade leading edge.

2. Fanti, R., "Elementary Incompressible Solution for the Performance of Airfoils of Arbitrary Shape in an Arbitrary Cascade," United Aircraft Corporation Research Department, Report R-23010-12, 23 February 1953.

   An exact two-dimensional potential flow solution is presented for the case of incompressible flow through airfoils of arbitrary shape in an arbitrary cascade. This work is an expansion on the theory presented in Durand (Reference 1) by von Karman and Burgers. Sources and sinks are applied along the surfaces of the flat plate airfoils to simulate the effects of airfoil thickness and shape on the potential flow field. This method of flow analysis is completely theoretical and does not allow for internal flow losses but does accurately describe the deviations between the streamlines and the blade surface in the region of the airfoil leading edge. Cavitation is not considered, restricting use of the solutions presented to single-phase flow.

b. Exact Methods: Cavitating

1. Stripling, L. B. and A. J. Costa, "Cavitation in Turbopumps," Parts I and II, ASME Papers No. 61-WA-112 and 61-WA-98, 25 July 1961.

An exact two-dimensional solution to the potential flow equations for the case of supercavitating flow is presented in Part I. The method of solution employs conformal mapping techniques similar to those used in the articles presented by Durand and Fanti for noncavitating flow. Part II illustrates the cavitation performance data of several helical inducers for various flow coefficients correlated with the theory from Part I. With the use of semi-empirical correlating factors, the streamline theory presented in Part I is said to serve as a useful basis for design.

Basic assumptions made in the streamline model are listed below:

- A distinct vapor cavity is formed by a free streamline which is attached to the leading edge of all blades
- Flow is two-dimensional, irrotational, inviscid and nonoscillatory
- Cavity is infinite in length.

These assumptions result in measurable deviations from the actual flow case. In particular, the combination of radius changes and rotation of the inducer would result in significant blade loadings due to Coriolis effects, which are not accounted for in the two-dimensional analysis. Other important real effects include flow losses due to friction, leakage and diffusion and three-dimensional cavities that collapse within the inducer. This method is also restricted to flow through cascades composed of parallel flat plate airfoils. Although this type analysis would not result in satisfactory determination of the flow field within cambered inducer passages, the exact theory could be used to indicate flow incidence effects on and near the airfoil leading edge, including the effects of cavitation.

2. Jakobson, J. K., "Supercavitating Cascade Flow Analysis," ASME Paper No. 64-FE-11, 27 February 1964.

Exact two-dimensional potential flow theory is presented for incompressible flow through a cascade of arbitrarily shaped airfoils, including the effects of cavitation. The assumptions that are made are essentially the same as those made by Stripling and Acosta. Flow is two-dimensional, irrotational, inviscid, and nonoscillatory. Cavity representation is made by a distinct (vapor) cavity of infinite length. This latter assumption again allows an exact mathematical solution of the potential flow equations for special cases using the techniques of conformal mapping. The general theory for flow through any cascade composed of blades of arbitrary

shapes results in an integral equation that cannot be solved directly and must rely on numerical integration techniques for its solution. It is indicated that a numerical integration of resulting integrals for cambered blades could be complex, requiring experimentation to develop computer programs that would be convergent and efficient. Although this paper covers the theory for the most general type of two-dimensional, ideal (steady, irrotational, lossless), potential flow, that of cavitating flow in a cascade of arbitrary shaped airfoils, the complexity of the resulting exact solutions may be unattractive for use in this program.

c. Numerical or Approximate Methods

1. Cooper, P. and H. B. Bosch, "Three Dimensional Analysis of Inducer Fluid Flow," NASA CR-54836, 11 February 1966.

   Solutions for the three-dimensional and quasi-three-dimensional potential flow fields are presented. The three-dimensional analysis, referred to as the "exact" analysis, results from a finite difference representation of the basic potential flow equations. The quasi-three-dimensional analysis, referred to as the "approximate" method, results from a finite difference solution of the basic flow equations in the hub-to-shroud direction with a superimposed assumed solution in the blade-to-blade direction.

   Use of these basic flow equations and their finite difference solution in defining three-dimensional flow fields is similar to methods which have been employed at FRDC as well as by others. Reference is made to Stanitz (Reference 5) and Stockman (Reference 6) in the literature survey. Both employed types of quasi-three-dimensional solutions for describing flow fields. Use of the method presented in this report is unique, however, in its treatment of cavitating flow.

   Both methods of analysis presented in this report account for internal flow losses due to friction and diffusion while also accounting for the effects of cavitation. The cavity model used in both models allows for cavities of finite length and consisting of a homogeneous, two-phase mixture. This cavity model differs significantly from the cavity model assumed by Stripling (Reference 2) and Jakobson (Reference 4) who assumed a distinct cavity filled with saturated vapor and infinite in length.

   The "exact" method completely describes the entire potential flow field including flow losses and cavitation effects. The "approximate" method, in describing the flow field two-dimensionally in the

hub-to-shroud direction only, cannot accurately account for the effects of leading edge loading (incidence) and trailing edge unloading (deviation). Both solutions compare favorably in the interior regions of the inducer.

The "exact" method, while representing a good design system capable of solving the most general of problems, including incidence effects, flow losses, cavitation, and general blade geometry, requires considerable computing time that would, in general, prohibit its use as a practical design tool.

2. STRESSES AND VIBRATIONS IN INDUCER BLADES

1. Argyris, J. H., "Recent Advances in Matrix Methods of Structural Analysis," Progress in Aeronautical Sciences, Vol 4, 1964, The MacMillan Company, Perganon Press.

   Sections of this book outline the technique by which a curved cover can be analyzed by replacing the surface with triangular elements. The vertices of the elements are first prescribed as coordinates of a common coordinate system. A local plane coordinate system is then defined for the element and the direction cosines of the axes of this system relative to the common system are determined. These direction cosines are then used to determine the local coordinates of the nodes. The stiffness matrix, which is a function of the local coordinates, can then be computed. This matrix is then transformed to the common axes by rotating local axes to the common axes.

2. McGrattan, R. J. and E. L. North, "Vibration Analysis of Shells Using Discrete Mass Techniques," Transactions of ASME, Journal of Engineering for Industry, 767-777, November 1967.

   In this paper, thin shells are idealized by a framework of elastic beams that have the equivalent mass and stiffness of the shell. The interesting part of this paper is not the part involving the equivalent shell, but the method of transforming stiffnesses and determining flexibility matrices. Because the general surface is curved, the stiffnesses of the individual beams must be transformed by rotating their coordinate system to a common coordinate system and translating from the midpoint of the element to an appropriate joint. The resulting stiffnesses are then summed. This general method can be adapted to the inducer problem by transforming the stiffness matrices of the triangular elements in the same manner.

   The flexibility matrix is determined by the conventional unit load method, in which the deflection vector due to a unit load is applied at the N joints.

3. Utku, Senol, "Stiffness Matrices for Thin Triangular Elements on Analyzed Gaussian Curvature," AIAA, Vol No. 9, pp 1659-1667, September 1967.

In this paper, curved surfaces with double curvature are triangulated and referred to a base triangle whose vertices are the nodes of the curved element. Shallow shell theory is used and the strain energy of the shell is expressed in terms of nodal displacements. If zero curvature for the element is assumed the curved elements degenerate into the flat triangular base plane elements as will be done for the inducer blade. The method of partitioning the bending, membrane, and shear stiffness matrices, and the method of avoiding the difficulty due to coupling of bending moments and membrane forces is discussed. These techniques should be applicable to the inducer blade problem.

4. Turner, M. J., R. W. Clough, H. C. Martin, and L. J. Topp, "Stiffness and Deflection Analysis of Complex Structures," Journal of the Aeronautical Sciences, Vol 25, pp 805-823, September 1956.

This is one of the basic papers from which the matrix analysis of structures was developed. Direct methods for determining stiffness matrices of frame elements, shear panels, box beams, spars, rectangular plates, and triangular plates are presented. These matrices are developed by considerations of statics and avoid the use of strain energy methods. Of particular interest is the membrane stiffness matrix for arbitrarily shaped triangular plates of uniform thickness.

APPENDIX C
FORMULATION OF HYDRODYNAMIC COMPUTER PROGRAM

Contained in this Appendix is the engineering formulation for the hydrodynamic computer program.

INTERNAL PROGRAM CONSTANTS

$$\nu = \frac{\mu}{\rho}$$

$$\omega = 2\pi N$$

$$U_T = \omega R_T$$

$$\bar{\beta}_T^* = \frac{\beta_{T(1)}^* + \beta_{T(NJ)}^*}{2.0}$$

$$\sigma = \frac{Z_{(NJ)} - Z_{(1)}}{\frac{2\pi}{N_b} R_T \sin \bar{\beta}_T^*}$$

$$C_e = \frac{0.284}{\sqrt{\sigma}}$$

INLET ROUTINE

INLET CONSTANTS:

$$\psi_H = \tan^{-1}\left[\frac{R_{H(2)} - R_{H(1)}}{Z_{(2)} - Z_{(1)}}\right]$$

$$\psi_T = \tan^{-1}\left[\frac{R_{T(2)} - R_{T(1)}}{Z_{(2)} - Z_{(1)}}\right]$$

$$\Delta\psi = \psi_T - \psi_H$$

$$\Delta R = R_{T(1)} - R_{H(1)}$$

INLET STREAMLINE CALCULATIONS:

Find R for each streamline (R_{ST}) by dividing the annulus area into NI equal areas such that ΔR^2 between streamlines equals a constant, i.e.,

$$R^2_{ST(i)} - R^2_{ST(i-1)} = \text{constant}$$

Find $\psi_{(i)}$ for each streamline by linear interpolation versus radius.

$$\psi_{(i)} = \psi_H + \frac{(R(i) - R_{H(1)})\Delta\psi}{\Delta R}$$

$$R \tan\beta^* = R_{T(1)} \tan\beta^*_{T(1)} - \frac{(R_{T1} - R(i))}{\Delta R} (R_{T(1)}\tan\beta^*_{T(1)} - R_{H(1)}\tan \beta^*_{H(1)})$$

$$\beta^* = \tan^{-1}\left[\frac{R\tan \beta^*}{R(i)}\right]$$

$$A(i) = \gamma(i) \quad \Delta y(i) \ \text{Cos}\ \psi_{(i)}$$

$$U = \omega R_{(i)}$$

$$V = \frac{V_{m(i)}}{\text{Sin}\ \alpha_{(i)}}$$

$$V_u = V \ \text{Cos}\ \alpha_{(i)}$$

$$W_u = U - V_u$$

$$\beta_{(i)} = \tan^{-1}\left[\frac{V_{m(i)}}{V_u}\right]$$

$$W_{(i)} = \frac{V_{m(i)}}{\text{Sin}\ \beta_{(i)}}$$

$$i_{o(i)} = \beta^*_{(i)} - \beta_{(i)}$$

$$P_{(i)} = P_{T(i)} - \frac{\rho}{2g} V^2$$

$$Q_D = \frac{\rho}{2g} W^2_{(i)}$$

$$Prel_{(i)} = P_{(i)} + Q_D$$

$$HIo_{(i)} = \frac{UVu}{g}$$

$$Ho_{(i)} = \frac{P_{T(i)}}{\rho}$$

$$Q_{(i)} = V_{m(i)} A_{(i)}$$

$$QI = \sum Q_{(i)} N_b$$

$$P_T = \frac{\sum P_{T(i)} Q_{(i)}}{QIN_b}$$

$$\phi = \frac{\sum V_{m(i)}}{NI\ U_T}$$

$$k = \frac{P_{(i)} - P_{SAT}}{Q_D}$$

$$M_{(i)} = P_{(i)} A_{(i)} \sin \beta^*_{(i)} + \frac{\rho}{g} Q_{(i)} W_{(i)} \cos i_{o(i)}$$

$$\theta_{(i)} = 0.278\sqrt{\frac{\nu}{W_{(i)}}}$$

$$\delta\beta^{*}_{(i)} = i_{o(i)}$$

Return to inlet streamline calculations repeat calculations for NI streamlines.

$$NPSH = \frac{P_T - P_{SAT}}{\rho}$$

$$\tau_{CAV} = \frac{2g\ NPSH}{U_T^2}$$

MAIN PROGRAM

J-STATION CONSTANTS:

$$\Delta Z = Z_{(j)} - Z_{(j-1)}$$

$$\Delta Z_e = Z_{(NJ)} - Z_{(j)}$$

$$\Delta R = R_{T(j)} - R_{H(j)}$$

STREAMLINE ITERATION:

$$R_{ST} = R_{H(j)} + PCR_{(i)}\ \Delta R$$

$$R_{(i)} = \frac{R_{ST} + R_{ST}'}{2.0}$$

$$\overline{R} = \frac{R_{(i)} + R_{(i)}'}{2.0}$$

$$\psi_{ST(i)} = \tan^{-1}\left[\frac{R_{ST} - R_{ST}'}{\Delta Z}\right]$$

$$\psi_{(i)} = \tan^{-1}\left[\frac{R_{(i)} - R'_{(i)}}{\Delta Z}\right]$$

$$\bar{\psi}_{(i)} = \frac{\psi_{(i)} + \psi'_{(i)}}{2.0}$$

$$\Delta y_{(i)} = R_{ST} - R'_{ST} - \frac{xx\,\delta^{*\prime}_{(i)}}{\cos\bar{\psi}_{(i)}}$$

where:

xx = 1 if hub or tip stream tube.

xx = 0 for all other stream tubes.

$$R\tan\beta^* = R_{T(j)}\tan\beta^*_{T(j)} - \frac{\left(R_{T(j)} - R_{(i)}\right)}{\Delta R}\left[R_{T(j)}\tan\beta^*_{T(j)} - R_{H(j)}\tan\beta^*_{H(j)}\right]$$

$$\beta^*_{(i)} = \tan^{-1}\left[\frac{R\tan\beta^*}{R_{(i)}}\right]$$

$$\bar{\beta}^* = \frac{\beta^*_{(i)} + \beta^{*\prime}_{(i)}}{2.0}$$

$$\Delta m_{(i)} = \frac{\Delta Z}{\cos\bar{\psi}_{(i)}\,\sin\bar{\beta}^*}$$

$$m_{(i)} = m'_{(i)} + \Delta m_{(i)}$$

$$\alpha_w = \alpha_{w_T} - \left[\frac{R_{T(j)} - R_{(i)}}{R_{T(j)} - R_{H(j)}}\right] \left(\alpha_{w_T} - \alpha_{w_H} \right)$$

$$t_{(i)} = t_{T(j)} + \gamma\left(R_{T(j)} - R_{(i)}\right)$$

$$t_{LE} = m_{(i)} \tan\alpha_w$$

If blade leading edge thickness (t_{LE}) is less than the maximum blade thickness $t_{(i)}$ at the given axial location use blade leading edge thickness.

$$\tau_{(i)} = \frac{2\pi}{N_b} R_{(i)} - \frac{t_{(i)}}{\sin\beta^*_{(i)}}$$

(EXIT DEVIATION)

$$\rho 2 = \frac{\Delta Z_e \; N_b}{2 \; R_{(i)} \; \sin\beta^*_{(i)}}$$

$$\delta_e = \left(\beta^*_{(i)} - \beta_{o(i)}\right) C_e$$

$$\delta_2 = \frac{\delta_e \; e^{P2}}{\left[1 - \frac{\delta_e \; (1.0 - e^{P2})}{\tan\beta^*_{(i)}}\right]}$$

CAVITY ITERATION:

If the cavity is growing the cavity slope ($\delta\beta^*_{(i)}$) is greater than zero ± tolerance and:

$$\overline{\delta\beta}^* = \frac{\delta\beta^*_{(i)} + \delta\beta^{*\prime}_{(i)}}{2.0}$$

$$\Delta b = \frac{\Delta m_{(i)} \ \mathrm{Sin}\ \overline{\delta\beta}^*}{\mathrm{Sin}\ (\overline{\beta}^* - \overline{\delta\beta}^*)}$$

$$b_{(i)} = b'_{(i)} + \Delta b$$

If the cavity has reached its maximum height ($\delta\beta^* = 0.0 \pm$ tolerance) or if cavity is collapsing, then:

$$b_{(i)} = b'_{(i)} - \frac{\left[\dfrac{\Delta Z \ \tan \delta_W}{\mathrm{Sin}^2 \ \beta^*_{(i)}}\right]}{\left[1.0 + \dfrac{\tan \ \delta_W}{\tan\beta^*_{(i)}}\right]}$$

(FLOW CALCULATIONS - START)

$$\tau_\ell = \tau_{(i)} - b_{(i)} - \frac{xx \ \ \delta^{*\prime}}{\mathrm{Sin}\beta^*_{(i)}}$$

where

xx = 1 if cavity exists on blades.

xx = 2 if no cavity exists.

$$\bar{\tau}_\ell = \frac{\tau_{(i)} - b_{(i)} + \tau'_{(i)} - b'_{(i)}}{2.0}$$

$$A_{(i)} = \Delta y_{(i)} \ \tau_\ell \ \mathrm{Cos} \ \ \psi_{(i)}$$

$$V_m = \frac{Q_{(i)}}{A_{(i)}}$$

(FLUID INERTIA EFFECTS - START)

$$\beta^*_{\mathrm{eff}} = \beta^*_{(i)} - 1/2 \ \ \delta\beta^*_{(i)}$$

$$P1 = -\frac{\pi \Delta m_{(i)}}{\tau_\ell \, \mathrm{Sin}\beta^*_{(i)}}$$

$$\delta_o = \beta^*_{eff} - \beta'_{(i)}$$

$$\delta_I = \frac{\delta_o \, e^{P1}}{\left[1 - \frac{\delta_o \, (1 - e^{P1})}{\tan\beta^*_{(i)}}\right]}$$

$$\beta_{(i)} = \beta^*_{eff} - \delta_I - \delta_2$$

(FLUID INERTIA EFFECTS - END)

For an inducer with blade leading edge sweep back, the relative flow angle ($\beta_{(i)}$) for streamtubes that have not crossed the leading edge is calculated through a conservation of angular momentum:

$$\beta_{(i)} = \tan^{-1}\left[\frac{Ym}{R_{(i)w} - \frac{R_{o(i)} \, Vu_{o(i)}}{R_{(i)}}}\right]$$

$$\bar{\beta} = \frac{\beta_{(i)} + \beta'_{(i)}}{2.0}$$

$$\Delta\beta = \beta_{(i)} - \beta'_{(i)}$$

$$\left.\frac{d\beta}{d_m}\right|_{(i)} = \frac{\Delta\beta}{\Delta m_{(i)}}$$

$$W_{(i)} = \frac{V_m}{\mathrm{Sin}\ \beta_{(i)}}$$

$$\bar{W} = \frac{W_{(i)} + W'_{(i)}}{2.0}$$

$$\overline{W}_u = \overline{W} \cos\overline{\beta}$$

$$\overline{U} = \omega \overline{R}$$

$$\overline{V}_u = \overline{U} - \overline{W}_u$$

$$Q_D = \frac{\rho}{2g} W_{(i)}^2$$

$$\overline{Q}_D = \frac{\rho}{2g} \overline{W}^2$$

$$\left.\frac{dW}{dm}\right)_{(i)} = \frac{W_{(i)} - W'_{(i)}}{\Delta m_{(i)}}$$

(BOUNDARY LAYER CALCULATIONS - START)

$$Re_\theta = \frac{W_{(i)} \quad \theta'_{(i)}}{\nu}$$

$$C_f = \frac{0.246}{10.0^{0.678H'_{(i)}} \; Re^{0.268}}$$

$$\frac{d\theta}{dm} = \frac{C_f}{2.0} - (H'_{(i)} + 2.0) \left[\frac{\theta'_{(i)}}{W_{(i)}} \left.\frac{dW}{dm}\right)_{(i)}\right]$$

$$CL = \frac{Re_\theta^{0.167} \; \theta'_{(i)}}{0.0135 \; e^{5(H'_{(i)} - 1.4)}}$$

$$H_{(i)} = 1.4 - \frac{Re_{\theta}^{0.167}}{0.0135}\left[\frac{\theta'_{(i)}}{W'_{(i)}}\left.\frac{dW}{dm}\right)_{(i)}\right]$$

$$H_{(i)} = H_{(i)} - \left(H_{(i)} - H'_{(i)}\right) e^{\frac{-\Delta m_{(i)}}{CL}}$$

$$\theta_{(i)} = \frac{d\theta}{dm}\Delta m_{(i)} + \theta'_{(i)}$$

$$\delta^*_{(i)} = \theta_{(i)} H_{(i)}$$

$$F = 1.0 - \frac{xx_2\ \theta_{(i)}}{\left(\tau_{(i)} - b_{(i)}\right)\operatorname{Sin}\beta^*_{(i)}}$$

where

xx = 1 if cavity exists.

xx = 2 if no cavity.

For either hub or tip stream tubes:

$$F = \left[1.0 - \frac{xx\ \theta_{(i)}}{2\left(\tau_{(i)} - b_{(i)}\right)\operatorname{Sin}\beta^*_{(i)}}\right]\left[1.0 - \frac{\theta_{(i)}}{2\left(R_{ST_{(i)}} - R_{ST_{(i-1)}}\right)\operatorname{Cos}\psi_{(i)}}\right]$$

(BOUNDARY LAYER CALCULATIONS - END)

If cavity is collapsing:

$$\Delta P_D = \frac{\rho}{2g}\left[W'_{(i)}\left(1.0 - \frac{W_{(i)}}{W'_{(i)}}\right)\right]^2 + \left(P'_{(i)} - P_{SAT}\right)\left[1.0 - \frac{W_{(i)}}{W'_{(i)}} - \frac{\left(\tau_\ell + \tau'_{(i)} - b'_{(i)}\right)\left(\Delta y_{(i)} - \Delta y_{(i)}\right)}{2\ \tau_\ell\ \Delta y_{(i)}}\right]$$

For all other cases $\Delta P_D = 0.0$

$$Prel_{(i)} = Prel'_{(i)} + \rho_{2g}\,\omega^2 \left(R^2_{(i)} - R'^2_{(i)}\right) - \Delta P_D$$

$$PO_{rel_{(i)}} = P_{rel_{(i)}} - (1.0 - F)\,Q_D$$

$$P_{(i)} = P_{rel_{(i)}} - Q_D$$

(CAVITY MOMENTUM BALANCE)

$$\Delta t = t_{(i)} - t'_{(i)}$$

$$\overline{\Delta y} = \frac{\Delta y_{(i)} + \Delta y'_{(i)}}{2.0}$$

$$\overline{A} = \left[\frac{A'_{(i)}\ \mathrm{Sin}\,\beta^{*\prime}_{(i)} + A_{(i)}\ \mathrm{Sin}\,\beta^{*}_{(i)}}{2.0}\right]$$

$$WP = xx\ \overline{\Delta y}$$

where

xx = 1 if cavity exists

xx = 2 if no cavity

For the hub stream tube:

$$WP = WP + \overline{\tau_\ell}\left[\frac{R_{H_{(j-1)}} + R_{H_{(j)}}}{R'_{(i)} + R_{(i)}}\right]\ \mathrm{Sin}\,\overline{\beta}^*$$

For the tip stream tube:

$$WP = WP + \overline{\tau}_{\ell} \left[\frac{R_{T(j-1)} + R_{T(j)}}{R'_{(i)} + R_{(i)}} \right] \operatorname{Sin}\overline{\beta}^{*}$$

$$\overline{P} = \frac{P_{(i)} + P'_{(i)}}{2.0}$$

$$F_D = C_f \, \overline{Q}_D \, WP \, \Delta m_{(i)}$$

$$F_C = \rho_{\overline{g}} \, \overline{A} \, \frac{\left(R_{(i)} - R'_{(i)}\right)}{\overline{R}} \, \overline{V}u^{2}$$

$$F_P = \Bigg[P_{SAT} \, \overline{\Delta y} \, \Delta t + P_{SAT} \, \overline{\Delta y} \, \Delta b \operatorname{Sin}\overline{\beta}^{*} + 2 \, \overline{P} \left(\overline{\Delta y} - \Delta y_{(i)}\right) \overline{\tau}_{\ell} \operatorname{Sin} \overline{\beta}^{*} + \frac{2\pi}{N_b} \left(R'_{(i)} \operatorname{Sin}\beta^{*\prime}_{(i)} - R_{(i)} \operatorname{Sin} \beta^{*}_{(i)}\right)\overline{\Delta y} \; P \Bigg] \operatorname{Cos} \overline{\psi}_{(i)}$$

$$\Delta M = F_C - F_C - F_D$$

$$M_{(i)} = P_{(i)} \, A_{(i)} \operatorname{Sin}\beta^{*}_{(i)} + \rho_{\overline{g}} \, Q_{(i)} \, W_{(i)} \operatorname{Cos}\left(\beta^{*}_{(i)} - \beta_{(i)}\right) \sqrt{F}$$

$$\text{Error} = M_{(i)} - M'_{(i)} - \Delta M_{(i)}$$

Calculate error in stream tube momentum ($M(i)$). If the error is not within tolerance adjust cavity slope ($\delta\beta^{*}$) and return to start of cavity iteration. Iterate until error in stream tube momentum is within tolerance. If a streamtube has not crossed the leading edge of a swept back blade, the momentum is calculated (with F=1.0) for reference.

(RADIAL PRESSURE GRADIENT CALCULATION - START)

$$\Delta P = P_{(i)} - P_{(i - 1)}$$

$$\Delta R = R_{(i)} - R_{(i-1)}$$

$$\frac{V^2_{u(i)}}{R_{(i)}} = \frac{\left[\omega R_{(i)} - W_{(i)} \cos\beta_{(i)}\right]^2}{R_{(i)}}$$

$$\frac{V^2_{u(i-1)}}{R_{(i-1)}} = \frac{\left[\omega R_{(i-1)} - W_{(i-1)} \cos\beta_{(i-1)}\right]^2}{R_{(i-1)}}$$

Simple radial equilibrium:

$$\left.\frac{dP}{dr}\right|_1 = \frac{\rho}{g}\left[\frac{1}{2}\left(\frac{V^2_{u(i)}}{R_{(i)}} + \frac{V^2_{u(i-1)}}{R_{(i-1)}}\right)\right]$$

For a streamtube that has not crossed the leading edge of a swept back blade, its radial location is found by satisfying simple radial angle librium.

$$\overline{\overline{V}}_m = \frac{W_{(i)} \sin\beta_{(i)} + W_{(i-1)} \sin\beta_{(i-1)}}{2.0}$$

$$\overline{\overline{V}}'_m = \frac{W'_{(i)} \sin\beta'_{(i)} + W'_{(i-1)} \sin\beta'_{(i-1)}}{2.0}$$

$$\frac{d\psi}{dZ} = \frac{\psi ST_{(i-1)} - \psi ST'_{(i-1)}}{\Delta Z}$$

$$\frac{dVm}{dZ} = \frac{\overline{\overline{V}}_m - \overline{\overline{V}}'_m}{\Delta Z}$$

Streamline curvature and radial acceleration:

$$\frac{dP}{dr}_2 = -\frac{\rho}{g}\left[\overline{\overline{V}}^2_m \frac{d\psi}{dZ} \cos^2 \psi ST_{(i-1)} + \frac{1}{2}\overline{\overline{V}}_m \frac{dV_m}{dZ} \sin\left(2\psi_{ST_{(i-1)}}\right)\right]$$

$$\frac{dP}{dr} = \left.\frac{dP}{dr}\right|_1 + \left.\frac{dP}{dr}\right|_2$$

$$\text{Error} = \frac{\Delta P}{\Delta R} - \frac{dP}{dr}$$

(RADIAL PRESSURE GRADIENT CALCULATION - END)

(Streamline Test and Adjustment Routine)

The error is determined for each streamline and compared with some tolerance. If each streamline error is within the prearranged tolerance, the program continues. If all or anyone of the streamlines is not within this tolerance, the errors of that streamline and its adjacent streamlines are used in the adjustment for locating the new streamline positions. After each streamline adjustment has been made, the program returns to the start of the streamline iteration in the main program.

END STREAMLINE ITERATION

J - STATION PARAMETERS:

(Blade Loading Calculations - Start)

$$\Delta P_{b_{(i)}} = 2.0\ \bar{\tau}_\ell\ \bar{Q}_D \frac{\sin^2\bar{\beta}}{\sin\beta^*_{(i)}} \left[\left(\frac{2\omega}{\bar{W}} - \frac{\cos\bar{\beta}}{R_{(i)}}\right)\sin\bar{\psi}_{(i)} + \left.\frac{d\beta}{dm}\right|_{(i)} - \left.\frac{dW}{dm}\right|_{(i)} \frac{1}{\bar{W}\tan\bar{\beta}}\right]$$

$$\Delta P_{b_{n_{(j,i)}}} = \Delta P_{b_{(i)}} + \frac{2.0\ \bar{\tau}_\ell\ \bar{Q}_D\ \sin^2\bar{\beta}}{\bar{W}\tan\bar{\beta}\ \sin\beta^*_{(i)}} \left.\frac{dW}{dm}\right|_i$$

(Blade Loading Calculations - End)

(Station Performance Calculations - Start)

$$U = \omega R_{(i)}$$

$$V = W_{(i)}\ \sin\beta_{(i)}$$

$$W_u = W_{(i)}\ \cos\beta_{(i)}$$

$$V_u = U - W_u$$

$$\alpha = \tan^{-1}\left[\frac{V_m}{V_u}\right]$$

$$V = \frac{V_m}{\sin\alpha}$$

$$PO_T = PO_{rel_{(i)}} + \frac{\rho}{2g}\left(V^2 - W^2_{(i)}\right)$$

$$H = \frac{PO_T}{\rho} - H_{o_{(i)}}$$

$$HI = \frac{UV_u}{g} - HI_{o_{(i)}}$$

$$\eta = \frac{H}{HI}$$

$$\delta = \beta^*_{(i)} - \beta_{(i)}$$

$$m^* = \frac{Z_{(j)}}{\sin\beta^*_{(i)}} + b_{(i)} \cos\beta^*_{(i)}$$

$$b_n = b_{(i)} \sin\beta^*_{(i)}$$

$$PCB = \frac{N_b\, b_{(i)}}{2\pi\, R_{(i)}}$$

$$RV_{u_{(i)}} = R_{(i)}\, V_u$$

END J - STATION PARAMETER CALCULATIONS

EXIT STATION CALCULATIONS:

$$P_{rel_{(i)}} = P'_{rel_{(i)}} + \frac{\rho}{2g}\,\omega^2\left(R^2_{(i)} - R'^2_{(i)}\right)$$

$$V_m = \frac{Q_{(i)}}{\left[\left(R_{ST_{(i)}} - R'_{ST_{(i)}}\right)\cos\psi_{(i)} - xx\delta^*\right]\dfrac{\frac{1}{2\pi R_{(i)}}}{N_b}}$$

where

xx = 1 for hub and tip stream tubes

xx = 0 for all other stream tubes

Note: Fluid angular momentum ($RV_{u(i)}$) is assumed constant for each stream tube between the last internal station and the exit station. Hence:

$$V_u = \frac{RV_{u(i)}}{R_{(i)}}$$

$$W_u = U - V_u$$

$$\beta_e = \tan^{-1}\left[\frac{V_m}{W_u}\right]$$

$$W_{(i)} = \frac{V_m}{\sin\beta_e}$$

$$\alpha = \tan^{-1}\left[\frac{V_m}{V_u}\right]$$

$$V = \frac{V_m}{\sin\alpha}$$

$$W_{(i)} = \frac{V_m}{\sin\beta_e}$$

$$Q_D = \frac{\rho}{2g} W^2_{(i)}$$

$$P_{(i)} = P_{rel_{(i)}} - Q_D$$

Adjust streamlines to satisfy simple radial equilibrium ($dP/dr|_1$). The procedure for streamline adjustment is the same as for the internal stations. Iterate until radial momentum is satisfied.

For hub and tip stream tubes:

$$PO_{rel_{(i)}} = PO_{rel_{(i)}} - \frac{2\theta_{(i)}\, Q_D}{\left(R_{ST_{(i)}} - R'_{ST_{(i)}}\right)\cos\psi_{(i)}}$$

For all other stream tubes:

$$PO_{rel_{(i)}} = P_{rel_{(i)}}$$

$$PO_T = PO_{rel_{(i)}} + \frac{\rho}{2g}(V^2 - W^2_{(i)})$$

$$H = \frac{PO_T}{\rho} - H_{o_{(i)}}$$

$$HI = \frac{UV_u}{g} - HI_{o_{(i)}}$$

$$\eta = \frac{H}{HI}$$

$$\delta = \beta^*_{(i)} - \beta_e$$

END EXIT STATION CALCULATIONS

OVERALL PERFORMANCE

$$H = \frac{N_b}{QI} \sum HQ_{(i)}$$

$$\eta = \frac{\sum H\ Q_{(i)}}{\sum HI\ Q_{(i)}}$$

$$\psi_s = \frac{g\ H}{(\omega\ R_{T_{(i)}})^2}$$

$$R_e = \frac{\omega R^2_{T_{(i)}}}{\nu}$$

$$SS = \frac{\omega\sqrt{QI}}{(g\ NPSH)^{3/4}}$$

END FLOW ANALYSIS CALL LOADING ROUTINE

Loading Routine

Curve fit following parameters from the main program.

$P_{(i)}$ as a function of $m_{(i)}$

$\Delta P_{bn(i)}$ as a function of $m(i)$

$$\tau \cos\beta^*(i) = \left[\frac{2\pi R(i)}{N_b} - \frac{t(i)}{\sin\beta^*(i)}\right] \cos\beta^*(i)$$

If the blades have tapered leading and/or trailing edges

$$\delta_T = \tan^{-1}\left[\frac{\left(t'(i) - t(i)\right)\sin\beta^*(i)}{2\Delta z}\right]$$

$$\zeta = \left[\frac{2\pi}{Nb}\ \frac{R_{(j,\ i)}}{2} - \frac{t(i)}{\sin\beta^*(i)}\right] \sin\beta^*(i)\ \tan\delta_T$$

If the blade leading and/or trailing edges are not tapered, $\zeta = 0$.

$$SMN_o = m_{(j,\ i)} - \frac{\tau \cos\beta^*(i)}{2.0} + \zeta$$

Suction Surface:

(Channel Region) SMN_o greater than 0.0

If cavity exists at station $b_{(i)} \neq 0.0$

$P_{s(i)} = P_{sat}$

If no cavity exists at station $b_{(i)} = 0.0$

$P(i)$ and $\Delta P_{bn(i)}$ found from curve fits at $m(i) = SMN_0$

$$P_{s(i)} = P_{(i)} - \frac{\Delta P_{bn(i)}}{2.0}$$

$$W_{s(i)} = \sqrt{\left(P_{rel_{(j,\ i)}} - P_{s(i)}\right)\frac{2g}{\rho}}$$

where:

$P_{rel(j,\ i)}$ is the total relative pressure at the Z location for which loadings are being calculated.

(Uncovered Leading Edge Region)

If cavity exists at station $b_{(i)} \neq 0.0$

$$P_{s(i)} = P_{sat}$$

If no cavity exists at station $b_{(i)}$ - 0.0

$$W_{(i)} = W_{o(i)} - (W_{o(i)} - W_{(1,\ i)})\ e^{\frac{SMN_o\ N_b}{R_{o(i)}\ \sin\beta^*_{o(i)}}}$$

$$P_{(i)} = P_{relo(i)} - \rho\ \frac{}{2g}\ W_{(i)}^2$$

$$\beta_{(i)} = \sin^{-1}\left[\frac{V_{m(i)}}{W_{(i)}}\right]$$

$$P_{bn(i)} = \rho\ \frac{}{g}\ \pi\ \frac{V_{m(i)}\ \sin^2\beta^*_{(i)}}{\cos\beta_{(i)}\ \sin^2\beta^*_{o(i)}}\ (W_{o(i)} - W_{(1,i)})\ e^{\frac{SMN_o\ N_b}{R_{o(i)}\ \sin\beta^*_{o(i)}}}$$

$$P_{s(i)} = P_{(i)} - \frac{\Delta P_{bn(i)}}{2.0}$$

$$W_{s(i)} = \sqrt{(P_{relo(i)} - Ps_{(i)})\ \frac{2g}{\rho}}$$

Pressure Surface:

$$SMN = m_{(j,\ i)} + \frac{\tau\cos\beta^*_{(i)}}{2.0} + \zeta$$

(Channel Region)

$P_{(i)}$ and $\Delta P_{bn(i)}$ are found from curve fits at $m_{(i)}$ = SMN

$$P_{p(i)} = P_{(i)} + \frac{\Delta P_{bn(i)}}{2.0}$$

If $P_{p(i)}$ is greater than $P_{rel(i)}$ at the Z location for which loadings are being calculated then

$$P_{p(i)} = P_{rel(i)}$$

$$Wp_{(i)} = \sqrt{(P_{rel(j,\ i)} - Pp_{(i)})\ \frac{2g}{\rho}}$$

(Uncovered Trailing Edge Region)

$$SMN_e = SMN - m_{(NJ,\ i)}$$

$$W_{(i)} = W_{e(i)} - (W_{e(i)} - W_{(NJ,\ i)})\ e^{\frac{-SMN_e\ N_b}{R_{e(i)}\ \sin\beta^*_{e(i)}}}$$

$$P_{(i)} = P_{rele(i)} - \frac{\rho}{2g}\ W_{(i)}^{\ 2}$$

$$\beta_{(i)} = \sin^{-1}\left[\frac{Vm_{(i)}}{W_{(i)}}\right]$$

$$\Delta P_{bn(i)} = \rho\frac{}{g}\pi\ \frac{Vm_{(i)}\ \sin^2\beta_{(i)}}{\cos\beta_{(i)}\ \sin^2\beta^*_{e(i)}}\ (W_{e(i)} - W_{(NJ,\ i)})\ e^{\frac{-SMN_e\ N_b}{R_{e(i)}\ \sin\beta^*_{e(i)}}}$$

$$P_{p(i)} = P_{(i)} + \frac{\Delta P_{bn(i)}}{2.0}$$

$$W_{p(i)} = \sqrt{(P_{rele(i)} - P_{p(i)})\ \frac{2g}{\rho}}$$

$$\Delta P_{b(i)} = P_{p(i)} - P_{s(i)}$$

$$\psi ss_{(i)} = g\ \frac{(P_{s(i)} - P_{To})}{\rho U_T^{\ 2}}$$

$$\psi sp_{(i)} = g\ \frac{(P_{p(i)} - P_{To})}{\rho U_T^{\ 2}}$$

APPENDIX D
DERIVATION OF BASIC RELATIONS FOR STRESS AND VIBRATION COMPUTER PROGRAMS

Contained in this appendix are the derivations of the basic relations used in the stress and vibration computer programs.

The discussion of the derivations of the various relations in matrix form are separated into relations that are common to both the stress and vibration programs and those apply specifically to only one of the programs, as outlined below.

Both Programs

(1) Direction Cosine Matrix $\left[R_1\right]$

(2) Nodal Coordinate Matrix $\left\{\bar{\Psi}_N\right\}$

(3) Triangular Surface Coordinate Matrix $\left\{\Psi\right\}$

(4) Thickness Matrix Relation

(5) Membrane Stiffness Matrix $\left[\bar{K}_M\right]$

(6) Bending Stiffness Matrix $\left[\bar{K}_B\right]$

Stress Program

(7) Pressure Force Matrix $\left\{\bar{F}_p\right\}_N$

(8) Centrifugal Force Matrix $\left\{\overline{F_c}\right\}_N$

(10) Approximate Centrifugal Force Matrix $\left\{F_c\right\}_N$

Vibration Program

(11) Membrane Inertia Matrix $\left\{\bar{M}_M\right\}$

(12) Bending Inertia Matrix $\left\{\bar{M}_B\right\}$

(13) Normal Direction Cosine Matrix $\left[R_1\right]_n$

(14) Relative Vibratory Bending Stress Matrix $\left\{\bar{\sigma}_B\right\}$

Integration of expressions containing variable thickness is accomplished by the Gaussian quadrature formula, using 100 internal nodal values of the integrand in the triangular element.

(1) Direction Cosine Matrix $\left[R_1\right]$ (See Figure 109.)

The direction cosine or rotation matrix $\left[R_1\right]$ establishes the relation between the directions of the axes of the common coordinate system and the local coordinate system. It is obtained by three operations:

1. Direction of $\bar{z}$ axis is obtained by determining direction of vector product of vectors in directions of two sides of triangle.
2. Direction of $\bar{x}$ axis is obtained by projection.
3. Direction of $\bar{y}$ axis is obtained by determining direction of vector product of vector along $\bar{z}$ axis and $\bar{x}$ axis.

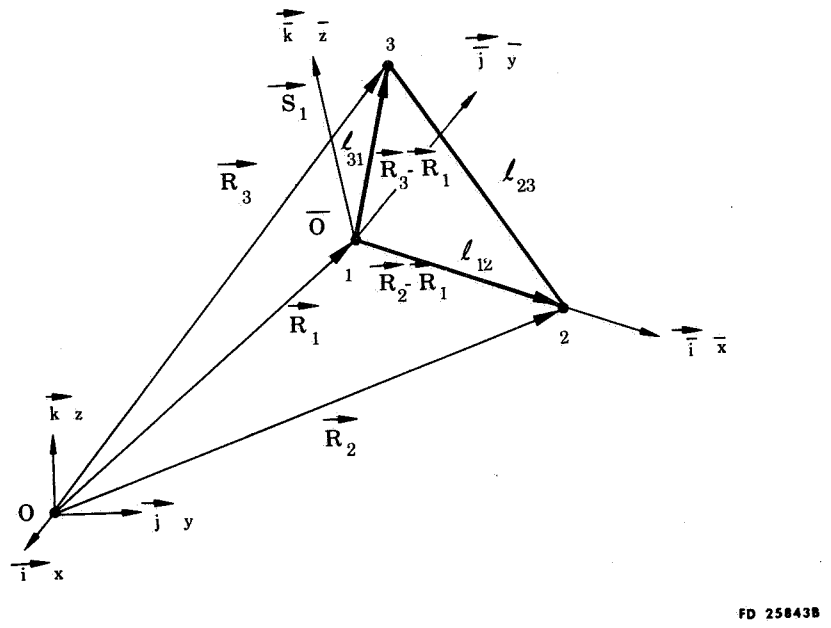

Figure 109. Geometry for Deriving $[R_1]$ FD 25843B

1. $\bar{z}$ Direction

Vector area of triangle relative to common system, (one half of vector product)

$$\vec{S}_1 = \frac{1}{2}\,(\vec{R}_2 - \vec{R}_1) \times (\vec{R}_3 - \vec{R}_1)$$

$$= \frac{1}{2}\begin{vmatrix} \vec{i} & \vec{j} & \vec{k} \\ x_2 - x_1 & y_2 - y_1 & z_2 - z_1 \\ x_3 - x_1 & y_3 - y_1 & z_3 - z_1 \end{vmatrix}$$

$$S_{1x} = \frac{1}{2}\left[(y_2 - y_1)(z_3 - z_1) - (y_3 - y_1)(z_2 - z_1)\right]$$

$$S_{1y} = \frac{1}{2}\left[(z_2 - z_1)(x_3 - x_1) - (z_3 - z_1)(x_2 - x_1)\right]$$

$$S_{1z} = \frac{1}{2}\left[(x_2 - x_1)(y_3 - y_1) - (x_3 - x_1)(y_2 - y_1)\right]$$

$$S_1 = \sqrt{S_{1x}^2 + S_{1y}^2 + S_{1z}^2}$$

$$\vec{S}_1 = \vec{i}S_{1x} + \vec{j}S_{1y} + \vec{k}S_{1z}$$

$$\vec{\bar{k}} = \vec{i}\frac{S_{1x}}{S_1} + \vec{j}\frac{S_{1y}}{S_1} + \vec{k}\frac{S_{1z}}{S_1}$$

$$\therefore \quad \cos(x,\bar{z}) = \vec{i} \cdot \vec{\bar{k}} = \frac{S_{1x}}{S_1}$$

$$\cos(y,\bar{z}) = \vec{j} \cdot \vec{\bar{k}} = \frac{S_{1y}}{S_1}$$

$$\cos(z,\bar{z}) = \vec{k} \cdot \vec{\bar{k}} = \frac{S_{1z}}{S_1}$$

2. $\bar{x}$ Direction

By inspection,

$$\cos(x,\bar{x}) = \frac{x_2 - x_1}{\ell_{12}}$$

$$\cos(y,\bar{x}) = \frac{y_2 - y_1}{\ell_{12}}$$

$$\cos(z,\bar{x}) = \frac{z_2 - z_1}{\ell_{12}}$$

$$\ell_{12} = \sqrt{(x_2 - x_1)^2 + (y_2 - y_1)^2 + (z_2 - z_1)^2}$$

3. $\bar{y}$ Direction

$\bar{y}$ axis is in direction of vector product, $\vec{S}_1 \times (\vec{R}_2 - \vec{R}_1)$

$$\vec{S}_1 \times (\vec{R}_2 - \vec{R}_1) = \begin{vmatrix} \vec{i} & \vec{j} & \vec{k} \\ S_{1x} & S_{1y} & S_{1z} \\ x_2 - x_1 & y_2 - y_1 & z_2 - z_1 \end{vmatrix}$$

$$= \vec{i}\left[S_{1y}(z_2 - z_1) - S_{1z}(y_2 - y_1)\right] +$$
$$\vec{j}\left[S_{1z}(x_2 - x_1) - S_{1x}(z_2 - z_1)\right] +$$
$$\vec{k}\left[S_{1x}(y_2 - y_1) - S_{1y}(x_2 - x_1)\right]$$

$$S_2 = \sqrt{\left[S_{1y}(z_2 - z_1) - S_{1z}(y_2 - y_1)\right]^2} + \sqrt{\left[S_{1z}(x_2 - x_1) - S_{1x}(z_2 - z_1)\right]^2} + \sqrt{\left[S_{1x}(y_2 - y_1) - S_{1y}(x_2 - x_1)\right]^2}$$

$$S_{2x} = S_{1y}(z_2 - z_1) - S_{1z}(y_2 - y_1)$$

$$S_{2y} = S_{1z}(x_2 - x_1) - S_{1x}(z_2 - z_1)$$

$$S_{2z} = S_{1x}(y_2 - y_1) - S_{1y}(x_2 - x_1)$$

$$\vec{S}_2 = \vec{i}\, S_{2x} + \vec{j}\, S_{2y} + \vec{k}\, S_{2z}$$

$$\vec{\bar{j}} = \vec{i}\,\frac{S_{2x}}{S_2} + \vec{j}\,\frac{S_{2y}}{S_2} + \vec{k}\,\frac{S_{2z}}{S_2}$$

$$\therefore \cos(x,\bar{y}) = \vec{i} \cdot \vec{\bar{j}} = \frac{S_{2x}}{S_2}$$

$$\cos(y,\bar{y}) = \vec{j} \cdot \vec{\bar{j}} = \frac{S_{2y}}{S_2}$$

$$\cos(z,\bar{y}) = \vec{k} \cdot \vec{\bar{j}} = \frac{S_{2z}}{S_2}$$

The direction cosine matrix is then:

$$\left[R_1\right] = \begin{bmatrix} \cos(x,\bar{x}) & \cos(x,\bar{y}) & \cos(x,\bar{z}) \\ \cos(y,\bar{x}) & \cos(y,\bar{y}) & \cos(y,\bar{z}) \\ \cos(z,\bar{x}) & \cos(z,\bar{y}) & \cos(z,\bar{z}) \end{bmatrix} = \begin{bmatrix} \dfrac{x_2 - x_1}{\ell_{12}} & \dfrac{S_{2x}}{S_2} & \dfrac{S_{1x}}{S_1} \\ \dfrac{y_2 - y_1}{\ell_{12}} & \dfrac{S_{2y}}{S_2} & \dfrac{S_{1y}}{S_1} \\ \dfrac{z_2 - z_1}{\ell_{12}} & \dfrac{S_{2z}}{S_2} & \dfrac{S_{1z}}{S_1} \end{bmatrix}$$

(2) <u>Nodal Coordinate Matrix $\left\{\bar{\Psi}_N\right\}$</u> (See Figure 110).

The matrix $\left\{\bar{\Psi}_N\right\}$ establishes the local coordinates of the nodes of the triangle in terms of the common coordinates of the nodes of the triangle. It is obtained by two operations:

1. Translation of origin of local coordinate system to origin of common coordinates system.
2. Rotation of axes of local coordinate system to axes of common system.

The operation $\left\{\Psi_N - \Psi_1\right\}$ or

$$\left\{\Psi_N - \Psi_1\right\} = \begin{Bmatrix} x_N - x_1 \\ y_N - y_1 \\ z_N - z_1 \end{Bmatrix} \qquad N = 1,2,3$$

translates the local coordinate system to the origin of the reference system. This operation, together with rotation of the axes, yields:

$$\left\{\bar{\Psi}_1\right\} = \begin{Bmatrix} \bar{x}_1 \\ \bar{y}_1 \\ \bar{z}_1 \end{Bmatrix} = \left\{0\right\}$$

$$\left\{\bar{\Psi}_2\right\} = \begin{Bmatrix} \bar{x}_2 \\ 0 \\ 0 \end{Bmatrix} = \begin{Bmatrix} (x_2 - x_1)\cos(\bar{x},x) + (y_2 - y_1)\cos(\bar{x},y) + (z_2 - z_1)\cos(\bar{x},z) \\ (x_2 - x_1)\cos(\bar{y},x) + (y_2 - y_1)\cos(\bar{y},y) + (z_2 - z_1)\cos(\bar{y},z) \\ (x_2 - x_1)\cos(\bar{z},x) + (y_2 - y_1)\cos(\bar{z},y) + (z_2 - z_1)\cos(\bar{z},z) \end{Bmatrix}$$

$$\left\{\bar{\Psi}_3\right\} = \begin{Bmatrix} \bar{x}_3 \\ \bar{y}_3 \\ 0 \end{Bmatrix} = \begin{Bmatrix} (x_3 - x_1)\cos(\bar{x},x) + (y_3 - y_1)\cos(\bar{x},y) + (z_3 - z_1)\cos(\bar{x},z) \\ (x_3 - x_1)\cos(\bar{y},x) + (y_3 - y_1)\cos(\bar{y},y) + (z_3 - z_1)\cos(\bar{y},z) \\ (x_3 - x_1)\cos(\bar{z},x) + (y_3 - y_1)\cos(\bar{z},y) + (z_3 - z_1)\cos(\bar{z},z) \end{Bmatrix}$$

or

$$\begin{Bmatrix} \bar{x}_2 \\ 0 \\ 0 \end{Bmatrix} = \begin{bmatrix} \cos(\bar{x},x) & \cos(\bar{x},y) & \cos(\bar{x},z) \\ \cos(\bar{y},x) & \cos(\bar{y},y) & \cos(\bar{y},z) \\ \cos(\bar{z},x) & \cos(\bar{z},y) & \cos(\bar{z},z) \end{bmatrix} \begin{Bmatrix} x_2 - x_1 \\ y_2 - y_1 \\ z_2 - z_1 \end{Bmatrix}$$

$$\begin{Bmatrix} \bar{x}_3 \\ \bar{y}_3 \\ 0 \end{Bmatrix} = \begin{bmatrix} \cos(\bar{x},x) & \cos(\bar{x},y) & \cos(\bar{x},z) \\ \cos(\bar{y},x) & \cos(\bar{y},y) & \cos(\bar{y},z) \\ \cos(\bar{z},x) & \cos(\bar{z},y) & \cos(\bar{z},z) \end{bmatrix} \begin{Bmatrix} x_3 - x_1 \\ y_3 - y_1 \\ z_3 - z_1 \end{Bmatrix}$$

In matrix notation:

$$\left\{\bar{\Psi}_N\right\} = \left[R\right]^T \left\{\Psi_N - \Psi_1\right\} \quad N = 1,2,3$$

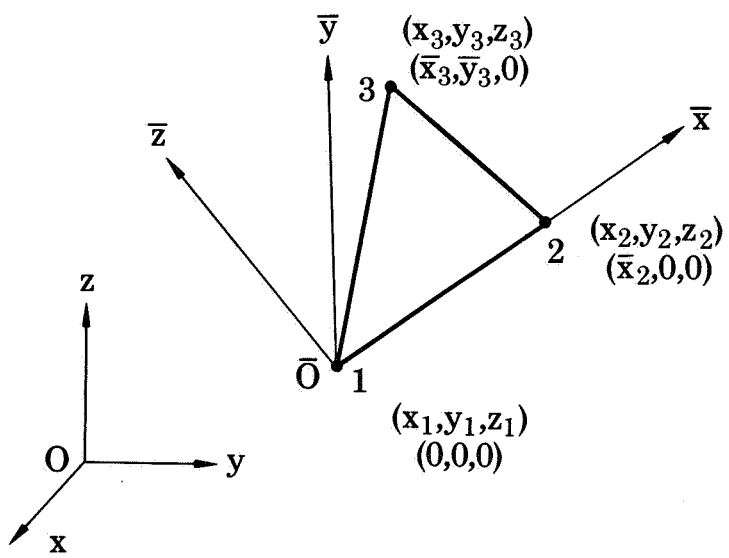

Figure 110. Geometry for Deriving $\left\{\Psi_N\right\}$ FD 25842

(3) Triangular Surface Coordinate Matrix $\left|\Psi\right|$ (See Figure 111.)

The matrix $\left|\Psi\right|$ establishes the relation between the local coordinates of points in the plane of the triangle and the common coordinates of these points. It is obtained by two operations:

1. Translation of origin of local system to origin of common system.
2. Rotation of axes of local system to axes of common system. (From figure 111.)

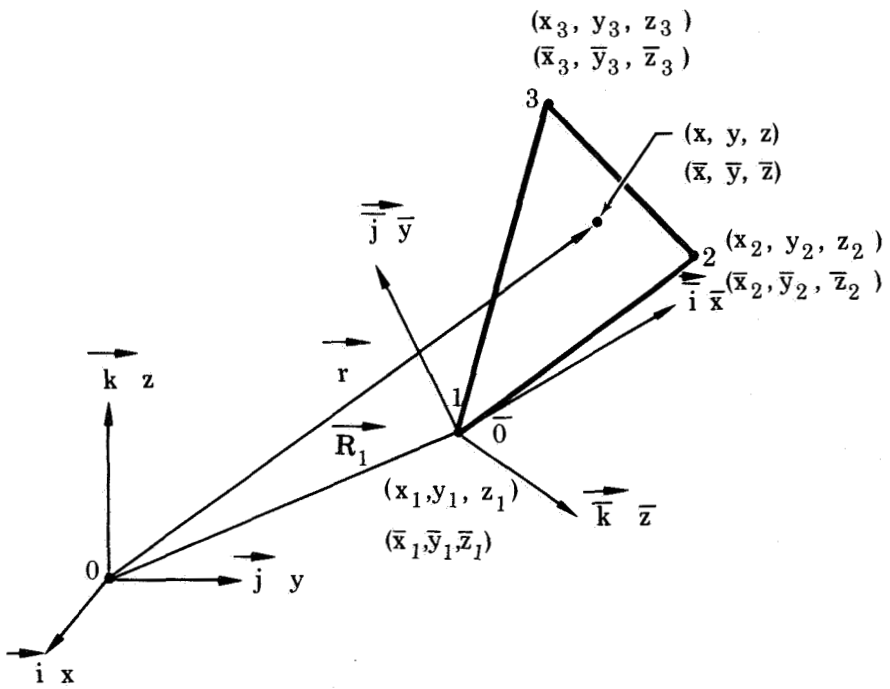

Figure 111. Geometry for Deriving $\left|\Psi\right|$ FD 25841A

$$\vec{r} = \vec{R}_1 + \vec{\bar{i}}\bar{x} + \vec{\bar{j}}\bar{y} + \vec{\bar{k}}\bar{z}$$

But

$$\vec{\bar{i}} = \vec{i} \cos(\bar{x},x) + \vec{j} \cos(\bar{x},y) + \vec{k} \cos(\bar{x},z)$$

$$\vec{\bar{j}} = \vec{i} \cos(\bar{y},x) + \vec{j} \cos(\bar{y},y) + \vec{k} \cos(\bar{y},z)$$

$$\vec{\bar{k}} = \vec{i} \cos(\bar{z},x) + \vec{j} \cos(\bar{z},y) + \vec{k} \cos(\bar{z},z)$$

$$\therefore \quad \vec{i}x + \vec{j}y + \vec{k}z = \vec{i}x_1 + \vec{j}y_1 + \vec{k}z_1 +$$

$$\bar{x}\left[\vec{i}\cos(\bar{x},x) + \vec{j}\cos(\bar{x},y) + \vec{k}\cos(\bar{x},z)\right] +$$

$$\bar{y}\left[\vec{i}\cos(\bar{y},x) + \vec{j}\cos(\bar{y},y) + \vec{k}\cos(\bar{y},z)\right] +$$

$$\bar{z}\left[\vec{i}\cos(\bar{z},x) + \vec{j}\cos(\bar{z},y) + \vec{k}\cos(\bar{z},z)\right]$$

$$\therefore \quad x = x_1 + \bar{x}\cos(x,\bar{x}) + \bar{y}\cos(x,\bar{y}) + \bar{z}\cos(x,\bar{z})$$

$$y = y_1 + \bar{x}\cos(y,\bar{x}) + \bar{y}\cos(y,\bar{y}) + \bar{z}\cos(y,\bar{z})$$

$$z = z_1 + \bar{x}\cos(z,\bar{x}) + \bar{y}\cos(z,\bar{y}) + \bar{z}\cos(z,\bar{z})$$

or

$$\begin{Bmatrix} x \\ y \\ z \end{Bmatrix} = \begin{Bmatrix} x_1 \\ y_1 \\ z_1 \end{Bmatrix} + \left[R_1\right] \begin{Bmatrix} \bar{x} \\ \bar{y} \\ \bar{z} \end{Bmatrix}$$

In matrix form

$$\left\{\Psi\right\} = \left\{\Psi_1\right\} + \left[R_1\right]\left\{\bar{\Psi}\right\}$$

(4) <u>Thickness Matrix Relation</u> (See Figure 112.)

This relation expresses the thickness at a point in the plane of the triangle in terms of the thicknesses at the three vertices, when the thickness is assumed to vary linearly with $\bar{x}$ and $\bar{y}$ over the triangle. It is derived by determining the coefficients of the linear form by matrix algebra.

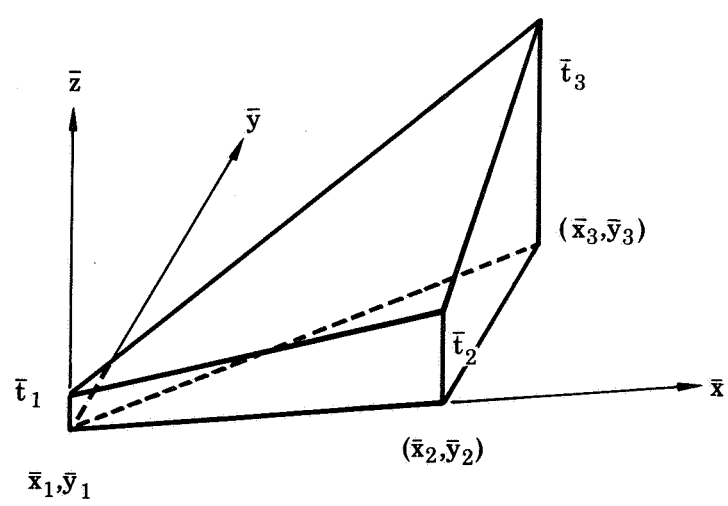

Figure 112. Geometry of Triangular Element With Linearly Varying Thickness FD 25840A

Assume

$$\bar{t} = \bar{a}_1\bar{x} + \bar{a}_2\bar{y} + \bar{a}_3 = \begin{bmatrix}\bar{x} & \bar{y} & 1\end{bmatrix} \begin{Bmatrix}\bar{a}_1\\ \bar{a}_2\\ \bar{a}_3\end{Bmatrix} = \left[\bar{A}_t\right]\left\{\bar{\alpha}_t\right\}$$

For nodal values, $\bar{t}_1$, $\bar{t}_2$, $\bar{t}_3$,

$$\begin{Bmatrix}\bar{t}_1\\ \bar{t}_2\\ \bar{t}_3\end{Bmatrix} = \begin{bmatrix}\bar{x}_1 & \bar{y}_1 & 1\\ \bar{x}_2 & \bar{y}_2 & 1\\ \bar{x}_3 & \bar{y}_3 & 1\end{bmatrix} \begin{Bmatrix}\bar{a}_1\\ \bar{a}_2\\ \bar{a}_3\end{Bmatrix}$$

$$\therefore \left\{\bar{\alpha}_t\right\} = \begin{Bmatrix}\bar{a}_1\\ \bar{a}_2\\ \bar{a}_3\end{Bmatrix} = \begin{bmatrix}\bar{x}_1 & \bar{y}_1 & 1\\ \bar{x}_2 & \bar{y}_2 & 1\\ \bar{x}_3 & \bar{y}_3 & 1\end{bmatrix}^{-1} \begin{Bmatrix}\bar{t}_1\\ \bar{t}_2\\ \bar{t}_3\end{Bmatrix} = \frac{1}{2\text{AREA}} \underbrace{\begin{bmatrix}\bar{y}_2-\bar{y}_3 & \bar{y}_3-\bar{y}_1 & \bar{y}_1-\bar{y}_2\\ \bar{x}_3-\bar{x}_2 & \bar{x}_1-\bar{x}_3 & \bar{x}_2-\bar{x}_1\\ \bar{x}_2\bar{y}_3-\bar{x}_3\bar{y}_2 & \bar{x}_3\bar{y}_1-\bar{x}_1\bar{y}_3 & \bar{x}_1\bar{y}_2-\bar{x}_2\bar{y}_1\end{bmatrix}}_{\left[\bar{A}_t\right]_N^{-1}} \begin{Bmatrix}\bar{t}_1\\ \bar{t}_2\\ \bar{t}_3\end{Bmatrix}$$

in matrix form

$$\bar{t} = \left[\bar{A}_t\right]\left\{\bar{\alpha}_t\right\}$$

$$\left\{\bar{t}\right\}_N = \left[\bar{A}_t\right]_N\left\{\bar{\alpha}_t\right\} \quad \text{or} \quad \left\{\bar{\alpha}_t\right\} = \left[\bar{A}_t\right]_N^{-1}\left\{\bar{t}\right\}_N$$

$$\therefore \bar{t} = \left[\bar{A}_t\right]\left[\bar{A}_t\right]_N^{-1}\left\{\bar{t}\right\}_N$$

(5) <u>Membrane Stiffness Matrix $\left[\bar{K}_M\right]$</u> (See Figure 113.)

The matrix $\left[\bar{K}_M\right]$ expresses the linear relation between statically equivalent nodal forces and nodal displacements in the plane of the triangle. It is derived by obtaining the internal strain energy in the form:

$$\bar{U}_M = \frac{1}{2}\left[\bar{\delta}_M\right]_N \left[\quad\right] \left\{\bar{\delta}_M\right\}_N$$

where $\left[\bar{\delta}_M\right]_N$ is the local nodal membrane displacement column matrix and the middle matrix $\left[\quad\right]$ is the local membrane stiffness matrix $\left[\bar{K}_M\right]$.

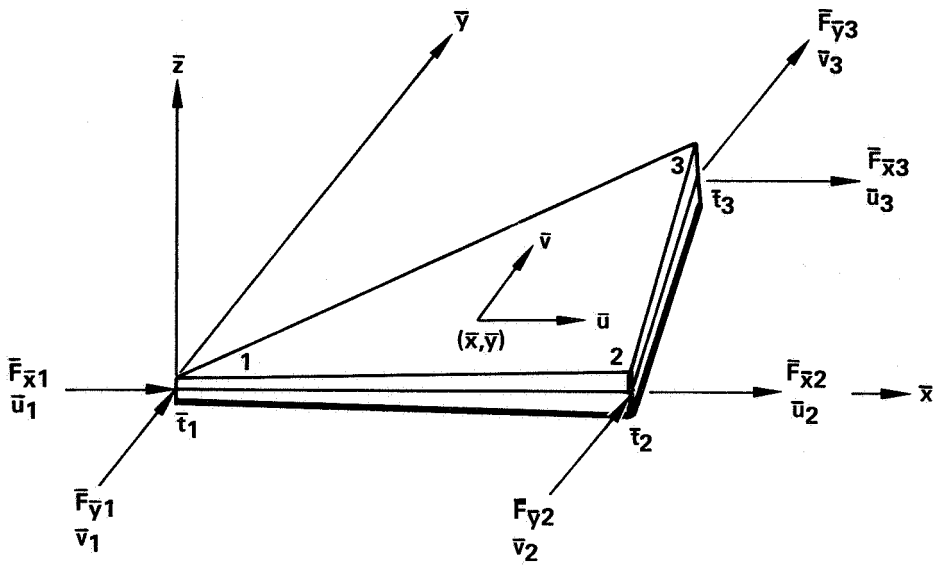

Figure 113. Generalized Nodal Local Membrane Displacements and Forces on Flat Triangular Element FD 25631B

Letting

$$\begin{Bmatrix} \bar{u} \\ \bar{v} \end{Bmatrix} = \underbrace{\begin{bmatrix} \bar{x} & 0 & \bar{y} & 0 & 1 & 0 \\ 0 & \bar{x} & 0 & \bar{y} & 0 & 1 \end{bmatrix}}_{\left[\bar{A}_M\right]} \begin{Bmatrix} \bar{a}_1 \\ \bar{a}_2 \\ \bar{a}_3 \\ \bar{a}_4 \\ \bar{a}_5 \\ \bar{a}_6 \end{Bmatrix}$$

or, in matrix form

$$\left\{\bar{\delta}_M\right\} = \left[\bar{A}_M\right] \left\{\bar{\alpha}_M\right\}$$

For nodal values

$$\begin{Bmatrix} \bar{u}_1 \\ \bar{v}_1 \\ \bar{u}_2 \\ \bar{v}_2 \\ \bar{u}_3 \\ \bar{v}_3 \end{Bmatrix}_N = \underbrace{\begin{bmatrix} \bar{x}_1 & 0 & \bar{y}_1 & 0 & 1 & 0 \\ 0 & \bar{x}_1 & 0 & \bar{y}_1 & 0 & 1 \\ \bar{x}_2 & 0 & \bar{y}_2 & 0 & 1 & 0 \\ 0 & \bar{x}_2 & 0 & \bar{y}_2 & 0 & 1 \\ \bar{x}_3 & 0 & \bar{y}_3 & 0 & 1 & 0 \\ 0 & \bar{x}_3 & 0 & \bar{y}_3 & 0 & 1 \end{bmatrix}}_{\left[\bar{A}_M\right]_N} \begin{Bmatrix} \bar{a}_1 \\ \bar{a}_2 \\ \bar{a}_3 \\ \bar{a}_4 \\ \bar{a}_5 \\ \bar{a}_6 \end{Bmatrix}$$

or, in matrix form

$$\left\{\bar{\delta}_M\right\}_N = \left[\bar{A}_M\right]_N \left\{\bar{\alpha}_M\right\}$$

$$\therefore \quad \left\{\bar{\alpha}_M\right\} = \left[A_M\right]_N^{-1} \left\{\bar{\delta}_M\right\}_N$$

and

$$\left\{\bar{\delta}_M\right\} = \left[\bar{A}_M\right] \left[\bar{A}_M\right]_N^{-1} \left\{\bar{\delta}_M\right\}_N$$

using

Strain Matrix

$$\left\{\bar{\epsilon}_M\right\} = \begin{Bmatrix} \epsilon_{\bar{x}\bar{x}} \\ \epsilon_{\bar{y}\bar{y}} \\ \epsilon_{\bar{x}\bar{y}} \end{Bmatrix} = \begin{Bmatrix} \dfrac{\partial \bar{u}}{\partial \bar{x}} \\ \dfrac{\partial \bar{v}}{\partial \bar{y}} \\ \dfrac{\partial \bar{u}}{\partial \bar{y}} + \dfrac{\partial \bar{v}}{\partial \bar{x}} \end{Bmatrix} = \underbrace{\begin{bmatrix} 1 & 0 & 0 & 0 & 0 & 0 \\ 0 & 0 & 0 & 1 & 0 & 0 \\ 0 & 1 & 1 & 0 & 0 & 0 \end{bmatrix}}_{\left[\bar{W}_M\right]} \left\{\bar{\alpha}_M\right\}$$

$$\therefore \quad \left\{\bar{\epsilon}_M\right\} = \left[\bar{W}_M\right]\left\{\bar{\alpha}_M\right\} = \left[\bar{W}_M\right]\left[\bar{A}_M\right]_N^{-1} \left\{\bar{\delta}_M\right\}_N$$

using

Stress Matrix

$$\begin{Bmatrix} \bar{\sigma}_{\bar{x}\bar{x}} \\ \bar{\sigma}_{\bar{y}\bar{y}} \\ \bar{\sigma}_{\bar{x}\bar{y}} \end{Bmatrix} = \begin{bmatrix} E_{11} & E_{12} & 0 \\ E_{12} & E_{22} & 0 \\ 0 & 0 & E_{44} \end{bmatrix} \begin{Bmatrix} \bar{\epsilon}_{\bar{x}\bar{x}} \\ \bar{\epsilon}_{\bar{y}\bar{y}} \\ \bar{\epsilon}_{\bar{x}\bar{y}} \end{Bmatrix} = \frac{E}{1-\nu^2} \begin{bmatrix} 1 & \nu & 0 \\ \nu & 1 & 0 \\ 0 & 0 & \frac{1-\nu}{2} \end{bmatrix} \begin{Bmatrix} \bar{\epsilon}_{\bar{x}\bar{x}} \\ \bar{\epsilon}_{\bar{y}\bar{y}} \\ \bar{\epsilon}_{\bar{x}\bar{y}} \end{Bmatrix}$$

$$\therefore \quad \left\{\bar{\sigma}_M\right\} = \left[\bar{E}_M\right] \left\{\bar{\epsilon}_M\right\}$$

Internal strain energy

$$\bar{U}_M = \frac{1}{2}\int \left[\bar{\epsilon}_M\right]\left\{\bar{\sigma}_M\right\} d\bar{V} = \int \left[\bar{\epsilon}_M\right]\left[\bar{E}_M\right]\left\{\bar{\epsilon}_M\right\} d\bar{V}$$

$$= \frac{1}{2}\int \left[\bar{\delta}_M\right]_N \left[\bar{A}_M\right]_N^{-1^T} \left[\bar{W}_M\right]^T \left[\bar{E}_M\right]\left[\bar{W}_M\right]\left[\bar{A}_M\right]_N^{-1} \left\{\bar{\delta}_M\right\}_N d\bar{V}$$

$$= \frac{1}{2}\left[\bar{\delta}_M\right]_N \left[\left[\bar{A}_M\right]_N^{-1^T} \left(\int \left[\bar{W}_M\right]^T \left[\bar{E}_M\right] \left[\bar{W}_M\right] d\bar{V}\right) \left[\bar{A}_M\right]_N^{-1}\right] \left\{\bar{\delta}_M\right\}_N$$

$$\therefore \quad \left[\bar{K}_M\right] = \left[\bar{A}_M\right]_N^{-1^T} \left(\int \left[\bar{W}_M\right]^T \left[\bar{E}_M\right]\left[\bar{W}_M\right] d\bar{V}\right) \left[\bar{A}_M\right]_N^{-1}$$

where $\quad d\bar{V} = \bar{t}d\bar{x}d\bar{y}$

and

$$\left[\bar{A}_M\right]_N^{-1} = \frac{1}{2\text{AREA}}\begin{bmatrix} \bar{y}_2-\bar{y}_3 & 0 & \bar{y}_3-\bar{y}_1 & 0 & \bar{y}_1-\bar{y}_2 & 0 \\ 0 & \bar{y}_2-\bar{y}_3 & 0 & \bar{y}_3-\bar{y}_1 & 0 & \bar{y}_1-\bar{y}_2 \\ \bar{x}_3-\bar{x}_2 & 0 & \bar{x}_1-\bar{x}_3 & 0 & \bar{x}_2-\bar{x}_1 & 0 \\ 0 & \bar{x}_3-\bar{x}_2 & 0 & \bar{x}_1-\bar{x}_3 & 0 & \bar{x}_2-\bar{x}_1 \\ \bar{x}_2\bar{y}_3-\bar{x}_3\bar{y}_2 & 0 & \bar{x}_3\bar{y}_1-\bar{x}_1\bar{y}_3 & 0 & \bar{x}_1\bar{y}_2-\bar{x}_2\bar{y}_1 & 0 \\ 0 & \bar{x}_2\bar{y}_3-\bar{x}_3\bar{y}_2 & 0 & \bar{x}_3\bar{y}_1-\bar{x}_1\bar{y}_3 & 0 & \bar{x}_1\bar{y}_2-\bar{x}_2\bar{y}_1 \end{bmatrix}$$

(6) <u>Bending Stiffness Matrix $\left[\bar{K}_B\right]$</u> (See Figure 114.)

The matrix $\left[\bar{K}_B\right]$ expresses the linear relation between statically equivalent nodal forces and nodal bending displacements in the triangle. It is derived by obtaining the internal strain energy in the form:

$$\bar{U}_B = \frac{1}{2}\left\{\bar{\delta}_B\right\}_N \left[\quad\right] \left\{\bar{\delta}_B\right\}_N$$

where $\left[\bar{\delta}_B\right]_N$ is the local nodal bending displacement column matrix and the middle matrix $[\ \ ]$ is the local bending stiffness matrix $\left[\bar{K}_B\right]$.

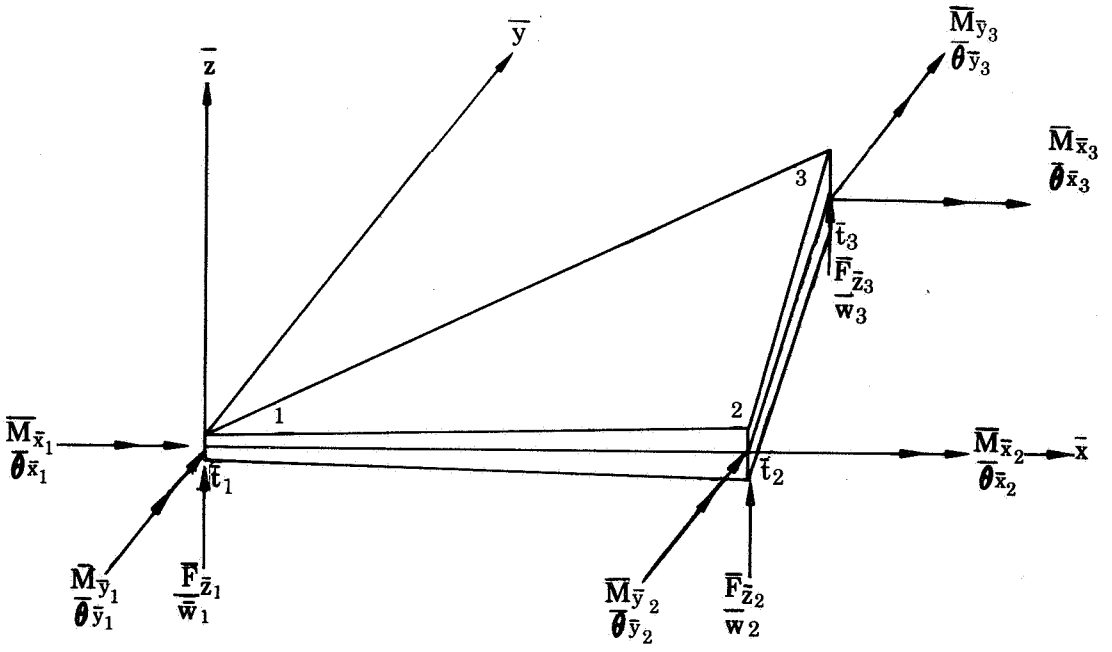

Figure 114. Generalized Nodal Bending Displacements and Forces on Flat Triangular Element FD 25652

Using displacement function

$$\bar{w} = \bar{a}_1 + \bar{a}_2\bar{x} + \bar{a}_3\bar{y} + \bar{a}_4\bar{x}^2 + \bar{a}_5\bar{y}^2 + \bar{a}_6\bar{x}^3 + \bar{a}_7\bar{x}^2\bar{y} + \bar{a}_8\bar{x}\bar{y}^2 + \bar{a}_9\bar{y}^3$$

$$\begin{Bmatrix} \bar{w} \\ \bar{\theta}_{\bar{x}} \\ \bar{\theta}_{\bar{y}} \end{Bmatrix} = \left\{\bar{\delta}_B\right\} = \begin{Bmatrix} \bar{w} \\ \dfrac{\partial \bar{w}}{\partial \bar{y}} \\ -\dfrac{\partial \bar{w}}{\partial \bar{x}} \end{Bmatrix} = \begin{bmatrix} 1 & \bar{x} & \bar{y} & \bar{x}^2 & \bar{y}^2 & \bar{x}^3 & \bar{x}^2\bar{y} & \bar{x}\bar{y}^2 & \bar{y}^3 \\ 0 & 0 & 1 & 0 & 2\bar{y} & 0 & \bar{x}^2 & 2\bar{x}\bar{y} & 3\bar{y}^2 \\ 0 & -1 & 0 & -2\bar{x} & 0 & -3\bar{x}^2 & -2\bar{x}\bar{y} & -\bar{y}^2 & 0 \end{bmatrix} \begin{Bmatrix} \bar{a}_1 \\ \bar{a}_2 \\ \bar{a}_3 \\ \bar{a}_4 \\ \bar{a}_5 \\ \bar{a}_6 \\ \bar{a}_7 \\ \bar{a}_8 \\ \bar{a}_9 \end{Bmatrix} = \left[\bar{A}_B\right]\left\{\bar{\alpha}\right\}$$

$$\left[\bar{A}_B\right]$$

In matrix form

$$\left\{\bar{\delta}_B\right\} = \left[\bar{A}_B\right]\left\{\bar{\alpha}_B\right\}$$

For nodal values

$$\left\{\bar{\delta}_B\right\}_N = \left[\bar{A}_B\right]_N \left\{\bar{\alpha}_B\right\}$$

$$\therefore \quad \left\{\bar{\alpha}_B\right\} = \left[A_B\right]_N^{-1} \left\{\bar{\delta}_B\right\}_N$$

and

$$\left\{\bar{\delta}_B\right\} = \left[\bar{A}_B\right] \left[\bar{A}_B\right]_N^{-1} \left\{\bar{\delta}_B\right\}_N$$

using

$$\left[\bar{E}_B\right]$$

Curvature Matrix

$$\left\{\bar{C}\right\} = \begin{Bmatrix} -\bar{w}_{\bar{y}\bar{y}} \\ -\bar{w}_{\bar{x}\bar{x}} \\ \bar{w}_{\bar{x}\bar{y}} \end{Bmatrix} = \begin{bmatrix} 0 & 0 & 0 & 0 & -2 & 0 & 0 & -2\bar{x} & -6\bar{y} \\ 0 & 0 & 0 & -2 & 0 & -6\bar{x} & -2\bar{y} & 0 & 0 \\ 0 & 0 & 0 & 0 & 0 & 0 & 2\bar{x} & 2\bar{y} & 0 \end{bmatrix} \left\{\bar{\alpha}_B\right\}$$

or

$$\left\{\bar{C}\right\} = \left[\bar{E}_B\right]\left\{\bar{\alpha}_B\right\} = \left[\bar{E}_B\right]\left[\bar{A}_B\right]_N^{-1} \left\{\bar{\delta}_B\right\}_N$$

Internal strain energy,

$$\bar{U}_B = \frac{1}{2} \int \bar{D} \left[\bar{w}_{\bar{x}\bar{x}}^2 + \bar{w}_{\bar{y}\bar{y}}^2 + 2\nu \bar{w}_{\bar{x}\bar{x}} \bar{w}_{\bar{y}\bar{y}} + 2(1-\nu)\bar{w}_{\bar{x}\bar{y}}^2\right] d\bar{x}d\bar{y}$$

$$= \frac{1}{2} \int \bar{D} \underbrace{\left[-\bar{w}_{\bar{y}\bar{y}} \;\; -\bar{w}_{\bar{x}\bar{x}} \;\; \bar{w}_{\bar{x}\bar{y}}\right]}_{\left[\bar{C}\right]} \underbrace{\begin{bmatrix} 1 & \nu & 0 \\ \nu & 1 & 0 \\ 0 & 0 & 2(1-\nu) \end{bmatrix}}_{\left[\bar{V}_B\right]} \underbrace{\begin{Bmatrix} -\bar{w}_{\bar{y}\bar{y}} \\ -\bar{w}_{\bar{x}\bar{x}} \\ w_{\bar{x}\bar{y}} \end{Bmatrix}}_{\left\{\bar{C}\right\}} d\bar{x}d\bar{y}$$

$$= \frac{1}{2} \int \bar{D} \left[\bar{C}\right]\left[\bar{V}_B\right]\left\{\bar{C}\right\} d\bar{x}d\bar{y}$$

$$= \frac{1}{2} \int \bar{D} \left[\bar{\delta}_B\right]_N \left[\bar{A}_B\right]_N^{-1^T} \left[\bar{E}_B\right]^T \left[\bar{V}_B\right] \left[\bar{E}_B\right] \left[\bar{A}_B\right]_N^{-1} \left\{\bar{\delta}_B\right\}_N d\bar{x}d\bar{y}$$

$$\bar{U}_B = \frac{1}{2}\left[\bar{\delta}_B\right]_N \left[\left[\bar{A}_B\right]_N^{-1^T} \left(\int \bar{D} \left[\bar{E}_B\right]^T \left[\bar{V}_B\right] \left[\bar{E}_B\right] d\bar{x}d\bar{y}\right) \left[\bar{A}_B\right]_N^{-1}\right] \left\{\bar{\delta}_B\right\}_N$$

$$\therefore \left[\bar{K}_B\right] = \left[A_B\right]_N^{-1^T} \left(\int \bar{D} \left[\bar{E}_B\right]^T \left[\bar{V}_B\right] \left[\bar{E}_B\right] d\bar{x}d\bar{y}\right) \left[\bar{A}_B\right]_N^{-1}$$

$$\bar{D} = \frac{E\bar{t}^3}{12(1-\nu^2)}$$

(7) Nodal Pressure Force Matrix $\left\{\bar{F}_p\right\}_N$ (See Figure 115.)

The matrix $\left\{\bar{F}_p\right\}_N$ is the column matrix of statically equivalent local nodal pressure forces. This is derived by obtaining the potential energy in the form:

$$\bar{V}_p = \left[\bar{\delta}_B\right]_N \left\{\ \right\}_N$$

where $\left[\bar{\delta}_B\right]_N$ is local nodal bending displacement row matrix and the latter matrix $\left\{\ \right\}_N$ is the desired local pressure force matrix $\left\{\bar{F}_p\right\}_N$.

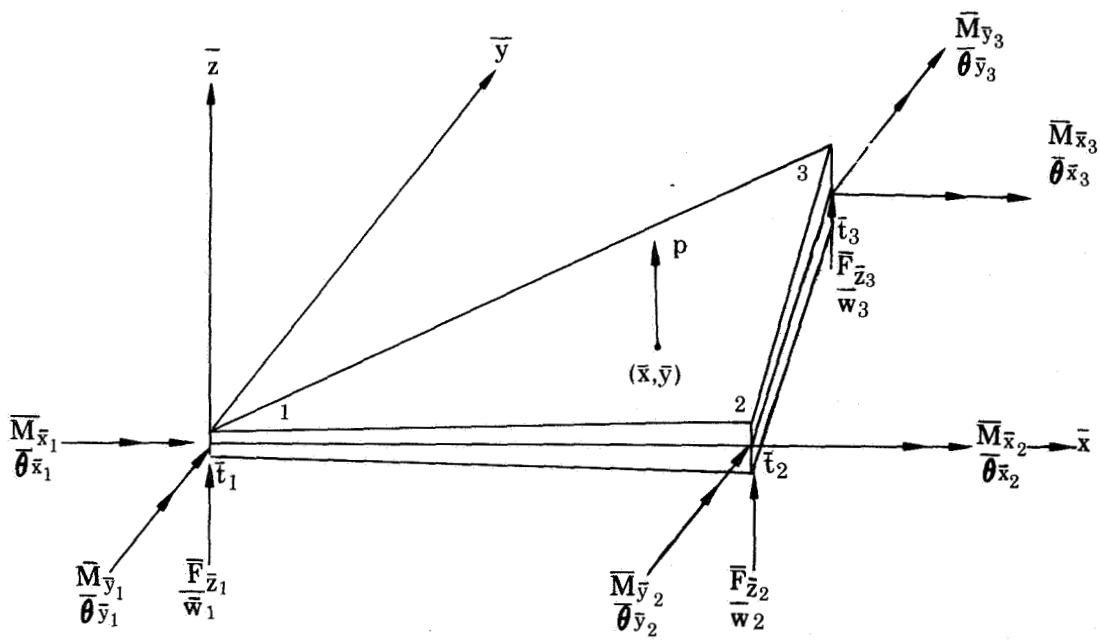

Figure 115. Generalized Nodal Bending Displacements and Forces on Flat Triangular Element FD 25652B

In local coordinates,

$$\bar{w} = \bar{a}_1 + \bar{a}_2\bar{x} + \bar{a}_3\bar{y} + \bar{a}_4\bar{x}^2 + \bar{a}_5\bar{y}^2 + \bar{a}_6\bar{x}^3$$
$$+\bar{a}_7\bar{x}^2\bar{y} + \bar{a}_8\bar{x}\bar{y}^2 + \bar{a}_9\bar{y}^3$$

or

$$\left\{\bar{\delta}_B\right\} = \begin{Bmatrix} \bar{w} \\ \bar{w}_{\bar{y}} \\ -\bar{w}_{\bar{x}} \end{Bmatrix} = \left[\bar{A}_B\right]\left\{\bar{\alpha}_B\right\}$$

For nodal values

$$\left\{\bar{\delta}_B\right\}_N = \left[\bar{A}_B\right]_N\left\{\bar{\alpha}_B\right\}$$

$$\therefore \quad \left\{\bar{\alpha}_B\right\} = \left[\bar{A}_B\right]_N^{-1} \left\{\bar{\delta}_B\right\}_N$$

$$\text{or} \quad \left\{\bar{\delta}_B\right\} = \left[\bar{A}_B\right]\left[\bar{A}_B\right]_N^{-1} \left\{\bar{\delta}_B\right\}_N$$

$$\text{and} \quad \left[\bar{\delta}_B\right] = \left[\bar{\delta}_B\right]_N\left[\bar{A}_B\right]_N^{-1T} \left[\bar{A}_B\right]^T$$

$$\therefore \quad \bar{w} = \left[\bar{\delta}_B\right]\begin{Bmatrix}1\\0\\0\end{Bmatrix}$$

$$= \left[\bar{\delta}_B\right]_N\left[\bar{A}_B\right]_N^{-1T} \left[\bar{A}_B\right]^T \begin{Bmatrix}1\\0\\0\end{Bmatrix}$$

The potential energy due to pressure loading is

$$\bar{V}p = \int p\bar{w}d\bar{x}d\bar{y} = \left[\bar{\delta}_B\right]_N \int p \left[\bar{A}_B\right]_N^{-1T} \left[\bar{A}_B\right]^T \begin{Bmatrix}1\\0\\0\end{Bmatrix} d\bar{x}d\bar{y}$$

$$\text{or } \bar{V}p = \left[\bar{\delta}_B\right]_N \left\{\bar{F}p\right\}_N$$

Therefore,

$$\left\{\bar{F}p\right\}_N = \int p\left[\bar{A}_B\right]_N^{-1T}\left[\bar{A}_B\right]^T \begin{Bmatrix}1\\0\\0\end{Bmatrix} d\bar{x}d\bar{y}$$

(8) <u>Nodal Centrifugal Force Matrix $\left\{\bar{F}_c\right\}_N$</u> (See Figure 116.)

The matrix $\left\{\bar{F}_c\right\}_N$ is the column matrix of statically equivalent local nodal centrifugal forces. This is derived by obtaining the potential energy in the form:

$$V_c = \left[\bar{\delta}\right]_N \left\{\quad\right\}_N$$

where $\left[\bar{\delta}\right]_N$ is the local nodal displacement row matrix and the latter matrix $\left\{\quad\right\}_N$ is the desired local "centrifugal" force column matrix $\left\{\bar{F}_C\right\}_N$.

The potential energy due to rotation is

$$V_c = \int \rho\omega^2\bar{t}r\ \delta_r\ dA$$

$$= \int \rho\omega^2\bar{t}r \left[u \cos\ (r,x) + v \cos\ (r,y) + w \cos\ (r,z)\right] dA$$

$$= \int \rho\omega^2\bar{t}r \left[uvw\right] \begin{Bmatrix}\cos\ (r,x)\\ \cos\ (r,y)\\ \cos\ (r,z)\end{Bmatrix} dA$$

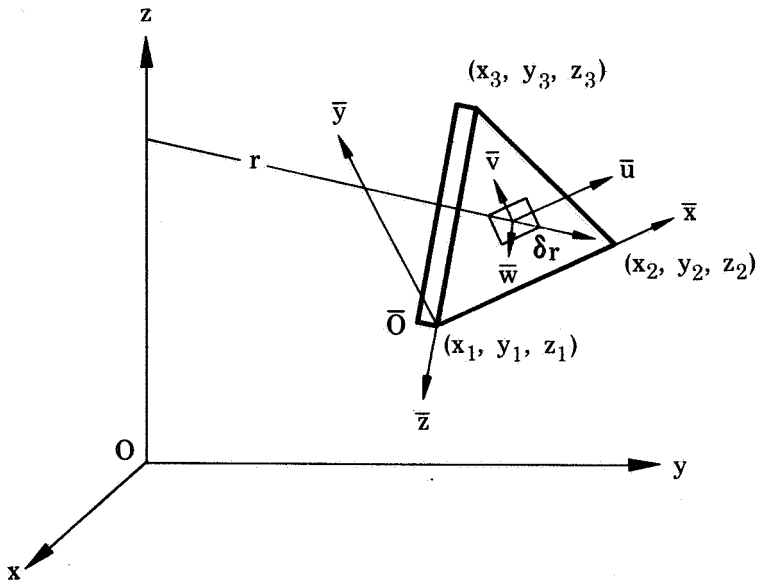

Figure 116. Geometry of Rotating Triangular Element FD 25844

But

$$\left\lfloor uvw \right\rfloor = \left\lfloor \bar{u}\bar{v}\bar{w} \right\rfloor \begin{bmatrix} \cos\ (x,\bar{x}) & \cos\ (y,\bar{x}) & \cos\ (z,\bar{x}) \\ \cos\ (x,\bar{y}) & \cos\ (y,\bar{y}) & \cos\ (z,\bar{y}) \\ \cos\ (x,\bar{z}) & \cos\ (y,\bar{z}) & \cos\ (z,\bar{z}) \end{bmatrix}$$

$$= \left\lfloor \bar{u}\bar{v}\bar{w} \right\rfloor \left\lfloor R_1 \right\rfloor^T$$

$$\therefore \delta_r = \left\lfloor \bar{u}\ \bar{v}\ \bar{w} \right\rfloor \left\lfloor R_1 \right\rfloor^T \begin{Bmatrix} \cos\ (r,x) \\ \cos\ (r,y) \\ \cos\ (r,z) \end{Bmatrix}$$

Or

$$\delta_r = \left\lfloor \bar{u}\ \bar{v}\ \bar{w} \right\rfloor \left\lfloor R_1 \right\rfloor^T \begin{Bmatrix} x/r \\ y/r \\ 0 \end{Bmatrix}$$

Since cos (r, z) = 0. Also

$$\begin{Bmatrix} x \\ y \\ 0 \end{Bmatrix} = \begin{Bmatrix} x_1 \\ y_1 \\ z_1 - z \end{Bmatrix} + \left\lfloor R_1 \right\rfloor \begin{Bmatrix} \bar{x} \\ \bar{y} \\ 0 \end{Bmatrix}$$

From which

$$z - z_1 = \bar{x} \cos\ (z,\bar{x}) + \bar{y} \cos\ (z,\bar{y})$$

Therefore

$$\begin{Bmatrix} x \\ y \\ 0 \end{Bmatrix} = \begin{Bmatrix} x_1 \\ y_1 \\ -\bar{x} \cos\ (z,\bar{x}) - \bar{y} \cos\ (z,\bar{y}) \end{Bmatrix} + \left\lfloor R_1 \right\rfloor \begin{Bmatrix} \bar{x} \\ \bar{y} \\ 0 \end{Bmatrix}$$

and

$$V_c = \int \rho\omega^2 \bar{t} \left[\bar{u}\ \bar{v}\ \bar{w}\right] \left[R_1\right]^T \left[\begin{Bmatrix} x_1 \\ y_1 \\ -\bar{x}\cos(z,\bar{x}) - \bar{y}\cos(z,\bar{y}) \end{Bmatrix} + \left[R_1\right] \begin{Bmatrix} \bar{x} \\ \bar{y} \\ 0 \end{Bmatrix}\right] dA$$

expanding

$$\left[\bar{u}\ \bar{v}\ \bar{w}\right] = \left[\bar{u}\ \bar{v}\ \bar{w}\ \bar{\theta}_x\ \bar{\theta}_y\ \bar{\theta}_z\right] \begin{bmatrix} 1 & 0 & 0 \\ 0 & 1 & 0 \\ 0 & 0 & 1 \\ 0 & 0 & 0 \\ 0 & 0 & 0 \\ 0 & 0 & 0 \end{bmatrix} = \left[\bar{\delta}\right] \begin{Bmatrix} I_3 \\ 0_3 \end{Bmatrix}$$

where

$$I_3 = \begin{bmatrix} 100 \\ 010 \\ 001 \end{bmatrix}$$

$$0_3 = \begin{bmatrix} 000 \\ 000 \\ 000 \end{bmatrix}$$

Therefore

$$\begin{Bmatrix} \bar{u} \\ \bar{v} \\ \bar{w} \end{Bmatrix} = \begin{bmatrix} 1 & 0 & 0 & 0 & 0 & 0 \\ 0 & 1 & 0 & 0 & 0 & 0 \\ 0 & 0 & 1 & 0 & 0 & 0 \end{bmatrix} \begin{Bmatrix} \bar{u} \\ \bar{v} \\ \bar{w} \\ \bar{\theta}_x \\ \bar{\theta}_y \\ \bar{\theta}_z \end{Bmatrix}$$

Also

$$\left\{\bar{\delta}\right\} = \begin{bmatrix} \left[\bar{A}_M\right]\left[\bar{A}_M\right]_N^{-1} & 0 & 0 \\ 0 & \left[\bar{A}_B\right]\left[\bar{A}_B\right]_N^{-1} & 0 \\ 0 & 0 & 0 \end{bmatrix} \left\{\bar{\delta}\right\}_N$$

Therefore

$$\left[\bar{\delta}\right] = \left[\bar{\delta}\right]_N \overset{[H]}{\begin{bmatrix} \left[\bar{A}_M\right]_N^{-1^T} \left[\bar{A}_M\right]^T & 0 & 0 \\ 0 & \left[\bar{A}_B\right]_N^{-1^T} \left[\bar{A}_B\right]^T & 0 \\ 0 & 0 & 0 \end{bmatrix}}$$

In matrix form

$$\left\{\bar{\delta}\right\} = \left[H\right] \left\{\bar{\delta}\right\}_N$$

$$\left[\bar{\delta}\right] = \left[\bar{\delta}\right]_N \left[H\right]^T$$

$$\therefore \; V_c = \rho\omega^2 \left[\bar{\delta}\right]_N \int_s \bar{t} \left[H\right]^T \begin{Bmatrix} I_3 \\ 0_3 \end{Bmatrix} \left[R_1\right]^T \left[\begin{Bmatrix} x_1 \\ y_1 \\ -\bar{x}\cos(z,\bar{x}) - \bar{y}\cos(z,\bar{y}) \end{Bmatrix} + \left[R_1\right] \begin{Bmatrix} \bar{x} \\ \bar{y} \\ 0 \end{Bmatrix} \right] d\bar{x}d\bar{y}$$

and

$$\left\{\bar{F}_c\right\}_N = \rho\omega^2 \int_s \bar{t} \left[H\right]^T \begin{Bmatrix} I_3 \\ 0_3 \end{Bmatrix} \left[R_1\right]^T \left[\begin{Bmatrix} x_1 \\ y_1 \\ -\bar{x}\cos(z,\bar{x}) \; -\bar{y}\cos(z,\bar{y}) \end{Bmatrix} + \left[R_1\right] \begin{Bmatrix} \bar{x} \\ \bar{y} \\ 0 \end{Bmatrix} \right] d\bar{x}d\bar{y} \quad \text{(D-1)}$$

Then, in common coordinates

$$\left\{F_c\right\}_N = \left[R_6\right]^T \left\{\bar{F}_c\right\}_N$$

(10) Approximate Centrifugal Force Matrix $\left\{F_c\right\}_N$

$$\left\{F_c\right\}_N = \begin{bmatrix} F_{x_1} \\ F_{y_1} \\ F_{z_1} \\ M_{x_1} \\ M_{y_1} \\ M_{z_1} \\ F_{x_2} \\ F_{y_2} \\ F_{z_2} \\ M_{x_2} \\ M_{y_2} \\ M_{z_2} \\ F_{x_3} \\ F_{y_3} \\ F_{z_3} \\ M_{x_3} \\ M_{y_3} \\ M_{z_3} \end{bmatrix}_N = \frac{\rho\omega^2\bar{A}_i}{3} \begin{bmatrix} \bar{t}_1 x_1 \\ \bar{t}_1 y_1 \\ 0 \\ 0 \\ 0 \\ 0 \\ \bar{t}_2 x_2 \\ \bar{t}_2 y_2 \\ 0 \\ 0 \\ 0 \\ 0 \\ \bar{t}_3 x_3 \\ \bar{t}_3 y_3 \\ 0 \\ 0 \\ 0 \\ 0 \end{bmatrix}_N \qquad \text{(D-2)}$$

$\bar{A}_i$ = Area of ith element

ρ = Density

ω = Angular velocity

This matrix (D-2) is used in lieu of (D-1) because of its simplicity. It should provide better accuracy than (D-1), particularly in cases where bending stresses are predominant; however, more experience is needed with this matrix (D-2) form before it can be used with a high degree of confidence. For this reason, the computer program contains an option that permits selection of either matrix (D-1) or (D-2). (D-1)

(11) <u>Membrane Inertia Matrix</u> $\left[\bar{M}_M\right]$ (See Figure 117)

The matrix $\left[\bar{M}_M\right]$ is the matrix of nodal masses and inertias. It is derived by obtaining the kinetic energy of motion in the form:

$$\bar{T} = \frac{1}{2}\left\{\dot{\bar{q}}\right\}_N \left[\quad\right] \left\{\dot{\bar{q}}\right\}_N$$

where $\left\{\bar{q}\right\}_N$ is the local nodal vibratory membrane velocity column matrix and the middle matrix $\left[\quad\right]$ is the desired local membrane inertia matrix $\left[\bar{M}_M\right]$.

$$\text{Kinetic Energy} = \int_s \frac{1}{2}\rho\bar{t}\left(\dot{\bar{u}}^2 + \dot{\bar{v}}^2\right)d\bar{x}d\bar{y} = \int \frac{1}{2}\rho\bar{t}\dot{\bar{q}}^2\, d\bar{x}d\bar{y}$$

Membrane Displacement Matrix

$$\left\{\bar{q}_M\right\} = \left\{\begin{matrix}\bar{u}\\ \bar{v}\end{matrix}\right\} = \begin{bmatrix}\bar{x} & 0 & \bar{y} & 0 & 1 & 0\\ 0 & \bar{x} & 0 & \bar{y} & 0 & 1\end{bmatrix}\left\{\begin{matrix}\bar{a}_1\\ \bar{a}_2\\ \bar{a}_3\\ \bar{a}_4\\ \bar{a}_5\\ \bar{a}_6\end{matrix}\right\}$$

or

$$\left\{\bar{q}_M\right\} = \left[\bar{A}_M\right]\left\{\bar{\alpha}_M\right\}$$

For nodal values

$$\left\{\bar{q}_M\right\}_N = \left[\bar{A}_M\right]\left[\bar{A}_M\right]_N^{-1}\left\{\bar{q}_M\right\}_N$$

$$\left\{\dot{\bar{q}}_M\right\}_N = \left[\bar{A}_M\right]\left[\bar{A}_M\right]_N^{-1}\left\{\dot{\bar{q}}_M\right\}_N$$

and

$$\text{Kinetic Energy} = \int \frac{1}{2}\rho\bar{t}\left[\dot{\bar{q}}_M\right]\left\{\dot{\bar{q}}_M\right\}d\bar{x}d\bar{y}$$

$$= \frac{1}{2}\left[\dot{\bar{q}}_M\right]_N \rho\left[\bar{A}_M\right]_N^{-1^T}\left(\int \bar{t}\left[\bar{A}_M\right]^T\left[\bar{A}_M\right] d\bar{x}d\bar{y}\right)\left[A_M\right]_N^{-1}\left\{\dot{\bar{q}}_M\right\}_N$$

$$= \frac{1}{2}\left[\dot{\bar{q}}_M\right]_N\left[\bar{M}_M\right]\left\{\dot{\bar{q}}_M\right\}_N$$

∴ Membrane inertia matrix is

$$\left[\bar{M}_M\right] = \rho \left[\bar{A}_M\right]_N^{-1^T} \left(\int \bar{t} \left[\bar{A}_M\right]^T \left[\bar{A}_M\right] d\bar{x}d\bar{y} \right) \left[\bar{A}_M\right]_N^{-1}$$

(12) Bending Inertia Matrix $\left[\bar{M}_B\right]$ (See Figure 115)

The matrix $\left[\bar{M}_B\right]$ is the matrix of nodal masses and inertias which resist vibratory transverse bending motion of the triangle. It is derived by obtaining the kinetic energy of motion in the form:

$$\bar{T} = \frac{1}{2} \left\{\dot{\bar{q}}\right\}_N \left[\quad\right] \left\{\dot{\bar{q}}\right\}_N$$

where $\left\{\dot{\bar{q}}\right\}_N$ is the local nodal vibratory transverse bending velocity column matrix and the middle matrix $\left[\quad\right]$ is the desired local bending inertia matrix $\left[\bar{M}_B\right]$.

$$\text{Kinetic Energy} = \int_V \frac{1}{2}\rho\bar{t} \left(\frac{\partial \bar{q}}{\partial t}\right)^2 d\bar{x}d\bar{y}$$

Transverse Displacement

$$\bar{q} = \bar{a}_1 + \bar{a}_2\bar{x} + a_3\bar{y} + a_4\bar{x}^2 + a_5\bar{y}^2 + a_6\bar{x}^3 + a_7\bar{x}^2\bar{y} + a_8\bar{x}\bar{y}^2 + a_9\bar{y}^3$$

or

$$\bar{q} = \left[\bar{A}_B\right] \left\{\bar{\alpha}_B\right\}$$

Using nodal values

$$\left\{\bar{q}_B\right\}_N = \left[\bar{A}_B\right]_N \left\{\bar{\alpha}\right\}_N$$

$$\left\{\bar{\alpha}\right\}_N = \left[\bar{A}_B\right]_N^{-1} \left\{\bar{q}_B\right\}_N$$

$$\bar{q} = \left[\bar{A}_B\right]\left[A_B\right]_N^{-1} \left\{\bar{q}_B\right\}_N$$

$$\dot{\bar{q}} = \left[\bar{A}_B\right]\left[A_B\right]_N^{-1} \left\{\dot{\bar{q}}_B\right\}_N$$

$$\text{Kinetic Energy} = \frac{1}{2}\rho\int_V \bar{t}\left[\dot{\bar{q}}\right]\left\{\dot{\bar{q}}\right\}d\bar{x}d\bar{y}$$

$$= \frac{1}{2}\left\{\dot{\bar{q}}_B\right\}_N\left[\rho\left[\bar{A}_B\right]_N^{-1^T}\left(\int \bar{t}\left[\bar{A}_B\right]^T\left[\bar{A}_B\right]d\bar{x}d\bar{y}\right)\left[\bar{A}_B\right]_N^{-1}\right]\left\{\dot{\bar{q}}_B\right\}_N$$

$$= \frac{1}{2}\left[\dot{\bar{q}}_B\right]_N\left[\bar{M}_B\right]\left\{\dot{\bar{q}}_B\right\}_N$$

$\therefore$ Bending inertia matrix is

$$\left[\bar{M}_B\right] = \rho\left[\bar{A}_B\right]_N^{-1^T}\left(\int \bar{t}\left[\bar{A}_B\right]^T\left[\bar{A}_B\right]d\bar{x}d\bar{y}\right)\left[\bar{A}_B\right]_N^{-1}$$

(13) Normal Direction Cosine Matrix $\left[R_1\right]_n$

The matrix $\left[R_1\right]_n$ establishes the relation between the directions of the axes of the common coordinate system and the axes of the quasi-normal system. It is obtained by averaging the directions of the $\bar{y}$ and $\bar{z}$ axes of the four triangular elements that have a common node and a common generator, with the x axis lying in the direction of the generator as shown in figure 123. The directions of the local axes of the individual triangular elements are obtained directly from the direction cosine matrix $\left[R_1\right]$.

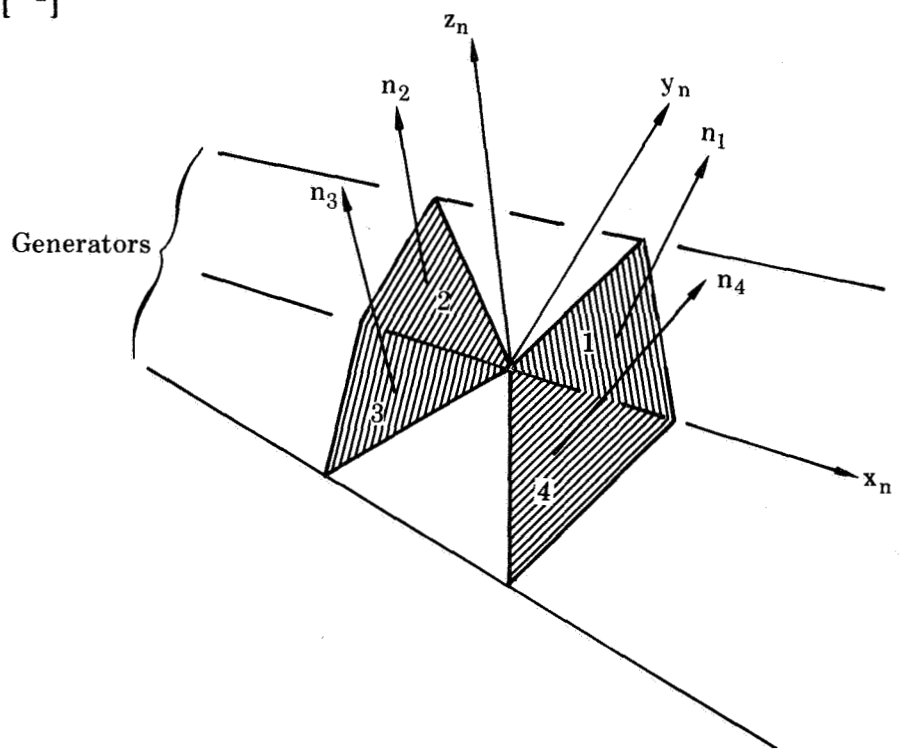

Figure 117. Definition of Quasi-Normal Coordinate System FD 25669

(14) Relative Vibratory Bending Stress Matrix $\left\{\bar{\sigma}_B\right\}$

The matrix $\left\{\bar{\sigma}_B\right\}$ is the column matrix of local vibratory bending stresses. These stresses are normalized in terms of the maximum stresses when the system vibrates in relative modal amplitudes. Using the local bending stress matrix:

$$\left\{\bar{\sigma}_B\right\} = \frac{6\bar{D}}{\bar{t}^2} \left[\bar{V}_{B_1}\right] \left[\bar{E}_B\right] \left[\bar{A}_B\right]_N^{-1} \left\{\begin{matrix} \bar{w} \\ \hline \bar{\theta} \end{matrix}\right\}_N$$

and the relations

$$\left[T\right] = \left[\begin{matrix} I \\ -B^{-1}C \end{matrix}\right], \left\{\begin{matrix} w \\ \hline \theta \end{matrix}\right\}_N = \left[T\right] \left\{w\right\}_N , \left\{\begin{matrix} \bar{w} \\ \hline \bar{\theta} \end{matrix}\right\}_N = \left[R_6\right]_n^T \left\{\begin{matrix} w \\ \hline \theta \end{matrix}\right\}_N$$

The local bending stress matrix in terms of the displacements in the quasi-normal system is:

$$\left\{\bar{\sigma}_B\right\} = \frac{6\bar{D}}{\bar{t}_c^2} \left[\bar{V}_{B_1}\right] \left[\bar{E}_B\right] \left[\bar{A}_B\right]_N^{-1} \left[R_6\right]_n^T \left[\begin{matrix} I \\ -B^{-1}C \end{matrix}\right] \left\{w\right\}_N$$

APPENDIX E
NOMENCLATURE

A. HYDRODYNAMIC

SYMBOL	DESCRIPTION	UNITS
A	Flow area normal to direction of relative velocity	L^2
b	Tangential vapor cavity height	L
C	Clearance	L
C_e	Exit deviation constant	
C_f	Surface friction coefficient	
E	Error in radial pressure gradient	FL^{-3}
F_{uc}	Centrifugal force	F
F_D	Drag force	F
F_p	Pressure force	F
F_{PC}	Pressure force due to vapor cavity formation	F
F_{PSC}	Pressure force due to streamline re-location	F
$F_{p\Delta\tau}$	Pressure force due to a change in blade passage width	F
F_1, F_2	Pressure forces due to mid channel pressure	F
F_R	Centrifugal force in the radial direction	F
g	Acceleration due to gravity	LT^{-2}
H	Total static head or boundary layer shape factor	L
h	Static head	L

SYMBOL	DESCRIPTION	UNITS
HI	Ideal head rise	L
i	Incidence angle	deg
k	Cavitation number	
m	Distance along streamline	L
$\dot{m}$	Mass flow rate	FTL^{-1}
M	Fluid momentum	FT
m*	Distance along the blade	L
NI	Number of streamlines	
NJ	Number of axial stations	
N_b	Number of blades	
N	Inducer rotative speed	T^{-1}
NPSH	Net positive suction head	L
PO_{rel}	Mixed out total relative pressure	FL^{-2}
P_{rel}	Total relative pressure	FL^{-2}
P_{SAT}	Fluid saturation pressure	FL^{-2}
P_T	Total absolute pressure	FL^{-2}
PO_T	Mixed out total absolute pressure	
P	Static pressure	FL^{-2}
ΔP_b	Blade pressure loading	FL^{-2}
ΔP_D	Total relative pressure loss due to cavity collapse	FL^{-2}
Q	Volumetric flow rate per blade passage	$L^3\ T^{-1}$
QI	Total volumetric flow rate	$L^3\ T^{-1}$
Q_D	Relative dynamic pressure	FL^{-2}

SYMBOL	DESCRIPTION	UNITS
R	Radius	L
Re	Reynolds number based on tip radius	
Re_θ	Reynolds number based on momentum thickness	
SS	Suction specific speed	
T	Torque	FL
t	Blade thickness	L
U	Inducer tangential velocity	LT^{-1}
u, v	Velocity components	LT^{-1}
V	Fluid absolute velocity	LT^{-1}
W	Fluid relative velocity	LT^{-1}
W.P.	Perimeter of wetted surface	L
Δy	Radial distance between streamlines	L
Z	Axial dimension	L
ΔZe	Axial distance from station to exit	L
α	Angle between fluid absolute velocity and tangential direction	deg
α_w	Blade leading edge wedge angle	deg
β	Angle between fluid relative velocity and tangential direction	deg
β^*	Angle between blade and tangential direction	deg
$<\gamma$	Blade taper angle	deg
δ	Deviation angle	deg
$\delta\beta^*$	Deviation angle due to vapor cavity or vapor cavity surface slope relative to the blade	deg
δ_e	Deviation angle at inducer exit	deg
δ_2	Deviation angle due to exit deviation (distributed value of δ_e)	deg
δ_o	Deviation angle due to inlet incidence	deg

SYMBOL	DESCRIPTION	UNITS
δ_I	Deviation due to fluid inertia (distributed value of δ_o)	deg
δ_w	Cavity collapse angle	deg
ϵ	Shear stress	FL^{-2}
δ^*	Boundary layer displacement thickness	L
η	Efficiency	
μ	Absolute viscosity	FTL^{-2}
ν	Kinematic viscosity	L^2T^{-1}
ρ	Density	FT^2L^{-4}
τ	Blade tangential spacing	L
τ_{cav}	Cavitation parameter	
τ_ℓ	Tangential space between blades occupied by fluid	L
τ_n	Blade spacing measured normal to blades	L
ϕ	Flow coefficient	
ϕ_{crit}	Critical flow coefficient	
ψ	Angle between streamtube and axial direction	deg
ψ_s	Head rise coefficient	
ψ_{ss}	Static head coefficient on the blade suction surface	
ψ_{sp}	Static head coefficient on the blade pressure surface	
ω	Inducer angular velocity	T^{-1}
σ	Blade solidity	
θ	Boundary layer momentum thickness	L
Λ	Hub/Tip radius ratio	
ξ	Blade camber	deg

Superscripts

'	Previous value

SYMBOL	DESCRIPTION	UNITS
-	Average value between axial stations	
=	Average value between streamtubes	
Subscripts		
e	Exit	
H	Hub	
i	Streamline number, 1,2,3 ---- NI	
j	Axial station number, 1,2,3 ----	
ℓ	Liquid or leakage	
LE	Leading edge	
m	Meridional direction	
n	Direction normal to the blade	
o	Inlet	
p	Pressure surface	
rel	Relative	
s	Suction surface	
ST	Streamline	
T	Tip	
z	Axial direction	
TE	Trailing edge	
u	Tangential	
v	Vapor condition	

B. STRESS AND VIBRATION

SYMBOL	DESCRIPTION	UNITS
$[A], [B], [C], [D], [E]$	Partitioned matrices of $[K]_T$	$[FL^{-1}], [FL]$
$[\bar{A}]$	Displacement function coordinate matrix	Mixed

SYMBOL	DESCRIPTION	UNITS
$\left[\bar{C}\right]$	Curvature matrix	$[L^{-1}]$
$\bar{D}$	Flexual rigidity $E\bar{t}^3/12(1 - \upsilon^2)$	[FL]
E	Modulus of elasticity	$[FL^{-2}]$
$\left[\bar{E}_B\right]$	Curvature coordinate matrix	Mixed
$\left[\bar{E}_M\right]$	Membrane elastic constants matrix	$[FL^{-2}]$
F_x, F_y, F_z	Force in coordinate direction	[F]
$\left\{F\right\}_N$	Generalized nodal force column matrix $\left[F_x, F_y, F_z, M_x, M_y, M_z\right]^T$	[F], [FL]
$\left[I\right]$	Unit diagonal matrix	[1]
$\left[K\right]$	Stiffness matrix	$[FL^{-1}]$
		[FL]
$\left[K\right]_T$ *	Reduced stiffness system matrix $\left[T\right]^T\left[K\right]_T\left[T\right]$	$[FL^{-1}]$ [FL]
M_x, M_y, M_z	Moment about coordinate axis	[FL]
$\left[M\right]$	Inertia matrix	$[FT^2L^{-1}]$, $[FT^2L]$
$\left[M\right]_T$ *	Reduced inertia system matrix $\left[T\right]^T\left[M\right]_T\left[T\right]$	$[FT^2L^{-1}]$, $[FT^2L]$
p	Pressure, + ve in + ve direction of $\bar{z}$	$[FL^{-2}]$
$\left\{q\right\}$	Generalized vibratory amplitude	[L] , [1]
R	Radius measured in x, y plane	[L]
R*	Radius measured along generator	[L]
R_G	Generator offset radius	[L]
$\left[R_1\right]$	Rotation matrix	[1]
T	Kinetic energy	[FL]

SYMBOL	DESCRIPTION	UNITS
$\left[T\right]$	Coordinate transformation matrix $\begin{bmatrix} I \\ -B^{-1}C \end{bmatrix}$	[1]
$\bar{t}$	Thickness of triangular element	[L]
$\left\{\bar{t}\right\}_N$	Nodal thickness column matrix $\left[\bar{t}_1 \ \bar{t}_2 \ \bar{t}_3\right]^T$	[L]
U	Internal strain energy	[FL]
u, v, w	Displacement in x, y, z directions	[L]
V	Potential energy	[FL]
$\left[\bar{V}_B\right]$	Bending elastic constants matrix $\begin{bmatrix} 1 & \upsilon & 0 \\ \upsilon & 1 & 0 \\ 0 & 0 & 2(1-\upsilon) \end{bmatrix}$	
$\left[\bar{V}_{B_1}\right]$	Bending stress elastic constants matrix $\begin{bmatrix} 1 & \upsilon & 0 \\ \upsilon & 1 & 0 \\ 0 & 0 & 1-\upsilon \end{bmatrix}$	
$\left[\bar{W}_M\right]$	Membrane strain coordinate matrix	
x, y, z	Rectangular coordinates	[L]
z_H	Lead height of generator measured at hub radius	[L]
$\left\{\bar{\alpha}\right\}$	Displacement function coefficient column matrix	Mixed
$\left\{\bar{\alpha}_t\right\}$	Thickness function coefficient column matrix	Mixed
$\left\{\delta\right\}$	Generalized displacement column matrix $\left[u \ v \ w \ \theta_x \ \theta_y \ \theta_z\right]^T$	[L], [1]

SYMBOL	DESCRIPTION	UNITS
$\bar{\epsilon}_{\bar{x}\bar{x}}, \bar{\epsilon}_{\bar{x}\bar{x}}$	Strain in x and y directions	[1]
$\bar{\epsilon}_{\bar{x}\bar{y}}$	Shear strain	[1]
$\left\{\bar{\epsilon}\right\}$	Membrane strain column matrix	[1]
θ	Wrap angle	deg
$\theta x, \theta y, \theta z$	Rotation about coordinate axis	[1]
λ	Generator lean angle	deg
ν	Poisson's ratio	[1]
ρ	Density	$[FL^{-3}]$
$\left\{\psi\right\}$	Coordinate matrix	[L]
ω	Natural frequency or angular velocity	$[T^{-1}]$
$\left\{\ \right\}$	Column matrix	
$\left\|\ \right\|$	Determinant	
cos $(x,\bar{y})$, etc.	Cosine of angle between x axis in common and $\bar{y}$ axis in local system	

Superscripts

-	Refers to local coordinate system
$\left[\ \right]^T$	Transpose of matrix $\left[\ \right]$

Subscripts

B	Bending
c	Centrifugal
H	Inducer hub
i	Parameter at node "i" (1,2,3)

SYMBOL	DESCRIPTION	UNITS
M	Membrane	
p	Pressure	
ss	Subsystem	
T	Inducer tip	
$[\ ]_N$	Matrix of nodal parameters	
$[\ ]_T$	System matrix	

NOTE: Symbol [1] represents dimensionless expression.